Wildfires, flowers and huddling penguins

Mathematical modelling of two-dimensional free boundary problems in nature

Samuel Joseph Harris

A dissertation submitted in partial fulfillment
of the requirements for the degree of
Doctor of Philosophy
of
University College London.

Department of Mathematics
University College London

March 28, 2025

Declaration

I, Samuel Joseph Harris, confirm that the work presented in this thesis is my own. Where information has been derived from other sources, I confirm that this has been indicated in the thesis.

Abstract

Natural phenomena are modelled as two-dimensional interfacial problems, and their equilibria, stability and evolution are considered analytically and numerically in this work. Wildfire spread is studied, where the harmonic pyrogenic wind induced by the fire and the resulting steady transport of oxygen to the fire line must be solved exterior to the wildfire. The corresponding coupled pair of conformally invariant governing equations - the Laplace and steady advection-diffusion equations - motivates the use of conformal mapping to determine the stability and nonlinear evolution of the fire line. The same conformal mapping method is applied to a free boundary problem with reciprocal growth law which offers a deterministic wildfire basic rate of spread effect rather than an ad-hoc constant traditionally used. Analytical solutions to this problem for growing ellipses and a class of polynomial lemniscates are also derived. Penguin huddle evolution is, from a mathematical modelling perspective, strikingly similar to wildfire spread, involving a steady transport of temperature by the wind. The penguin huddle interior is also modelled as a continuum, where the penguins rearrange themselves in the huddle to spread their heat. The resulting Poisson equation is conformally variant and so interior temperature is instead solved using the adaptive Antoulas–Anderson–least squares (AAA-LS) algorithm. This algorithm also solves Laplace problems in multiply connected domains, enabling the spread and merger of multiple wildfires to be computed by this method. Both ambient and pyrogenic winds are included into the single and multiple wildfire models and the results are compared, with good agreement, against experimental data and an existing wildfire model. A new algorithm based on the AAA-LS method is developed to solve mixed boundary value two-domain problems and to examine the electrostatic interaction between flowers and their pollinators. The two-domain AAA-LS algorithm is also applied to problems in vortex dynamics.

Impact statement

The research presented in this thesis could be put to beneficial use both inside and outside of academia. In an academic setting, this thesis presents and expands upon new and existing numerical methods which can efficiently and accurately solve interfacial problems. Such problems appear often in fluid dynamics, for example in two-dimensional potential flows, phase-change dynamics and viscous Stokes flow. New free boundary problems, such as wildfire fingering and reciprocal growth law problems, are proposed, with the resulting dynamics considerably different to classical viscous fingering. The development of the AAA-LS algorithm also offers a new approach to find numerical solutions of problems with multiple evolving free boundaries, and mixed boundary value problems involving coupled interior and exterior fluid regions. These new numerical tools can be easily used and adapted by future researchers to tackle further problems in fluid dynamics.

In a non-academic setting, this thesis is applicable in various fields. First is the study of wildfire spread, which is the primary focus of this thesis. Existing wildfire models are computationally expensive and/or include little to no wildfire-atmosphere coupling, limiting their ability to quickly and accurately predict dynamic wildfire spread. In this thesis, two substantial, alternative, conceptually simple and computationally efficient mathematical models describing wildfire spread and merger, including a two-way coupling with the surrounding wind field, are developed. These methods could be incorporated into wildfire modelling practices to more accurately capture the wildfire-atmosphere interaction without sacrificing computational efficiency. Furthermore, two new concepts in wildfire research are here proposed: the effect of oxygen transport on the wildfire spread; and the development of a deterministic equation for the basic rate of spread of the fuel. These effects reproduce phenomena observed in real-world wildfire spread, and hence offer potential insight into new mechanisms driving wildfire spread.

Second, penguin huddling is here researched. Such modelling has helped improve understanding of the thermodynamic processes involved in huddling, including the heat generation and spread within the huddle and the heat loss to the surrounding wind. It has also provided insight into the evolution of the penguin huddle over time and identified the optimum penguin huddle shape for given weather conditions. The penguin huddle problem is also analogous to two-phase melting/freezing problems, which have numerous applications in industry such as modelling freeze pipes and aircraft icing.

Third, the electrostatic interaction between a flower and its pollinators is explored. Electroreception among terrestrial arthropods is an emergent field of study and there is continued research into how these additional electrical cues help arthropods navigate the world around them. The efficient tools

developed here can be used to analyse this floral-arthropod electrostatic interaction and to understand how flowers present themselves electrically to potential pollinators. Improving this understanding is paramount to ensuring these crucial pollination channels remain open, especially in such an electrically noisy world.

Finally, vortex equilibria are here studied and found numerically. Such persistent vortex structures play a role in the dynamics of quasi-2D turbulence, such as in the Earth's oceans and atmosphere and those of the giant planets.

UCL Research Paper Declaration Form: referencing the doctoral candidate's own published work(s)

1. **For a research manuscript that has already been published** (if not yet published, please skip to section 2):

(a) **What is the title of the manuscript?** Fingering instability in wildfire fronts

(b) **Please include a link to or doi for the work:** https://doi.org/10.1017/jfm.2022.452

(c) **Where was the work published?** Journal of Fluid Mechanics

(d) **Who published the work?** Cambridge University Press

(e) **When was the work published?** 14 June 2022

(f) **List the manuscript's authors in the order they appear on the publication:** S.J. Harris and N.R. McDonald

(g) **Was the work peer reviewed?** Yes

(h) **Have you retained the copyright?** Yes

(i) **Was an earlier form of the manuscript uploaded to a preprint server (e.g. medRxiv)? If 'Yes', please give a link or doi:**

If 'No', please seek permission from the relevant publisher and check the

box next to the below statement:

☒ I acknowledge permission of the publisher named under 1d to include in this thesis portions of the publication named as included in 1c.

2. **For a research manuscript prepared for publication but that has not yet been published** (if already published, please skip to section 3):

(a) **What is the current title of the manuscript?**

(b) **Has the manuscript been uploaded to a preprint server e.g. medRxiv' ?**

If **'**Yes', please please give a link or doi:

(c) **Where is the work intended to be published?**

(d) **List the manuscript's authors in the intended authorship order:**

(e) **Stage of publication:**

3. **For multi-authored work, please give a statement of contribution covering all authors (if single-author, please skip to section 4):**

SJH: Writing, Conceptualization, Methodology, Software, Validation, Investigation, Visualization, Original draft preparation.

NRM: Writing, Conceptualization, Methodology, Investigation, Supervision, Reviewing and Editing.

4. **In which chapter(s) of your thesis can this material be found?** Chapters 1 and 3.

e-Signatures confirming that the information above is accurate (this form should be co-signed by the supervisor/ senior author unless this is not appropriate, e.g. if the paper was a single-author work):

Candidate signature: [redacted]

Date: 09/12/24

Supervisor/Senior Author signature (where appropriate): [redacted]

Date: 9 Dec 2024

UCL Research Paper Declaration Form: referencing the doctoral candidate's own published work(s)

1. **For a research manuscript that has already been published** (if not yet published, please skip to section 2):

(a) **What is the title of the manuscript?** Penguin huddling: a continuum model.

(b) **Please include a link to or doi for the work:** https://doi.org/10.1007/s10440-023-00578-2

(c) **Where was the work published?** Acta Applicandae Mathematicae

(d) **Who published the work?** Springer

(e) **When was the work published?** 14 June 2023

(f) **List the manuscript's authors in the order they appear on the publication:** Samuel J. Harris and N.R. McDonald

(g) **Was the work peer reviewed?** Yes

(h) **Have you retained the copyright?** Yes

(i) **Was an earlier form of the manuscript uploaded to a preprint server (e.g. medRxiv)? If 'Yes', please give a link or doi:** https://arxiv.org/abs/2305.07324

If 'No', please seek permission from the relevant publisher and check the

box next to the below statement:

☒ I acknowledge permission of the publisher named under 1d to include in this thesis portions of the publication named as included in 1c.

2. **For a research manuscript prepared for publication but that has not yet been published** (if already published, please skip to section 3):

(a) **What is the current title of the manuscript?**

(b) **Has the manuscript been uploaded to a preprint server e.g. medRxiv' ?**

If **'**Yes', please please give a link or doi:

(c) **Where is the work intended to be published?**

(d) **List the manuscript's authors in the intended authorship order:**

(e) **Stage of publication:**

3. **For multi-authored work, please give a statement of contribution covering all authors (if single-author, please skip to section 4):**

SJH: Writing, Conceptualization, Methodology, Software, Validation, Investigation, Visualization, Original draft preparation.

NRM: Writing, Conceptualization, Methodology, Investigation, Supervision, Reviewing and Editing.

4. **In which chapter(s) of your thesis can this material be found?** Chapters 1 and 4.

e-Signatures confirming that the information above is accurate (this form should be co-signed by the supervisor/ senior author unless this is not appropriate, e.g. if the paper was a single-author work):

Candidate signature: [redacted]

Date: 09/12/24

Supervisor/Senior Author signature (where appropriate): [redacted]

Date: 9 Dec 2024

UCL Research Paper Declaration Form: referencing the doctoral candidate's own published work(s)

1. **For a research manuscript that has already been published** (if not yet published, please skip to section 2):

(a) **What is the title of the manuscript?** Exact and numerical solutions of a free boundary problem with a reciprocal growth law.

(b) **Please include a link to or doi for the work:**
https://doi.org/10.1093/imamat/hxae014

(c) **Where was the work published?** I*MA Journal of Applied Mathematics*

(d) **Who published the work?** Oxford University Press

(e) **When was the work published?** 04 June 2024

(f) **List the manuscript's authors in the order they appear on the publication:** N.R. McDonald and Samuel J. Harris

(g) **Was the work peer reviewed?** Yes

(h) **Have you retained the copyright?** Yes

(i) **Was an earlier form of the manuscript uploaded to a preprint server (e.g. medRxiv)? If 'Yes', please give a link or doi:**

If 'No', please seek permission from the relevant publisher and check the

box next to the below statement:

☒ I acknowledge permission of the publisher named under 1d to include in this thesis portions of the publication named as included in 1c.

2. **For a research manuscript prepared for publication but that has not yet been published** (if already published, please skip to section 3):

(a) **What is the current title of the manuscript?**

(b) **Has the manuscript been uploaded to a preprint server e.g. medRxiv' ?**

If **'**Yes', please please give a link or doi:

(c) **Where is the work intended to be published?**

(d) **List the manuscript's authors in the intended authorship order:**

(e) **Stage of publication:**

3. **For multi-authored work, please give a statement of contribution covering all authors (if single-author, please skip to section 4):**

SJH: Writing, Conceptualization, Methodology, Software, Validation, Investigation, Visualization, Original draft preparation, Reviewing and Editing.

NRM: Writing, Conceptualization, Methodology, Software, Validation, Investigation, Supervision, Original draft preparation, Reviewing and Editing.

4. **In which chapter(s) of your thesis can this material be found?** Chapters 1 and 5.

e-Signatures confirming that the information above is accurate (this form should be co-signed by the supervisor/ senior author unless this is not appropriate, e.g. if the paper was a single-author work):

Candidate signature: [redacted]

Date: 09/12/24

Supervisor/Senior Author signature (where appropriate): [redacted]

Date: 9 Dec 2024

UCL Research Paper Declaration Form: referencing the doctoral candidate's own published work(s)

1. **For a research manuscript that has already been published** (if not yet published, please skip to section 2):

(a) **What is the title of the manuscript?** Modelling wildfire spread and spotfire merger using conformal mapping and AAA-least squares methods

(b) **Please include a link to or doi for the work:**
https://doi.org/10.1016/j.envsoft.2024.106303

(c) **Where was the work published?** Environmental Modelling & Software

(d) **Who published the work?** Elsevier

(e) **When was the work published?** 18 December 2024

(f) **List the manuscript's authors in the order they appear on the publication:** Samuel J. Harris, N.R. McDonald

(g) **Was the work peer reviewed?** Yes

(h) **Have you retained the copyright?** Yes

(i) **Was an earlier form of the manuscript uploaded to a preprint server (e.g. medRxiv)? If 'Yes', please give a link or doi:** https://arxiv.org/abs/2408.06205

If 'No', please seek permission from the relevant publisher and check the

box next to the below statement:

☒ I acknowledge permission of the publisher named under 1d to include in this thesis portions of the publication named as included in 1c.

2. **For a research manuscript prepared for publication but that has not yet been published** (if already published, please skip to section 3):

(a) **What is the current title of the manuscript?**

(b) **Has the manuscript been uploaded to a preprint server e.g. medRxiv'?**

(c) **Where is the work intended to be published?**

(d) **List the manuscript's authors in the intended authorship order:**

(e) **Stage of publication:**

3. **For multi-authored work, please give a statement of contribution covering all authors (if single-author, please skip to section 4):**

SJH: Writing, Conceptualization, Methodology, Software, Validation, Investigation, Visualization, Original draft preparation.

NRM: Writing, Conceptualization, Methodology, Investigation, Supervision, Reviewing and Editing.

4. **In which chapter(s) of your thesis can this material be found?** Chapters 1,6,7 and 10.

e-Signatures confirming that the information above is accurate (this form should be co-signed by the supervisor/ senior author unless this is not appropriate, e.g. if the paper was a single-author work):

Candidate signature: [redacted]

Date: 06/01/25

Supervisor/Senior Author signature (where appropriate): [redacted]

Date: 6 Jan 2025

UCL Research Paper Declaration Form: referencing the doctoral candidate's own published work(s)

1. **For a research manuscript that has already been published** (if not yet published, please skip to section 2):

(a) **What is the title of the manuscript?**

(b) **Please include a link to or doi for the work:**

(c) **Where was the work published?**

(d) **Who published the work?**

(e) **When was the work published?**

(f) **List the manuscript's authors in the order they appear on the publication:**

(g) **Was the work peer reviewed?**

(h) **Have you retained the copyright?**

(i) **Was an earlier form of the manuscript uploaded to a preprint server (e.g. medRxiv)? If 'Yes', please give a link or doi:**

If 'No', please seek permission from the relevant publisher and check the

box next to the below statement:

I acknowledge permission of the publisher named under 1d to include in this thesis portions of the publication named as included in 1c.

2. **For a research manuscript prepared for publication but that has not yet been published** (if already published, please skip to section 3):

(a) **What is the current title of the manuscript?** Modelling floral and arthropod electrostatics using a two-domain AAA-least squares algorithm

(b) **Has the manuscript been uploaded to a preprint server e.g. medRxiv'?** Yes

If **'**Yes', please please give a link or doi: https://arxiv.org/abs/2411.02195

(c) **Where is the work intended to be published?** SIAM Journal on Applied Mathematics

(d) **List the manuscript's authors in the intended authorship order:** Samuel J. Harris, Ryan A. Palmer and N.R. McDonald

(e) **Stage of publication:** Reviewed, in submission

3. **For multi-authored work, please give a statement of contribution covering all authors (if single-author, please skip to section 4):**

SJH: Writing, Conceptualization, Methodology, Software, Validation, Investigation, Visualization, Original draft preparation.

RAP: Writing, Conceptualization, Methodology, Software, Validation, Investigation, Visualization, Supervision, Original draft preparation.

NRM: Writing, Conceptualization, Methodology, Investigation, Supervision, Reviewing and Editing.

4. **In which chapter(s) of your thesis can this material be found?** Chapters 1 and 8.

e-Signatures confirming that the information above is accurate (this form should be co-signed by the supervisor/ senior author unless this is not appropriate, e.g. if the paper was a single-author work):

Candidate signature: [redacted]

Date: 09/12/24

Supervisor/Senior Author signature (where appropriate): [redacted]

Date: 9 Dec 2024

UCL Research Paper Declaration Form: referencing the doctoral candidate's own published work(s)

1. **For a research manuscript that has already been published** (if not yet published, please skip to section 2):

(a) **What is the title of the manuscript?**

(b) **Please include a link to or doi for the work:**

(c) **Where was the work published?**

(d) **Who published the work?**

(e) **When was the work published?**

(f) **List the manuscript's authors in the order they appear on the publication:**

(g) **Was the work peer reviewed?**

(h) **Have you retained the copyright?**

(i) **Was an earlier form of the manuscript uploaded to a preprint server (e.g. medRxiv)? If 'Yes', please give a link or doi:**

If 'No', please seek permission from the relevant publisher and check the

box next to the below statement:

I acknowledge permission of the publisher named under 1d to include in this thesis portions of the publication named as included in 1c.

2. **For a research manuscript prepared for publication but that has not yet been published** (if already published, please skip to section 3):

(a) **What is the current title of the manuscript?** Vortex equilibria using least-squares methods.

(b) **Has the manuscript been uploaded to a preprint server e.g. medRxiv'?** No

If **'**Yes', please please give a link or doi:

(c) **Where is the work intended to be published?** Theoretical and Computational Fluid Dynamics

(d) **List the manuscript's authors in the intended authorship order:** Samuel J. Harris and N.R. McDonald

(e) **Stage of publication:** In submission

3. **For multi-authored work, please give a statement of contribution covering all authors (if single-author, please skip to section 4):**

SJH: Writing, Conceptualization, Methodology, Software, Validation, Investigation, Visualization, Original draft preparation, Reviewing and Editing.

NRM: Writing, Conceptualization, Methodology, Software, Validation, Investigation, Supervision, Original draft preparation, Reviewing and Editing.

4. **In which chapter(s) of your thesis can this material be found?** Chapters 1 and 9.

e-Signatures confirming that the information above is accurate (this form should be co-signed by the supervisor/ senior author unless this is not appropriate, e.g. if the paper was a single-author work):

Candidate signature: [redacted]

Date: 09/12/24

Supervisor/Senior Author signature (where appropriate): [redacted]

Date: 9 Dec 2024

Acknowledgements

When writing my Master's dissertation, I made very few acknowledgments, thinking they had to be very official like those in journal articles. For my PhD, I wish to rectify that by acknowledging everyone! (As a warning, this may be quite long).

First and foremost, I want to thank my amazing PhD supervisor Robb. I have truly appreciated the wisdom, dedication, kindness and patience you have shown me during my PhD, I really would not have made it this far without you. Our meetings together would always brighten my day, and I always thoroughly enjoyed everything we discussed, from conformal mapping to departmental cakes to news of your dog Sid and two cats Bert and Ernie. Thank you as well for all the proofreading you've done for me over the years! I am really proud of the work we have produced and I shall truly miss our weekly meetings together.

I also want to thank Ryan for your kindness, friendship and great humour. Thank you for reaching out to me at conferences and for taking a chance on me to help in your research. Our collaboration has been extremely fruitful and enjoyable and it has been your friendliness, optimism and 'blue-sky thinking' that has done that. Thank you also for your enormous support in my future career steps and I thoroughly look forward to continuing to work with you during my Postdoc.

I also extend my thanks to the UKRI Engineering and Physical Sciences Research Council (EPSRC) for funding my PhD for the past four years.

Thank you to Luciano and Niki, who I met when I was applying to UCL nine years ago. They have always been incredibly supportive during my entire journey through UCL; it is a pleasure and an inspiration to know you both and to have seen your progressions through UCL also.

Thank you to my Master's supervisor Robert for making my first research experience such an enjoyable one, and for encouraging me to apply for a PhD. Thank you to Steven and Mohit for examining my PhD upgrade, your comments and feedback were invaluable in improving my work and in motivating me to continue my PhD. And thank you to my thesis examiners Sergei and Ian for agreeing to assess my final thesis; I truly appreciate your time, consideration and care in examining my work. Thanks also to my second supervisor Philip for your kindness, support and useful advice throughout my PhD.

I want to acknowledgment UCL and the Department of Mathematics in particular for accommodating me for eight years. I have always felt very welcomed at UCL, which has allowed me to thrive during my time here. Thank you for making me feel at home. A shoutout goes to the departmental Green Team, of

which I was an active member throughout my PhD. Thank you to all the staff and postdocs of the maths department and for the hardworking office staff. Thank you Holly for all of your invaluable support, especially during difficult times, for your friendship and for making the office a brighter and happier place for all. Thank you Soheni for all your help with expense claims (sorry I got so much wrong!) and for everything else you have done for me during my entire time at UCL. Thanks also to Des for your kindness, for helping me with expenses and finances and for catching things that I missed! Thank you Nancy for our fun chats in the KLB and for all the effort you put into making sure us PhD students had everything we needed. Special shoutouts go to Helen, Sidrah, Ibrahim and Richard also for your help in all things PhD and teaching related. I also want to thank the department for all the amazing food I've eaten and events I've attended over the years, the De Morgan dinners and Christmas parties were absolute highlights!

I have also had the pleasure of working alongside many other fantastic PhD students and close friends during the past four years. Everyone has been incredibly friendly, supportive and an absolute inspiration, and they should all be very proud of what they have achieved and what they continue to achieve during their PhDs.

I first want to thank my Master's and PhD buddy and close friend TD, who let me know of the PhD opportunity in the first place and is the reason I'm here. Thank you for all the game nights, for your amazing cooking, your shared love of puns and for being a true friend I can confide in. A shoutout goes to TD's very comfy sofa too, on which I have crashed many times, and her 'flatmates' Bearnoulli and Mallorca! I also want to thank Ellen and her partner Dom for all the fun nights on boardgame arena, for our many fun trips together, for Pingu and for making me cry laughing on multiple occasions.

A big thank you goes to Molly for making my time in the office so fun. I always thoroughly enjoyed our deep and lengthy 'networking' chats, and seeing the many amazing photos of your dog Dug, the floofiest boy there is. You always made me smile and laugh whenever I needed it most, and have made my PhD experience truly unique and enjoyable, thank you! I want to thank the other members of the 'KLB Black Hole' too and our fun post-it note back-and-forths. Thank you to Emily who has an absolute heart of gold, and has always been so kind and supportive to me. It was always a pleasure to chat to you about research, and I'm glad I could convince you of the merits of Paint 3D. Thank you to Aporv, who always greeted me with a big smile followed by a contagious laugh; thank you for making me smile too and for your shared appreciation of Essex. Thank you Giovanni for always amazing me with your knowledge, your warmth, your stellar piano playing and your amazing jumpers. Thanks also to Kelvin for all our fun office chats and for helping us stomp to victory in the PhD pub quiz. And thank you to Haeng for your

shared enthusiasm of the departmental food, and for being a great desk mate over the years.

I also want to thank Courteney, my PhD little sister. It has been a pleasure to get to know you and to see you progress through your PhD. It has been an incredibly difficult journey, but I am inspired by your perseverance, your wisdom and your drive. Thank you for all your support in my PhD journey too, and for being my friend. I wish you the best of luck for the rest of your studies.

Thank you to Claudia and Antonio (and his partner David too) for all the fun hangouts, chats and coffee/cake breaks we had. Thank you to Anushka for always greeting me with such happiness, and for our great chats in the office. Thank you to Myles and Luke for our early morning office chats, and to Bishal and Devi for the late night office chats. Thank you to Enric for your shared love of Doctor Who, and Yohance for your shared love of the Nintendo Switch. Thanks to Gareth and Gwen for all the friendliness and support you've shown me over the years (I've forgiven you for the paint incident). Thank you to Amalia for being one of the first and continued friends I made during my PhD, and for the fun post-Covid office days we had. Thank you to Maria for your warmth and for the greatly appreciated updates on your three dogs! Thank you to Zonglun for your inspiring idioms and your amazing role as the lunchtime marshall. Thanks to Vivienne for sharing the UCL experience with me for the past eight years. Thanks to Dan for the office pizza parties and our fun Just Dance nights. Thank you Ivan for your friendliness and for teaching me how to pronounce your name correctly (my biggest achievement of the PhD). Thank you Les for your continual kindness, enthusiasm and support in saving the koalas and penguins. Thank you Alexis for making me laugh and trying to convince me to join you for running, and thank you Ella for always greeting me with a smile and teaching me all about giraffes. Thank you to Arjun and Nikhita for convincing me to add more spices to my life. Thank you to Michael, Kobe, Megan, Elvar and Teymour, Tomasz, Jamie, Ewan, Wesley, Alice, Helena, Clara and Sara, Tiger, Venkata, Edwina, Adrian, Spencer and everyone else in the office for your friendliness and for the fun Friday night drinks and lunchtime chats we all had.

And thank you to the KLB office. It is hard to describe this office, the temperature is forever variable and the furnishings are notably dated. But there is a warmth and camaraderie about the place that I can't explain, which makes it such a wonderful environment to work (and oftentimes not work) in. Thank you for all the memories: the golf ball of fame; the afternoons solving the Chalkdust cryptic crosswords; the intense poll for naming the new plants; cake LB; the antics of Possum O'Possum; and the introduction of Dr. Priscilla Hogarth-Snookerman as the KLB patron saint, to name but a few.

Thank you also to all the friends and wonderful people I met at conferences, specifically those at the

Coimbra Forest Fire Conference and the Banff Looping Networks Workshop. I also want to thank Carole for their inspiring conference talk on Adélie penguins and our useful discussion afterwards.

Thank you to Sophia, my salsa buddy! Thank you for our dances together, our lunchtime meetups and for your continual and heartfelt support during my PhD. I want to shoutout the UCL Salsa Society as well for sparking my passion for dance. Thanks especially to the wonderful teachers Daniel, Steve, Maria, Feda and Alexa for your kindness and enthusiasm.

I also want to thank my friends from undergraduate and my friends around the world. Thank you to Lea, who has been a close friend of mine since we first met at the start of our undergrad. Thank you for always believing in me, for introducing me to Ceroc dancing and for all the fun hangouts and visits I've had to your home. Thank you to Sara for your warmth, kindness and compassion, our fun meetups and our shared love of cats. Thank you Claire for the amazing times we had at undergraduate and when I visited you in South Korea over the summer. And thank you to my German penpal Sarah, my French penpal (and undergrad friend) Caroline and my Japanese penpal Ayaka; I always get such a buzz receiving your letters and messages.

Thank you as well to my friends at home in Essex who have always been enthusiastic and supportive of my PhD and who have always helped me have fun, especially during difficult times in my PhD. Thank you to Lewis (and his brother Dean) for all the fun gaming nights, F1 racing days, the continual (and much appreciated) tech support and for helping inspire my love of maths back when we were at school together. Thank you to Will and Connor for many a fun night out drinking, watching the boxing and go-kart racing together. Thanks to Billy for all the fun DnD and Chinese takeaway nights we had, for your great music recommendations and the many fun online games we've played over the years.

Thank you to Alex (also known as Alexa) and her two dogs Sparky and Blondie for all our fun times together. Your messages always make me laugh far too hard and your continual support never fails to motivate me and cheer me up. Thank you to Kai and Bex for the many fun game nights, our shared enthusiasm for puzzles and Pokémon, for all your care and support and for making me feel so welcome in your lovely home. Thanks also to their son Noah: thank you for always being excited to see me, for making me laugh and for always showing me all the cool toys and jigsaw puzzles you got! Thank you to Matt, Rob and Riley for all the fun times at Wayland Games and the great meals at the Roebuck, it is always a fun night out with you. And thank you to Chloe, Beth, Joe, Chris, Nathan, Ben and Maddie.

I also want to thank my friend Phoebe, who is one of my closest and oldest friends. She is an inspiration

to me and so many others, and has been a continual source of support throughout my PhD. Thank you for your belief in me, for our many years of amazing friendship, and our in depth Doctor Who discussions. Thank you also to Karl, Nina, and Phoebe's beautiful dog Nola and duprasi Peanut for all of the fun memories we've had.

Thank you to Swimming Tales: the swimming pool I worked at for six years and have since regularly swum at throughout my four year PhD. Everyone I've met and worked with there has always been incredibly friendly, funny and supportive of my journey throughout UCL. It has been an absolute pleasure to work and swim there, and a crucial reminder how important exercise is for your physical and mental health. I especially want to thank Tracy and Shaun for their continual support and regular morning inspiration, and special shoutouts go to Lee, Dina, Freddie, Robyn, Paige, Josh, Alex and Hannah. I also want to thank the Hullbridge scout group for helping shape the person I am today. Thanks especially to Ian, Jackie, Jason, Don and Kevin for all of your support.

A special thanks to the Sweyne Park School where I studied my GCSE and A-Levels. Thanks especially to Mr Kashem, Mr Garrod, Mrs Seal and Mrs Pemberton for inspiring my love of maths, in addition to all the other amazing teachers in the maths department. Thank you to Mr Hodgkinson for being a fantastic mentor and inspiration to me, and Dr Robertson for all his support and help in getting me into UCL. Thank you also to Ms Smith for her care and dedication both to me and to my year group, and to Ms Jameson for being a supportive and friendly form tutor.

And last but certainly not least, I want to thank my amazing family. In particular, I want to thank Mum, Dad, Beth and Joe. My family has been my absolute rock throughout my PhD, and have always given me an incomparable amount of love, support and enthusiasm in everything that I do. They have guided me during my lows and celebrated the hardest during my highs. I would not have been able to make it through my PhD without my family, I love them all dearly and I am truly grateful for everything they have done and continue to do for me. Thank you Mum for our good late night hangouts, our maths chats and salsa lessons, for being my Pokémon Go buddy and for always reassuring me that today will be a good day. Thank you Dad for the Mario Kart, the Warhammer, our classic Doctor Who binge and our yearly golf holidays which are always so fun. Thank you to Beth, you are my continual source of inspiration and guidance and I always thoroughly enjoy our cinema trips, baking sessions and Monday movie and TV nights together. And thank you Joe for your kindness and compassion, you are a valued addition to our family and I always enjoy our videogame chats and our theme park visits!

I also want to thank our beautiful cats Ron, Minnie and Dora who always brighten my days at home,

despite the numerous birds and mice they bring in! I also want to remember our former cats Dave, Gypsy and Trampy who I also had many happy memories with.

I want to thank my extended family too. Thank you Granny for all the lovely phone chats and visits we've had, we always have a good laugh together! Thank you to Grandad Colin, Uncle Neil and their lovely dog Emma for all the great visits I've had to see you at Alice Holt and on Hayling Island. Thank you to my Uncle Steve, Aunty Al and my cousins Becky, Millie and Dan for introducing me to UCL in the first place. I also want to remember and thank my family members who have passed away: Grandad, Grandma, Nannie and Grandad Teabag. This thesis is dedicated to you.

Finally, I want to thank my work laptop and my gaming PC for all the coding jobs they have done for me over the past four years (sorry!). Thank you to my work chair and desk for being the comfiest and best positioned in the KLB. I want to thank Nintendo for always giving me amazing games to play and inspiring music to listen to. And I want to thank anyone and everyone I have interacted with who I haven't mentioned in these acknowledgements. Every person I have ever met, however briefly, has influenced the direction my life has taken, and so I want to thank each and every one of you for getting me to where I am today.

Contents

List of abbreviations

The following abbreviations are used throughout this thesis. Each abbreviation is also defined the first time it appears in this thesis:

- AAA = adaptive Antoulas Anderson,
- AAA-LS = adaptive Antoulas–Anderson–least squares,
- AR = aspect ratio,
- CA = cellular automata,
- CFD = computational fluid dynamics,
- CFE = curvature flow equation,
- CS = curve-shortening,
- FEM = finite element method,
- LHS/RHS = left/right hand side,
- LS = least-squares,
- ODE/PDE/SDE = ordinary/partial/stochastic differential equation,
- PG = Polubarinova-Galin,
- RCA/RCL = rate of change of area/length,
- RE = relative error,
- RK = Runge-Kutta,
- RK1/RK2/RK4 = first/second/fourth order Runge-Kutta timestepping,
- RMSE = root mean-squared error,
- ROS = rate of spread,
- SC = Schwarz-Christoffel,
- WOZ = Wu, Overman and Zabusky (Wu et al., 1984).

Chapter 1

Introduction

1.1 Interfacial problems in nature

Nature gives rise to a plethora of physical systems and environmental problems, which are as diverse and intricate as they are fascinating. However, upon closer examination, many of these problems share common characteristics, to the extent that they may be mathematically modelled by similar systems of governing equations.

Furthermore, it is equally fascinating how simple, reduced-order, two-dimensional models of complex three-dimensional problems are still capable of reproducing the fundamental features of these physical systems at a fraction of the computational cost and complexity. In the physical systems considered in this thesis, the problems can be reduced to the analysis of a free boundary: the finite, closed curve separating two distinct regions, which is allowed to move and spread freely (i.e. unimpeded by walls). The only inputs then required are the boundary data and a handful of relevant physical parameters.

The original aim of this thesis was to examine in detail one such physical system: the spread and evolution of wildfires. Indeed, the bulk of this thesis remains focused on the modelling of wildfire spread. However, the research has expanded to include the application and extension of the mathematical modelling techniques developed to a range of other environmental problems. This section comprehensively introduces the wildfire problem and the other related natural boundary value problems that can be solved using similar methods.

1.1.1 The global wildfire challenge

Wildfires are an inevitable and necessary feature of the Earth, with periodic and controlled burns helping to regulate ecosystems (Pausas and Keeley, 2019). Yet climate change predictions indicate a continued, substantial shift in global weather, with fire weather conditions (as defined in e.g. Jolly et al. (2015)) forecast to increase worldwide over the coming decades. This would result in an enhanced level of 'fire danger' and an increased risk of catastrophic wildfire development (Arnell et al., 2021; Masson-Delmotte et al., 2021; Hetzer et al., 2024). The growing prevalence of wildfires is now a global phenomenon with large, dynamic wildfires - so called mega fires - increasing in frequency and intensity worldwide (Attiwill and Binkley, 2013). Consequently, wildfire research is receiving growing attention and there is a renewed effort to improve our understanding of the complex, nonlinear dynamics and thermodynamics associated with wildland fire spread.

There are many active branches of wildfire study, each presenting their own persisting challenges. These include (but are not limited to): the combustion of different fuel types (Santoni et al., 2014; Liu et al., 2021; Sullivan et al., 2022); distribution of fuels in a fuel bed (Catchpole et al., 1989; Khan et al., 2023); investigation of terrain influence on fire spread (Malangone et al., 2011; Ambroz et al., 2019; Hilton and Garg, 2021; Ribeiro et al., 2023); generation and spread of spotfires (Boychuk et al., 2009; Martin and Hillen, 2016; Bonta et al., 2017; Urban et al., 2019); and the deployment and optimisation of fire management and suppression efforts (Izhaki and Adar, 1997; Hu and Sun, 2007; Ausonio et al., 2021; Yfantidou et al., 2023). The wildfire research presented in this thesis focuses on the following two topics: the modelling and simulation of wildfire spread (Weber, 1991; Papadopoulos and Pavlidou, 2011; Bakhshaii and Johnson, 2019); and the coupled interaction of the wildfire with the atmosphere (Clark et al., 1996a; Sun et al., 2009; Mandel et al., 2011; Bakhshaii and Johnson, 2019).

1.1.2 Classification and summary of existing wildfire models

Wildfire modelling is used in all three regimes of pre-, mid- and post-fire analysis: to model a hypothetical future wildfire and assess the wildfire risk on a given landscape; to predict the future spread of a currently active wildfire; and to reproduce and analyse the spread of a previous wildfire event. Experimental, observational, mathematical and computational techniques have all been used to develop a variety of wildfire models over the past 80 years - see the review articles of Weber (1991); Perry (1998); Pastor et al. (2003); Sullivan (2009a,b,c) and Bakhshaii and Johnson (2019).

Wildfire spread - ie flame propagation across a fuel bed - is described physically as follows (Weber, 1991): an ignition source, (e.g. a lit match) heats up some element(s) of fuel (e.g. grass) to its 'ignition

temperature', at which point it ignites. The now burning fuel then transfers heat to surrounding fuel elements until they ignite, and hence the fire propagates. The ignition and combustion processes, and the relative contributions of the conductive, convective and radiative heat transfer methods, are still not fully understood and are the subject of ongoing research (Weber, 1991; Sullivan, 2009a; Frankman et al., 2012; Hilton et al., 2016). Such an investigation is not performed in this thesis; instead the propagation of the wildfire over time is to be modelled.

Pastor et al. (2003) defines four types of wildfire

- Surface fires: fires spreading across a low layer of surface fuel, for example grasses, heather, fallen leaves and twigs, and shrubs less than 1.8m tall (Mell et al., 2007).
- Crown fires: for example forest fires, where the wildfire extends up into the canopy layer of the trees.
- Spotting fires: firebrands are ejected from the main fire to ignite smaller 'spotfires' ahead of the main fire line.
- Ground fires: fire spread through the organic soil level, below the surface.

Surface fires are primarily considered in this thesis, with some investigation into spotting fires and how these multiple wildfires interact and influence each other. It should be noted that the stochastic generation of these spotfires is not explored in this thesis, nor is the fully 3D scenario of crown fires. Weber (1991) then defines three types of wildfire model

- Statistical: these ignore the physical mechanisms of fire spread and instead try to match the model outputs to test fires.
- Empirical: some physical mechanisms are included to some degree, e.g. heat transfer is acknowledged but the methods of heat transfer are not distinguished between.
- Physical: all fundamental physical mechanisms of fire spread are included.

Terminology varies between reviewers (Perry, 1998; Pastor et al., 2003) and some break the definitions down further (Sullivan, 2009a,b). Statistical and empirical models can give accurate fits to test fires but often fail to sufficiently match real world fire data. Physical models offer more detail, yet much is still unknown about the combustion and heat transfer processes, leaving these models incomplete. Empirical models thus seem a good compromise.

The first surface fire spread model was that of Fons (1946), a physical model measuring the rate of spread between discrete fuel blocks (or 'particles'). Thereafter, a flurry of physical models were developed (see table 1 of Pastor et al. (2003)) with varying preferences for certain heat transfer mechanisms over others. Statistical and empirical models were more favoured practically; the two most widely-used and successful models (which are still used today (Finney, 1998; Andrews, 2018)) were those of Rothermel (1972) and McArthur (1966).

Another model of note is the empirical model of Markstein (1951). In this work, the effects of radiative and convective heat transfer are combined into a single 'basic rate of spread' term and a curvature correction term is included to better match the model outputs to experimental results. The resulting equation for the normal velocity of the fire line is similar to equations seen in curve-shortening (CS) literature (Gage and Hamilton, 1986; Grayson, 1987; Dallaston and McCue, 2016). In the case of wildfires, the area enclosed by the curve grows. The effects of ambient wind and terrain can be easily added to the model (Roberts, 1993; Mallet et al., 2009; Hilton et al., 2016) and Markstein (1964) also included a term involving the normal flow of gas from the unburnt region to the flame front, see their equation (B-6). This was not a pre-existing flow, but rather a wind generated by the fire itself.

1.1.3 Wildfire-atmosphere modelling

Despite the success of models such as that of Rothermel (1972), there was still the need to include additional physics into the wildfire modelling. In particular, there was growing interest in coupling the wildfire spread to the surrounding wind field (Clark et al., 1996b). Dynamic weather conditions such as strong, volatile winds cause equally dynamic and often unpredictable wildfire spread (Viegas et al., 2012; Wheeler et al., 2015; Thomas et al., 2017). Furthermore, the wildfire itself affects the overall wind field: the wildfire generates its own wind source known as the pyrogenic wind (Smith et al., 1975; Beer, 1991; Hilton et al., 2018) and ejects air into the atmosphere via a 'fire plume'. Both the fire plume and the pyrogenic wind perturb the background wind field, which in turn affects the wildfire spread, resulting in a two-way coupling between the fire dynamics and the wind field.

Advances in computational fluid dynamics (CFD) allowed for the creation of such coupled wildfire-atmosphere models. A review of these are given in Papadopoulos and Pavlidou (2011) and Bakhshaii and Johnson (2019) and include the semi-coupled models FIRETEC (Linn et al., 2002) and WFDS (Mell et al., 2007), and the fully coupled models CAWFE (Clark et al., 1996b,a), WRF-FIRE (Mandel et al., 2011) and ForeFire/Meso-NH (Filippi et al., 2011). While able to incorporate complex, coupled wildfire-atmosphere interactions, these three-dimensional CFD models come with a high computation cost, and

are largely not able to reproduce wildfire data in real time - see table 1 of Bakhshaii and Johnson (2019). These models are thus well suited to pre- and post-fire research, yet there remains a demand for accurate wildfire-atmosphere models which run faster than real time and hence can be used operationally in mid-fire scenarios.

To develop these types of operational wildfire-atmosphere models, there are two current trajectories. The first is to rely on the creation of even more powerful supercomputers which can perform CFD techniques quickly. The second is to create a simplified, reduced-order model, which still produces a sufficiently accurate approximation of the coupled wildfire-atmosphere iteraction and the resulting wildfire spread, yet requires much simpler numerical models that are computationally efficient and quick to run. The second approach that is taken in this thesis.

One common simplification is to reduce the fully three-dimensional problem to two-dimensions, and model the propagation of the two-dimensional fire line[1] - the boundary separating the burnt and unburnt regions of fuel. This is particularly suitable when modelling surface fires which are sufficiently flat when compared to their horizontal length scale (Sharples et al., 2013; Hilton et al., 2016). Existing fast and accurate numerical methods can then be used to model the surface fire spread. Cellular automata (CA) models have been used successfully (Achtemeier, 2012; Freire and DaCamara, 2019; Quaife and Speer, 2021); these essentially split the domain into a grid and classify each square by whether the fuel there is unburnt, burning or fully burnt. These methods are only as accurate as their mesh and implementing a finer mesh for improved accuracy can cause a rapid increase in computation time. Furthermore, CA can struggle to respond to changes in wind speed and fuel moisture, and may not be able to reproduce all the physical processes of wildfire spread (Finney, 1998; Achtemeier, 2012).

An alternative approach is to develop a continuum model which directly tracks the evolving fire line, viewing it as a two-dimensional Jordan curve evolving over time. Sethian (1985) explored such a model derived from experimental results in Markstein (1951), and Osher and Sethian (1988) subsequently developed a numerical method based on Huygens' principle (see e.g. Finney (1998)) to compute the evolution of the fire line. This was the foundation of the level set method (Sethian, 2001) which has since been used successfully (Mallet et al., 2009; Sharples et al., 2013; Hilton et al., 2016) and is the basis of the SPARK framework (Miller et al., 2015).

[1] This is also called the fire front or fire perimeter.

1.1.4 The pyrogenic potential model of Hilton et al. (2018)

Over nearly the past decade, Hilton, Sharples and their colleagues have also developed a successful two-dimensional continuum model of surface fire spread which incorporates a dynamic wildfire-atmosphere interaction, see for example Hilton et al. (2018); Sharples and Hilton (2020) and Sharples et al. (2022). In their model, it is assumed that the wildfire spreads on flat terrain through a single type, homogeneously distributed surface fuel, thus the wildfire evolution is affected by only two factors. The first is a basic rate of spread (ROS) term: some (known) constant capturing the physical, chemical and thermodynamic processes of combustion and heat transfer for a given fuel element. The second is the surrounding wind field: this is in turn composed of some constant, unidirectional ambient wind and the self-induced pyrogenic wind.

As introduced in Sect.1.1.3, wildfires generate their own wind field known as a pyrogenic (or fire) wind (see e.g. Hilton et al. (2018)). This is caused due to a buoyant upflow of air over the burnt region of the wildfire - the feature known as the fire plume - which draws in surrounding air at the surface level (Smith et al., 1975). Pyrogenic winds with velocities of up to 3 ms^{-1} have been observed (Lareau and Clements, 2017) and Trelles and Pagni (1997) found from their numerical simulation of the 1991 Oakland Hills fire that the pyrogenic wind rapidly increased from 2.6 ms^{-1} to 13.0 ms^{-1} as the fire intensified. Following the work of Hilton et al. (2018), the pyrogenic wind can be written as the gradient of some pyrogenic potential function ϕ, which must be solved for in the region exterior to the fire line.

The so-called 'pyrogenic potential model' of Hilton et al. (2018) and its resulting extensions (a summary is given in Sharples et al. (2022)) have been shown to perform well, demonstrating good agreement between experimental wildfire data on the metre and tens of metres scales, with outputs computed in the order of seconds (Sharples and Hilton, 2020). It can replicate features of wildfire spread that existing two-dimensional models cannot, including the rounding of the fire line into a parabolic shape and the attraction of two disjoint fire lines towards each other. Additional factors can also be incorporated into the model, including terrain (Hilton and Garg, 2021) and vorticity effects (Sharples and Hilton, 2020).

The main aim of the wildfire research performed in this thesis is to develop an alternative, simple, two-dimensional wildfire-atmosphere model inspired by the pyrogenic potential model of Hilton et al. (2018) which is also computationally efficient and captures the main features of the wildfire spread. The techniques developed here are immediately capable of incorporating numerous extensions, such as heterogeneous fuelbeds and firebreaks, terrain effects, wildfire merger and fire-related vortices, with no substantial change in the fundamentals of the numerical methods and no significant addition to their runtime. While the pyrogenic potential model uses the SPARK framework (Miller et al., 2015), this

thesis introduces two new numerical methods to the field of wildfire research.

1.1.5 Conformal mapping method

The first numerical procedure is based on conformal mapping and is used exclusively for scenarios involving the growth of only a single wildfire. Conformal mapping is the transformation of a two-dimensional domain in the 'physical' $z-$plane to a corresponding domain in another 'canonical' $\zeta-$plane, where the angles between curves are locally conserved under the mapping (Brown and Churchill, 2009). By the Riemann mapping theorem, such a map between domains always exists and thus the exterior wildfire region (and the fire line itself) can be transformed to the desired canonical domain - for example the exterior of the unit disk - for all time as the fire line evolves. Some partial differential equations (PDEs) are said to be 'conformally invariant' - they are unchanged under the conformal mapping (Cummings et al., 1999; Bazant, 2004). The Laplace equation, which governs the pyrogenic wind, is an example of such a conformally invariant equation which permits the pyrogenic potential to be solved for in the canonical domain. Wind and other dynamical effects on the wildfire can then be incorporated into a single equation of Polubarinova-Galin (PG) type (see e.g. Howison (1986)) in terms of the time-dependent conformal map $z = f(\zeta, t)$ from the unit disk exterior to the fire line exterior at time t.

Similar approaches have been used in finding analytical and numerical solutions of similar classes of two-dimensional, free boundary problems (Bazant and Crowdy, 2005). Foremost among these is the classical Hele-Shaw free boundary problem and its extensions, including Saffman-Taylor fingering (a consequence of injecting a fluid into another, more viscous fluid) (Saffman and Taylor, 1958; Howison, 1986; Paterson, 1981; Miranda and Widom, 1998), the expansion and contraction of bubbles in a Hele-Shaw cell (Taylor and Saffman, 1959; Entov and Etingof, 1991; Dallaston and McCue, 2013, 2016) and the dissolution of soluble objects in two-dimensional potential flow (Ladd et al., 2020). Solidification and melting problems have also been extensively studied using analogous techniques, see e.g. Mullins and Sekerka (1964); Goldstein and Reid (1978); Cummings et al. (1999); Choi et al. (2005); Tsai and Wettlaufer (2007); Rycroft and Bazant (2016); Grodzki and Szymczak (2019), as well as the dynamics of dendritic crystal growth (Langer, 1980; Brower et al., 1984).

The numerical task is then to find the conformal map f. This map can be written as a Laurent series in ζ, truncated at N terms for numerical purposes. For some special fire line shapes, the conformal map for all time is well approximated by this truncated Laurent series - these are referred to as 'Laurent shapes' throughout this thesis. For a general fire line shape, the truncated Laurent series is a poor approximation of the map f. Therefore for these types of shapes, known as 'non-Laurent shapes', the conformal map

is instead written as a truncated power series in ζ, plus the initial conformal map $f(\zeta, 0) = g(\zeta)$. This initial map is found numerically by means of the Schwarz-Christoffel (SC) Toolbox: a MATLAB package developed in Driscoll and Trefethen (2002); Driscoll (2005) for finding conformal maps between polygons and various canonical domains, including the unit disk. The conformal map f then contains $n = 2N + 3$ unknown (real) functions in time. To solve for these functions, n points around the unit $\zeta-$disk are selected to give a system of n ordinary differential equations (ODEs). These can then be solved using any numerical ODE solver; MATLAB's *ode15i* is used throughout this thesis.

1.1.6 The AAA-least squares algorithm

The second numerical method is able to handle multiple, interacting wildfires which may have started independently or be a configuration of multiple spotfires resulting from one main wildfire. These fires interact via each wildfire's perturbation of the wind field, in particular, it is observed that two wildfires will grow towards each other until they eventually merge (Hilton et al., 2018). A conformal mapping method is difficult to implement in the multiple wildfire scenario: there is no simple form for the conformal map of this multiply connected domain to some desirable canonical domain (which is no longer the simple unit disk exterior) that is valid for all time, especially if some (or all) of the wildfires merge and thus change the connectedness of the domain at some time $t > 0$.

Instead, the pyrogenic potential is solved directly in the physical plane via a rational approximation of the potential, which is then found numerically using a combination of the adaptive Antoulas Anderson (AAA, pronounced 'triple A') algorithm and a least-squares (LS) method. This combined 'AAA-LS' algorithm has been developed by Trefethen, Costa, Gopal and co-workers over the past five years (Nakatsukasa et al., 2023) and has been applied to a variety of problems in mathematics, physics, chemistry and biology (Trefethen, 2018; Nakatsukasa et al., 2018, 2023; Xue et al., 2023; Kehry et al., 2023) and extended (Gopal and Trefethen, 2019c; Nakatsukasa et al., 2023) to incorporate multiply connected domains (Trefethen, 2020; Costa and Trefethen, 2023) and other governing equations such as the Stokes (Brubeck and Trefethen, 2022) and Helmholtz equations (Gopal and Trefethen, 2019a). Extensions to the Poisson equation and two-domain problems are also introduced in this thesis.

The approximation of the pyrogenic potential is composed of a polynomial and a sum of rational terms involving simple poles in the unphysical interior domains: the burnt regions of each wildfire. The AAA-LS method calculates these poles and the unknown (complex) coefficients using boundary data and the corresponding Dirichlet boundary condition for the pyrogenic potential. The algorithm is fast, running in seconds on a standard laptop, and boasts root-exponential convergence with respect to the number

of simple poles produced (Gopal and Trefethen, 2019c). An explicit Runge-Kutta (RK) time stepping method (Butcher, 1996) can then be implemented to track the fire line progression over time with the simple MATLAB function *union* used to detect and merge any overlapping fire lines.

Both of the proposed numerical procedures, the conformal mapping and AAA-LS methods, offer their own merits and drawbacks. While the conformal mapping method is restricted to computing the evolution of a single wildfire, it is simple and fast even for a large number of time steps and fundamentally consists only of a basic, implicit ODE solver. The AAA-LS method is more sophisticated yet still conceptually simple and fast, requiring the *chebfun* package (see e.g. Costa and Trefethen (2023)) to couple the AAA algorithm to a standard LS fitting procedure. It also requires an explicit RK timestepping routine which adds to the computation speed and introduces associated numerical errors. However, the AAA-LS method can model both single and multiple wildfire spread and is easily adaptable to the case of wildfire merger. Furthermore, the algorithm can handle sharp fire line shapes involving corners and cusps; the conformal mapping method is less equipped to handle such geometries due to the crowding phenomenon, see e.g. Driscoll (2005). As both methods offer different advantages and disadvantages, both are presented in this thesis.

1.1.7 Oxygen transport and fire fingering

In addition to the effects of the basic ROS and the ambient and pyrogenic winds included in the pyrogenic potential model of Hilton et al. (2018), an additional factor affecting the wildfire evolution is considered in this thesis. Oxygen is an essential ingredient for combustion and Beer (1991) presents a stoichiometric argument that this oxygen must be supplied to the wildfire by turbulent mixing from an inward horizontal flow. In the absence of an ambient wind, it is the pyrogenic wind that supplies the necessary oxygen to the fire line. Thus it is expected that the rate of spread of the wildfire also depends upon the advective and diffusive transport of oxygen to the fire line via the pyrogenic wind, hence an explicit term for oxygen transport can be included in the equation for the fire line velocity.

Treating oxygen explicitly like this has not been considered previously in the literature in the context of wildfires. The effects of oxygen advection and diffusion in relation to general combustion have been studied in more detail, for example in the experimental investigation by Zik et al. (1998) and the numerical work of Conti and Marconi (2002, 2010). The former describes experiments in which solid fuel in a Hele-Shaw cell is forced to burn against an oxidising wind; a 'fingering' instability, the growth of perturbations in the flame front, is observed. Kagan and Sivashinsky (2008) then derive a nonlinear PDE which models the free boundary between the fuel and air in these experiments, showing that the fingering is similar to

the instability occurring in premixed gas flames. Conti and Marconi (2002, 2010) also observe fingering in their numerical lattice model for the diffusion of heat and oxygen on an advancing fire front; the front develops into either a cellular or dendritic pattern depending on the initial parameters chosen e.g. the initial oxygen concentration.

Fingering instabilities have also been observed to develop on the fire lines of wildfires, a process referred to in this thesis as 'fire fingering'. Clark et al. (1996b) discuss the 1985 Onion sage brush fire in Owens Valley, California, where the fire line developed fingers spaced about 1 km apart (see their figure 1). The authors developed a three-dimensional coupled wildfire-atmosphere numerical model (later developed into the CAWFE model) to attribute fire line fingering to vorticity generation and the breakup of the buoyancy-driven fire plume into smaller cells (see also Clark et al. (1996a)). Dold et al. (2005) propose that the fire plume partially blocks incoming airflow and, along with a stably stratified atmosphere, the overall effect is to accelerate incoming air in the direction normal to the fire line. This results in an increased burning rate at the more advanced parts of the fire line, resulting in the growth of fire fingers. Quaife and Speer (2021) develop a two-dimensional, reduced physics, CA model of wildfire-atmosphere interaction, which incorporates a fire plume induced convective sink. Fingering is one of the behaviours observed, with the fire line breaking up into multiple, advancing heads.

It is demonstrated in this thesis that the oxygen effect may be another cause of fingering in wildfires, much the same way that oxygen transport induces fingering in flame combustion. Oxygen necessary for combustion is supplied to the fire line by the pyrogenic wind (Beer, 1991); the more advanced parts of the fire line receive the oxygen fastest and hence grow quicker, developing into fire fingers. Though oxygen is not explicitly mentioned in their work, this appears consistent with the conclusions of Dold et al. (2005) who state that the burn rate, or fire line speed, is proportional to the oncoming airflow.

Incorporating the oxygen effect into the wildfire model (in the absence of an ambient wind) is straightforward. The oxygen transport and pyrogenic wind flow are governed by the steady, two-dimensional, advection-diffusion equation and the Laplace equation, respectively. Both equations are conformally invariant and hence the conformal mapping method detailed in Sect.1.1.5 can be used once again.

1.1.8 Penguin huddling

Next, this thesis considers a free boundary problem which, at first sight, is the polar opposite of burning wildfires: the huddling behaviour of Antarctic penguins. Among all the penguin species living in the Antarctic region (Le Maho, 1977), the emperor penguin (Aptenodytes forsteri) experiences the most extreme weather conditions, enduring winds over 30ms^{-1} at temperatures below $-40°\text{C}$ (Le Maho, 1977;

Gerum et al., 2013; McCafferty et al., 2013; Williams et al., 2015). Unlike other species such as the gentoo and the Adélie (Kooyman et al., 1976), emperor penguins have no fixed nest (Waters et al., 2012; Gerum et al., 2018), allowing the birds to huddle together for warmth in severe wind conditions. This strategy is very effective; ambient temperatures within the huddle often exceed 20°C, with a maximum temperature of 37.5°C having been recorded (Gilbert et al., 2006). Such huddling is crucial for the penguins' survival, especially during foraging trips (Kirkwood and Robertson, 1999) and throughout their breeding season, which coincides with the Antarctic winter (Williams et al., 2015).

Over the few hours that huddling events typically last (Gilbert et al., 2006; Waters et al., 2012), the penguins are continuously (albeit slowly) on the move. The birds constantly reorganise their position in the huddle, where Le Maho (1977) observes that "birds that at first are in the center of the huddle become members of the rear flank [the side most exposed to the wind] and move, in their turn, up the sideline". This process benefits all members of the huddle and allows the heat to be equally shared: those at the edge do not remain cold and those at the centre do not overheat. These individual penguin movements affect the evolution of the huddle as a whole - the huddle is seen to propagate downwind (Ancel et al., 2015) and the shape traced out by the edge of the huddle, or huddle boundary, may change over time (Waters et al., 2012; Gerum et al., 2013).

Modelling the dynamics of these penguin huddle events has received increased attention over the last decade, but still remains sparse in the literature despite numerous field observations, see Le Maho (1977); McCafferty et al. (2013); Ancel et al. (2015); Williams et al. (2015). The works Zitterbart et al. (2011); Gerum et al. (2013, 2018) draw the analogy between penguin huddle/colony formation and condensed matter physics. Lennard-Jones-like forces are used to represent attractive and repulsive interactions between penguins, which allow complex, lattice structures (such as huddles) to form. This idea is expanded upon in Mina and Min (2018), where Gaussian processes are used to test if robots could adopt this penguin inspired huddling strategy. Similarly, Richter et al. (2018) liken the rearrangement of the penguin huddle to a phase transition from solid (dense huddle) to liquid (loose huddle) to gas (no huddle) depending on environmental factors such as temperature and wind speed. A rigorous fluid dynamics approach is taken in Gu et al. (2018), where a finite difference method is used to solve the full Navier-Stokes equations of the surrounding fluid (the exterior wind), giving a two-way coupling between the environment and the behaviour of the huddle. Using a simpler fluids based model, Waters et al. (2012) assume the exterior wind to be a two-dimensional, irrotational flow of an incompressible fluid and from this model, the temperature profile exterior to the huddle and individual penguin movements can be found.

In this thesis, a model for the evolution of the penguin huddle over time during an Antarctic blizzard

is developed. A similar approach to that of Waters et al. (2012) is adopted with two key differences. First, a simple model for the effect of interior penguin reorganisation as a result of self-generation of heat throughout the entire huddle, as observed in Le Maho (1977), is included. In Waters et al. (2012), while penguin reorganisation around the huddle boundary was acknowledged, it was assumed that interior penguins were so tightly packed that they could not change their position in the huddle. Here, it is instead assumed that interior penguins are free enough to move around, yet it is still also assumed that the penguins are packed tightly enough such that wind does not permeate through the huddle, thus the wind flow remains entirely in the exterior region.

Second, in keeping with the themes and other models developed in this thesis, the penguin huddle itself is treated as a continuum. Existing huddle models treat penguins as discrete elements (or particles) such that individual penguin movements can easily be tracked. For sufficiently large huddles on the order of a thousand penguins (Le Maho, 1977), these discrete models quickly become computationally expensive. Continuum models are computationally more efficient and faster and hence preferred when studying the change in shape and position of the overall huddle. Note that the penguin huddle problem is remarkably similar to the continuum model developed in Goldstein and Reid (1978) of the freezing of porous media flow by freeze pipes, where the velocity of the free boundary is dependent on both interior and exterior temperature gradients. It is also speculated that continuum models may be used to model other collective behaviours (Gerum et al., 2013; Burger et al., 2013; Bernardi and Scianna, 2020) such as fish schooling (Katz et al., 2011), bird flocking (Bhattacharya and Vicsek, 2010), bat swarming (Herreid, 1963; Ryan et al., 2019) and ant colony formation (Nave Jr et al., 2020; Ko et al., 2022).

There are two heat transfer mechanisms in the penguin problem, which formulate a suitable boundary condition for the propagation of the huddle boundary. The first is the cooling effect of the wind on the huddle. As in Waters et al. (2012), the incompressible wind flow is assumed irrotational and flowing sufficiently faster than the propagation of the huddle, thus the flow can be treated as steady. Hence the wind flow and temperature transport in the region exterior to the penguin huddle can be modelled by the Laplace and the steady advection-diffusion equations, respectively. As in the oxygen wildfire problem of Sect.1.1.7, this coupled pair of PDEs is conformally invariant and hence the conformal mapping methods introduced in Sect.1.1.5 can be used to solve for this exterior wind effect. The second is the uniform, self-generation of heat by the penguins in the huddle interior. Its steady diffusion amongst the densely packed penguins is modelled by a Poisson equation for the interior temperature with a constant forcing term. This Poisson equation is not conformally invariant and hence this interior effect is instead solved by the AAA-LS method introduced in Sect.1.1.6.

1.1.9 Biological electrostatics

Another problem considered in this thesis is in the field of biological electrostatics. Relationships between plants and their pollinators vitally underpin the health of global ecosystems and food production. Arthropods such as bees and spiders have thus acquired a variety of sensory receptors to detect floral cues such as scent, shape and colour. The recent discovery of electroreception - the ability for arthropods to detect and locate changes in electrical fields (Palmer et al., 2023a) - amongst terrestrial arthropods (Clarke et al., 2013; Morley and Robert, 2018) such as bees (Greggers et al., 2013; Clarke et al., 2017), spiders (Morley and Robert, 2018) and hoverflies (Khan et al., 2021) motivates investigation into whether flowers use their presence in an electrical field as another floral cue to attract pollinators. In particular, can a flower transmit information about its morphology and material properties (such as its available pollen) through the electrical field to nearby arthropods? While several papers have considered the electrostatics of plants, see e.g. Montgomery et al. (2021); Hunting et al. (2022); Molina-Montenegro et al. (2023), further research into the generation and characteristics of floral electrical fields is still required.

Consider the scenario of a bee and a flower. It has been shown that bees are predominantly positively charged to $\mathcal{O}(10) - \mathcal{O}(100)$ pC (Clarke et al., 2013). When approaching an uncharged flower, the pollinator's presence is hypothesised to polarise the flower, producing an electric field (Clarke et al., 2017). The strength and characteristics of this floral electric field depends on its shape, proximity to the arthropod and its propensity to polarise (i.e. its relative permittivity). On this last point, the petals and pollen of flowers are broadly considered to be dielectric since, at their surface, they consist of waxy material with little conductivity (Nanda et al., 2022).

Therefore, the physics of the studied system is that of two-domain dielectric polarisation. Both the electrical field exterior to the flower and that induced within the (dielectric) flower structure must be considered, with suitable matching conditions (such as continuity of the electric potential) imposed on the flower boundary. This is an added level of complexity from the simple one-domain problem, and from multiply connected domains which still consider only one region punctured by multiple 'holes'. In the two-domain scenario, the coupled system of both interior and exterior governing equations must be solved simultaneously. In this thesis, a two-domain extension of the AAA-LS method introduced in Sect.1.1.6 is developed to solve this problem. At the time of producing the work for this thesis, such an extension was new to the literature, though the idea had been hinted at in e.g. Nakatsukasa et al. (2023); Gopal and Trefethen (2019c). An alternative approach to model problems in magnetostatics using rational approximation has also been developed in Costa et al. (2024), which was the first application of the AAA algorithm in modelling physical objects.

1.1.10 Vortex patches

The two-domain AAA-LS method is applied to another problem, this time in the field of vortex dynamics. Persistent, coherent vortex structures appear in many physical systems, such as in the quasi-two dimensional flow of the Earth's oceans and in the atmospheres of the giant planets (McWilliams, 1985; Brueshaber et al., 2019). The systematic search and study for such equilibrium vortex solutions has a considerable and ever-growing body of literature, see e.g. Newton (2001); Krishnamurthy et al. (2020). Furthermore, these problems typically involve more complex vortical structures beyond the simple point vortex; in this thesis, problems involving vortex patches are considered.

Vortex patches have a finite, non-zero area of constant vorticity. The main challenge lies in finding the shape of the equilibrium patch, which then essentially becomes a two-dimensional, nonlinear free boundary problem. Contour dynamics methods in which the velocity field is numerically computed through knowledge of the boundary shape have proved successful in finding families of both translating and rotating equilibria, see e.g. Pierrehumbert (1980); Wu et al. (1984); Dritschel (1985); Xue et al. (2017). Exact solutions for equilibrium vortex patches are scarce: in addition to the classic Kirchhoff vortex - an elliptical vortex patch in steady rotation (Saffman, 1995) - analytic progress in finding equilibrium rotating solutions is possible only for limited classes e.g. using techniques based on conformal mapping and the Schwarz function of the patch boundary e.g. Crowdy (1999); Crowdy and Marshall (2004); Riccardi (2020).

In this thesis, an alternative method for computing equilibria is proposed: the two-domain AAA-LS method as introduced in Sect.1.1.9. The only difference here is that flow inside the patch is governed by Poisson's equation with constant right hand side equivalent to the constant vorticity ω. It is straightforward to find solutions by introducing a particular solution to transform the Poisson equation into Laplace's equation, then adjust the boundary conditions appropriately. The same technique was used in solving for the interior region of the penguin problem introduced in Sect.1.1.8.

1.2 Thesis outline

This doctoral thesis is divided into three parts. The first part develops a simple wildfire model (in the absence of direct wind effects) and a related model of penguin huddling. Ch.2 presents the simplest wildfire model based on the work of Markstein (1951), where the wildfire spread is affected by two terms: a constant basic ROS and a curvature effect. Here, the conformal mapping method is introduced to solve the wildfire spread numerically. Ch.3 then adds an additional effect into the model dependent on

the advective-diffusive transport of oxygen to the fire line. An analysis into the competing effects of stabilising curvature and destabilising oxygen transport is also performed. Ch.4 considers the penguin huddle problem and introduces the AAA-LS method to solve for the interior temperature transport via the Poisson equation.

The second part extends the wildfire model further, including the introduction of explicit pyrogenic and ambient wind effects. Ch.5 explores a free boundary problem where the velocity of the free boundary is dependent on a reciprocal, stabilising growth law; it is speculated this could be used as a deterministic equation for the basic ROS of a wildfire. Ch.6 then develops a wildfire model which incorporates basic ROS, pyrogenic and ambient wind effects; this model is inspired by the pyrogenic potential model of Hilton et al. (2018). As only a single wildfire is considered in this chapter, the conformal mapping method is used to compute the wildfire evolution. Ch.7 then extends this model to consider the evolution and eventual merger of multiple wildfires, as well as incorporating firebreaks - regions of unburnable fuel - into the model. The AAA-LS method is here used and extended to this multiply-connected scenario.

The third part then introduces a two-domain extension to the AAA-LS method and applies this to two problems. Ch.8 studies the electrostatic interaction between dielectric flowers and positively charged arthropods to determine whether flowers can transmit biologically relevant information, such as their morphology and material proporties, through an electric field to potential pollinators. Ch.9 considers vortex patches, with the AAA-LS method used to find equilibrium solutions to certain vortex patch and point configurations. Finally, Ch.10 presents some concluding remarks on the research performed in this thesis.

Part I

SIMPLE WILDFIRES AND PENGUIN HUDDLING

Chapter 2

Basic rate of spread and curvature

In this chapter, a basic model of wildfire spread is formulated and studied. In addition to the assumptions used throughout this thesis as stated in the upcoming Sect.2.1, the effects of the combined ambient and pyrogenic winds (see Ch.6) and the resulting steady transport of oxygen to the wildfire (see Ch.3) are here also neglected. Only two drivers of wildfire spread are considered: a constant basic ROS v_0 and the local curvature κ of the fire line.

2.1 Surface fire model assumptions

In addition to the wildfire model developed in this chapter, the following modelling assumptions hold true for all wildfire scenarios (specifically those in Ch.3, Ch.5, Ch.6 and Ch.7) studied in this thesis.

Consider a single or multiple wildfires spreading freely across a flat bed of homogeneously distributed, single-type, bone-dry fuel. Surface fires are exclusively considered in this thesis, i.e. the wildfire spreads through surface fuels such as grasses, heather, fallen leaves and twigs and shrubs less than 1.8m tall (Mell et al., 2007). This means that the horizontal length scale of the wildfire is suitably larger than the vertical flame height H and thus the problem can be treated as two-dimensional, with the (x, y)-plane analogous to a top-down (plan) view of the wildfire. The non-overlapping, two-dimensional fire line curve γ is defined as the boundary separating the burnt R and unburnt Ω regions of fuel. The velocity v_n normal to the fire line curve is sought; any transverse velocities play no role in the (forward) propagation of the fire line. Here, v_n is the velocity of the fire line in the direction of the outward unit normal $\hat{\boldsymbol{n}}$ to the fire line curve, i.e. pointing from the burnt region inside the fire line to the unburnt region ahead of the fire line.

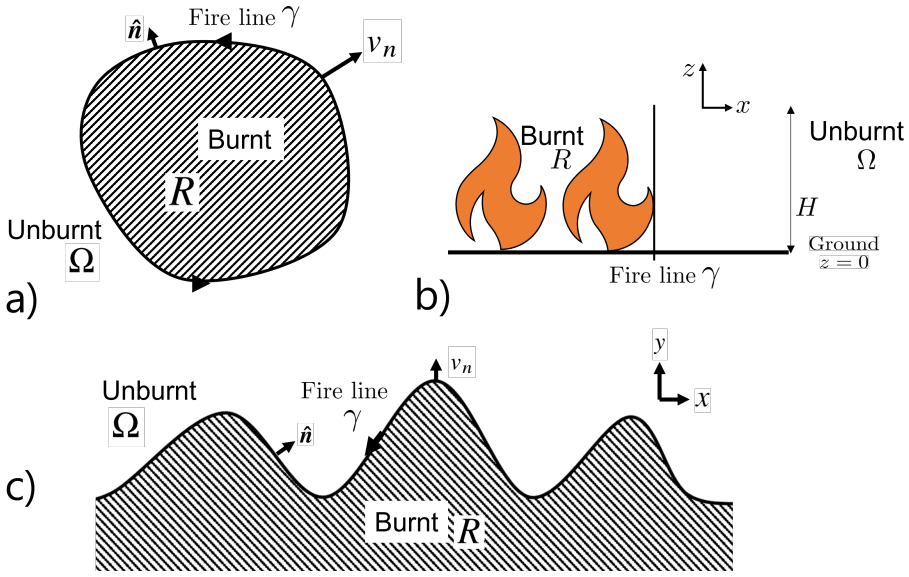

Figure 2.1: The wildfire problem (a) plan view of the radial problem, (b) side view, (c) plan view of the infinite problem.

2.2 The Markstein model

Two scenarios of the wildfire problem considered in this chapter are illustrated in figure 2.1. The first is that of a radial wildfire as shown from a plan view in figure 2.1a, where the fire line γ is finite and closed i.e. the entirety of the wildfire can be viewed from above. Figure 2.1c shows an infinite fire which is analogous to focusing in on a local segment of the fire line and treating the curve γ as infinitely large. Radial wildfires are considered when the motion of the entire wildfire is to be found, whereas infinite wildfires are useful for sufficiently large fire lines where the local behaviour of one portion of the free boundary is to be studied. While radial wildfires are primarily considered in this thesis, both radial and infinite fire lines are studied in this chapter. The equation used in this chapter for the normal velocity v_n of the fire line γ in the direction of its outward unit normal $\hat{\boldsymbol{n}}$ was first presented in Markstein (1951) and reads as follows

$$v_n = \hat{\boldsymbol{n}} \cdot \frac{\partial \boldsymbol{x}}{\partial t} = v_0 - \delta\kappa. \tag{2.2.1}$$

where $\boldsymbol{x}$ is the position vector of a point on the fire line, κ is the curvature and t is time. Thus this equation is here referred to as the Markstein model and consists of two terms.

First is the constant v_0 which is the basic rate of spread (ROS) term. This constant encapsulates the physical, chemical and thermodynamic properties of the fuel, in particular how long it will take a fuel element to combust, how long it will burn for, and how much heat it transfers to neighbouring fuel cells via radiation and convection. Quantifying this term is highly non-trivial: the exact value of the basic ROS for given fuel types is still an open question, see the review articles by e.g. Sullivan (2009a) and Morvan

et al. (2022). This is (primarily) due to a continued lack of understanding of the ignition process and of the relative magnitudes of convection and radiation in wildfire heat transfer. Some have proposed that the ROS can be calculated deterministically, rather than found as some ad-hoc constant; such a model and exploration of this idea is discussed in Ch.5. An in-depth study into the value of v_0 is not undertaken in this thesis and instead it is simply assumed that v_0 is some constant, either given or to be found. The distinction between radiative and convective basic ROS is also not taken in this chapter - this is instead introduced in Ch.6.

While the basic ROS alone provides an adequate model of fire spread - the models of Rothermel (1972) and McArthur (1966) are essentially both formulae for the basic ROS - Markstein (1951) was the first to introduce an additional term dependent on the curvature κ of the fire line in order to better match the model with experimental results. This model has since been used successfully to describe fire and wildfire spread, such as in the works of Sethian (1985); Sharples et al. (2013) and Hilton et al. (2016). Physically, the curvature relates the geometry of the fire line with radiative heat transfer. Segments of the fire line which are curved towards the unburnt fuel, i.e. regions of positive curvature, radiate heat to a wider area. Fuel elements closest to these sections will receive less heat from the wildfire in a given time and so will take longer to ignite, slowing the progression of that section of the fire line. Conversely, regions of fuel enclosed by a concave fire line segment (of negative curvature) receive greater heat more quickly and hence ignite faster, thus the normal velocity of the fire line in these regions is larger. The constant velocity $\delta\kappa$, noting that curvature has units $1/L$ for length scale L, quantifies the strength of the curvature effect. Typically $0 < \delta\kappa \ll v_0$ such that the curvature effect is (at least) an order of magnitude lower than the basic ROS term. This helps to ensure that the entropy condition remains satisfied in the model: the condition that the fire line must always progress from the burnt to the unburnt region (Sethian (1985)).

It is useful to write equation (2.2.1) in terms of dimensionless quantities. Let $\boldsymbol{x} \to L\boldsymbol{x}^*$, $t \to (L/v_0)t^*$ and $\kappa \to (1/L)\kappa^*$, where the starred quantities are dimensionless and L is a characteristic length scale, which is here chosen to be the initial conformal radius of the wildfire - see e.g. Bazant and Crowdy (2005). Dropping stars immediately gives the equation

$$v_n = \hat{\boldsymbol{n}} \cdot \frac{\partial \boldsymbol{x}}{\partial t} = 1 - \epsilon\kappa; \qquad \epsilon = \frac{\delta}{v_0 L}. \tag{2.2.2}$$

The problem now only depends on the single parameter ϵ, where $0 < \epsilon \ll 1$. Note that equation (2.2.1) and equation (2.2.2) are curve shortening equations; these are variants of the curve-shortening problem considered by Dallaston and McCue (2016) and are equations which appear frequently in the subject of

mean curvature flows, see for example Brakke (2015). As the area enclosed by the fire line increases under equation (2.2.2), despite the curvature still acting to shorten the curve, the equation shall be referred to more generally as a curvature flow equation (CFE). A derivation of this CFE from physical principles is given in chapter A.

2.3 Stability analysis

A stability analysis can be performed to see how small perturbations evolve under the dimensionless CFE equation (2.2.2). Perturbations of the form $\delta_m(t)\cos mx$ are applied to 'base states' - fire line curves which do not change shape (only their scale changes) under equation (2.2.2). The magnitude of these perturbations $\delta_m(t)$ are sufficiently small ($0 < \delta_m \ll \epsilon \ll 1$ for all m) such that terms of $O(\delta_m^2)$ can be neglected, where δ_m^2 defines any product $\delta_m\delta_n$, for all m, n. The growth rate $g(m)$ of these perturbations is then sought

$$g(m) = \frac{\dot{\delta}_m(t)}{\delta_m(t)}, \tag{2.3.1}$$

where the dot denotes differentiation with respect to time t.

2.3.1 Radial fire lines

A suitable base state for radial fire lines is a circle of radius $R(t)$, which has the same value of curvature $\kappa = 1/R(t)$ at every point $\boldsymbol{x} = r(\theta, t)\hat{\boldsymbol{r}}$ on the curve. Small perturbations are then induced onto the circle

$$r(\theta, t) = R(t) + \sum_{m=1}^{\infty} \delta_m(t)\cos m\theta. \tag{2.3.2}$$

To leading order, the normal velocity can be written as

$$v_n = \frac{\partial \boldsymbol{x}}{\partial t}\cdot\hat{\boldsymbol{n}} = \frac{\partial r}{\partial t} = \dot{R} + \sum_{m=1}^{\infty}\dot{\delta}_m(t)\cos m\theta. \tag{2.3.3}$$

The curvature in polar coordinates is

$$\kappa = \frac{r^2 + 2r'^2 - rr'}{(r^2 + r'^2)^{3/2}}, \tag{2.3.4}$$

where the primes indicate differentiation with respect to θ. Note that,

$$r^2 = R^2 + \sum_{m=1}^{\infty} 2R(t)\delta_m(t)\cos m\theta + O(\delta_m^2), \tag{2.3.5}$$

$$r'^2 = \left[\sum_{m=1}^{\infty} -m\delta_m(t)\sin m\theta\right]^2 = O(\delta_m^2), \tag{2.3.6}$$

$$r' = \sum_{m=1}^{\infty} -m^2\delta_m(t)\cos m\theta. \tag{2.3.7}$$

Thus, the curvature equation (2.3.4) is

$$\begin{aligned}\kappa = \frac{r^2 - rr'}{r^3} + O(\delta_m^2) &= \frac{1}{r^2}[r - r'] + O(\delta_m^2) \\ &= \frac{1}{R^2[1 + \sum_{m=1}^{\infty} 2R^{-1}\delta_m(t)\cos m\theta]}\left[R + \sum_{m=1}^{\infty}(m^2+1)\delta_m(t)\cos m\theta\right] + O(\delta_m^2) \\ &= \frac{1}{R^2}\left[1 - 2R^{-1}\sum_{m=1}^{\infty}\delta_m(t)\cos m\theta\right]\left[R + \sum_{m=1}^{\infty}(m^2+1)\delta_m(t)\cos m\theta\right] + O(\delta_m^2) \\ &= \frac{1}{R}\left[1 + \frac{1}{R}\sum_{m=1}^{\infty}(m^2-1)\delta_m(t)\cos m\theta\right] + O(\delta_m^2). \end{aligned} \tag{2.3.8}$$

Substituting equation (2.3.3) and equation (2.3.8) into equation (2.2.2) gives

$$\dot{R} + \sum_{m=1}^{\infty}\dot{\delta}_m(t)\cos m\theta = 1 - \frac{\epsilon}{R}\left(1 + \frac{1}{R}\sum_{m=1}^{\infty}(m^2-1)\delta_m(t)\cos m\theta\right). \tag{2.3.9}$$

At leading order in δ_m in equation (2.3.9)

$$\dot{R} = 1 - \frac{\epsilon}{R}. \tag{2.3.10}$$

which is the CFE (2.2.2) for a circle. Note that in the dimensionless system $R(0) = 1 \gg \epsilon$ and thus the circular wildfire will always grow, as it must physically. Extracting the $O(\delta_m)$ terms gives,

$$\sum_{m=1}^{\infty}\left[\dot{\delta}_m + \frac{\epsilon(m^2-1)\delta_m}{R^2}\right]\cos m\theta = 0. \tag{2.3.11}$$

As equation (2.3.11) must hold for all $0 \le \theta \le 2\pi$, it follows that

$$g(m) = \frac{\dot{\delta}_m}{\delta_m} = -\frac{\epsilon(m^2-1)}{R^2}. \tag{2.3.12}$$

Thus $g(m) \le 0$ for all m and so perturbations decay over time. The case when $m = 1$ for which $g(m) = 0$ is equivalent to a uniform translation of the circle (Brower et al., 1984) which is also neutrally stable and

thus the circle $r(\theta, t) = R(t)$ is linearly stable.

2.3.2 Infinite fire lines

Consider infinite fire lines which have a base state of the form $y = kt$ (i.e. a horizontal line fire), with $k = 1$ required to solve equation (2.2.2) exactly. A general perturbation term is applied to the fire line such that

$$y = t + \sum_{m=1}^{\infty} \delta_m(t) \cos mx. \tag{2.3.13}$$

The normal velocity v_n of the fire line can be evaluated as

$$v_n = \frac{\partial \boldsymbol{x}}{\partial t} \cdot \hat{\boldsymbol{n}} = \left(1 + \sum_{m=1}^{\infty} \dot{\delta}_m(t) \cos mx\right) \boldsymbol{j} \cdot \left(\boldsymbol{j} + O(\delta_m^2)\right) \approx 1 + \sum_{m=1}^{\infty} \dot{\delta}_m(t) \cos mx, \tag{2.3.14}$$

and the curvature as

$$\kappa = \frac{-y'}{[1 + (y')^2]^{3/2}} = \frac{\sum_{m=1}^{\infty} m^2 \delta_m(t) \cos mx}{[1 + O(\delta_m^2)]^{3/2}} = \sum_{m=1}^{\infty} m^2 \delta_m(t) \cos mx + O(\delta_m^2). \tag{2.3.15}$$

Substituting equation (2.3.14) and equation (2.3.15) into equation (2.2.2), and ignoring higher order terms, gives

$$\sum_{m=1}^{\infty} \left[\dot{\delta}_m(t) + \epsilon m^2 \delta_m(t)\right] \cos mx = 0. \tag{2.3.16}$$

As equation (2.3.16) holds for all values of x, it follows that

$$g(m) = \frac{\dot{\delta}_m(t)}{\delta_m(t)} = -\epsilon m^2 < 0. \tag{2.3.17}$$

Thus all perturbation terms decay and the horizontal line $y = t$ is linearly stable. This is expected physically; radiative heat transfer (the curvature effect) speeds up concave fire line regions and slows down convex segments, which causes the fire line to 'flatten out' as it grows.

2.4 Conformal mapping method

To find the evolution of more general fire line shapes, numerical solutions must be found. As the problem is two-dimensional, the physical (x, y) plane is analogous to the complex $z-$plane, where the complex variable $z = x + iy$ represents the position vector $\boldsymbol{x} = (x, y)$. This allows the use of methods based on complex analysis, in particular an approach involving conformal mapping. By the Riemann mapping theorem (see e.g. Brown and Churchill (2009)), there always exists a conformal map $z = f(\zeta, t)$ from the

exterior of the fire line γ at time t in the physical $z-$plane to the interior (or exterior) of the unit disk in some canonical $\zeta-$plane. This transformation consequently maps the fire line to the unit $\zeta-$disk, and this approach is also particularly advantageous for functions satisfying conformally invariant governing equations in these singly-connected domains - this is seen in Ch.3. In either case, the domain boundary reduces from a complicated, time varying fire line to a simple, unit circle in which known solutions can be found. The task is then to find the conformal map $z = f(\zeta, t)$.

The CFE (2.2.2) can be written in terms of z and ζ. Noting that $z = f(\zeta, t)$, the LHS becomes

$$\hat{\boldsymbol{n}} \cdot \frac{\partial \boldsymbol{x}}{\partial t} = \mathrm{Re}\Big[\bar{n}\frac{\partial f}{\partial t}\Big], \tag{2.4.1}$$

where $\bar{n}$ is the complex conjugate of the unit normal vector in complex form. By definition, (non-unit) tangent and outward normal vectors to a curve can be written as

$$\boldsymbol{t} = \left(\frac{\partial x}{\partial \theta}, \frac{\partial y}{\partial \theta}\right), \quad \boldsymbol{n} = \left(\frac{\partial y}{\partial \theta}, -\frac{\partial x}{\partial \theta}\right), \tag{2.4.2}$$

where θ is the angle between the tangent vector to the curve and the $x-$axis. Therefore, the complex form n of the unit, normal vector $\hat{\boldsymbol{n}}$ is

$$n = \frac{1}{|x_\theta^2 + y_\theta^2|}\left(- i\frac{\partial x}{\partial \theta} + \frac{\partial y}{\partial \theta}\right) = -\frac{i f_\theta}{|f_\theta|}. \tag{2.4.3}$$

where subscript notation indicates differentiation with respect to that variable. On the unit $\zeta-$disk, it holds that $\zeta = \exp(i\theta)$ for $0 \leq \theta < 2\pi$. Thus $\partial\theta = i\zeta\partial\zeta$ by the chain rule and so, noting that $|\zeta| = 1$, equation (2.4.3) can be written as

$$n = \frac{\zeta f_\zeta}{|f_\zeta|}. \tag{2.4.4}$$

The LHS of the CFE then becomes

$$v_n = \hat{\boldsymbol{n}} \cdot \frac{\partial \boldsymbol{x}}{\partial t} = \frac{\mathrm{Re}\Big[f_t\overline{\zeta f_\zeta}\Big]}{|f_\zeta|}. \tag{2.4.5}$$

Following Dallaston and McCue (2013), the curvature can be written as

$$\kappa = \frac{\mathrm{Re}\Big[\zeta(\zeta f_\zeta)_\zeta\overline{\zeta f_\zeta}\Big]}{|f_\zeta|^3}. \tag{2.4.6}$$

Then, substituting equations (2.4.5) and (2.4.6) into the CFE (2.2.2) and simplifying gives

$$\mathrm{Re}\Big[f_t\overline{\zeta f_\zeta}\Big] = |f_\zeta| - \frac{\epsilon \mathrm{Re}\Big[\zeta(\zeta f_\zeta)_\zeta \overline{\zeta f_\zeta}\Big]}{|f_\zeta|^2}. \tag{2.4.7}$$

The conformal map $f(\zeta, t)$ is then to be found by solving equation (2.4.7).

2.4.1 Radial fire lines

For radial fire lines, it is assumed that the conformal map $f(\zeta, t)$ from the interior of the unit disk to the exterior of the fire line at time t can be written in the following form

$$z = f(\zeta, t) = a_{-1}(t)g(\zeta) + \sum_{k=0}^{\infty} c_k(t)\zeta^k. \tag{2.4.8}$$

This is a power series in ζ plus the initial conformal map $g(\zeta)$, noting that $a_{-1}(0) = 1$ and $c_k(0) = 0, \forall k$. The conformal radius of the fire line at time t is $a_{-1}(t)A$, where A is the conformal radius of the map g. General initial fire line shapes for which g must be found (numerically) are explored in Ch.5. For the preceding chapters, special initial fire line shapes are instead considered.

The most common initial fire line shape considered in this thesis is an $n-$fold symmetric shape as was considered in Dallaston and McCue (2016). For these shapes, it holds that $g(\zeta) = \zeta$, effectively extending the power series to a Laurent series. The restraint that $c_k = 0, \forall k$ is also dropped. These shapes shall henceforward be referred to as 'Laurent shapes', with general fire line shapes often called 'non-Laurent shapes', accordingly. In this chapter and in Ch.3, one line of symmetry is taken to be the real axis and thus the coefficients c_k are real. Altering the summation in equation (2.4.8) and rewriting the coefficients c_k with a_m, the conformal map now becomes

$$z = a_{-1}(t)\zeta^{-1} + \sum_{m=1}^{\infty} a_m(t)\zeta^{nm-1}. \tag{2.4.9}$$

The infinite series in equation (2.4.9) is then truncated at N terms to give $N+1$ unknown real functions in time: $a_{-1}, a_1, ..., a_N$. Substituting $N+1$ uniformly distributed points on the unit $\zeta-$disk into equation (2.4.7) gives a system of $N+1$ ODEs to solve for the $N+1$ unknown functions. As the fire line has $n-$fold symmetry, the $\zeta-$disk is split into the intervals $\arg\zeta = [0, \pi/n)$ and points chosen as

$$\zeta_j = e^{i\pi j/nN}, \quad j = 0, 1, ..., N. \tag{2.4.10}$$

The values $N = 32, 64$ and 128 are typically chosen throughout this thesis and the MATLAB ODE solver *ode15i* is used to solve the resulting system of $N + 1$ equations.

2.4.2 Infinite fire lines

The following form of the conformal map $f(\zeta, t)$ from the interior of the unit $\zeta-$disk to the exterior of the infinite fire line is used

$$z = f(\zeta, t) = -i \log \zeta + \frac{i}{2} \sum_{m=-\infty}^{\infty} c_m \zeta^m. \tag{2.4.11}$$

The coefficients are complex $c_m(t) = a_m(t) + ib_m(t)$ as the infinite fire line is not taken to be symmetric in the real axis. The infinite fire lines considered in this thesis are assumed to not be multi-valued, and hence $c_{-m} = \bar{c}_m$ giving that $c_0 = a_0 \in \mathbb{R}$. Noting that $\zeta = \exp(i\theta) = \cos\theta + i \sin\theta$, equation (2.4.11) can be written as follows

$$\begin{aligned} z &= -i \log(\exp(i\theta)) + \frac{i}{2} \sum_{m=-\infty}^{\infty} c_m \big[\cos(m\theta) + i \sin(m\theta) \big] \\ &= \theta + \frac{i}{2} a_0 + \frac{i}{2} \sum_{m=-\infty}^{-1} c_m e^{im\theta} + \sum_{m=1}^{\infty} c_m e^{im\theta} = \theta + \frac{i}{2} a_0 + \frac{i}{2} \sum_{m=1}^{\infty} c_m e^{im\theta} + c_{-m} e^{-im\theta} \\ &= \theta + \frac{i}{2} a_0 + \frac{i}{2} \sum_{m=1}^{\infty} (a_m + ib_m)(\cos m\theta + i \sin m\theta) + (a_m - ib_m)(\cos m\theta - i \sin m\theta) \\ &= \theta + \frac{i}{2} a_0 + i \sum_{m=1}^{\infty} a_m \cos m\theta - b_m \sin m\theta. \end{aligned} \tag{2.4.12}$$

and therefore

$$x = \mathrm{Re}\big[z\big] = \theta, \tag{2.4.13}$$

$$y = \mathrm{Im}\big[z\big] = \frac{a_0}{2} + \sum_{m=1}^{\infty} a_m \cos mx + (-b_m) \sin mx. \tag{2.4.14}$$

Observe that equation (2.4.14) is a Fourier series and thus the initial values of the coefficients a_0, a_m and b_m can be found from the Fourier series of the initial fire line $y = f(x)$.

The conformal map equation (2.4.11) is once again truncated at N terms, with $n = 2N+1$ points selected around the unit $\zeta-$disk to solve for the n unknown functions $a_0, a_1, ...a_N, b_1, ..., b_N$. Note that if the initial fire line can be written as an even function, i.e. a function such that $f(-x) = f(x)$, then $b_m \equiv 0, \ \forall m$. Similarly, a fire line expressed by an odd function $f(-x) = -f(x)$ means that $a_m \equiv 0, \ \forall m$ (including $m = 0$).

2.5 Area and length laws

Two useful laws arise as a consequence of the CFE (2.2.1); the absolute error of these can then be computed to assess the accuracy of the upcoming numerical results.

2.5.1 Radial fire lines

The radial fire line is the finite, closed curve γ defined by the coordinates (s, θ), where s is the arclength and θ is the angle between the tangent to γ at a given point and the real axis. Let $L = \int_\gamma \mathrm{d}s$ be the length of curve γ, and A be the area of the burnt region R enclosed by γ. The integral of the curvature κ over the fire line curve is

$$\int_\gamma \kappa \mathrm{d}s = \int_\gamma \frac{\mathrm{d}\theta}{\mathrm{d}s}\mathrm{d}s = \int_0^{2\pi} \mathrm{d}\theta = 2\pi. \tag{2.5.1}$$

By Green's Theorem, the rate of change of the area A can be evaluated as follows

$$\begin{aligned}\frac{\mathrm{d}A}{\mathrm{d}t} = \frac{\mathrm{d}}{\mathrm{d}t}\left(\int\int_R \mathrm{d}A\right) = \frac{\mathrm{d}}{\mathrm{d}t}\left(\frac{1}{2}\int_\gamma x\mathrm{d}y - y\mathrm{d}x\right) = \frac{\mathrm{d}}{\mathrm{d}t}\left(\frac{1}{2}\int_0^{2\pi} x\frac{\mathrm{d}y}{\mathrm{d}\theta}\mathrm{d}\theta - y\frac{\mathrm{d}x}{\mathrm{d}\theta}\mathrm{d}\theta\right)\\ = \frac{1}{2}\int_0^{2\pi}\Big(xy_{\theta t} + x_t y_\theta - yx_{\theta t} - y_t x_\theta\Big)\mathrm{d}\theta.\end{aligned}$$

Integration by parts on $xy_{\theta t}$ and $yx_{\theta t}$ can be used to evaluate further

$$\begin{aligned}\frac{\mathrm{d}A}{\mathrm{d}t} &= \frac{1}{2}\int_0^{2\pi} 2(x_t y_\theta - x_\theta y_t)\mathrm{d}\theta = \int_0^{2\pi}\begin{pmatrix}x_t\\ y_t\end{pmatrix}\cdot\begin{pmatrix}y_\theta\\ -x_\theta\end{pmatrix}\mathrm{d}\theta\\ &= \int_0^{2\pi}\frac{\partial \boldsymbol{x}}{\partial t}\cdot\frac{1}{|y_\theta, -x_\theta|}\begin{pmatrix}y_\theta\\ -x_\theta\end{pmatrix}|y_\theta, -x_\theta|\mathrm{d}\theta = \int_0^{2\pi}\hat{\boldsymbol{n}}\cdot\frac{\partial \boldsymbol{x}}{\partial t}\sqrt{\mathrm{d}\theta^2\left[\left(\frac{\mathrm{d}y}{\mathrm{d}\theta}\right)^2 + \left(\frac{\mathrm{d}x}{\mathrm{d}\theta}\right)^2\right]}\\ &= \int_\gamma v_n\ \sqrt{\mathrm{d}y^2 + \mathrm{d}x^2} = \int_\gamma (1 - \epsilon\kappa)\mathrm{d}s = \int_\gamma \mathrm{d}s - \epsilon\int_\gamma \kappa\mathrm{d}s.\end{aligned}$$

Using equation (2.5.1) then gives the following rate of change of area (RCA) law

$$\frac{\mathrm{d}A}{\mathrm{d}t} = L(t) - 2\epsilon\pi. \tag{2.5.2}$$

This is equivalent to the RCA law presented in equation (1.4) of Dallaston and McCue (2016) with $\epsilon = 1$ and their $q(t) = 1, \forall t$.

Next, consider the rate of change of the curve length L

$$\frac{\mathrm{d}L}{\mathrm{d}t} = \frac{\mathrm{d}}{\mathrm{d}t}\int_\gamma \mathrm{d}s = \frac{\mathrm{d}}{\mathrm{d}t}\int_{\gamma(u)}\sqrt{\left(\frac{\mathrm{d}x}{\mathrm{d}u}\right)^2 + \left(\frac{\mathrm{d}y}{\mathrm{d}u}\right)^2}\mathrm{d}u = \int_{\gamma(u)}\frac{\partial g(u,t)}{\partial t}\mathrm{d}u, \tag{2.5.3}$$

where the variable u is introduced s.t. $g(u,t) = \sqrt{(x_u)^2 + (y_u)^2} = \mathrm{d}s/\mathrm{d}u$. The Serret-Frenet formulae (Adams, 1975) in terms of the variable u are

$$\frac{\partial \hat{\boldsymbol{t}}}{\partial u} = g(u,t)\bar{\kappa}\hat{\boldsymbol{n}}, \qquad \frac{\partial \hat{\boldsymbol{n}}}{\partial u} = -g(u,t)\bar{\kappa}\hat{\boldsymbol{t}} = g\kappa\boldsymbol{t}. \tag{2.5.4}$$

where $\bar{\kappa} = -\kappa$. The derivative in t of the quantity g^2 is evaluated

$$\begin{aligned}\frac{\partial}{\partial t}g^2 = \frac{\partial}{\partial t}\left(\left|\frac{\partial \boldsymbol{x}}{\partial u}\right|^2\right) = \frac{\partial}{\partial t}\left(\frac{\partial \boldsymbol{x}}{\partial u}\cdot\frac{\partial \boldsymbol{x}}{\partial u}\right) = 2\frac{\partial \boldsymbol{x}}{\partial u}\cdot\frac{\partial^2 \boldsymbol{x}}{\partial t \partial u} = 2\Big(g\frac{\partial \boldsymbol{x}}{\partial s}\Big)\cdot\frac{\partial}{\partial u}\left(\frac{\partial \boldsymbol{x}}{\partial t}\right) \\ = 2g\hat{\boldsymbol{t}}\cdot\frac{\partial}{\partial u}\Big[(1-\epsilon\kappa)\hat{\boldsymbol{n}}\Big] = 2g(1-\epsilon\kappa)\hat{\boldsymbol{t}}\cdot\frac{\partial \hat{\boldsymbol{n}}}{\partial u} = 2g^2\kappa(1-\epsilon\kappa).\end{aligned} \tag{2.5.5}$$

Noting also by the chain rule that

$$\frac{\partial}{\partial t}g^2 = 2g\frac{\partial g}{\partial t}, \tag{2.5.6}$$

then equations (2.5.5) and (2.5.6) are compared to give an expression for the derivative of g

$$\frac{\partial g}{\partial t} = g\kappa(1-\epsilon\kappa). \tag{2.5.7}$$

Hence equation (2.5.3) can now be evaluated to give

$$\frac{\mathrm{d}L}{\mathrm{d}t} = \int_{\gamma[u]}\frac{\partial g(u,t)}{\partial t}\mathrm{d}u = \int_{\gamma[u]}\kappa(1-\epsilon\kappa)(g\mathrm{d}u) = \int_{\gamma}\kappa\mathrm{d}s - \epsilon\int_{\gamma}\kappa^2\mathrm{d}s,$$

and using equation (2.5.1) gives the rate of change of length (RCL) law

$$\frac{\mathrm{d}L}{\mathrm{d}t} = 2\pi - \epsilon\int_{\gamma}\kappa^2\mathrm{d}s. \tag{2.5.8}$$

The curve length $L(t)$ decreases or increases (i.e. the curve either shrinks or grows) according to the sign of equation (2.5.8). This RCL law is equivalent to that presented in equation (1.5) in Dallaston and McCue (2016) with $\epsilon = 1$ and their constant β chosen such that $2\pi - \beta = L$.

2.5.2 Infinite fire lines

Consider an infinite fire line which in particular is periodic with period $2l$. One period of the fire line is considered for $x \in [-l, l]$, with this curve γ_l described parametrically by the arclength s and azimuthal angle θ. The outward unit normal $\hat{\boldsymbol{n}}$ and curvature κ can be written as

$$\hat{\boldsymbol{n}} = \frac{1}{(1+y'^2)^{1/2}}\begin{pmatrix}-y'\\1\end{pmatrix}, \quad \kappa = -\frac{y'}{(1+y'^2)^{3/2}}, \tag{2.5.9}$$

where dots and dashes represent differentiation with respect to t and x, respectively. Then the CFE equation (2.2.2) becomes

$$\frac{\dot{y}}{(1+y'^2)^{1/2}} = 1 + \epsilon \frac{y'}{(1+y'^2)^{3/2}}. \tag{2.5.10}$$

Let L be the length of γ_l, and A be the area of domain D enclosed between γ_l and the $x-$axis. The following definitions for L and the integral of curvature can be written

$$L(t) = \int_{\gamma_l} \mathrm{d}s = \int_{-l}^{l} \sqrt{1+y'^2}\mathrm{d}x. \tag{2.5.11}$$

$$\int_{\gamma_l} \kappa \mathrm{d}s = \int_{\theta_i}^{\theta_f} \mathrm{d}\theta = \theta_f - \theta_i = 0, \tag{2.5.12}$$

The RCA law is evaluated as

$$\begin{aligned} \frac{\mathrm{d}A}{\mathrm{d}t} = \frac{\mathrm{d}}{\mathrm{d}t}\left(\iint_D \mathrm{d}A \right) = \frac{\mathrm{d}}{\mathrm{d}t}\left(\int_{-l}^{l} y \mathrm{d}x \right) = \int_{-l}^{l} \dot{y}\mathrm{d}x \\ = \int_{\gamma_l} \frac{\dot{y}}{(1+y'^2)^{1/2}} \mathrm{d}s = \int_{\gamma_l} (1-\epsilon\kappa)\mathrm{d}s = \int_{\gamma_l} \mathrm{d}s - \epsilon \int_{\gamma_l} \kappa \mathrm{d}s = L(t). \end{aligned} \tag{2.5.13}$$

The RCL law is

$$\begin{aligned} \frac{\mathrm{d}L}{\mathrm{d}t} = \frac{\mathrm{d}}{\mathrm{d}t}\left(\int_{-l}^{l} \sqrt{1+y'^2}\mathrm{d}x \right) = \int_{-l}^{l} \frac{y'}{(1+y'^2)^{1/2}} (\dot{y'})\mathrm{d}x \\ = -\int_{\gamma_l} \left(\frac{y'}{1+y'^2} \right) \left(\frac{\dot{y}}{(1+y'^2)^{1/2}} \right) \frac{\mathrm{d}s}{(1+y'^2)^{1/2}} = \int_{\gamma_l} \kappa(1-\epsilon\kappa)\mathrm{d}s = -\epsilon \int_{\gamma_l} \kappa^2 \mathrm{d}s. \end{aligned} \tag{2.5.14}$$

Note that equation (2.5.14) is non-positive and so the curve will decay unless the curvature is zero along the entire fire line segment i.e. γ_l is a straight line. This suggests that all periodic infinite fire lines governed by equation (2.2.2) decay into a horizontal line over time, in agreement with the stability analysis in Sect.2.3.2.

2.5.3 Numerical evaluation of the RCA and RCL laws

Various quantities in the RCA laws (equations (2.5.2) and (2.5.13)) and the RCL laws (equations (2.5.8) and (2.5.14)) must be found numerically. The length L of a radial fire line curve can be found using the MATLAB *perimeter* function on the list $z_b = x_b + iy_b$ of boundary data. The distance between neighbouring boundary points can also be manually calculated and summed to give the length L, as is required to do for the periodic, infinite fire line segment γ_l. The area A between the curve γ_l and the real axis can be found simply using the *trapz* function; this immediately gives A by definition. For a radial fire line, the area A of the burnt region R can be found using the MATLAB function *polyarea*(x_b, y_b) on

the boundary data. Alternatively, the area can be approximated using a result from Green's theorem. Noting that $\int_\gamma x\mathrm{d}x + y\mathrm{d}y = 0$, the area A is evaluated as

$$A = \int\int_R \mathrm{d}x\mathrm{d}y = \frac{1}{2i}\int_\gamma i(x\mathrm{d}y - y\mathrm{d}x)$$
$$= \frac{1}{2i}\int_\gamma (x\mathrm{d}x + y\mathrm{d}y) + i(x\mathrm{d}y - y\mathrm{d}x) = \frac{1}{2i}\int_\gamma (x - iy)(\mathrm{d}x + i\mathrm{d}y) = \frac{1}{2i}\int_\gamma \bar{z}\mathrm{d}z. \quad (2.5.15)$$

Introducing the (truncated) conformal map $z = f(\zeta, t)$ from equation (2.4.9), and noting that $\bar{\zeta} = \zeta^{-1}$, gives

$$A = \frac{1}{2i}\int_\gamma \bar{z}\frac{\mathrm{d}z}{\mathrm{d}\zeta}\mathrm{d}\zeta = \frac{1}{2i}\int_\gamma \Big(a_{-1}\zeta + \sum_{n=0}^{N} a_n\zeta^{-n}\Big)\Big(-a_{-1}\zeta^{-2} + \sum_{n=0}^{N} n a_n\zeta^{n-1}\Big)\mathrm{d}\zeta$$
$$= \frac{1}{2i}\int_\gamma \Big[-\frac{(a_{-1})^2}{\zeta} + \sum_{n=0}^{N}\frac{n a_n^2}{\zeta} + O(\zeta^n)\Big]\mathrm{d}\zeta. \quad (2.5.16)$$

Using Cauchy's integral formula then gives

$$A = 2\pi i\Big(\frac{1}{2i}\big(-a_{-1}^2 + \sum_{n=0}^{N} n a_n^2\big)\Big) = \pi\Big(\sum_{n=0}^{N} n a_n^2 - a_{-1}^2\Big). \quad (2.5.17)$$

The derivatives in time of A and L are then approximated using the *gradient* function, noting that a finer mesh of the time interval $[t_{\min}, t_{\max}]$ provides a more accurate approximation.

Finally, the curvature at each point is approximated by the Menger curvature κ_M. From Léger (1999), the curvature at y in the triple of points (x, y, z) is approximated as

$$\kappa \approx \kappa_M = \frac{4 \text{ x (Area of triangle } xyz)}{|x - y||y - z||z - x|}. \quad (2.5.18)$$

Note that equation (2.5.18) does not give the sign of the curvature, yet this is of no consequence as it is κ^2 that is calculated.

2.6 Results

First, consider various $n-$fold symmetric radial fire lines. Each initial fire line has conformal radius $L = 1$ and evolves between $t = [0, 1]$ with ten isochrones (contours of the fire line at specific times) plotted at equal time increments. The Laurent series truncation $N = 128$ is also chosen throughout.

Figure 2.2a shows the evolution of an elliptical fire line ($n = 2$) with major and minor axes 1.25 and 0.75,

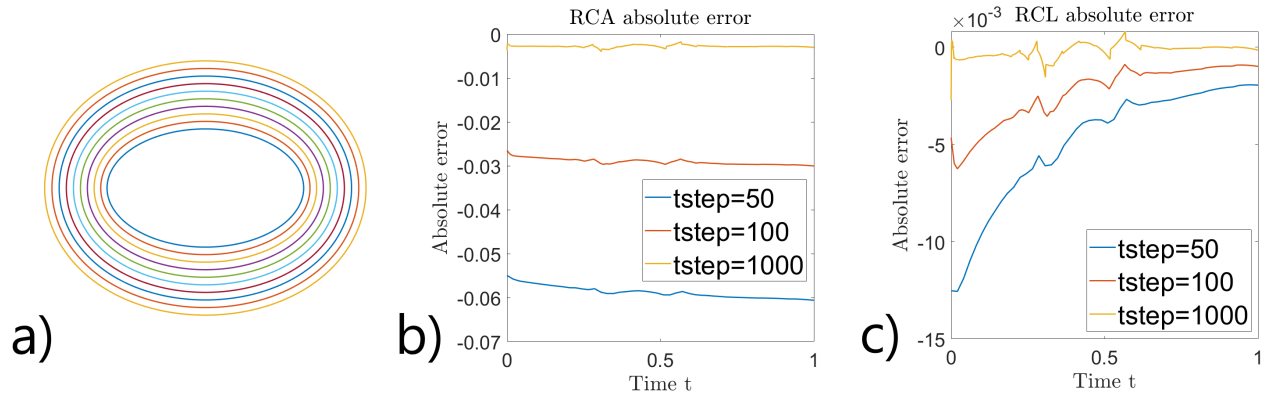

Figure 2.2: (a) Evolution of an elliptical fire line, where ten isochrones have been plotted. The subsequent plots show the absolute error of the RCA (b) and RCL (c) laws for various values of the time step '*tstep*'.

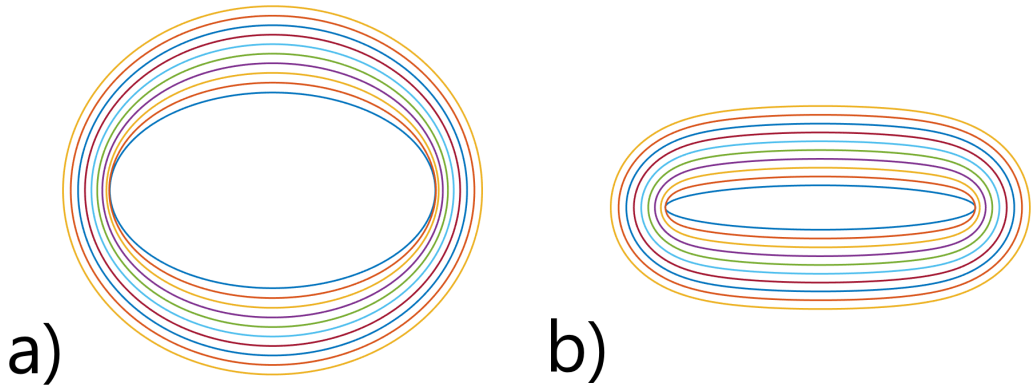

Figure 2.3: (a) Evolution of the elliptical fire line in figure 2.2a with $\epsilon = 0.5$. (b) Evolution of an elliptical fire line with eccentricity $e = 0.99$ with curvature effect $\epsilon = 0.1$.

respectively, and thus eccentricity $e = 0.8$. The curvature parameter is $\epsilon = 0.1$, where the curvature acts to dilate the ellipse into a more circular shape as it grows. The absolute error of the RCA and RCL laws over time are plotted in figures 2.2b and 2.2c, respectively, for various values of *tstep* - the number of time steps between $t = 0$ and $t = 1$. As expected, increasing *tstep* improves the absolute error: both the RCA and RCL laws give an error of $\mathcal{O}(10^{-2})$ for *tstep*$= 50$, which runs in 5 seconds, and $\mathcal{O}(10^{-3})$ for *tstep*$= 1000$, which runs in 9 seconds. This is an order of magnitude of improvement on the absolute error of the RCA and RCL laws with little increase in the runtime of the code. Thus the value *tstep*$= 1000$ is chosen for the remainder of the examples, with an $\mathcal{O}(10^{-3})$ absolute error achieved for all upcoming radial examples.

The strength of the curvature effect on the same elliptical fire line as in figure 2.2a is increased in figure 2.3a to $\epsilon = 0.5$ and it is observed that there is a quicker deformation of the elliptical fire line into a circle, as expected. The eccentricity of the ellipse in figure 2.2a is increased to $e = 0.99$ and evolves with $\epsilon = 0.1$ in figure 2.3b. Due to its areas of larger curvature, this ellipse deforms more rapidly into a circle than

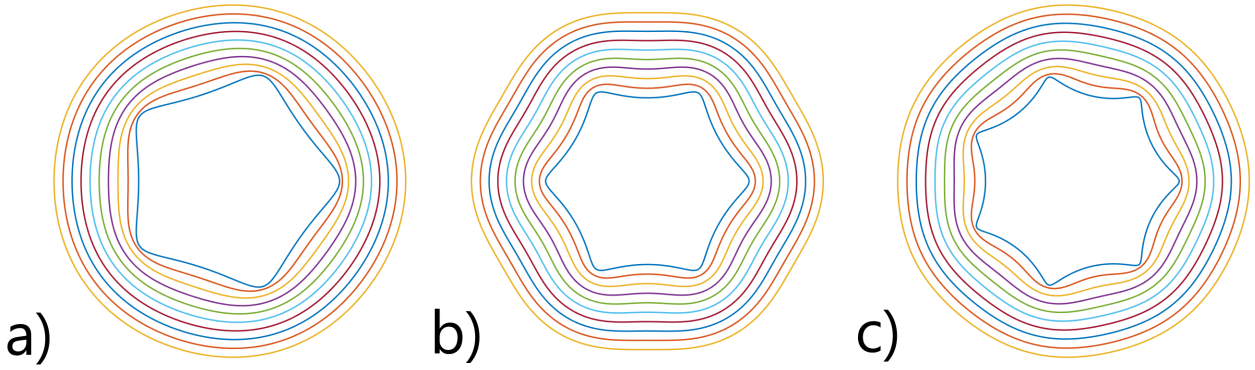

Figure 2.4: Evolution of various $n-$fold symmetric fire line shapes. (a) A five-pointed star with $\epsilon = 0.2$. (b) A six-pointed star with $\epsilon = 0.05$. (c) A seven-pointed star with $\epsilon = 0.1$.

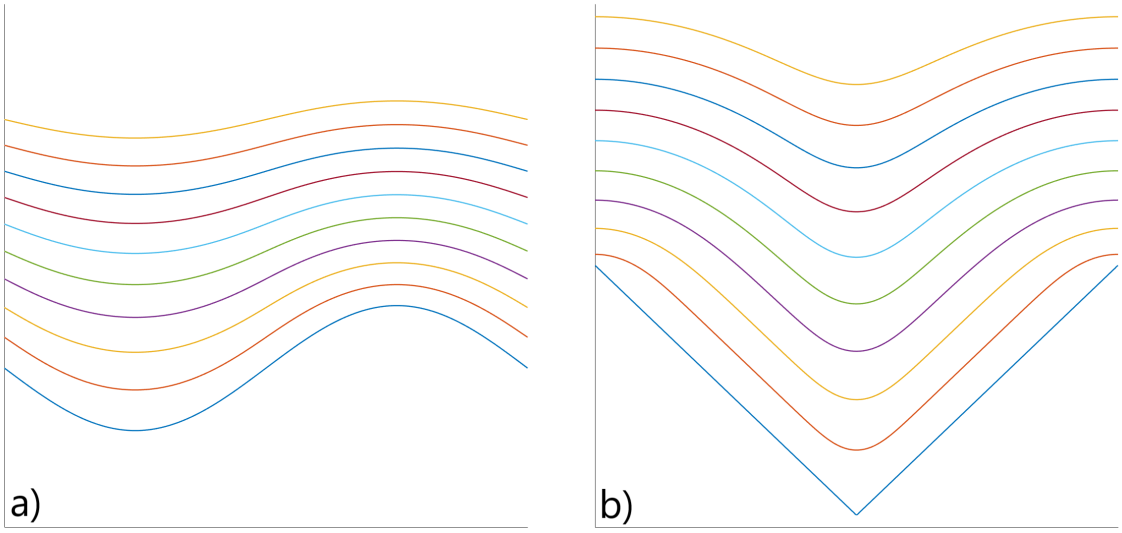

Figure 2.5: Evolution of periodic, infinite fire lines. (a) Sinusoidal fire line (odd function) evolving between $t = [0, 3]$. (b) Triangular fire line (even function) evolving between $t = [0, 4]$.

the previous ellipse did. Increasing the eccentricity of the ellipse further would result in a shape similar to a line fire; this observation is utilised in this thesis, see for example Ch.6. Finally, the evolution of a variety of $n-$fold symmetric shapes under different curvature effects (as given in the figure caption) are showcased in figure 2.4a-c, including a five-, six- and seven-pointed star, respectively. All of these shapes eventually approach a circular fire line, as expected. Finally, note that each radial fire line result was produced in under 15 seconds on runtime.

Next, consider a segment of a periodic, infinite fire line. Figure 2.5a shows the growth of a sinusoidal fire line (an odd function) and figure 2.5b shows that of a triangular fire line (an even function). These wildfires evolve between $t = [0, 3]$ and $t = [0, 4]$, respectively, with each using 1000 time steps per unit time and evolving under the curvature effect $\epsilon = 0.25$. The runtime was 38 seconds for the sinusoidal fire line and 68 seconds for the triangular fire line. The sinusoidal fire line has the single, initial non-zero

Laurent coefficient $b_1(0) = 0.75$ whereas the triangular fire line has the following coefficients

$$a_m(0) = \frac{-12\sin^2(\pi(m-1)/2)}{\pi^2(m-1)^2}, \quad \forall m \in [1, N]. \tag{2.6.1}$$

The evolution of both fires are as expected, with perturbations in the fire line eventually smoothed out by the curvature effect in agreement with the linear stability analysis. The absolute error of the RCA and RCL laws are of $\mathcal{O}(10^{-1})$ for the sinusoidal fire line and of $\mathcal{O}(10^{-2})$ for the triangular fire line. Finally, note in particular that the triangular fire is a good approximation of a junction fire - a wedge shaped fires which are often examined experimentally, see for example Sharples and Hilton (2017); Sullivan et al. (2019). Junction fires will be considered elsewhere in this thesis, see Ch.7.

2.7 Discussion

In this chapter, a basic wildfire model has been considered. This is named the 'Markstein' model in reference to the paper Markstein (1951) which first identified the two key elements necessary to model fire spread: a constant basic rate of spread term plus a curvature correction term. A linear stability analysis shows that perturbations in the fire line decay over time, and a conformal mapping method was then developed to obtain numerical results of the fire line evolution. These results were produced quickly (on the order of seconds) and were of good accuracy, which was verified by study of the absolute error of the RCA and RCL laws.

The Markstein model has been used previously with good success to model wildfire evolution that agrees with experimental data, see for example Viegas et al. (2012); Sharples et al. (2013); Sharples and Hilton (2017). This basic model also introduces many of the techniques used in later chapters of this thesis, namely the conformal mapping method used to obtain numerical solutions. However, this basic model does not consider the wildfire-atmosphere interaction, which is one of the main focuses of this thesis. In upcoming chapters, therefore, this basic model is built upon to incorporate other factors affecting wildfire spread.

Chapter 3

Oxygen transport and the development of fire fingers

The basic Markstein model of wildfire spread formulated in Ch.2 currently predicts that all radial wildfires will smooth into some steadily growing base state: a circular fire line. However, this is clearly not the case for real world wildfires which evolve into a variety of shapes, even in the simple flat terrain setup of Sect.2.1. Consider in particular the 1985 Onion sage brush fire in Owens Valley, California as seen in figure 1 of Clark et al. (1996b). The fire line here is notably unstable, where a number of protrusions have developed and continue to grow as the wildfire spreads - these are called 'fire fingers'. The Markstein model does not predict this 'fire fingering' behaviour (it is stable, see Sect.2.3) and therefore an additional effect needs to be included into the wildfire model in order to produce this fingering phenomenon. In this chapter, it is hypothesised that the effect of steady oxygen transport to the fire line could be a mechanism for fire fingering. This dynamic effect, which is coupled to the so-called 'pyrogenic wind' flow induced by the wildfire itself, is incorporated into the existing Markstein model, with the stability analysis and numerical method developed in Ch.2 extended to account for this new effect. Note that the work completed in this chapter was published in Harris and McDonald (2022).

3.1 Radial model

Consider first the radial wildfire problem as depicted in figure 3.1. The assumptions outlined in Sect.2.1 are made and the outward normal velocity v_n of the fire line is sought. The key difference from the wildfire problem of Ch.2 is that there is a self-induced pyrogenic (or 'fire') wind flowing in the exterior region Ω - the region of unburnt fuel. It is assumed this fire wind is also a shallow, horizontal inflow of depth

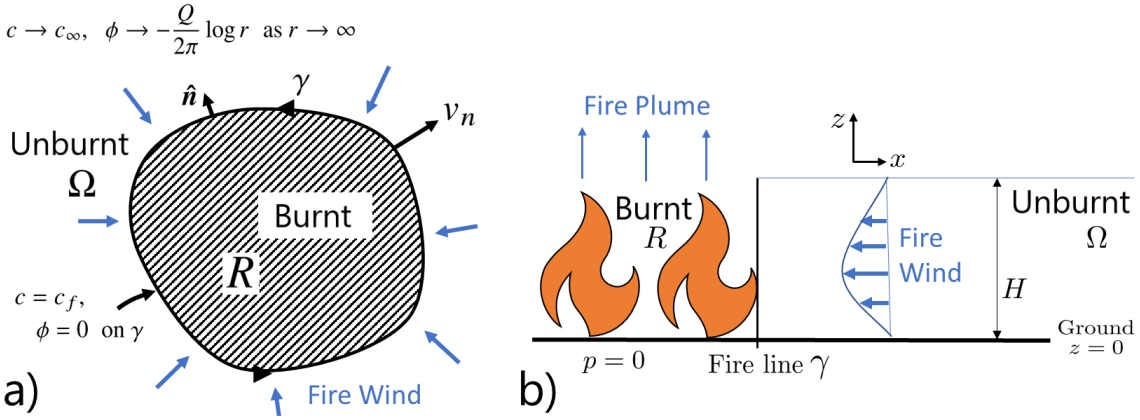

Figure 3.1: The radial wildfire model from plan (a) and side (b) views. The blue arrows represent the direction of the pyrogenic wind governed by the potential ϕ.

H - the flame height of the wildfire. Hence the pyrogenic wind is also treated as two-dimensional where $\boldsymbol{u}_p$ is the average fire wind velocity over the shallow layer of depth H. This fire wind transports oxygen to the fire line where it is then used in combustion, thus a concentration gradient between the far field and the fire line is sustained. Note that there is still assumed to be zero ambient wind - ambient winds are introduced in Ch.6. Whereas the problem in Ch.2 could be solved entirely on the fire line γ itself, the exterior region Ω must now also be considered. The burnt region R is treated simply as a sink of air known as the fire plume, with the pyrogenic wind being ejected vertically from the system upon crossing the fire line γ into R.

The effects of basic ROS v_0 and curvature $\delta\kappa$ from the Markstein model of Ch.2 are retained in the equation for the outward normal fire line velocity v_n. The effect of oxygen transport to the fire line is incorporated using a Stefan-like boundary condition, with the fire line velocity dependent on the local (normal) oxygen concentration gradient c. The (dimensional) equation for v_n is then

$$v_n = v_0 - \delta\kappa + \alpha \hat{\boldsymbol{n}} \cdot \boldsymbol{\nabla} c \quad \text{on } \gamma, \tag{3.1.1}$$

where α is some constant.

In order to solve for c, the pyrogenic wind flow in the exterior region Ω must also be modelled. To good agreement with experimental data (see e.g. Hilton et al. (2018)), the pyrogenic wind can be treated as a two-dimensional irrotational flow of an incompressible fluid. Furthermore, it is assumed that the pyrogenic wind velocity $\boldsymbol{u}_p$ is far greater than the fire line velocity v_n and hence the wind is assumed to be quasi-steady. Therefore, oxygen concentration c and the pyrogenic wind $\boldsymbol{u}_p = \boldsymbol{\nabla}\phi$, where ϕ is the

(scalar) pyrogenic potential, satisfy the coupled system

$$\nabla^2 \phi = 0, \tag{3.1.2}$$

$$\boldsymbol{u}_p \cdot \boldsymbol{\nabla} c = D \nabla^2 c, \tag{3.1.3}$$

where D is the diffusivity of c. These are the Laplace and steady advection-diffusion equations, respectively. Note that modelling the (pyrogenic) wind flow exterior to wildfires and plumes using solutions to the 2D Laplace equation has also been used previously by e.g. Weihs and Small (1986); Kaye and Linden (2004); Maynard et al. (2016); Sharples and Hilton (2020); Quaife and Speer (2021).

Finally, suitable boundary and far field conditions are needed. Consider the pressure p over the wildfire and in particular at the fire line γ itself; pressure anomalies have been used previously to model fire-induced surface winds, see for example Achtemeier (2012). Following the work and numerical model of Smith et al. (1975), strong buoyant acceleration over the burnt region of the wildfire generates low pressure locally at the fire line. This then leads to a horizontal pressure gradient which in turn generates the pyrogenic wind. This strong inflow is quite different in nature to the weak, entraining inflows commonly associated with turbulent plume dynamics, and is best modelled using dynamic pressure, which communicates the effect of fire-driven, buoyant air to the surrounding fluid. Without loss of generality, the low pressure at the fire line can be represented by the condition $p = 0$ on γ; this also assumes that the driving pressure of the wind flow is constant on the fire line.

A relation between the potential ϕ and the dynamic pressure p can then be attained. Consider the Reynolds number $\mathrm{Re} = UH/D$, where U is the typical fire wind velocity at the fire line, H is the height of the shallow layer in which the pyrogenic wind is flowing and D is the momentum diffusivity. Typical values of these quantities for a small starting wildfire are taken from table III of Beer (1991) and figure 6 of Bebieva et al. (2020): $U \sim 0.004\mathrm{ms}^{-1}$, $H \sim 0.5\mathrm{m}$ and $D \sim 1\mathrm{m}^2\mathrm{s}^{-1}$, which gives $\mathrm{Re} \approx 0.002$. To reasonable approximation, the exterior, shallow pyrogenic wind flow is thus governed by the Stokes flow equations. This approximation 'improves' further from the wildfire where the inflow velocity decreases. As the fire intensifies, the velocity scale U will increase, yet the diffusion coefficient D is also expected to increase owing to increased turbulent mixing, thus keeping Re sufficiently small. Assuming the approximation remains reasonable, such shallow flows are analogous to those in a Hele-Shaw cell and a standard derivation involving integration of the Stokes equations over the layer depth (see e.g. Gustafsson and Vasil'ev (2006)) shows that $\boldsymbol{u}_p = \boldsymbol{\nabla}\phi \sim -\boldsymbol{\nabla} p$. Thus the velocity potential ϕ is proportional to the (negative) pressure p and so $\phi = 0$ on the fire line γ without loss of generality.

The low pressure at the fire plume over the burnt region appears as an effective sink in the far field and so $\phi \to (-Q/2\pi)\log r$ as $r \to \infty$, where $Q > 0$ is the strength of the sink. As the wildfire grows, so too does the fire plume which begins to draw in more of the surrounding air. Thus the sink strength Q of the plume increases over time, leading to a larger fire wind flux (Trelles and Pagni, 1997). Let $Q = Q(t) = Q_0 q(t)$ where $q(0) = 1$ and Q_0 is some constant.

Combustion of unburnt fuel depletes the oxygen concentration to some level $c = c_f$ at the fire line, with oxygen rich air of concentration $c = c_\infty > c_f$ being delivered from the far field to the fire line by the pyrogenic wind. The boundary condition $c = c_f$ results from the assumption that the wildfire is uniform in its intensity at all points around the fire line and consumes oxygen to the same level; the actual value of $c_f < c_\infty$ is immaterial. Such a Dirichlet boundary condition on the moving interface for the quantity undergoing advection and diffusion is used in other free boundary problems, see for example Cummings et al. (1999) and Tsai and Wettlaufer (2007). To summarise, the boundary and far field conditions for ϕ and c are

$$\phi = 0, \quad c = c_f \ \text{ on } \gamma, \tag{3.1.4}$$

$$\phi \to -\frac{Q}{2\pi}\log r, \ \ c \to c_\infty \ \text{ as } r \to \infty. \tag{3.1.5}$$

3.1.1 Non-dimensionalisation and the Péclet number

As in Ch.2, equations (3.1.1) to (3.1.5) are non-dimensionalised using a characteristic length scale L which is here chosen as the initial conformal radius $L = R_0$ of the wildfire. Scalings are chosen to give rise to an $\mathcal{O}(1)$ oxygen driven contribution to v_n, since oxygen effects are of particular interest in this chapter. Thus the dimensionless (starred) variables are

$$\nabla = \frac{1}{L}\nabla^*, \quad \kappa = \frac{1}{L}\kappa^*, \quad \phi = \frac{Q}{2\pi}\phi^*, \ \ c^* = \frac{c - c_f}{c_\infty - c_f}, \quad t = \frac{L}{U\mathrm{Pe}_0}t^*, \quad U = \frac{\alpha(c_\infty - c_f)}{L}, \tag{3.1.6}$$

where $\mathrm{Pe}_0 = Q_0/2\pi D$ is the constant initial value of the Péclet number. Dropping stars immediately, the non-dimensional system for the wildfire problem is

$$\mathrm{Pe}_0\, v_n = V_0 - \bar{\epsilon}\kappa + \hat{\boldsymbol{n}} \cdot \boldsymbol{\nabla} c \quad \text{on } \gamma, \tag{3.1.7}$$

$$\nabla^2 \phi = 0 \quad \text{in } \Omega, \tag{3.1.8}$$

$$\mathrm{Pe}\, \boldsymbol{u}_p \cdot \boldsymbol{\nabla} c = \nabla^2 c \quad \text{in } \Omega, \tag{3.1.9}$$

$$\phi = 0, \quad c = 0 \quad \text{on } \gamma, \tag{3.1.10}$$

$$\phi \to -\log r, \quad c \to 1 \quad \text{as } r \to \infty, \tag{3.1.11}$$

where the new, dimensionless constants V_0 and $\bar{\epsilon}$, representing the basic ROS and magnitude of the curvature effect respectively, are

$$V_0 = \frac{L v_0}{\alpha(c_\infty - c_f)}, \quad \bar{\epsilon} = \frac{\delta}{\alpha L (c_\infty - c_f)}. \tag{3.1.12}$$

Note that the quantity $\tilde{\epsilon}$ is distinct from the constant ϵ used in Ch.2.

The non-dimensional, time-varying Péclet number Pe in equation (3.1.9) is

$$\mathrm{Pe} = \frac{Q(t)}{2\pi D} = \frac{Q_0 q(t)}{2\pi D} = \mathrm{Pe}_0 q(t). \tag{3.1.13}$$

Recall that the plume strength $Q(t) = Q_0 q(t)$ is assumed to grow in time as the fire expands, thus the Péclet number also increases in time. Choosing $q(t) \sim R(t)$, where $R(t)$ is the radius of the burnt region R, gives

$$\mathrm{Pe} = \frac{\mathrm{Pe}_0}{R_0} R(t). \tag{3.1.14}$$

In this chapter, it is assumed that $R_0 = 1$ throughout and so the Péclet number is simply $\mathrm{Pe} = \mathrm{Pe}_0 R(t)$. Note also that Pe_0 has been incorporated in the scale for time t^* in equation (3.1.6).

Finally, the (entropy) condition that the wildfire always progress from the burnt to the unburnt region (Sethian, 1985) must once again be satisfied. Violating the entropy condition would not affect the upcoming linear stability analysis in Sect.3.2, since the fire line does not move, but such unphysical behaviour could be possible in the numerical, nonlinear evolution of the fire line computed in Sect.3.3. No explicit mechanism to enforce the entropy condition is included in equation (3.1.7) as violations to the condition are likely very rare. This is because both the basic ROS and oxygen effects cause the fire line to propagate toward the unburnt region, and it is taken that $0 < \delta\kappa \ll v_0$ as in Ch.2 so the curvature effect is relatively

small. If there were a non-zero ambient wind present, such a mechanism would be necessary to include - see Ch.6.

3.2 Stability analysis

The stability of a perturbed fire line curve γ evolving under equations (3.1.7) to (3.1.11) is studied. Whereas the linear stability analysis performed in Ch.2 showed that all perturbations decayed over time due to the stabilising effect of curvature, it is here expected that there is some range of (unstable) wavenumbers which grow over time; this would be an example of fire fingering. This is because the effect of steady oxygen transport to the fire line is destabilising, thus the overall stability is determined by the competing effects of curvature (stabilising) and oxygen consumption (destabilising), quantified by the parameters $\bar{\epsilon}$ and Pe respectively.

First, consider an unperturbed base state γ given by the circle $r = R(t)$, with $R(0) = 1$ so that $\mathrm{Pe} = \mathrm{Pe}_0 R(t)$. The solution to equations (3.1.8) to (3.1.11) is

$$\phi(r) = -\log\frac{r}{R}, \quad c(r) = 1 - \left(\frac{R}{r}\right)^{\mathrm{Pe}}. \tag{3.2.1}$$

Using that $\kappa = R^{-1}$, the normal velocity equation (3.1.7) of the fire line γ is

$$\mathrm{Pe}_0 v_n = \mathrm{Pe}_0 \dot{R} = V_0 - \frac{\bar{\epsilon}}{R} + \frac{\mathrm{Pe}}{R}, \tag{3.2.2}$$

where the dot denotes the time derivative. Dividing through by Pe then gives the growth rate of the radius R

$$\frac{\dot{R}}{R} = \frac{V_0}{\mathrm{Pe}_0 R} - \frac{\sigma}{R} + \frac{1}{R} = \frac{1}{R}\left[\frac{V_0}{\mathrm{Pe}_0} - \sigma + 1\right], \tag{3.2.3}$$

where $\sigma = \sigma(t) = \bar{\epsilon}/\mathrm{Pe}$. Provided that $\bar{\epsilon} < V_0 + \mathrm{Pe}_0$ (which is necessarily true as $\bar{\epsilon} \ll V_0$), this means that the radius $R(t)$ (and hence also the Péclet number) grow in time.

Now, consider the perturbed, circular fire line

$$r = r_p = R(t) + \sum_{n=1}^{\infty} \delta_n(t) \cos n\theta, \tag{3.2.4}$$

where $\delta_n \ll 1, \forall n$. The summation sign is dropped henceforth. Note that the $n = 1$ mode corresponds to a uniform translation of the fire line (Brower et al., 1984) and is stable, so only the stability of perturbations $n \geq 2$ are considered. The following expression for ϕ solves the Laplace equation (3.1.8) and satisfies the

far field condition in equation (3.1.11)

$$\phi = -\log\frac{r}{R} + \beta_n \frac{R^n}{r^n}\cos n\theta, \tag{3.2.5}$$

where $\beta_n \ll 1$ is a constant. Then, equations (3.2.1) and (3.2.5) suggest writing

$$c = 1 - \left(\frac{R}{r}\right)^{\mathrm{Pe}} + \gamma_n \frac{R^{\alpha_n}}{r^{\alpha_n}}\cos n\theta, \tag{3.2.6}$$

where $\gamma_n \ll 1$ and $\alpha_n > 0$ are constants, which satisfies the far field condition equation (3.1.11). The boundary conditions in equation (3.1.10) give $\beta_n = \delta_n/R$ and $\gamma_n = -\mathrm{Pe}\delta_n/R$. Substituting equations (3.2.5) and (3.2.6) into equation (3.1.9), and retaining terms to $\mathcal{O}(\delta_n)$, it then follows that $\alpha_n = n + \mathrm{Pe}$.

The normal velocity equation (3.1.7) of the fire line $\gamma : r = r_p$ can now be written to $\mathcal{O}(\delta_n^2)$ where δ_n^2 defines any product $\delta_n\delta_m$, for all m, n (as introduced in Ch.2). Each term of equation (3.1.7) is evaluated as

$$v_n = \frac{\partial \boldsymbol{x}}{\partial t} \cdot \hat{\boldsymbol{n}} = \dot{R} + \dot{\delta_n}\cos n\theta + \mathcal{O}(\delta_n^2), \tag{3.2.7}$$

$$\kappa = \frac{1}{R}\left[1 + \frac{\delta_n(n^2-1)}{R}\cos n\theta\right] + \mathcal{O}(\delta_n^2), \tag{3.2.8}$$

$$\hat{\boldsymbol{n}} \cdot \boldsymbol{\nabla} c = \frac{\partial c}{\partial r} + O(\delta_n^2) = \frac{\mathrm{Pe}}{R}\left[1 + \frac{\delta_n(n-1)}{R}\cos n\theta\right] + \mathcal{O}(\delta_n^2). \tag{3.2.9}$$

Thus the normal velocity equation (3.1.7) becomes

$$\mathrm{Pe}_0\Big(\dot{R} + \dot{\delta_n}\cos n\theta\Big) = V_0 + \frac{1}{R}\left[-\bar{\epsilon} + \mathrm{Pe} + \frac{\delta_n}{R}\Big(-\bar{\epsilon}(n^2-1) + \mathrm{Pe}(n-1)\Big)\cos n\theta\right] + \mathcal{O}(\delta_n^2). \tag{3.2.10}$$

The leading order term of equation (3.2.10) is simply a restatement of equation (3.2.3). To $\mathcal{O}(\delta_n)$, the growth rate for the n^{th} mode of perturbation is

$$\frac{\dot{\delta_n}}{\delta_n} = \frac{1}{R}\Big[-\sigma n^2 + n + (\sigma - 1)\Big]. \tag{3.2.11}$$

Taking the difference of equations (3.2.3) and (3.2.11) gives the relative growth rate, denoted in this chapter by $g(n)$; this is the growth of perturbations relative to the overall growth of the wildfire. The relative growth rate was not found in Ch.2 as all perturbation modes were stable regardless of the growth of the wildfire. However, it is necessary to consider the relative growth now that unstable modes are possible:

if perturbations grow slower than the wildfire radius R, the observed behaviour is that of stability rather than instability (see also Dallaston and Hewitt (2014)). The relative growth rate is thus

$$g(n) = \frac{\partial}{\partial t}\left(\log\left(\frac{\delta_n}{R}\right)\right) = \frac{\dot{\delta_n}}{\delta_n} - \frac{\dot{R}}{R} = \frac{1}{R}\Big(-\sigma n^2 + n + 2(\sigma - 1) - \lambda\Big), \tag{3.2.12}$$

where $\lambda = V_0/\mathrm{Pe}_0$. Instability occurs when $g(n) > 0$. If $\sigma = 0$, i.e. $\bar{\epsilon} = 0$ (zero curvature effect), then $g(n) = (n - 2 - \lambda)/R$ and all modes $n > 2 + \lambda$ are unstable. However, if the initial Péclet number is very small, then $\sigma, \lambda \to \infty$ and $g(n) \to (\sigma(2 - n^2) - \lambda)/R$, so all modes $n \geq 2$ are stable. This demonstrates that both stable and unstable fire line behaviour is possible.

The stability of perturbations depends on the sign of the numerator of equation (3.2.12)

$$f(n) = -\sigma n^2 + n + 2(\sigma - 1) - \lambda, \tag{3.2.13}$$

where $f(n) > 0$ for $n_- < n < n_+$, with

$$n_\pm = \frac{1 \pm \sqrt{\Delta}}{2\sigma}, \qquad \Delta = 8\sigma^2 - 4\sigma(2 + \lambda) + 1. \tag{3.2.14}$$

The real roots $n_\pm$ exist when $\Delta > 0$. Note that if $\Delta = 0$, then $n_- = n_+ = n^*$ and $f(n^*) = 0$, which is stable. The function Δ is positive for $\sigma_- > \sigma$ and $\sigma_+ < \sigma$, where

$$\sigma_\pm = \frac{2 + \lambda \pm \sqrt{\lambda^2 + 4\lambda + 2}}{4}. \tag{3.2.15}$$

As $\lambda > 0$, these roots always exist and if $\sigma_- \leq \sigma \leq \sigma_+$, then all modes are stable. If $\sigma_- > 0$, the instability region $\sigma_- > \sigma$ is observable for $\sigma > 0$, however the limit $\sigma \to \infty$ gives $n_+ < 2$ meaning that the instability region $\sigma > \sigma_+$ is generally not observable. Finally, differentiating equation (3.2.12) with respect to n gives the maximum growth rate g_{max} as

$$n_{max} = \frac{1}{2\sigma}, \qquad g_{max} = \frac{1}{R}\Big(\frac{1}{4\sigma} + 2(\sigma - 1) - \lambda\Big), \tag{3.2.16a}$$

where n_{max} is the mode of perturbation corresponding to g_{max}. If all modes of perturbation are stable, g_{max} is the slowest rate of decay. In an unstable regime, the fastest growing mode n_{max} becomes the dominant perturbation, but as σ decreases in time, (since $\mathrm{Pe} = \mathrm{Pe}_0 R(t)$ increases as the wildfire expands) the dominant mode n_{max} also changes. This behaviour is explored in Sect.3.3.

For a given value of $\lambda = V_0/\mathrm{Pe}_0$, the (σ, n)-parameter space stability diagram can be constructed as in

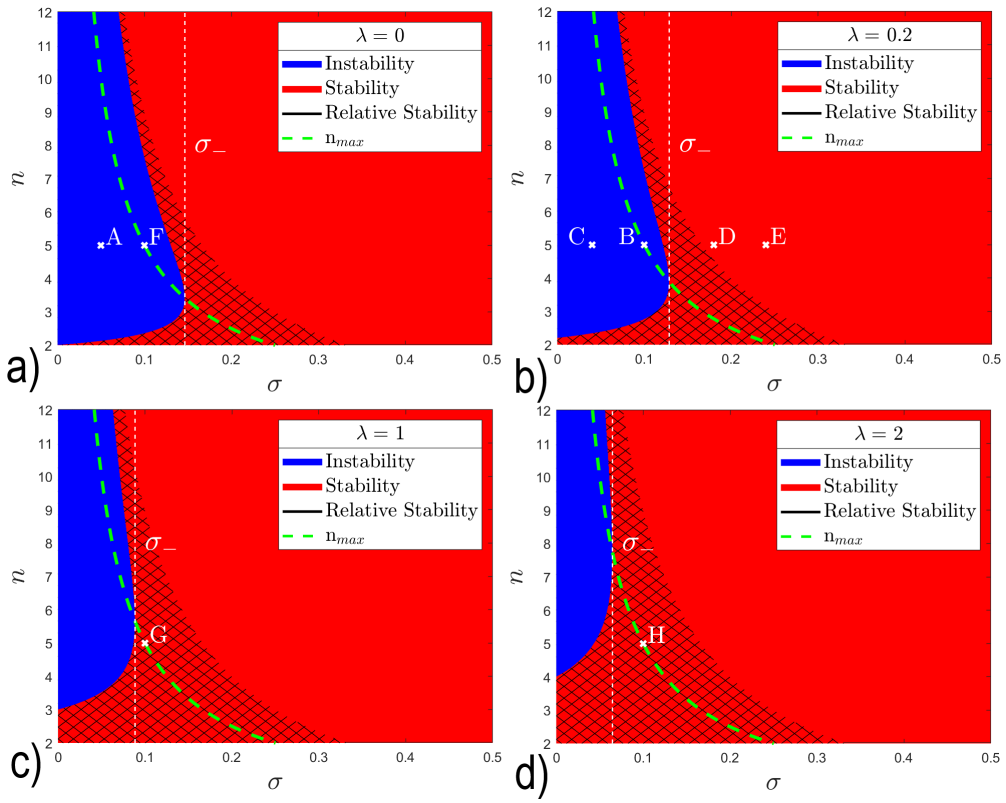

Figure 3.2: Parameter space stability diagrams for the perturbed fire line equation (3.2.4). Regions of instability are in blue, stability in red and the cross-hatched areas (denoted by the black line in the graph key) are regions of 'relative stability'. The mode of maximum growth n_{max} as in equation (3.2.16) for a given σ is shown by the green, dashed line. The points A-H correspond to initial choices of σ and n in figures in Sect.3.3 as follows: A - figure 3.3; B - figures 3.4, 3.5b, 3.7b; C - figure 3.5a; D - figure 3.5c; E - figure 3.5d; F - figure 3.7a; G - figure 3.7c; H - figure 3.7d.

figure 3.2. Regions of instability ($g(n) > 0$, blue) and stability ($g(n) \leq 0$, red) are shaded, along with a cross-hatched area in the stability region where perturbations grow but are outpaced by the growing radius of the fire line. Four such stability diagrams are given in figure 3.2, the points A-H corresponding to initial σ and n values for specified numerical results in Sect.3.3. It is important to note that as σ decreases over time, the points A-H will propagate to the left as t increases. This is also discussed in Sect.3.3.

3.3 Numerical simulation of nonlinear evolution

3.3.1 Conformal mapping method

An extension to the conformal mapping method introduced in Sect.2.4 is developed to numerically compute the nonlinear evolution of the fire line γ. It is now specified that the conformal map $z = f(\zeta, t)$ transforms the interior of the unit ζ-disk to the unburnt region Ω, with $\zeta = 0$ getting mapped to infin-

ity. The Laplace and steady advection-diffusion equations (3.1.8) and (3.1.9) are conformally invariant under the transformation, with the boundary and far field conditions (equations (3.1.10) and (3.1.11)) becoming

$$\phi = 0, \quad c = 0 \ \text{ on } |\zeta| = 1, \tag{3.3.1}$$

$$\phi \to \log|\zeta|, \ \ c \to 1 \ \text{ as } \zeta \to 0. \tag{3.3.2}$$

Exact solutions for ϕ and c in the $\zeta-$plane are then found

$$\phi(\zeta) = \log|\zeta|, \quad c(\zeta) = 1 - |\zeta|^{\mathrm{Pe}}. \tag{3.3.3}$$

The numerical task is now to find the conformal map $z = f(\zeta, t)$. In this chapter, only Laurent shapes are considered. As defined in Ch.2, these are fire line shapes for which the conformal map f can be written as the following Laurent series for all time

$$z = f(\zeta, t) = a_{-1}(t)\zeta^{-1} + \sum_{m=1}^{\infty} a_m(t)\zeta^{nm-1}. \tag{3.3.4}$$

The fire line γ consequently has n-fold symmetry where $n \geq 1$, with one line of symmetry taken to be the real axis such that the coefficients a_m are real. Note that a_{-1} is the conformal radius and is a measure of the horizontal length scale of the wildfire; this is identical to $R(t)$ for a circular wildfire. Hence the Péclet number can be written as $\mathrm{Pe} = \mathrm{Pe}_0 R(t) = \mathrm{Pe}_0 a_{-1}(t)$, where $a_{-1}(0) = 1$ is chosen in all upcoming numerical tests.

Following the approach in Sect.2.4 and that used in other free boundary problems such as Hele-Shaw flows (Howison, 1986) and the dissolution of solids in potential flow (Ladd et al., 2020), the normal velocity of the free boundary equation (3.1.7) is formulated in terms of the map $z = f(\zeta, t)$ in equation (3.3.4), yielding an equation of the Polubarinova-Galin class. From Dallaston and McCue (2013)

$$v_n = \frac{\mathrm{Re}\big[f_t \overline{\zeta f_\zeta}\big]}{|f_\zeta|}, \qquad \kappa = \frac{\mathrm{Re}\big[\zeta(\zeta f_\zeta)_\zeta \overline{\zeta f_\zeta}\big]}{|f_\zeta|^3}, \tag{3.3.5}$$

and the oxygen concentration gradient is

$$\hat{\boldsymbol{n}} \cdot \boldsymbol{\nabla} c = \mathrm{Re}[n\overline{\nabla} c] = 2\mathrm{Re}\left[n\frac{\partial c}{\partial z}\right] = 2\mathrm{Re}\left[\frac{\zeta f_\zeta}{|f_\zeta|}\frac{\partial c}{\partial \zeta}\frac{1}{f_\zeta}\right] = -\frac{\mathrm{Pe}}{|f_\zeta|} \quad \text{on } |\zeta| = 1, \tag{3.3.6}$$

where $\overline{\nabla} = 2\partial_z = \partial_x - i\partial_y$, $n = n_x + in_y$ is the complex representation of the normal vector in the

$z-$plane, and $f_\zeta = \partial f/\partial\zeta$. Also used is the result $n = \zeta f_\zeta/|f_\zeta|$, and that c in the $\zeta-$disk is given by equation (3.3.3), so $\partial c/\partial\zeta = -\mathrm{Pe}/2\zeta$ on $|\zeta| = 1$.

Now, equations (3.3.5) and (3.3.6) can be substituted into equation (3.1.7), then multiplying through by $|f_\zeta|/\mathrm{Pe}_0$ gives

$$\mathrm{Re}\Big[f_t\overline{\zeta f_\zeta}\Big] = \lambda|f_\zeta| - \frac{\sigma_0\mathrm{Re}\Big[\zeta(\zeta f_\zeta)_\zeta\overline{\zeta f_\zeta}\Big]}{|f_\zeta|^2} - a_{-1}(t), \tag{3.3.7}$$

recalling that $\lambda = V_0/\mathrm{Pe}_0$ and $\sigma_0 = \bar{\epsilon}/\mathrm{Pe}_0$. Choosing $V_0 = \bar{\epsilon} = 0$ is analogous to the problem of viscous fingering of a fluid with zero surface tension in a Hele-Shaw cell e.g. Howison (1986); Mineev-Weinstein (1998); Gustafsson and Vasil'ev (2006). Omitting the $a_{-1}(t)$ term in equation (3.3.7) (the case of no oxygen effect) reproduces equation (2.4.7) for the Markstein model from Ch.2, noting that the scalings would need to be modified such that $\lambda \to 1$ and $\sigma_0 \to \epsilon$. The infinite series in equation (3.3.4) is once again truncated at N terms and $N+1$ uniformly distributed points $\zeta = \zeta_j$ on the $\zeta-$disk are chosen to give a system of $N+1$ coupled first-order ODEs in t for the unknown coefficients $a_m(t)$; this is solved using the MATLAB routine *ode15i*.

3.3.2 Rate of change of area law

As in Ch.2, a rate of change of area (RCA) law can be found for the radial wildfire problem. This can then be used to assess the accuracy of the upcoming numerical outputs. Let $A(t)$ be the area enclosed by the fire line γ, and denote the length of γ by $L(t)$. The following geometrical properties of a smooth, non-intersecting, two-dimensional closed curve γ (Brower et al., 1984; Dallaston and McCue, 2016) are used

$$2\pi = \int_\gamma \kappa \mathrm{d}s, \qquad L(t) = \int_\gamma \mathrm{d}s, \qquad \frac{\mathrm{d}A}{\mathrm{d}t} = \int_\gamma v_n \mathrm{d}s. \tag{3.3.8}$$

Substituting equation (3.1.7) into the expression for $\mathrm{d}A/\mathrm{d}t$ in equation (3.3.8) gives

$$\frac{\mathrm{d}A}{\mathrm{d}t} = \frac{V_0}{\mathrm{Pe}_0}\int_\gamma \mathrm{d}s - \frac{\bar{\epsilon}}{\mathrm{Pe}_0}\int_\gamma \kappa \mathrm{d}s + \frac{1}{\mathrm{Pe}_0}\int_\gamma \frac{\partial c}{\partial n}\mathrm{d}s. \tag{3.3.9}$$

The first two terms on the right hand side of equation (3.3.9) can be simplified using equation (3.3.8). To evaluate the third term, the integral is first transformed to the unit $\zeta-$disk, $\zeta = e^{i\theta}$ where $0 \le \theta < 2\pi$. Note the result $\partial c/\partial n = \mathrm{Pe}_0 a_{-1}(t)/|f_\zeta|$, which is similar to equation (3.3.6) but necessarily positive as the normal is directed outwards to γ. Since $\mathrm{d}s = |f_\zeta|\mathrm{d}\theta$, the RCA law is

$$\frac{\mathrm{d}A}{\mathrm{d}t} = \frac{V_0}{\mathrm{Pe}_0}L(t) + 2\pi\left[a_{-1}(t) - \frac{\bar{\epsilon}}{\mathrm{Pe}_0}\right]. \tag{3.3.10}$$

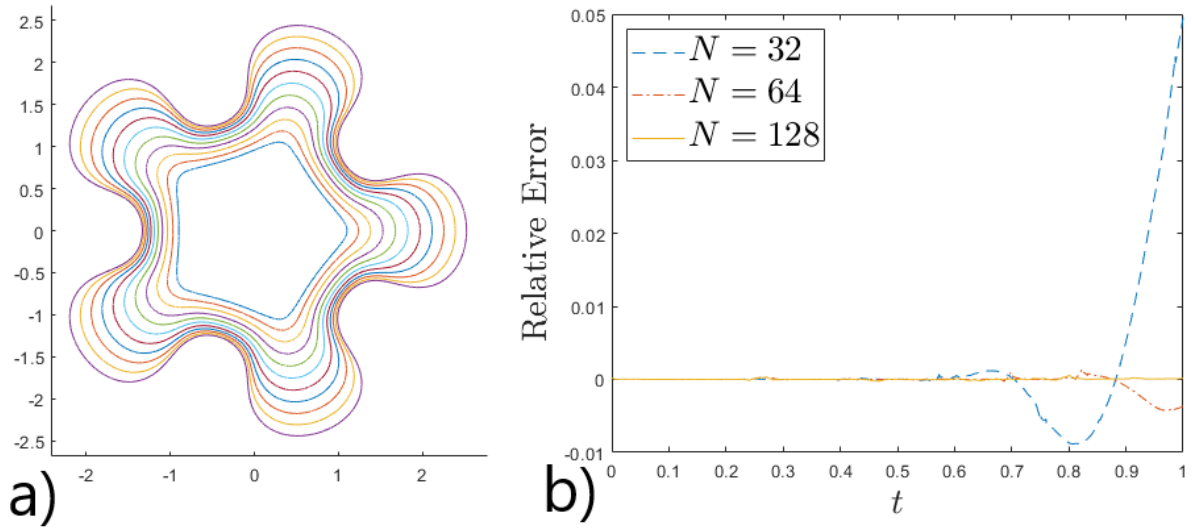

Figure 3.3: a) Evolution of fire fingers for a fire-star $n = 5$ with $V_0 = 0$, $\bar{\epsilon} = 0.1$, $\mathrm{Pe}_0 = 2$, $\lambda = 0$, $\sigma_0 = 0.05$, $N = 128$ and $t_{max} = 1$. b) Relative error of the RCA law equation (3.3.10) of figure (a) for $N = 32, 64$ and 128.

The RCA law equation (3.3.10) is used to check the accuracy of the numerical results using the relative error (RE)

$$RE = \frac{LHS - RHS}{RHS}, \tag{3.3.11}$$

where LHS and RHS are the left and right hand sides of equation (3.3.10) respectively.

3.3.3 Results

Fire-stars

The nonlinear evolution of a 5-fold symmetric shape ($n = 5$), or fire-star, is computed. Figure 3.3a shows the evolution of a fire line with zero basic ROS $V_0 = 0$ and a small curvature effect $\bar{\epsilon} = 0.1$. The initial Péclet number $\mathrm{Pe}_0 = 2$ is chosen, thus $\lambda = V_0/\mathrm{Pe}_0 = 0$ and $\sigma_0 = \bar{\epsilon}/\mathrm{Pe}_0 = 0.05$, corresponding to point A on the stability diagram in figure 3.2a. The Laurent series in equation (3.3.4) is truncated at N=128 terms and the fire line evolves to $t_{max} = 1$ in 1000 time steps, following the spacing used in Ch.2. Sections of the fire line penetrating the unburnt region grow more quickly and fire fingers develop from the tips of the initial perturbations. This behaviour is in agreement with the stability diagram: the evolution begins in the instability region and remains unstable as σ decreases over time as a result of an increasing Péclet number. Fingering is also expected owing to the Mullins-Sekerka mechanism (Mullins and Sekerka, 1964; Brower et al., 1984).

The relative error RE in equation (3.3.11) of the RCA law equation (3.3.10) for figure 3.3a is plotted in figure 3.3b. Each of the three plots corresponds to a different value of the Laurent series truncation:

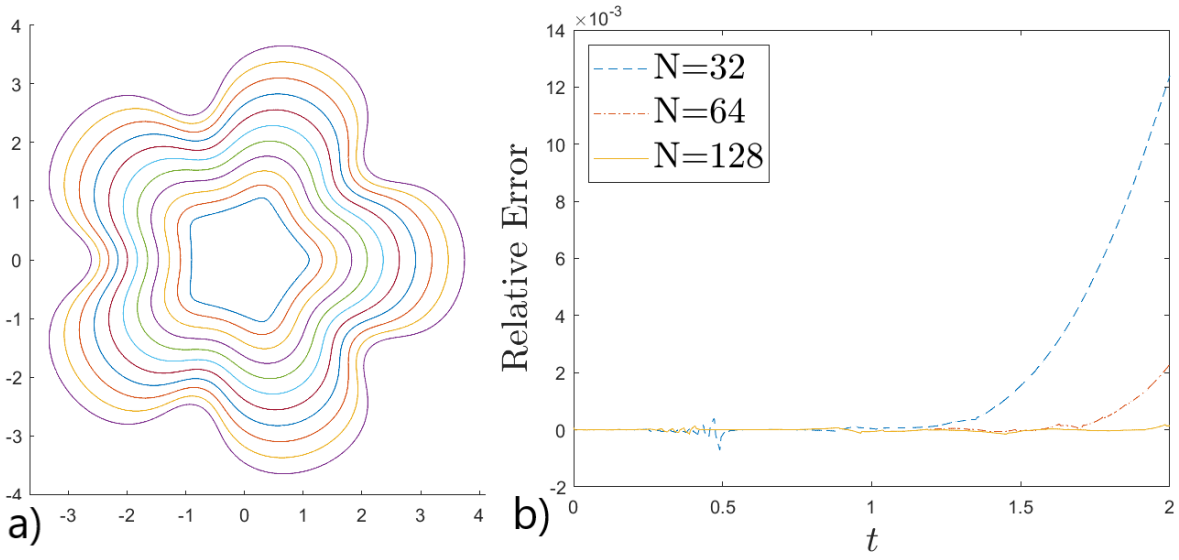

Figure 3.4: a) Evolution of fire fingers for $n = 5$, $V_0 = 1$, $\bar{\epsilon} = 0.5$, $\mathrm{Pe}_0 = 5$, $\lambda = 0.2$, $\sigma_0 = 0.1$, $N = 128$ and $t_{max} = 2$. b) Relative error of the RCA law equation (3.3.10) of plot (a), for varying N.

$N = 32, 64$ and 128, where the higher the series truncation, the further in time the fire line can evolve before significant, numerical errors appear. The cause of these errors is likely the lack of resolution in the 'valleys' of the fingers, due to a crowding of points at the 'finger tips'. While the points in the $\zeta-$plane are uniformly distributed, when mapped with equation (3.3.4) to the $z-$plane, their distribution becomes non-uniform around the fire line, hence the crowding. Evolution with larger $\bar{\epsilon}$ and V_0 can be computed accurately for larger times; the stronger curvature effect means that finger formation, and consequent crowding, take longer to develop.

Figure 3.4a gives an example of a more stable case; its initial state is the same as that of figure 3.3a, but now with $V_0 = 1$, $\bar{\epsilon} = 0.5$, $\lambda = 0.2$ and $\sigma_0 = 0.1$, and evolving up to a time $t_{max} = 2$. The burnt area R grows to a larger size due to the non-zero V_0 and, though fingers still develop as predicted in the stability diagram figure 3.2b (point B), they are less pronounced as in figure 3.3a due to the increased $\bar{\epsilon}$ effects. The relative errors plotted in figure 3.4b are significantly smaller in magnitude than those in figure 3.3b, with the RE decreasing as N is increased. Henceforth, all plots shall use $N = 128$, unless stated otherwise.

The result of increasing the curvature effect is shown in figure 3.5 for four choices of $\bar{\epsilon}$. As expected (Sethian, 1985; Hilton et al., 2016), increasing $\bar{\epsilon}$ smooths the fire line, reducing the amplitude of the fingers and valleys. The value $\lambda = 0.2$ is chosen, hence the stability diagram figure 3.2b is considered, with figures 3.5a,b,c,d corresponding to the points C, B, D and E respectively. Figures 3.5a,b are unstable and figure 3.5d is stable, in agreement with the initial position of each experiment in figure 3.2b. The

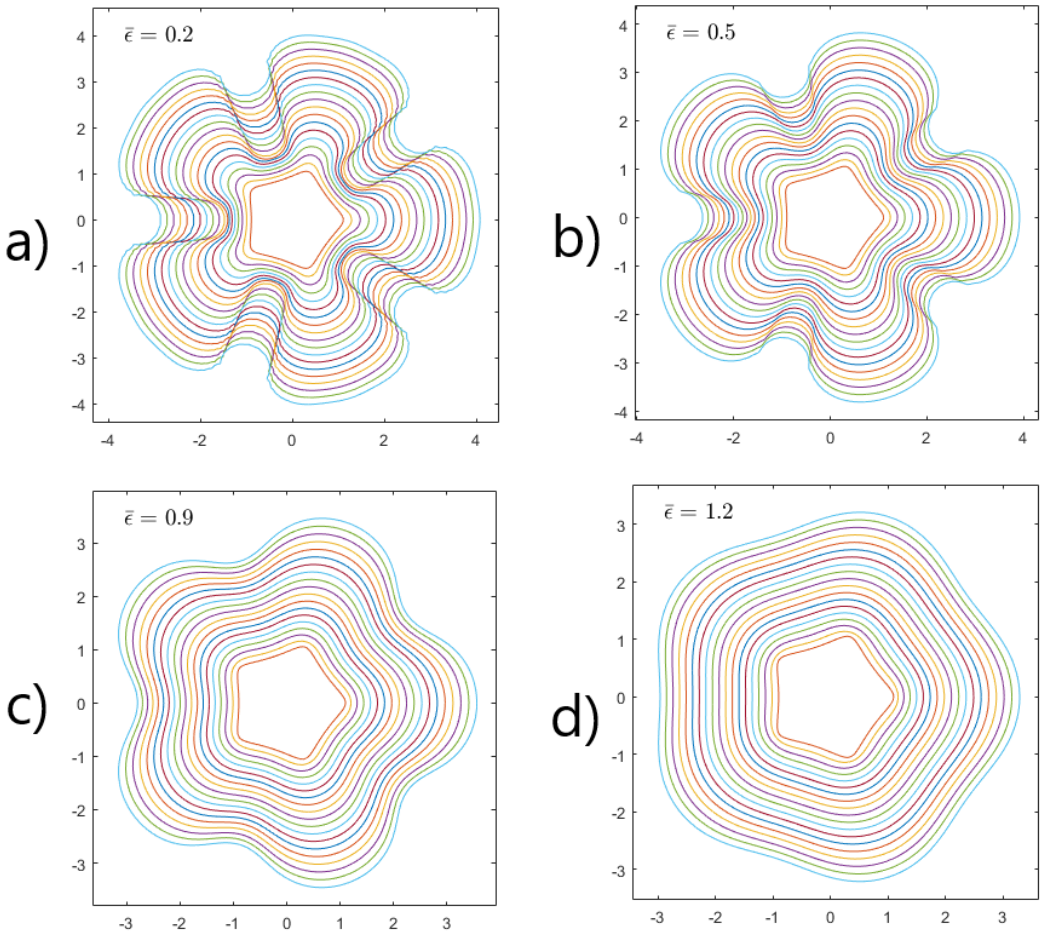

Figure 3.5: The effect of increasing $\bar{\epsilon}$: evolution of a fire-star with $n = 5$, $V_0 = 1$, $\mathrm{Pe}_0 = 5$, $\lambda = 0.2$, $N = 128$, $t_{max} = 2$ and a) $\bar{\epsilon} = 0.2$, $\sigma_0 = 0.04$ b) $\bar{\epsilon} = 0.5$, $\sigma_0 = 0.1$ c) $\bar{\epsilon} = 0.9$, $\sigma_0 = 0.18$ d) $\bar{\epsilon} = 1.2$, $\sigma_0 = 0.24$.

perturbations in figure 3.5c initially decay but then eventually grow to an amplitude larger than the initial perturbations. Considering figure 3.2b, the wildfire starts at point D in the stability region then enters the instability regime as σ decreases.

This type of behaviour is here called 'dormant fire instability', as the fire fingers appear to recede before growing again. Any initially stable fire line will eventually become unstable as Pe will continue to grow; the physical likelihood of this is discussed in Sect.3.5. Figure 3.6a gives an example of a dormant fire instability for a 7-pointed ($n = 7$) fire-star. The corresponding translation of the fire line on the stability diagram is also shown in figure 3.6b as a white line with markers at each time step of 1.25. Initially, the fire line is stable with $\lambda = 0$ and $\sigma_0 = 0.25$. Perturbations then start to grow at $t = 1.25$ but are slower than the overall growth of the wildfire, hence the fire line is in the relative stability regime. The fire line does not become unstable until around $t = 1.8$ when $\sigma = 0.106$, yet fire fingers only become noticeable from $t = 5$.

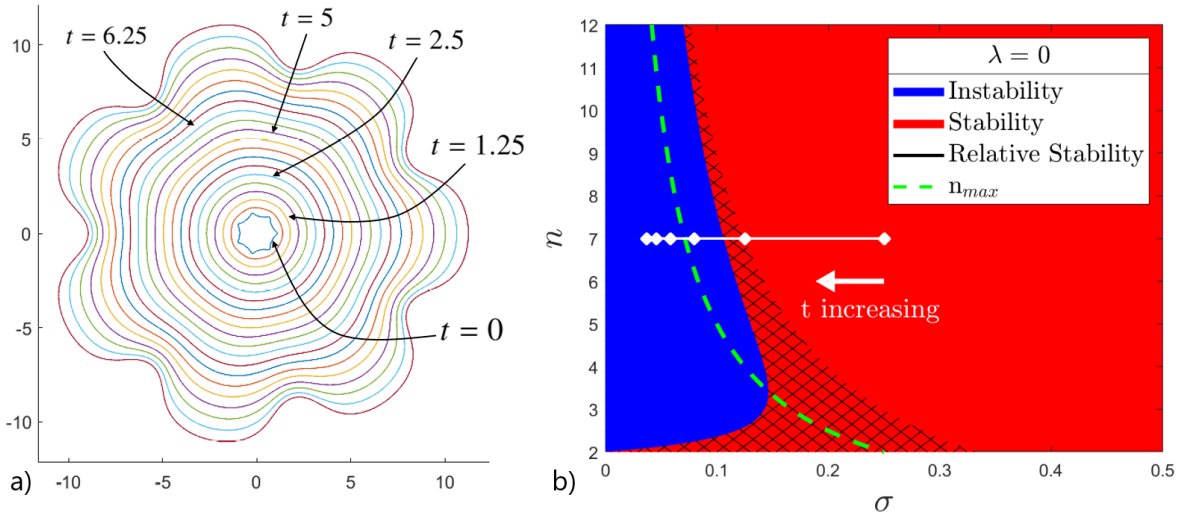

Figure 3.6: a) The evolution of a dormant fire instability of a 7-pointed star with $n = 7$, $V_0 = 0$, $\bar{\epsilon} = 0.5$, $\mathrm{Pe}_0 = 2$, $\lambda = 0$, $\sigma_0 = 0.25$, $N = 128$ and $t_{max} = 10$. b) The parameter space stability diagram of (a); each marker represents a time step of $t = 1.25$, from $t = 0$ (furthest right) to $t = 6.25$ (furthest left).

Finally, the effect of increasing V_0 on fire line evolution is shown in figure 3.7. The figures 3.7a,b,c,d correspond to the points F, B, G and H in the figures 3.2a,b,c,d, respectively. Increasing V_0 thins and shifts the instability region of the stability diagram such that instability only occurs for smaller values of σ, with some lower modes such as $n = 3$ always remaining relatively stable. Fire-stars ($n = 5$) with $\lambda \leq 2$ always eventually enter the instability region; even figure 3.7d has distinct valleys despite looking almost circular in shape. It is concluded that increasing V_0 causes fire fingers to widen, but not necessarily to flatten.

Fire lines with elliptical starting shapes

In addition to weakly, n-fold symmetrically perturbed circular fire lines, such as fire-stars ($n = 5$) and those considered in the stability analysis in Sect.3.2, the numerical method is also able to compute the evolution of fire lines with non-small initial perturbations. Elliptical starting shapes ($n = 2$) are here considered, where choosing an eccentricity e close to 1 provides a good approximation of a one-dimensional fire line segment, known as a line fire. As perturbations are non-small, the stability analysis of Sect.3.2 is not relevant in this case.

Figure 3.8 shows a series of results for initial ellipses with $e = 0.9986$, all of which use $N = 128$, $t_{max} = 9$ and $\mathrm{Pe}_0 = 2$. The effect of increasing V_0 is shown in figures 3.8a-c. As in figure 3.7 for a fire-star, the wildfires grow to a larger conformal radius as V_0 increases, as noted by the axes scales in each figure. There is also evidence of finger widening, however as there are only two fingers, this is seen as the valley between the fingers decreasing in depth and width, but still the valley is preserved. Flattening of the

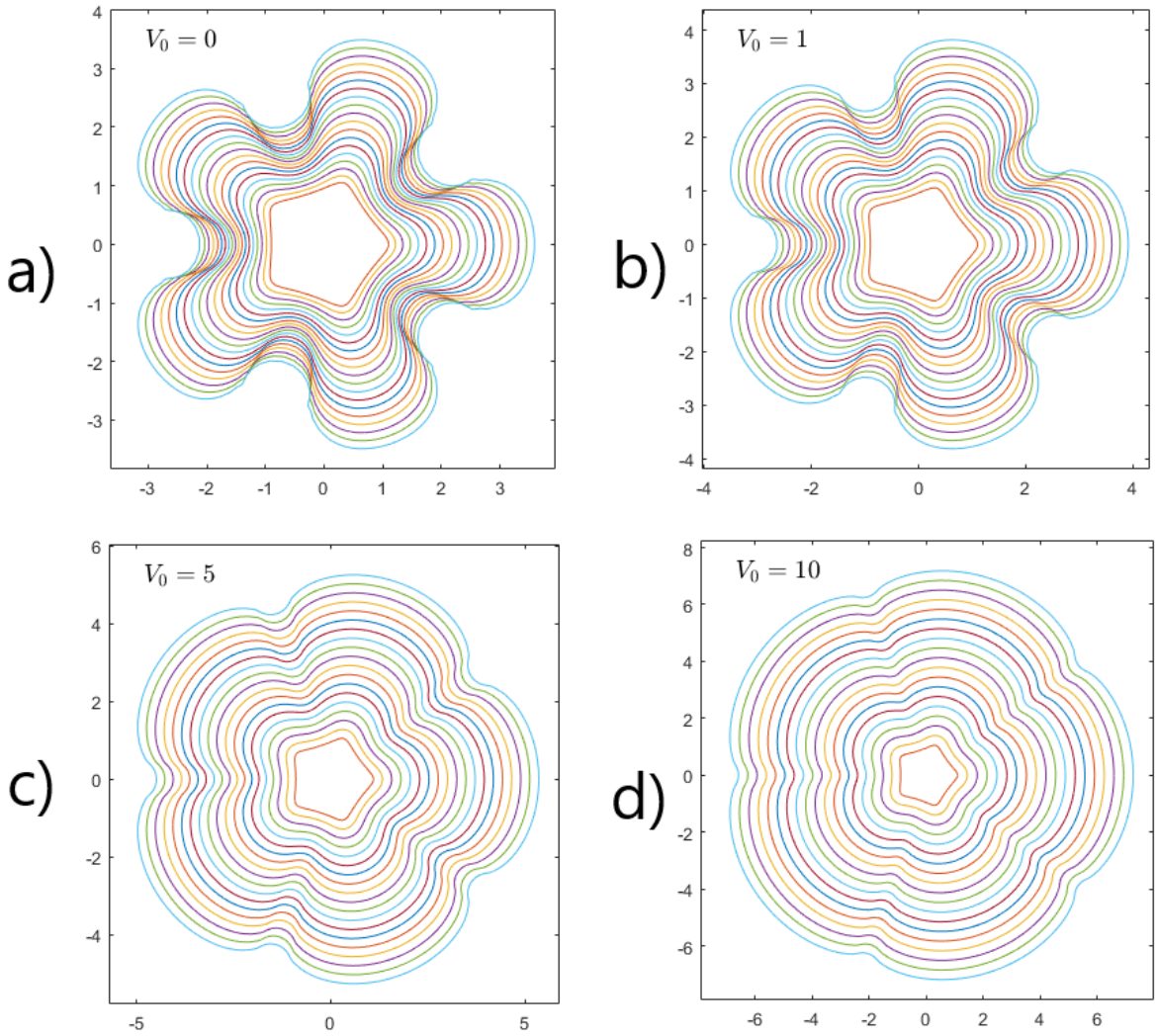

Figure 3.7: The effect of increasing V_0: evolution of a fire-star with $\bar{\epsilon} = 0.5$, $\mathrm{Pe}_0 = 5$, $\sigma_0 = 0.1$, $N = 128$, $t_{max} = 2$ and a) $V_0 = 0$, $\lambda = 0$, b) $V_0 = 1$, $\lambda = 0.2$, c) $V_0 = 5$, $\lambda = 1$, d) $V_0 = 10$, $\lambda = 2$.

fingers is achieved by increasing the curvature effect, as seen in figure 3.8d where $\bar{\epsilon}$ has increased to 0.9, as opposed to 0.5 for the other plots in figure 3.8. Finally, numerical instabilities are visible in figure 3.8a at around $t = 7$, due to the high curvature of the developing valleys. The model fails when the fire line begins to intersect previous iterations of itself from $t = 8$ onwards. This violates the entropy condition (Sethian, 1985) and hence the results are unphysical from this time; results are displayed up to $t_{max} = 9$ to show the self-intersection of the fire line more clearly

Emergence of a dominant mode

So far, only one mode of perturbation has been induced on a circular fire line. For fire-stars, this was the mode $n = 5$ (or $n = 7$ for a 7−pointed star) and for an ellipse it was $n = 2$. Now, multiple modes of (small) perturbation will be imposed at once and the resulting wildfire evolution explored. To allow

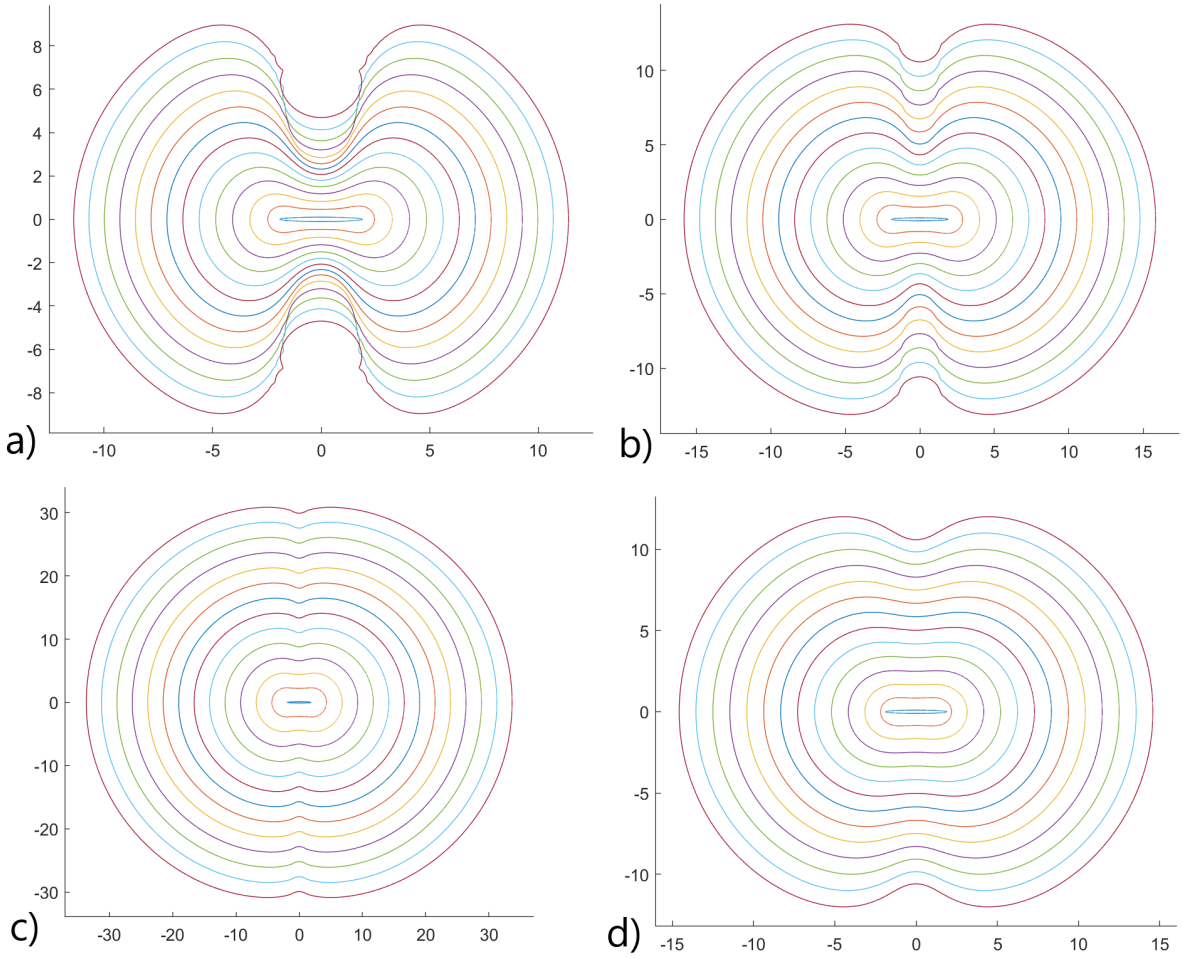

Figure 3.8: Evolution of an initially elliptical fire line with $\mathrm{Pe}_0 = 2$, $N = 128$, $t_{max} = 9$, $e = 0.9986$ and a) $V_0 = 0, \bar{\epsilon} = 0.5$, $\sigma_0 = 0.25$ b) $V_0 = 1, \bar{\epsilon} = 0.5$, $\sigma_0 = 0.25$ c) $V_0 = 5, \bar{\epsilon} = 0.5$, $\sigma_0 = 0.25$ d) $V_0 = 1, \bar{\epsilon} = 0.9$, $\sigma_0 = 0.45$.

many (co-prime) modes to be added, only $1-$fold symmetry ($n = 1$) is assumed and thus the Laurent coefficients in equation (3.3.4) are still real. The mode with the highest growth rate for a given σ will eventually dominate the wildfire evolution, yet because the value of σ decreases over time as the Péclet number increases, this dominant mode may also change over time - see Sect.3.2.

First consider the case where Pe is a constant in time. This differs from the radial wildfire model setup in Sect.3.1, but means the values of σ (and hence n_{max}) are unchanging in time. The stability analysis in Sect.3.2 is unchanged except that $\sigma = \bar{\epsilon}/\mathrm{Pe}$ is constant, and the only difference to the PG equation (3.3.7) is that the '$-a_{-1}(t)$' term is simply replaced by '-1'. Perturbations of modes $n = 3, 5$ and 7 are induced, each of small and equal amplitude, onto an initially circular fire line. Evolution of the fire line is then computed up to $t_{max} = 9$ with zero ROS ($V_0 = 0$) and a series truncation $N = 128$. Figures 3.9a,b,c show the results for the different choices of $\sigma = 0.08$, 0.1 and 0.14, respectively. In each plot, a different

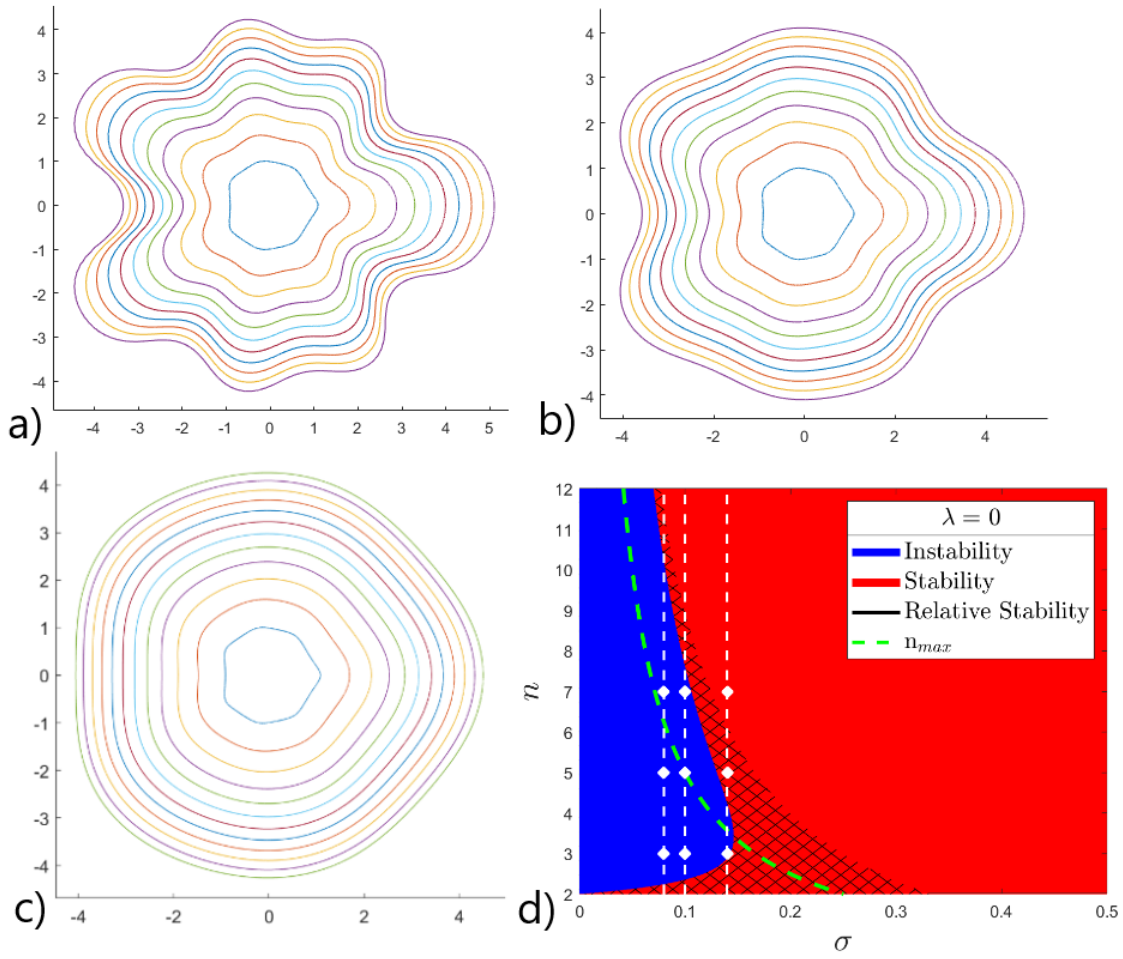

Figure 3.9: Evolution of a fire line with 3rd, 5th and 7th order perturbations and Pe constant. (a)-(c) $V_0 = 0$, $\text{Pe}_0 = 5$, $\lambda = 0$, $t_{max} = 9$, $N = 128$ and a) $\sigma = 0.08$, b) $\sigma = 0.1$, c) $\sigma = 0.14$. (d) Stability diagram; each vertical, dashed line represents the σ value for results (a)-(c) (from left to right) and each node on these vertical lines represents the 3rd, 5th and 7th order perturbation terms.

dominant mode emerges; (a) when $\sigma = 0.08$, the 7th mode dominates, (b) for $\sigma = 0.1$, it's the 5th mode and (c) for $\sigma = 0.14$, the 3rd mode. This agrees with the stability diagram in figure 3.9d; for each choice of σ, the positions of the 3rd, 5th and 7th order perturbations are plotted as nodes. For $\sigma = 0.1$, $n = 5$ is exactly $n = n_{max}$ which has the highest growth rate g_{max} of all possible modes (see Sect.3.2). For $\sigma = 0.08$, $n = 7$ has the highest growth rate of the three perturbations and hence dominates, and similarly for $n = 3$ in the $\sigma = 0.14$ case.

Now consider the time dependent Péclet number $\text{Pe} = \text{Pe}_0 a_{-1}(t)$. As σ decreases, the value of n_{max} increases (see equation (3.2.16)) so it is expected that the highest numbered excited mode will eventually dominate. Though it should be cautioned that once perturbations grow sufficiently large enough, they are no longer 'small' and so the stability analysis of Sect.3.2 can no longer be expected to hold. Figure 3.10 shows the evolution of the same initial fire line as in figure 3.9, with the same initial conditions $V_0 = 0$

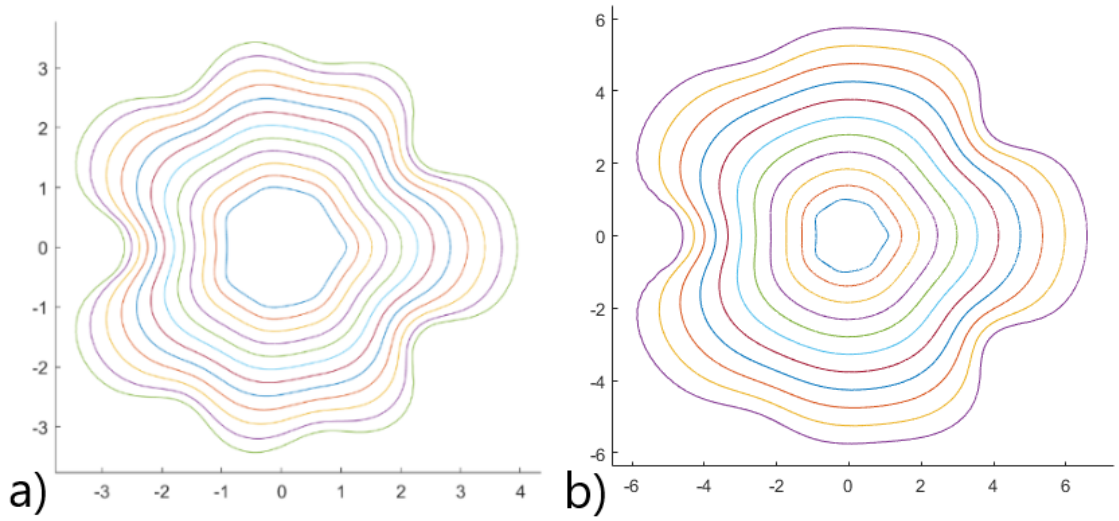

Figure 3.10: Evolution of the same initial fire line in figure 3.9 for a time dependent Pe, with $V_0 = 0$ and $N = 128$. (a) $\sigma_0 = 0.14$, $\sigma_f = 0.04$, $t_{max} = 2.5$. (b) $\sigma_0 = 0.02$, $\sigma_f = 0.033$, $t_{max} = 5.2$.

and $N = 128$, but with different choices of σ_0. The value of t_{max} in each experiment corresponds to the maximum time possible before the routine *ode15i* fails to compute any further time steps.

There is immediately a difference to the constant Pe case. Figure 3.10a has the same starting value $\sigma_0 = 0.14$ as in figure 3.9c, yet now the 7^{th} order perturbation dominates rather than the 3^{rd} order mode, with the final value of σ found as $\sigma_f = 0.04$. The fire fingers grow faster too, achieving a similar result to figure 3.9a but at a quicker time of $t = 2.5$. Any lower, initial values of σ_0 also result in the 7^{th} order perturbation dominating.

Figure 3.10b shows an example where the 5^{th} order mode dominates, where $\sigma_0 = 0.2$ and the simulation is terminated at $t_{max} = 5.2$ when $\sigma_f = 0.033$. The fact that this mode dominates over the higher $n = 7$ mode seems to contradict what is expected, though it is likely that the numerical method ended before the $n = 7$ mode could begin to grow sufficiently. Closer inspection of figure 3.10b suggests that there are perhaps seven fingers growing, not five.

3.4 Periodic infinite fire lines

Infinite fire lines are now considered. As introduced in Ch.2 and depicted in figure 3.11, these are infinitely long fire lines that are analogous to studying a sufficiently large wildfire at a local scale. It is assumed that the fire line curve $\gamma = \gamma_L$ is periodic in $2L\pi$, hence the fire line over one period $[-L\pi, L\pi]$ is considered. The dimensionless system equations (3.1.7) to (3.1.11) for radial wildfires can also be applied to periodic infinite fire lines where L is used as the characteristic length scale for non-dimensionalisation. However,

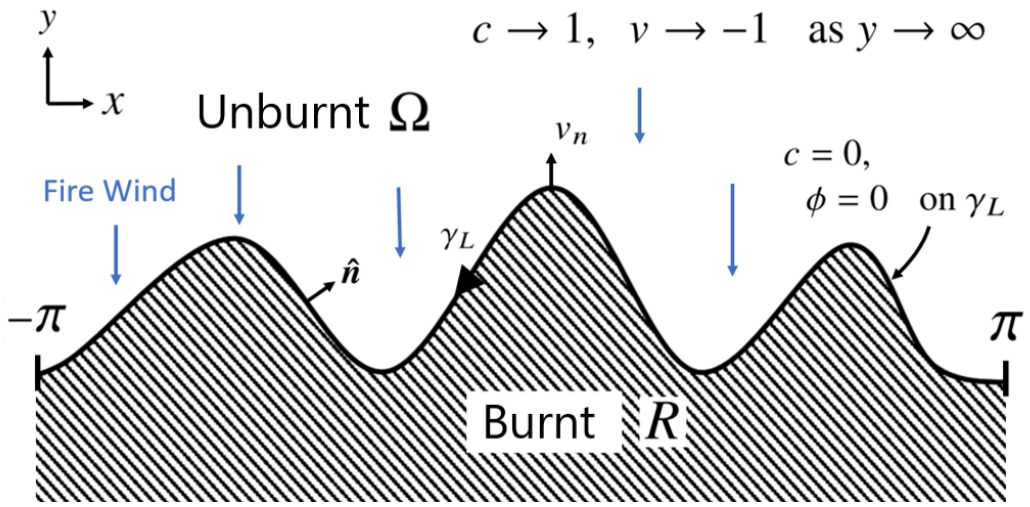

Figure 3.11: Plan view of the dimensionless wildfire problem for a periodic infinite fire line.

there are two main differences. First, on the local scale that is considered here, the Péclet number is treated as a constant $\mathrm{Pe} = \mathrm{Pe}_0$ rather than a function of time. Second, the far field condition is now a uniform flow in the negative $\hat{\boldsymbol{y}}$ direction, as the effective oxygen sink is on the line $y = A(t)$ which draws in oxygen-rich air from the unburnt region at $y \to +\infty$.

The non-dimensional system for periodic infinite fire lines is thus

$$\mathrm{Pe}\, v_n = V_0 - \bar{\epsilon}\kappa + \hat{\boldsymbol{n}} \cdot \boldsymbol{\nabla} c \quad \text{on } \gamma_L, \tag{3.4.1}$$

$$\nabla^2 \phi = 0 \quad \text{in } \Omega, \tag{3.4.2}$$

$$\mathrm{Pe}\, \boldsymbol{u}_p \cdot \boldsymbol{\nabla} c = \nabla^2 c \quad \text{in } \Omega, \tag{3.4.3}$$

$$c = 0, \quad \phi = 0 \quad \text{on } \gamma_L, \tag{3.4.4}$$

$$c \to 1, \quad v \to -1 \quad \text{as } y \to \infty. \tag{3.4.5}$$

3.4.1 Stability analysis

A stability analysis similar to that of Sect.2.3.2 is now performed. Consider first an unperturbed base state $y = A(t)$. Assuming ϕ and c are independent of x, the following solve equations (3.4.1) to (3.4.5)

$$\phi(y) = A(t) - y, \quad c(y) = 1 - e^{\mathrm{Pe}(A(t)-y)}. \tag{3.4.6}$$

Perturbations $y = y_p = A(t) + \delta_n \cos nx$ are then added, where the summation sign has been dropped and $\delta_n \ll 1, \forall n$. The mode $n = 1$ is now not a simple translation as in the radial case, hence perturbations

$n \geq 1$ are retained. The following solutions for ϕ and c are assumed

$$\phi(x,y) = A(t) - y + \beta_n e^{n(A(t)-y)} \cos nx, \quad c(x,y) = 1 - e^{\mathrm{Pe}(A(t)-y)} + \gamma_n e^{\alpha_n(A(t)-y)} \cos nx, \tag{3.4.7}$$

with constants $\beta_n, \gamma_n \ll 1$ and α_n. Substitution of equation (3.4.7) into equations (3.4.3) and (3.4.4) gives $\beta_n = \delta_n$, $\gamma_n = -\mathrm{Pe}\delta_n$ and $\alpha_n = n + \mathrm{Pe}$.

The normal velocity equation (3.1.7) can be written in terms of y_p and extracting $\mathcal{O}(\delta_n)$ terms gives the growth rate

$$g(n) = n(1 - \sigma n), \tag{3.4.8}$$

once again with no dependence on V_0 and where $\sigma = \bar{\epsilon}/\mathrm{Pe}$. Instability occurs when $n < 1/\sigma$, for $n \geq 1$. The maximum growth rate g_{max} and its corresponding mode n_{max} can also be found

$$n_{max} = \frac{1}{2\sigma}, \quad g_{max} = \frac{1}{4\sigma}. \tag{3.4.9}$$

Interestingly, this is the same value of n_{max} as for the radial case. Finally, the parameter space stability diagram for a perturbed, periodic infinite fire line is given in figure 3.12. As σ is now unchanging in time, each $(t,n)-$stability diagram is constructed for given σ values and the lines A-D correspond to upcoming numerical results.

3.4.2 Numerical results

An extension to the conformal mapping method introduced in Sect.2.4 is again used to produce numerical results. For one period of a periodic infinite fire line, the following conformal map from the interior of the unit ζ-disk to the unburnt region Ω is used

$$z = f(\zeta,t) = -i\log\zeta + ia_0(t) + i\sum_{m=1}^{\infty} a_m(t)\zeta^m. \tag{3.4.10}$$

For all results produced in this chapter, symmetry about the $y-$axis is assumed and so the unknown coefficients a_m are real. The normal velocity equation (3.4.1) is evaluated as in Sect.3.3 to give

$$\mathrm{Re}\Big[f_t\overline{\zeta f_\zeta}\Big] = \lambda|f_\zeta| - \frac{\sigma\mathrm{Re}\Big[\zeta(\zeta f_\zeta)_\zeta\overline{\zeta f_\zeta}\Big]}{|f_\zeta|^2} - 1, \tag{3.4.11}$$

where $\lambda = V_0/\mathrm{Pe}$ and $\sigma = \bar{\epsilon}/\mathrm{Pe}$ are both constants. Note that the final term on the RHS is '-1' rather than the '$a_{-1}(t)$' term seen in equation (3.3.7); this is because Pe is now not scaled in time. For all upcoming

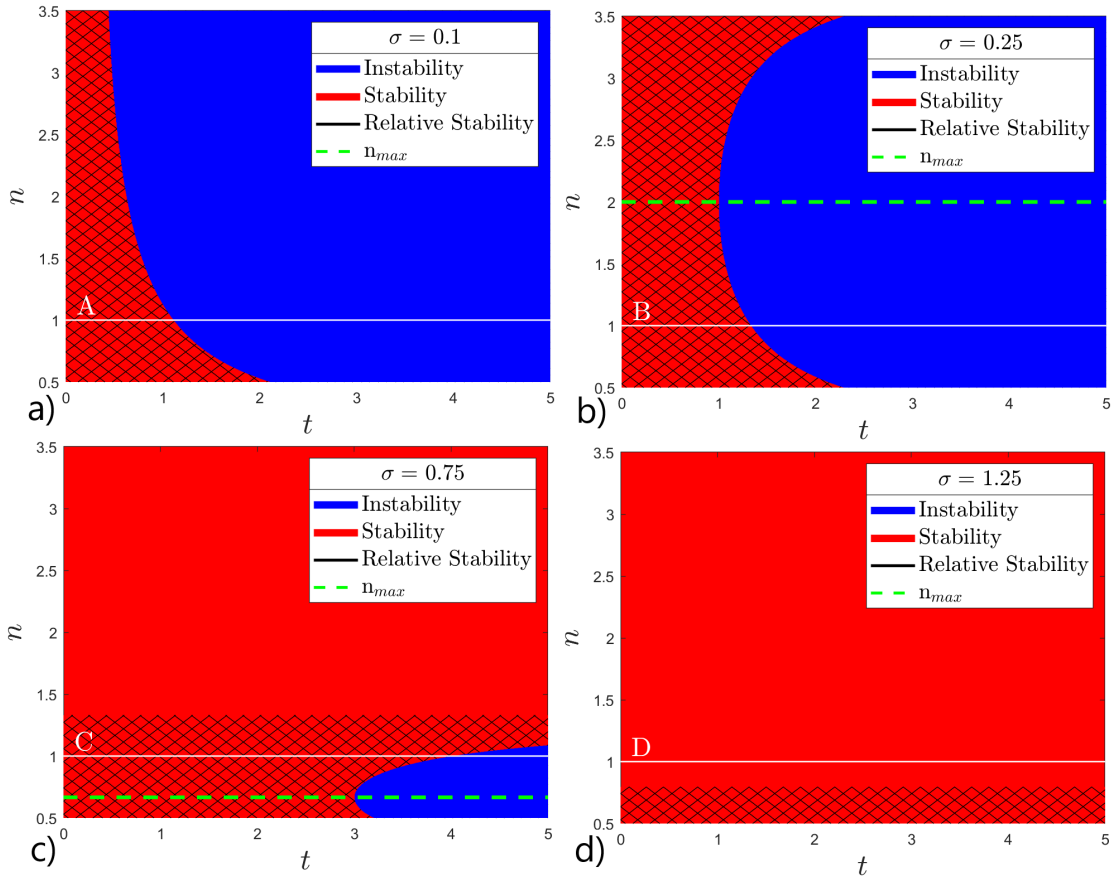

Figure 3.12: Parameter space stability diagrams for the perturbed, periodic infinite fire line. Lines A-D represent upcoming numerical results as follows: A - figure 3.13a; B - figure 3.13b, 3.14; C - figure 3.13c; D - figure 3.13d.

results, the initial fire line is a straight line segment with a simple 'bump', i.e. a perturbation of $n = 1$. Also, the axes have been inverted (y is the horizontal) to clearer show the wildfire evolution.

Figure 3.13 shows the effect of increasing the curvature by comparing the values $\bar{\epsilon} = 0.2, 0.5, 1.5$ and 2.5, with $\mathrm{Pe} = 2$, $V_0 = 1$, $N = 128$ and $t_{max} = 5$ for all plots. Similar to the radial fire line evolution seen in figures 3.13a,b, the rate of finger growth decreases as the curvature effect increases. A sufficiently large curvature effect, such as $\bar{\epsilon} = 2.5$ seen in figure 3.13d, is strong enough to stop finger growth altogether. For a small curvature effect, e.g. in figure 3.13a ($\bar{\epsilon} = 0.2$), numerical instabilities eventually appear, likely due to crowding phenomenon once more. Figures 3.13a,b,c,d correspond to the straight lines A, B, C and D on the parameter space stability diagram figure 3.12, respectively. In agreement with the parameter space diagram, the only stable solution is in figure 3.13d where $\bar{\epsilon} = 2.5$, which remains stable as Pe is constant in time.

Figure 3.14 shows the effect of increasing the basic ROS, comparing the values $V_0 = 0, 1, 5$ and 10, with

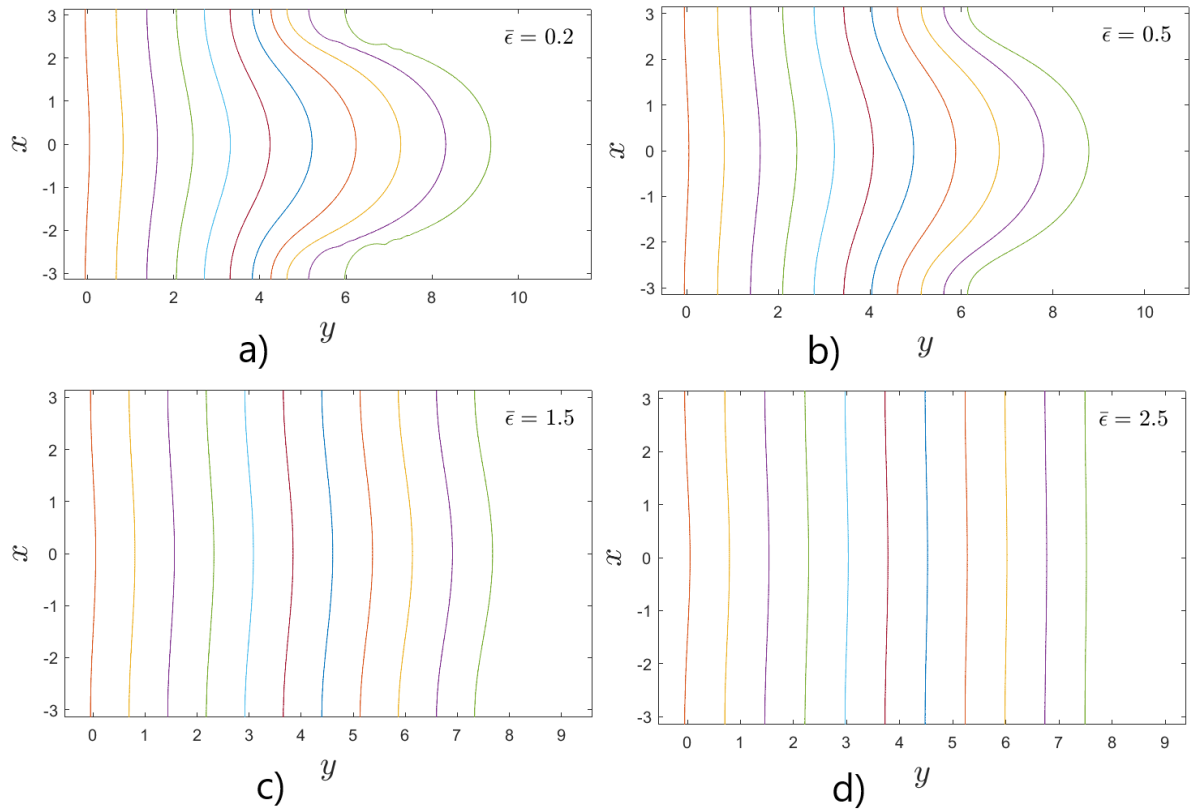

Figure 3.13: The effect of increasing $\bar{\epsilon}$: evolution of a periodic infinite fire line with $V_0 = 1$, Pe $= 2$, $N = 128$, $t_{max} = 5$ and a) $\bar{\epsilon} = 0.2$, $\sigma = 0.1$, b) $\bar{\epsilon} = 0.5$, $\sigma = 0.25$, c) $\bar{\epsilon} = 1.5$, $\sigma = 0.75$, d) $\bar{\epsilon} = 2.5$, $\sigma = 1.25$.

Pe $= 2$, $\bar{\epsilon} = 1$, $\sigma = 0.1$, $N = 128$ and $t_{max} = 5$ for all plots. All figures correspond and agree with the straight line B in the parameter diagram figure 3.12, showing that each result is unstable. Increasing V_0 causes the fire line to propagate faster (note the scale of the $y-$axis) and the finger to widen; the finger in figure 3.14d almost covers the entire period. Once more, finger widening should not be confused with finger flattening.

3.5 Discussion

In this chapter, the Markstein model of radial and infinite wildfire spread developed in Ch.2 was extended to include the dynamical effect of steady oxygen transport to the wildfire via the fire-induced pyrogenic wind. While the advection and diffusion of oxygen concentration in relation to fires has been acknowledged (Zik et al., 1998; Conti and Marconi, 2002) and the phenomenon of pyrogenic wind is well known (Smith et al., 1975; Beer, 1991; Hilton et al., 2018), the explicit inclusion of the oxygen term in the normal velocity equation of the fire line is new. Mathematically, the model combines aspects of curve-shortening flow (Dallaston and McCue, 2016), fingering in a Hele-Shaw cell in the absence of surface tension (Howison, 1986) and two-dimensional melting/freezing free boundary problems featuring the advection-diffusion

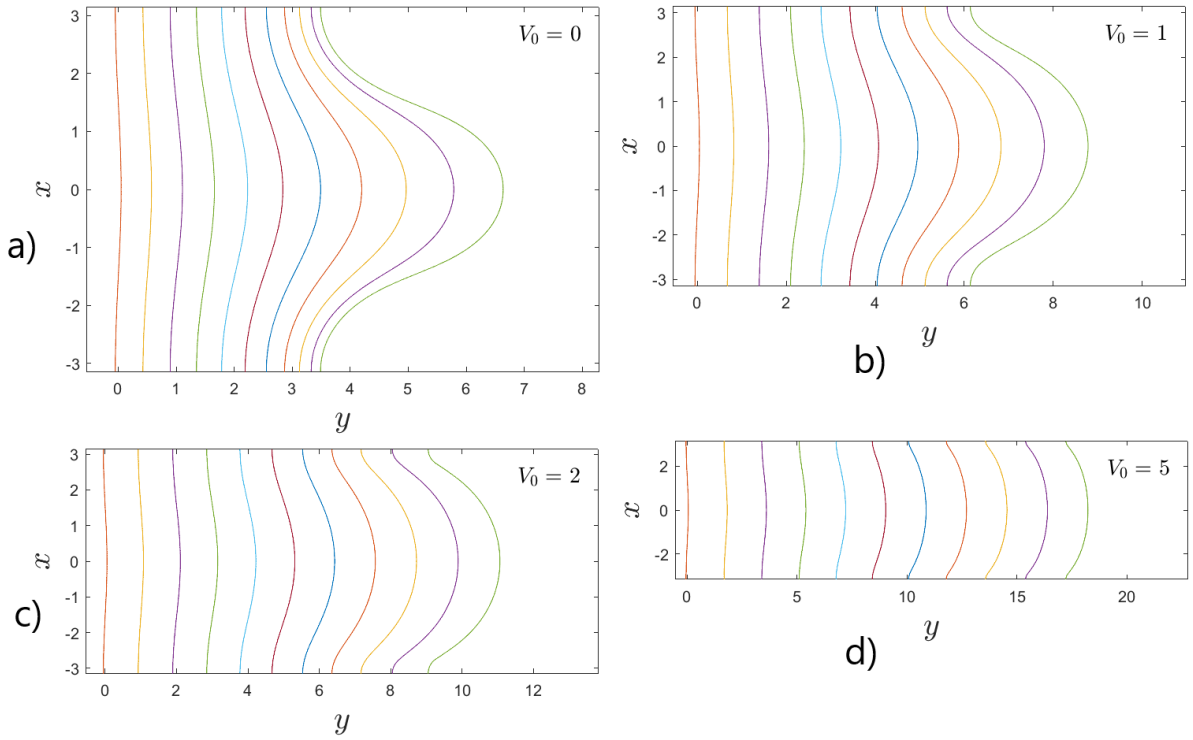

Figure 3.14: The effect of increasing V_0: evolution of a periodic infinite fire line with $\bar{\epsilon} = 0.5$, Pe $= 2$, $\sigma = 0.25$, $N = 128$, $t_{max} = 5$ and a) $V_0 = 0$, b) $V_0 = 1$, c) $V_0 = 2$, d) $V_0 = 5$.

equation (3.1.9) e.g. Cummings et al. (1999); Rycroft and Bazant (2016); Ladd et al. (2020).

The motivation for including such an oxygen term was that it could provide a mechanism for the observed phenomenon of fire finger formation (Clark et al., 1996b; Dold et al., 2005; Quaife and Speer, 2021). Performing a linear stability analysis, it was found that such fingering instabilities were possible for certain values of σ - the ratio between curvature $\bar{\epsilon}$ (stabilising) and oxygen Pe (destabilising) effects. Numerical results obtained via a conformal mapping based method demonstrated both stable and unstable fire line growth. A third type of behaviour was also found: 'dormant fire' behaviour, where fire finger growth would change from stable to unstable over time. This was a consequence of the Péclet number increasing in time as the radial wildfire, and hence the strength of the fire plume, grew. In cases where multiple modes of perturbation were excited, the mode with the highest growth rate would eventually dominate. Geometrically identical fire lines would consequently evolve into different fire finger patterns, depending on the initial value of σ.

While the wildfire model in this chapter captures more physical features of wildfire spread than the Markstein model of Ch.2, there are still numerous extensions to consider. One key addition is to include the direct effects of ambient and pyrogenic winds - this is introduced in Ch.6 and extended to the problem of multiple wildfires spreading in Ch.7. As noted in Ch.3.1, a mechanism to enforce the entropy condition

- the condition that the fire line does not intersect previous iterations of itself - must necessarily be included into the model. The effect of terrain, heterogeneous fuelbed distributions and firebreaks also significantly affect wildfire spread; the latter of these is explored in Ch.7 with some discussion of the former two extensions also. Further, only 'Laurent shapes' have been considered up to this point in the thesis whereas the nonlinear evolution of any arbitrary fire line shape, often in the form of a 'non-Laurent shape', is desired. This extension is detailed in Ch.5: the fire line is approximated as a many sided polygon and its initial conformal map found numerically for use in the general conformal map equation (2.4.8) introduced in Ch.2.

A final discussion on whether oxygen transport constitutes as a viable mechanism for fire fingering in real world wildfires is here made. On the one hand, fingering instabilities were indeed found using the model of this chapter. Consider the associated dimensions: using a representative value of $L \approx 20\text{m}$ for the initial wildfire radius and $U = 0.025\text{ms}^{-1}$ for the fire wind speed gives an estimate for the initial strength of the fire plume as $Q = 2\pi \times 0.5\text{m}^2\text{s}^{-1}$. These values are consistent with large-scale experimental grass fires reported in Hilton et al. (2018). Bebieva et al. (2020) estimate that, within 1 m of ground level, the horizontal diffusivity D in fire conditions is $\mathcal{O}(1)$ m^2s^{-1}, although the actual value will depend on vegetation type among other factors. Hence the initial Péclet number is $\text{Pe}_0 = Q/2\pi D \approx 0.5$. The value of $\bar{\epsilon}$ is more difficult to estimate. In the combustion wind-tunnel experiments discussed by Hilton et al. (2016) (see e.g. their figure 6), fires typically have a length scale of 0.5m, and they found by comparison with their numerical experiments (which included curvature) that, dimensionally, the curvature term's contribution to the normal velocity is $\approx 2\times10^{-4}$ ms^{-1}. In the same experiments, a typical fire line velocity in the absence of wind was 3×10^{-3} ms^{-1} and so $\bar{\epsilon} \approx 0.1$. Thus choosing this value as being representative of larger scale fire, it follows that $\sigma_0 = \bar{\epsilon}/\text{Pe}_0 \approx 0.2$. With caveats about applying these estimates to larger scale fires and questions about how different fuel-types and vegetation affect wildfires, the estimate for σ_0 suggests that fingering owing to the oxygen effect is a possibility in real world wildfires.

On the other hand, many important factors affecting wildfire spread and thus oxygen transport have been neglected in this chapter. For example, additional oxygen is also transported to the fire line by the ambient wind. Interestingly, Beer (1991) argues that the presence of an ambient wind seeks to reduce the pyrogenic wind generated by the fire plume over the burnt region, in turn reducing the instability mechanism of enhanced oxygen to the fire line. Depending on their direction, ambient winds may also transport oxygen from the burnt region to the fire line. This provides a stabilising effect since now the finger tips receive comparatively less oxygen than the valleys between fingers. Fire fingers are only occasionally observed in real world wildfires, despite the prediction here that all radial wildfires must eventually become unstable

as Pe increases with fire size. In reality, it seems likely that the strength of the pyrogenic wind cannot grow indefinitely and that there is a bound on Pe, meaning a wildfire may remain stable. Moreover, inclusion of additional factors affecting wildfire spread - such as ambient winds, topography, natural and artificial fire breaks, fuel type and fire spotting - may inhibit or mask finger formation by oxygen.

Chapter 4

Penguin huddling

Before the wildfire model of Ch.3 is extended to include explicit wind effects, the methods and techniques developed are applied to a rather different (but mathematically speaking very similar) scenario.

Antarctic penguins experience some of the most extreme weather conditions on Earth, enduring winds over 30ms^{-1} and temperatures below $-40°\text{C}$ (McCafferty et al., 2013; Gerum et al., 2013; Williams et al., 2015). The emperor penguin has no fixed nest, allowing colonies consisting of thousands of the birds to huddle together for warmth in such severe blizzards. Furthermore, it is seen that the penguins are consistently moving around and reorganising themselves within the huddle, where Le Maho (1977) observes that "birds that at first are in the center of the huddle become members of the rear flank [the side most exposed to the wind] and move, in their turn, up the sideline". This process benefits all members of the huddle and allows the heat to be equally shared: those at the edge do not remain cold and those at the centre do not overheat. Moreover, this movement causes the entire huddle to propagate over time.

In this chapter, a two-dimensional continuum model is developed to solve for the evolution of the huddle boundary - the Jordan curve surrounding the penguins. Furthermore, the steady advection and diffusion of temperature by a potential wind flow is considered in the penguin problem, analogous to the transport of oxygen in the wildfire problem. Conformal mapping techniques are again used in the numerical method, however the interior of the penguin huddle is also described in this problem which necessitates the use of another numerical method involving a variant of the AAA-LS algorithm. This algorithm is only briefly introduced in this chapter, but is used to a greater degree later in this thesis, see Ch.7,8 and 9. Note that the work completed in this chapter was published in Harris and McDonald (2023).

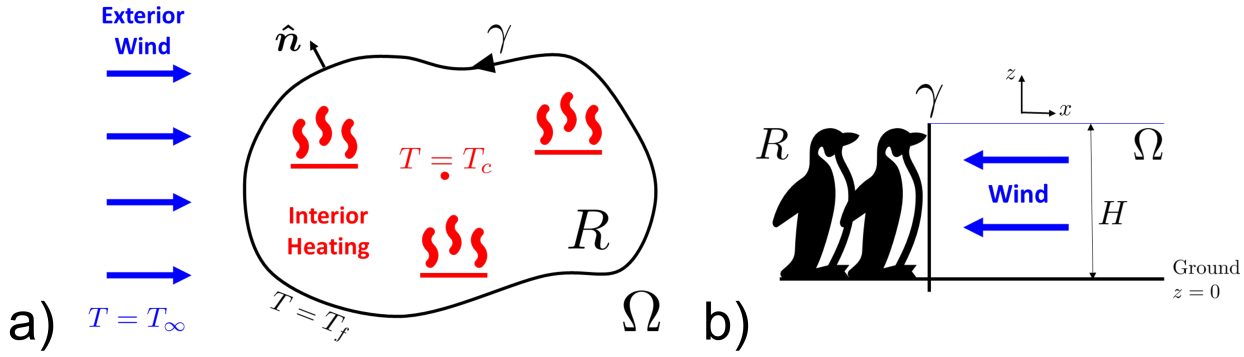

Figure 4.1: Schematic diagram of the full penguin problem showing the interior region R and exterior region Ω. a) Plan view where T_c denotes the maximum temperature T inside the huddle, b) side view.

4.1 Continuum model setup

Consider a huddle of penguins with horizontal length scale L where the penguins are assumed homogeneous in size and shape. The huddle is considered as a continuum with penguins packed as tightly as possible while still allowing for huddle reorganisation (Zitterbart et al., 2011), hence uniform spacing between each penguin can be assumed constant across the entire huddle and for all time. Emperor penguins have a typical height of $H = 1$m (Le Maho, 1977) and their tight packing means that background winds are diverted around the huddle, allowing the dynamics to be considered as two-dimensional, see figure 4.1. The boundary of the penguin huddle $\gamma(t)$ is defined as the two-dimensional, non-overlapping curve enclosing the huddle; the finite, simply connected interior of the curve occupied by the huddling penguins is labelled R and the penguin-free exterior as Ω. The boundary curve γ is orientated anti-clockwise such that the unit normal vector $\hat{\boldsymbol{n}}$ points from the interior to the exterior.

The huddle R is buffeted by a unidirectional and constant strength wind of magnitude U which, without loss of generality, flows in the positive $\hat{\boldsymbol{x}}$ direction. The wind is the irrotational flow of air, which is considered to be an inviscid and incompressible fluid which flows sufficiently rapidly compared to the evolution of the penguin huddle as a whole, so that the transport of temperature can be treated as steady (Waters et al., 2012). In reality, viscous effects taking the form of thin boundary layers around the exterior of the penguin huddle are present. In this chapter, these are ignored in order to facilitate the accurate computation of the exterior potential flow using conformal mapping based methods. Denote the temperature far from the huddle as T_∞, the temperature on the huddle boundary as T_f and the maximum temperature in the huddle interior as T_c - this maximum temperature can reach as high as 37.5°C (Gilbert et al., 2006).

The equations governing the wind and exterior temperature transport are, respectively, the Laplace

equation and the steady advection-diffusion equation

$$\nabla^2\phi = 0 \quad \text{in } \Omega, \tag{4.1.1}$$

$$\boldsymbol{u}\cdot\boldsymbol{\nabla}T_\Omega = D_\Omega\nabla^2 T_\Omega \quad \text{in } \Omega, \tag{4.1.2}$$

where ϕ is the wind velocity potential, $\boldsymbol{u} = \boldsymbol{\nabla}\phi$ is the wind velocity, T_Ω is the temperature in Ω and D_Ω is the diffusivity of temperature in air. These are the same dimensional exterior governing equations (equations (3.1.2) and (3.1.3)) as used in the wildfire problem, except with exterior temperature T_Ω as the transported quantity rather than oxygen c. The associated boundary and far field conditions are

$$T_\Omega = T_f, \;\; \frac{\partial\phi}{\partial n} = 0 \quad \text{on } \gamma, \tag{4.1.3}$$

$$T_\Omega \to T_\infty, \;\; \phi \to Ux \quad \text{as } r \to \infty. \tag{4.1.4}$$

Now, consider the interior R of the huddle where there is no wind flow. Owing to their ability to self-generate heat which subsequently diffuses within the huddle as the penguins reorganise themselves, the birds nearer the huddle centre are warmer than those at the boundary (Le Maho, 1977; Zitterbart et al., 2011), i.e. $T_c > T_f$. This source of heat provides a further contribution to the heat flux at the boundary γ. Consistent with the continuum assumption, it is assumed that heat is generated uniformly across the huddle. Furthermore, as in the exterior, it is assumed the interior heat diffuses quickly compared to the evolution of the boundary. Thus the temperature distribution in R is modelled by the steady heat equation

$$\nabla^2 T_R = -\frac{Q}{D_R} \quad \text{in } R, \tag{4.1.5}$$

where D_R is the diffusivity of the interior temperature T_R through the penguin huddle and Q is the (constant) source term representing the self-generation of heat by the penguins.

In order to obtain parameter estimates for the interior problem, it is helpful to first consider a circular penguin huddle of radius L, noting that $T_R(0) = T_c$. The Poisson equation (4.1.5) can be solved exactly, giving

$$T_R = T(r) = T_c - \frac{Q}{4D_R}r^2, \quad \text{where } \frac{Q}{D_R} = \frac{4(T_c - T_f)}{L^2}. \tag{4.1.6}$$

The quantity Q/D_R is used in Sect.4.1.1 to non-dimensionalise the problem for cases when the region R is non-circular.

Finally, a condition on $\gamma(t)$ is sought by specifying its outward normal velocity v_n. Following Waters et al.

(2012), the idea that the boundary evolves owing to the heat loss of penguins on the boundary is used. Consequently, the problem has some similarity to the two-phase Stefan problem (Goldstein and Reid, 1978; Cummings et al., 1999; Rycroft and Bazant, 2016; Gupta, 2017) with the boundary temperature gradient driving its evolution, yet, unlike such problems, no phase change occurs. Waters et al. (2012) move individual boundary penguins according to their heat loss to the exterior, whereas here both exterior and interior heat fluxes are considered. First, the heat loss to the exterior wind is the flux $\kappa_\Omega \hat{\boldsymbol{n}} \cdot \boldsymbol{\nabla} T_\Omega$ evaluated on $\gamma(t)$, where κ_Ω is the thermal conductivity of air. Second, the heat gain due to the warm huddle interior is $-\kappa_R \hat{\boldsymbol{n}} \cdot \boldsymbol{\nabla} T_R$ evaluated on $\gamma(t)$, where κ_R is the thermal conductivity of huddling penguins. Equating the normal velocity with the net heat flux gives

$$A v_n = \kappa_\Omega \hat{\boldsymbol{n}} \cdot \boldsymbol{\nabla} T_\Omega - \kappa_R \hat{\boldsymbol{n}} \cdot \boldsymbol{\nabla} T_R, \quad \text{on} \quad \gamma(t), \tag{4.1.7}$$

where the constant term A is chosen to ensure a match in dimensions between both sides of equation (4.1.7), with the particular choice of A affecting the timescale for the boundary evolution. For convenience in the non-dimensionalisation process upcoming in Sect.4.1.1, let $A = \lambda \rho_\Omega c_\Omega (T_f - T_\infty)$, where ρ_Ω and c_Ω are the density and specific heat capacity of the air, respectively, and λ is a non-dimensional constant to be chosen later.

The right hand side of equation (4.1.7) is the jump in heat flux at the boundary. This observation reinforces the analogy with the Stefan problem where typically the normal velocity of the boundary depends on the jump in the heat flux (Gupta, 2017). For example, analogous boundary conditions arise in other natural free boundary problems, including the dissolution of finite objects, where only the gradient of the agent undergoing advection and diffusion exterior to the object is important (Rycroft and Bazant, 2016; Ladd et al., 2020), or in porous media flow about freeze pipes, in which the temperature gradient in both the exterior fluid and interior ice regions are significant (Goldstein and Reid, 1978). However it is emphasised that equation (4.1.7) is here purely a modelling assumption.

Rewriting equation (4.1.7) gives the following condition on γ

$$\lambda \rho_\Omega c_\Omega (T_f - T_\infty) \hat{\boldsymbol{n}} \cdot \frac{\partial \boldsymbol{x}}{\partial t} = \kappa_\Omega \hat{\boldsymbol{n}} \cdot \boldsymbol{\nabla} T_\Omega - \kappa_R \hat{\boldsymbol{n}} \cdot \boldsymbol{\nabla} T_R + \overline{C}(t). \tag{4.1.8}$$

The additional term $\overline{C}$(t) in equation (4.1.8) is needed to enforce conservation of penguins, or, equivalently, area conservation (Waters et al., 2012), namely that

$$\int_\gamma \hat{\boldsymbol{n}} \cdot \frac{\partial \boldsymbol{x}}{\partial t} \mathrm{d}s = \int_\gamma v_n \mathrm{d}s = 0. \tag{4.1.9}$$

4.1.1 Non-dimensionalisation and parameter values

In order to identify the parameters of the problem, equations (4.1.1) to (4.1.5) and equation (4.1.8) are non-dimensionalised, with non-dimensional quantities temporarily labelled as starred variables. Let L characterise the length scale of region R i.e. $\boldsymbol{x} = L\boldsymbol{x}^*$, and use the far field wind magnitude U as the characteristic velocity scale, $\boldsymbol{u} = U\boldsymbol{u}^*$. The following scalings are also used

$$\boldsymbol{\nabla} = \frac{1}{L}\boldsymbol{\nabla}^*, \quad T^* = \frac{T - T_\infty}{T_f - T_\infty}, \quad t = \frac{1}{\tau}t^*, \quad \tau = \frac{U}{L}. \tag{4.1.10}$$

Using equation (4.1.6), the non-dimensional form of the Poisson equation (4.1.5) can be written (now dropping the stars) as

$$\nabla^2 T_R = -\alpha, \qquad \alpha = \frac{4(T_c - T_f)}{T_f - T_\infty}. \tag{4.1.11}$$

The normal velocity equation (4.1.8) becomes

$$\lambda \mathrm{Pe}\ \hat{\boldsymbol{n}} \cdot \frac{\partial \boldsymbol{x}}{\partial t} = \hat{\boldsymbol{n}} \cdot \boldsymbol{\nabla} T_\Omega - \beta \hat{\boldsymbol{n}} \cdot \boldsymbol{\nabla} T_R + C(t), \tag{4.1.12}$$

where $\mathrm{Pe} = UL/D_\Omega$ is the Péclet number, with $D_\Omega = \kappa_\Omega/\rho_\Omega c_\Omega$ the thermal diffusivity of air, $\beta = \kappa_R/\kappa_\Omega$ is the ratio of thermal conductivities and $C(t)$ is the dimensionless area conserving term, an explicit expression for which can be found by substituting equation (4.1.12) into equation (4.1.9) (see equation (4.1.13g) below). Note that the appearance of Pe on the left hand side of equation (4.1.12) affects the time scaling reported in the results. The real world dimensional time scale 't_r' is therefore $t_r = \lambda \mathrm{Pe}\ (L/U)t^*$. In what follows, the choice $\lambda = 1$ is made and justified *a posteriori* by comparing the time for the huddle to evolve with observations - see Sect.4.4.

There are three parameters: Pe, β and α. Following the justification in Waters et al. (2012), the wind around the penguin huddle is likely turbulent and hence the Péclet number can be approximated by a turbulent Reynolds number, which is $\mathcal{O}(100)$ for Antarctic winds at this scale. Consistent with Waters et al. (2012), this chapter considers Péclet values between 1 and 100. The values of the remaining two parameters, α and β, are estimated as follows. The air temperature far upstream is taken to be $T_\infty = -40°\mathrm{C}$ (McCafferty et al., 2013; Williams et al., 2015) while ambient temperatures in the huddle are above freezing (Zitterbart et al., 2011). It seems reasonable then to let $T_f = 0°\mathrm{C}$. The centre of a huddle can exceed 20°C, with a maximum temperature of 37.5°C having been recorded (Gilbert et al., 2006). Using, therefore, $T_c = 30°\mathrm{C}$ gives $\alpha = 3$.

From table C.5 of Basu (2018), the thermal conductivity of air at $-40°\mathrm{C}$ is approximately $\kappa_\Omega \approx 0.022$,

units $Wm^{-1}K^{-1}$. The thermal conductance of penguins is $1.3Wm^{-2}K^{-1}$ from Le Maho (1977), however this is not the same as the thermal conductivity - it has different units for example. To find the thermal conductivity, the conductance must be multiplied by the thickness of the penguin insulation layer which is $d = 0.024m$ (Dawson et al., 1999). Therefore, $\kappa_R = 0.0312Wm^{-1}K^{-1}$ and so $\beta = 1.4182 \approx 1.5 = \mathcal{O}(1)$. This estimate for β depends on the wind flow being either laminar or turbulent, with β decreasing as the flow becomes more turbulent and the effective thermal conductivity of air increases (Kittel et al., 1996). In this chapter, a range of β values between $\beta = 0$ and $\beta = 1.5$ are considered with $\beta = 0.14 \approx 0.1 = \mathcal{O}(10^{-1})$ taken to be a representative value.

To summarise, the full dimensionless system for the penguin problem is

$$\text{Pe } v_n = \hat{\boldsymbol{n}} \cdot \boldsymbol{\nabla} T_\Omega - \beta \hat{\boldsymbol{n}} \cdot \boldsymbol{\nabla} T_R + C(t), \quad \text{on } \gamma, \tag{4.1.13a}$$

$$\nabla^2 \phi = 0 \quad \text{in } \Omega, \tag{4.1.13b}$$

$$\text{Pe } \boldsymbol{u} \cdot \boldsymbol{\nabla} T_\Omega = \nabla^2 T_\Omega \quad \text{in } \Omega, \tag{4.1.13c}$$

$$\nabla^2 T_R = -\alpha \quad \text{in } R, \tag{4.1.13d}$$

$$T_\Omega = T_R = 1, \ \ \frac{\partial \phi}{\partial n} = 0 \quad \text{on } \gamma, \tag{4.1.13e}$$

$$T_\Omega \to 0, \ \ \phi \to x \quad \text{as } r \to \infty, \tag{4.1.13f}$$

$$C(t) = \frac{-\int_\gamma (\hat{\boldsymbol{n}} \cdot \boldsymbol{\nabla} T_\Omega - \beta \hat{\boldsymbol{n}} \cdot \boldsymbol{\nabla} T_R) \mathrm{d}s}{\int_\gamma \mathrm{d}s}. \tag{4.1.13g}$$

The task is to solve equations (4.1.13a) to (4.1.13g) and, in particular, find the evolution of the huddle boundary $\gamma(t)$ for some given initial huddle shape $\gamma(0)$. This is done in Sect.4.3 with the following choices: $\text{Pe} \in [1, 100]$, $\beta \in [0, 1.5]$ and $\alpha = 3$.

4.2 Numerical method

As in Ch.2 and Ch.3, the conformal invariance of equations (4.1.13b) and (4.1.13c) is exploited and a conformal mapping method used to numerically compute the evolution of the penguin huddle. Following the work of e.g. Goldstein and Reid (1978); Ladd et al. (2020), the free boundary problem (equations (4.1.13a) to (4.1.13g)) is reduced to a single PG type equation (Bazant and Crowdy, 2005) in terms of a conformal map $z = f(\zeta, t)$ from the exterior of the unit disk in the canonical $\zeta-$plane to the exterior region Ω in the physical $z-$plane (Choi et al., 2005; Waters et al., 2012). While the wildfire problem only involved the exterior region Ω, the interior region R is now also considered in the penguin problem. The interior of the unit $\zeta-$disk is not correspondingly transformed to R using the conformal map $f(\zeta, t)$, thus a different

numerical method is instead used in calculating the interior temperature T_R.

First, note the following which hold on the unit disk $r = |\zeta| = 1$ (Dallaston and McCue, 2013; Ladd et al., 2020)

$$v_n = \frac{\mathrm{Re}\Big[f_t\zeta\overline{f_\zeta}\Big]}{|f_\zeta|}, \quad \hat{\boldsymbol{n}}\cdot\boldsymbol{\nabla}T_\Omega = \mathrm{Re}[n\overline{\nabla}T_\Omega] = \frac{1}{|f_\zeta|}\frac{\partial T_\Omega}{\partial r} = \frac{\sigma(\theta)}{|f_\zeta|}, \tag{4.2.1}$$

where $\overline{\nabla} = \partial_x - i\partial_y$, $\zeta = e^{i\theta}$, $f_\zeta = \partial f/\partial\zeta$ and $n = n_x + in_y = \zeta f_\zeta/|f_\zeta|$ is the complex representation of the normal vector in the $z-$plane as in Ch.3. The function $\sigma(\theta)$ is found by solving the following integral equation (Goldstein and Reid, 1978; Choi et al., 2005; Ladd et al., 2020)

$$\pi = \int_0^\pi K\big[\mathrm{Pe}(\cos\theta - \cos\theta')\big]\sigma(\theta')\mathrm{d}\theta', \tag{4.2.2}$$

where $K(x) = e^x K_0(|x|)$ and K_0 is the modified Bessel function. The function σ is the heat flux (due to the exterior effect alone) around the unit $\zeta-$disk (Ladd et al., 2020). A numerical solution to equation (4.2.2) can be found at M equally spaced points on the upper half of the unit disk $\theta \in (0, \pi)$, see appendix A of Ladd et al. (2020). To evaluate σ on the remainder of the disk, note that $\sigma(\theta^*) = \sigma(\pi + \theta^*)$, where $0 \leq \theta^* < \pi$, and $\sigma(\theta) \to 1/\pi$ as $\theta \to 0$ (Choi et al., 2005; Ladd et al., 2020).

Second, consider the contribution from the interior $\hat{\boldsymbol{n}}\cdot\boldsymbol{\nabla}T_R$. This is found by direct computation in the $z-$plane. To begin, introduce the function $u = T_R + \alpha r^2/4$; from equations (4.1.13d) and (4.1.13e), u satisfies

$$\nabla^2 u = 0 \quad \text{in } R, \tag{4.2.3}$$

$$u = 1 + \frac{\alpha r^2}{4} \quad \text{on } \gamma. \tag{4.2.4}$$

This is a Laplace problem in the interior of a smooth, simply connected domain with Dirichlet boundary condition $u = h(z)$ on γ. Efficient methods developed by Trefethen and colleagues are here used to solve the Laplace problem directly (Gopal and Trefethen, 2019c; Trefethen, 2020; Costa and Trefethen, 2023). These are based on a rational approximation of u in the complex $z-$plane: there exists an analytic function $F(z)$ such that $u = \mathrm{Re}[F(z)]$ which can be approximated by the series solution

$$F(z) = A_0 + \sum_{k=1}^{N_1} A_k(z - c_0)^k + \sum_{k=1}^{N_2}\frac{B_k}{z - p_k}, \tag{4.2.5}$$

where A_0, A_k and B_k are constants, N_1 is the power series truncation, c_0 is a point in the interior R (in this chapter, the conformal centre of the polygon is used (Ladd et al., 2020)) and p_k are some N_2 poles in

the exterior Ω. The first sum is known as the 'Runge' (or smooth) part and the second as the 'Newman' (or singular) part (Gopal and Trefethen, 2019c; Costa, 2020).

Suitable poles p_k are found by the AAA algorithm (Nakatsukasa et al., 2018; Costa, 2020) and the unknown coefficients A_0, A_k and B_k by a standard LS fitting method (Trefethen, 2018; Baddoo, 2020; Brubeck et al., 2021): combining these into a AAA-LS method (Costa and Trefethen, 2023) can thus find $F(z)$ numerically. While it is only lightly introduced in this chapter, the AAA-LS method is used and significantly developed in later chapters of this thesis: see Ch.7 and Ch.8 for more details. From Trefethen (2018), it then follows that

$$\nabla u = \nabla \mathrm{Re}[F(z)] = \overline{F'(z)}, \tag{4.2.6}$$

where the primed notation indicates differentiation, in this case with respect to z. Therefore,

$$\overline{\nabla} T_R = \overline{\nabla}[u - \alpha r^2/4] = F'(z) - \frac{\alpha}{2}\overline{z}, \tag{4.2.7}$$

recalling that $\overline{\nabla} = 2\partial_z$ and $r^2 = z\overline{z}$. This gives

$$\hat{\boldsymbol{n}} \cdot \boldsymbol{\nabla} T_R = \mathrm{Re}[n\overline{\nabla} T_R] = \frac{1}{|f_\zeta|}\mathrm{Re}[\zeta f_\zeta (F'(z) - \alpha\overline{z}/2)] \equiv \frac{\omega(\theta)}{|f_\zeta|}, \tag{4.2.8}$$

where the boundary points z in equation (4.2.8) are considered in the $\zeta-$plane so that the right hand side of equation (4.2.8) is purely a function of θ. Drawing an analogue with σ, the function $-\beta\omega$ is the heat flux around the unit $\zeta-$disk due to the interior effect alone.

Third, equation (4.1.13g) for the area conserving term $C(t)$ can be transformed to the $\zeta-$plane, noting that $\mathrm{d}s = |f_\zeta|\mathrm{d}\theta$. Substituting the relevant expressions from equations (4.2.1) and (4.2.8) into equation (4.1.13g) gives

$$C(t) = \frac{-\int_{-\pi}^{\pi} \big(\sigma - \beta\omega\big)\mathrm{d}\theta}{\int_{-\pi}^{\pi} |f_\zeta| \mathrm{d}\theta}. \tag{4.2.9}$$

Therefore, using equations (4.2.1), (4.2.8) and (4.2.9), the PG form of equation (4.1.13a) is

$$\mathrm{Pe}\ \mathrm{Re}[f_t\overline{\zeta f_\zeta}] = \sigma(\theta) - \beta\omega(\theta) + C(t)|f_\zeta|, \tag{4.2.10}$$

where $\sigma(\theta)$ satisfies equation (4.2.2) and $\omega(\theta) = \mathrm{Re}[\zeta f_\zeta(F'(z) - \alpha\overline{z}/2)]$, with $F(z)$ given by equation (4.2.5). Note that $\sigma(\theta) - \beta\omega(\theta)$ is the total heat flux across the unit $\zeta-$disk $|\zeta| = 1$; recall that the heat flux across the huddle boundary γ is $\hat{\boldsymbol{n}} \cdot \boldsymbol{\nabla} T_\Omega - \beta \hat{\boldsymbol{n}} \cdot \boldsymbol{\nabla} T_R$.

It remains to find the conformal map $z = f(\zeta, t)$. As in Ch.3, Laurent shapes are exclusively considered

in this chapter and thus the conformal map can be written as the Laurent series

$$z = f(\zeta, t) = a_{-1}(t)\zeta + \sum_{k=0}^{\infty} c_k(t)\zeta^{-k}, \tag{4.2.11}$$

where $a_{-1}(t)$ is a real function in time (the conformal radius of the penguin huddle at time t) and $c_k(t) = a_k(t) + ib_k(t)$ are complex functions in time. Unlike Ch.3, no lines of symmetry are assumed for the huddle boundary and so the coefficients c_k are complex. This allows non-symmetric initial huddle shapes to be considered. The coefficient c_0 is the conformal centre of the penguin huddle (Ladd et al., 2020), the same c_0 as used in constructing the power series solution equation (4.2.5) for the Poisson problem in R. The Laurent series equation (4.2.11) is once again truncated at N terms, now giving $n = 2(N+1)+1 = 2N+3$ unknown real functions in time: $a_{-1}(t)$, $a_k(t), b_k(t)$, $k = 0, 1, \cdots, N$. Likewise, n equally spaced points around the unit $\zeta-$disk are chosen; the first point is at $\theta = 0$, the next $N+1$ points are in the interval $\theta \in (0, \pi)$ and the final $N+1$ points in $\theta \in (\pi, 2\pi)$. Hence the choice $M = N+1$ in $(0, \pi)$ is made when numerically solving the integral equation (4.2.2) for $\sigma(\theta)$. The PG equation (4.2.10) becomes a system of n coupled ODEs determining the time evolution of the n Laurent coefficients; these are solved using the MATLAB routine *ode15i*.

4.3 Results

In the results presented here, the evolution of the huddle boundary is plotted at equal time intervals in the range $[0, t_{max}]$, where t_{max} is the maximum time. The series truncation $N = 128$ is chosen, leading to a system of $n = 259$ ODEs to be solved. The initial starting shape of the penguin huddle is taken to be either a circle, a slanted ellipse, a triangle, an irregular pentagon or an hourglass. The initial Laurent coefficients $a_{-1}(0)$, $c_k(0)$ for the conformal map equation (4.2.11) of these shapes are taken from Rycroft and Bazant (2016) (see their figures 2a, 2b, 2d, 5a and 7a, respectively) and scaled such that each shape encloses the same area[1]. Area conservation of the huddle was monitored during each numerical experiment and found to hold with a relative error of $\mathcal{O}(10^{-5})$. As a test, experiments were run which neglected the interior (i.e. $\beta = 0$) and the area conserving ($C(t)$) terms; the geometry of the obtained solutions matched quantitatively with results in Ladd et al. (2020) who considered an analogous problem in this class.

First, consider the 'exterior only' penguin problem when $\beta = 0$. This is a continuum analog of the discrete model developed in Waters et al. (2012), where the penguin huddle evolves in response to the

[1]This scaling can be found analytically using the complex form of Green's theorem (McDonald and Mineev-Weinstein, 2014) to find the exact area from the conformal map $z = f(\zeta, 0)$.

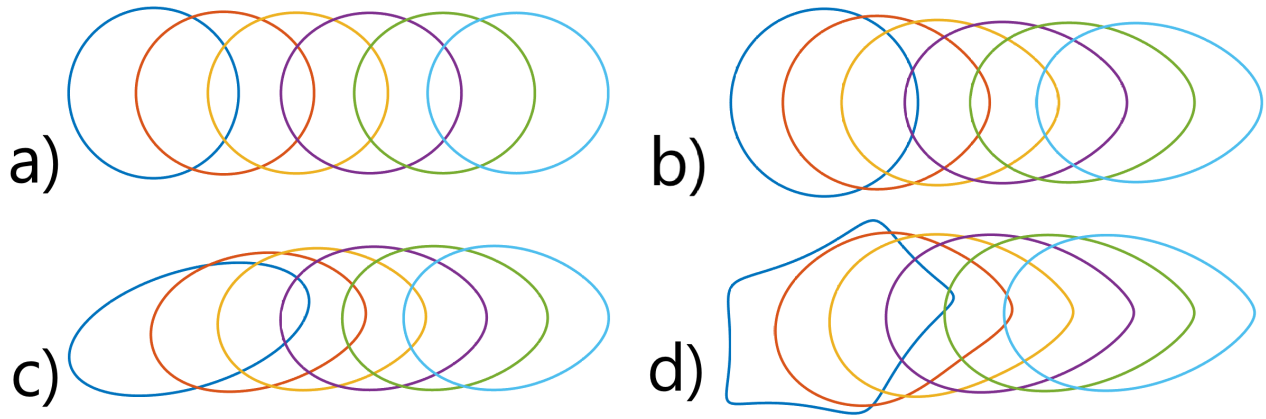

Figure 4.2: Exterior only ($\beta = 0$) penguin problem. Shapes are plotted at equal time intervals up to a maximum time t_{max}. The x and y axes (not shown) are scaled at a 1-to-1 aspect ratio. Each description refers to the initial penguin huddle shape, the Péclet number and the value of t_{max}: a) circle with Pe = 1, $t_{max} = 10$, b) circle with Pe = 10, $t_{max} = 20$, c) slanted ellipse with Pe = 10, $t_{max} = 20$, d) irregular pentagon with Pe = 100, $t_{max} = 50$.

wind but the reorganisation of individual penguins is not represented. Figure 4.2 shows results for various Péclet values and initial starting shapes of the huddle. In general, these show good agreement to the experiments of Waters et al. (2012): the huddle propagates in the windward direction and evolves into a more streamlined shape over time. For large time ($t \gtrapprox t_{max}/2$), the huddle approaches an invariant egg-shape which continues to propagate downwind with some constant velocity. To test this observation, a root mean-squared error (RMSE) measuring the deviation between consecutive plotted huddle shapes is computed for the examples in figure 4.2 and found to approach a constant value with a relative error of $\mathcal{O}(10^{-4})$. This permits the reasonable conclusion that huddles do evolve into a steady shape and thus in all experiments presented, the maximum time t_{max} is chosen such that the penguin huddle has reached a steady shape prior to or at time t_{max}.

Now, consider the full penguin problem where exterior, interior ($\beta \neq 0$) and area conserving terms are all included - recall from Sect.4.1.1 that $\beta = 0.1$ is used. Figures 4.3a-e present the evolution of the same initial circular starting shape for Pe = 1, 5, 10, 50 and 100. The final plot in each experiment is the steady shape and these are compared in figure 4.3f, where the shapes have been re-centered so that they share the same centre of mass. As the Péclet number is increased, the steady shape becomes less circular and more egg like.

Similarly, the effect of changing the parameter β can be explored. Figures 4.4a-e show the evolution of the circle with the values $\beta = 0$, 0.1, 0.5, 1 and 1.5, respectively, where Pe = 10 and $t_{max} = 20$ are taken for all plots. While a low value of β gives results that look similar to the exterior only penguin problem, a high value of β causes the penguin huddle to retain a more circular shape. This is shown in figure 4.4f,

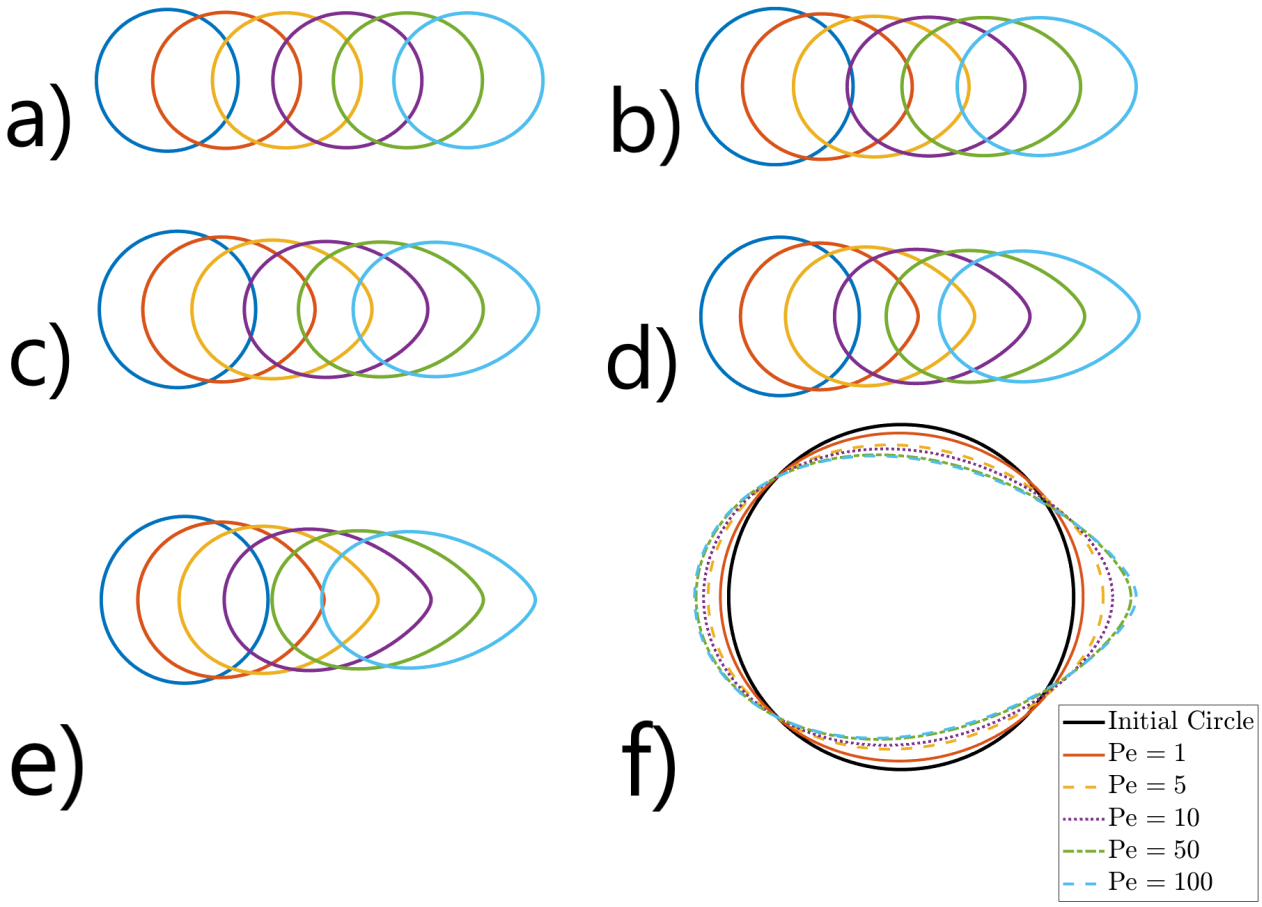

Figure 4.3: The effect of different Péclet numbers on the evolution of the huddle is shown by plotting its shape at equal time intervals. The initial starting shape of the penguin huddle is a circle, with $\beta = 0.1$ and a) Pe $= 1$, $t_{max} = 10$, b) Pe $= 5$, $t_{max} = 15$, c) Pe $= 10$, $t_{max} = 20$, d) Pe $= 50$, $t_{max} = 40$, e) Pe $= 100$, $t_{max} = 50$. f) Comparison of the steady shapes of (a)-(e), the initial (circular) huddle shape is also plotted for comparison.

where the steady shapes of figures 4.4a-e are compared.

The dependence of the final steady shape of the huddle on the values of the Péclet number and β is explored further. A given steady shape can be quantified by its aspect ratio (AR): the ratio between its major and minor axes with AR $= 1$ being a circle and increasing AR > 1 becoming more egg-shaped. Figures 4.5a,b show the dependence of AR on Pe and β, respectively. Each marker on the diagram represents a numerical experiment: each curve contains 21 markers, all run to a maximum time of $t_{max} = 80$, which is sufficiently long to reach the steady state huddle shape.

The results from figure 4.5 agree with the conclusions drawn from figures 4.3 and 4.4. First, as Pe increases, AR increases and thus a higher Péclet number results in a more egg-like steady shape, with a lower value of β giving higher values of AR for all time. This is also consistent with the parameter study in Waters et al. (2012) - see their figure 3 - which shows that the huddle thickness decreases with an

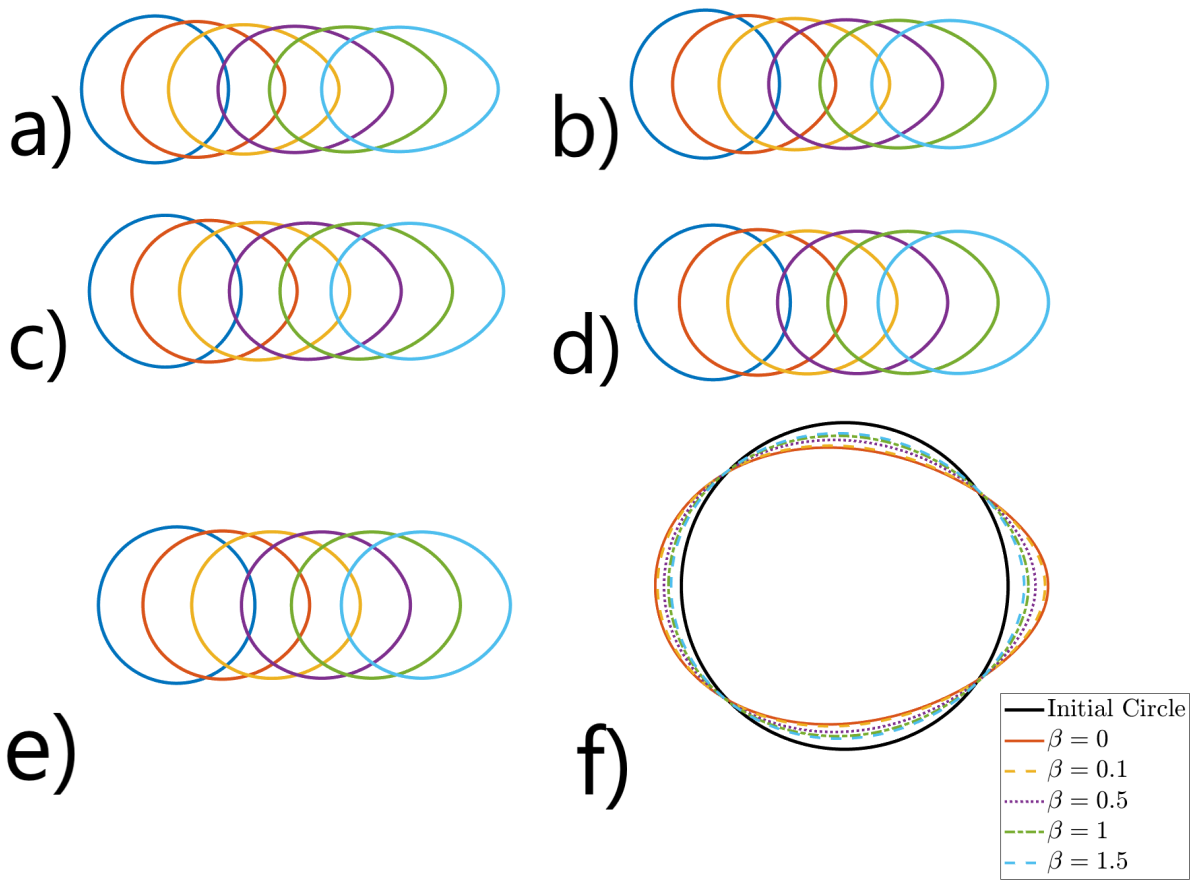

Figure 4.4: Interior β effect: initial starting shape of a circle with Pe $= 10$, $t_{max} = 20$ and a) $\beta = 0$, b) $\beta = 0.1$, c) $\beta = 0.5$, d) $\beta = 1$, e) $\beta = 1.5$. f) Comparison of the steady shapes of (a)-(e), the initial (circular) huddle shape is also plotted for comparison.

increasing Péclet number. As Pe $\to 0$, AR$\to 1$, consistent with the limit of a circular steady shape when there is no wind, as expected. Second, as β increases, AR decreases, where lower values of Pe result in lower values of the AR for all time.

Figure 4.6 shows how huddles of different starting shapes evolve under the same Péclet number Pe $= 10$, the same interior effect $\beta = 0.1$ and up to the same maximum time $t_{max} = 35$. Figures 4.6a-e show the evolution of a circle, a slanted ellipse, a triangle, an irregular pentagon and an hourglass, respectively, and figure 4.6f compares the steady shapes of these five experiments. The results show that, irrespective of the starting shape of the huddle and even those starting with significant concave boundaries, the same steady shape is reached.

The along-boundary variation of the total heat flux across the huddle boundary of the steady shape of figure 4.6f is considered. By symmetry, only the upper half of the boundary need be considered; this is plotted in figure 4.7a. The arrows point in the normal direction of the given point on the boundary and their lengths represent the total physical heat flux at that point. Recall from Sect.4.2 that the total heat

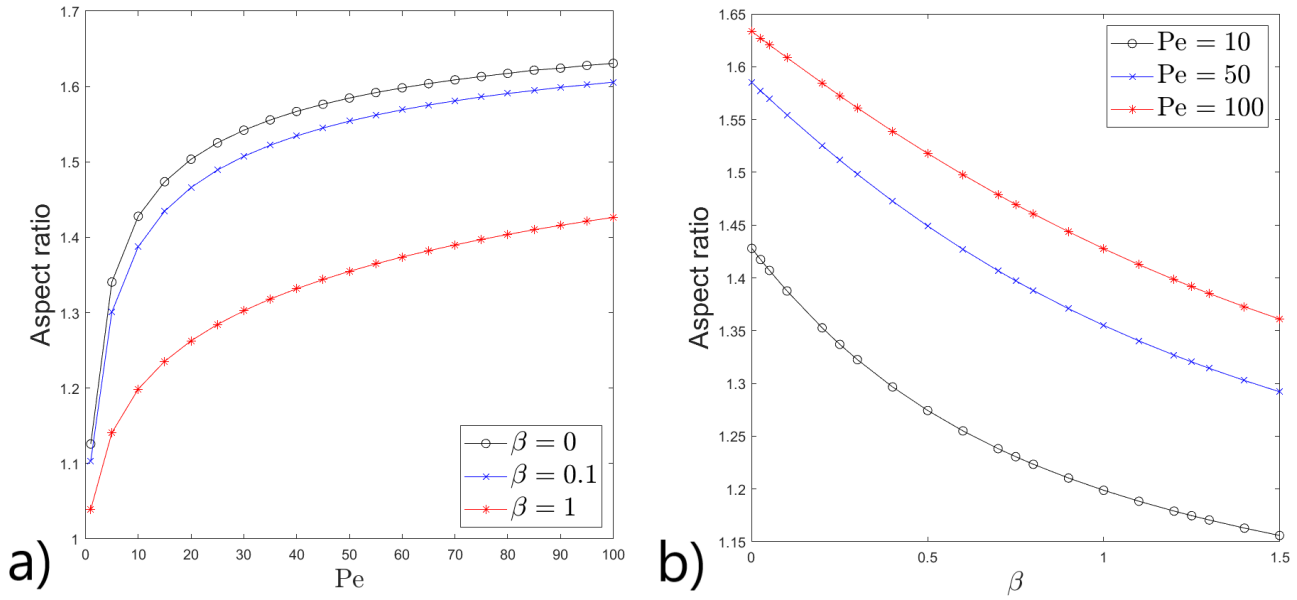

Figure 4.5: The aspect ratio of the final steady shape of the penguin huddle as a function of a) Péclet number, for the three given values $\beta = 0, 0.1$ and 1, and b) β, for the three given values $\mathrm{Pe} = 10, 50$ and 100. Each marker represents a numerical experiment.

flux in the physical domain across the huddle boundary γ is given by $\hat{\boldsymbol{n}} \cdot \boldsymbol{\nabla} T_\Omega - \beta \hat{\boldsymbol{n}} \cdot \boldsymbol{\nabla} T_R$ whereas the total heat flux in the canonical domain across the unit $\zeta-$disk is given by $\sigma(\theta) - \beta\omega(\theta)$. The canonical heat flux in the upper half $\zeta-$disk vs θ is plotted in figure 4.7b and the physical heat flux vs x is plotted in figure 4.7c. There is a much larger heat flux on the windward side of the penguin huddle (the side of the penguin huddle directly facing the oncoming wind) compared to the leeward side. This is expected and is in agreement with the exterior temperature profile presented in Waters et al. (2012) - see their figure 1 - which shows that there is a steeper temperature gradient, and hence a higher total heat flux, on the windward side.

Finally, there is randomness associated with penguin movements owing to, for example, inhomogeneities in the thermal properties of penguins on the boundary or fluctuating wind velocity in the exterior. Waters et al. (2012) incorporate time-varying perturbations by randomly varying the heat loss of boundary penguins at each time step. Owing to the deterministic ODE solvers used in the numerical model here, such time-dependent random perturbations are not tackled in this thesis. However, as a step towards considering random effects, a steady random perturbation to the exterior heat flux from the penguin huddle to the wind is considered using a modified version of equation (4.2.10)

$$\mathrm{Pe}\ \mathrm{Re}[f_t \overline{\zeta f_\zeta}] = (1 + \epsilon\mu)\sigma(\theta) - \beta\omega(\theta) + C(t)|f_\zeta|. \tag{4.3.1}$$

Here $0 < \epsilon \ll 1$ is some constant and, when the equation is discretised in θ, the random numbers

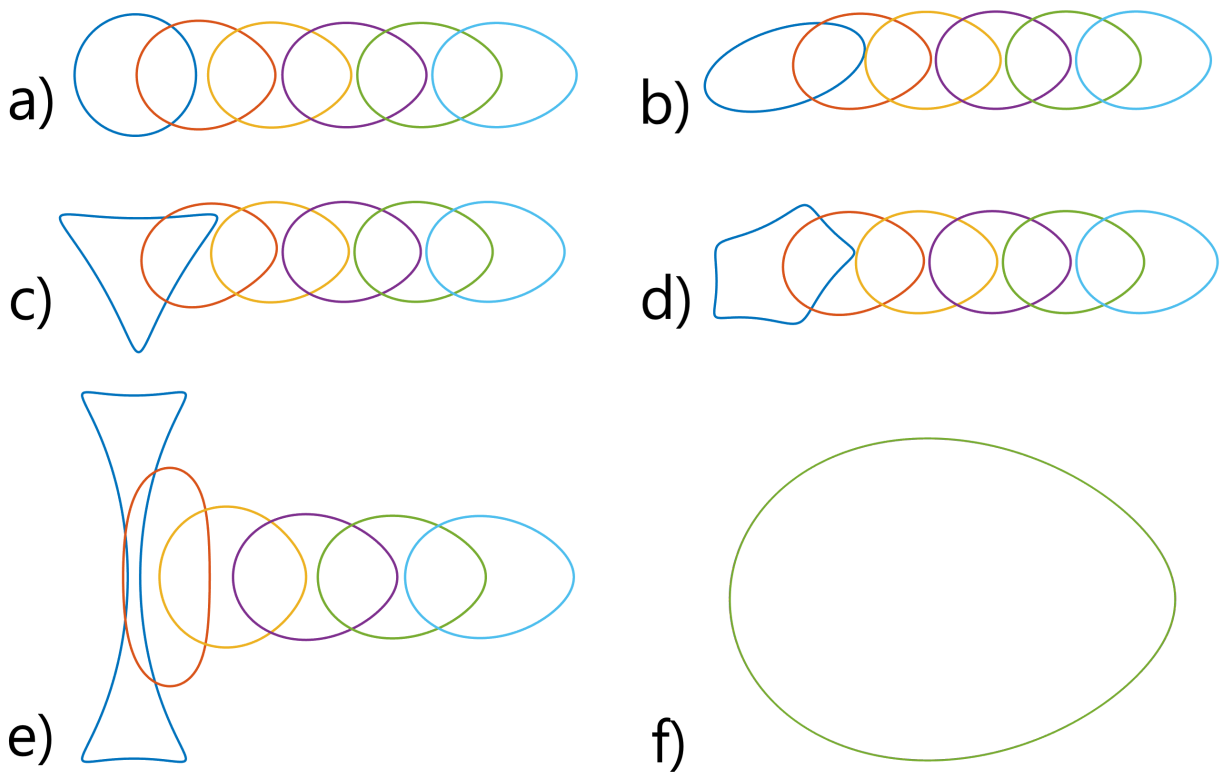

Figure 4.6: Initial shape effect. Shapes are plotted at equal time intervals with Pe = 10, $\beta = 0.1$, $t_{max} = 35$ and the initial starting shape of a) a circle, b) a slanted ellipse, c) a triangle, d) an irregular pentagon, e) an hourglass. f) Comparison of the steady shapes of (a)-(e): all of the steady shapes are overlapped.

$\mu(\theta_j) = \mu_j$, $j = 1, \cdots, 2N + 3$ are selected from a uniform distribution between -1 and 1.

Figure 4.8 compares the steady shapes of four experiments, each simulating the propagation of an initially circular penguin huddle with Pe $= 10$, $\beta = 0.1$, $t_{max} = 20$ and different amplitudes ϵ of the random function $\mu(\theta)$: $\epsilon = 0$ (no randomness), $\epsilon = 0.01$, $\epsilon = 0.1$ and $\epsilon = 0.2$. The $\epsilon = 0.01$ experiment shows no discernible difference between the $\epsilon = 0$ experiment, and while there are some slight variation between the $\epsilon = 0.1, 0.2$ and $\epsilon = 0$ experiments, these are very minor. All experiments result in the same general egg-shaped steady shape which, along with those of figure 4.6, demonstrate the persistence of the steady egg-shaped huddles.

4.4 Discussion

In this chapter, a two-dimensional continuum model for the evolution of a penguin huddle in a uniform wind flow is developed. Two key thermodynamic processes drive the huddle motion: exterior cooling by the ambient wind and interior heating generated by the penguins themselves, who then reorganise themselves within the huddle to help diffuse the heat. This free boundary problem is very similar to the wildfire problem of Ch.3 with some notable differences: the area of the huddle interior is conserved rather

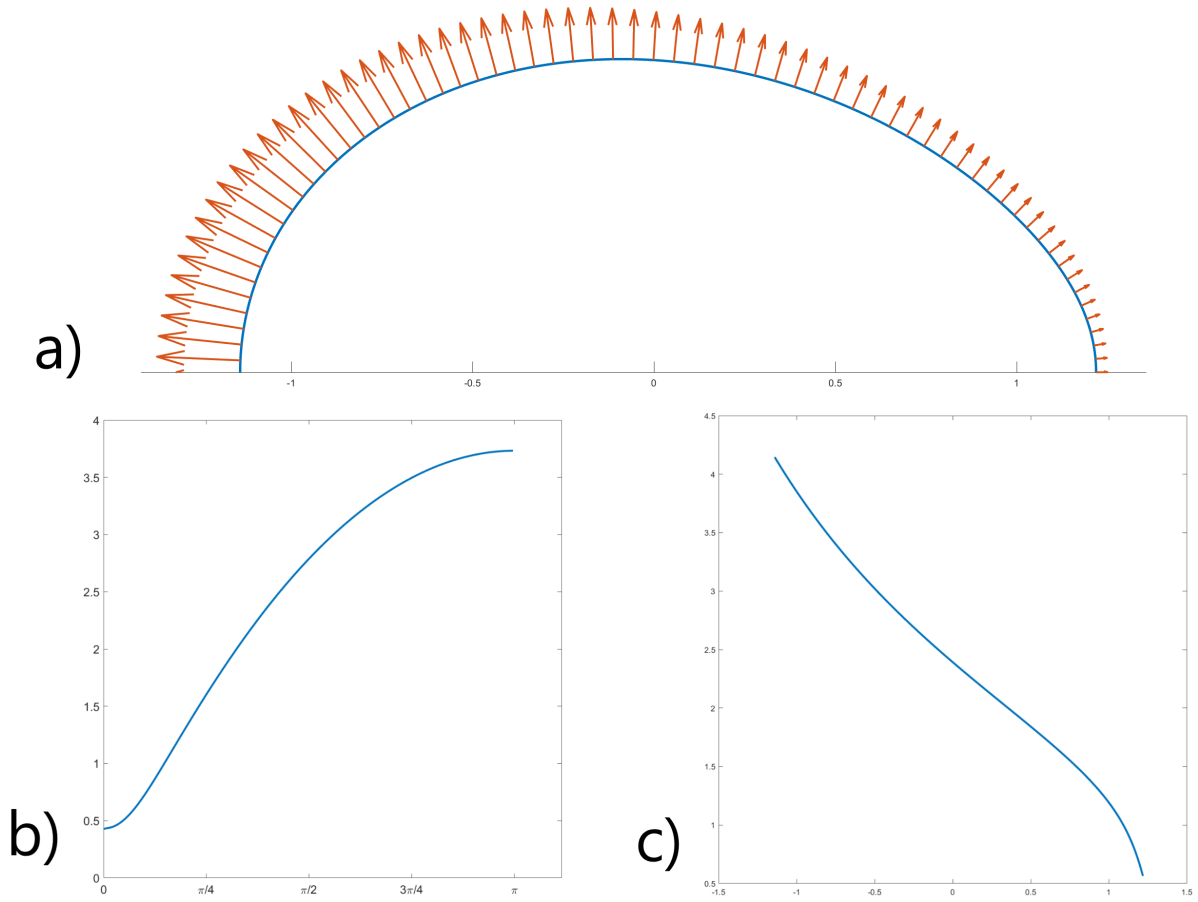

Figure 4.7: a) Total heat flux across the boundary of the steady shape of figure 4.6f. The arrows point in the normal direction of the given boundary point and their magnitude is proportional to the local heat flux across the boundary. b) Canonical heat flux in the upper half $\zeta-$disk vs θ. c) Physical heat flux in the upper half of the huddle boundary vs x.

than growing (the basic ROS term is replaced by an area conservation term); there is no curvature effect and; the transport of exterior temperature (rather than oxygen) affects the huddle propagation as does the interior temperature profile.

As in Ch.3, a conformal mapping method reduces the system of equations (4.1.13a) to (4.1.13g) to a single PG type equation (4.2.10) in terms of the conformal map $z = f(\zeta, t)$ which is approximated as a truncated Laurent series (equation (4.2.11)). Numerical results show that the huddle boundary eventually reaches a steady shape - the huddle remains as a fixed shape that propagates downwind. As the wind strength increases, the huddle becomes increasingly egg-shaped, minimising the portion of the huddle boundary directly facing the oncoming wind. For a stronger interior heating effect (parameterised by β), the huddle approaches a more circle-like steady shape, to optimise interior heat regulation. For given wind and interior effects, any initial huddle shape eventually approaches the same steady shape, suggesting there is some optimum penguin huddle shape for given environmental conditions. There is also a greater total

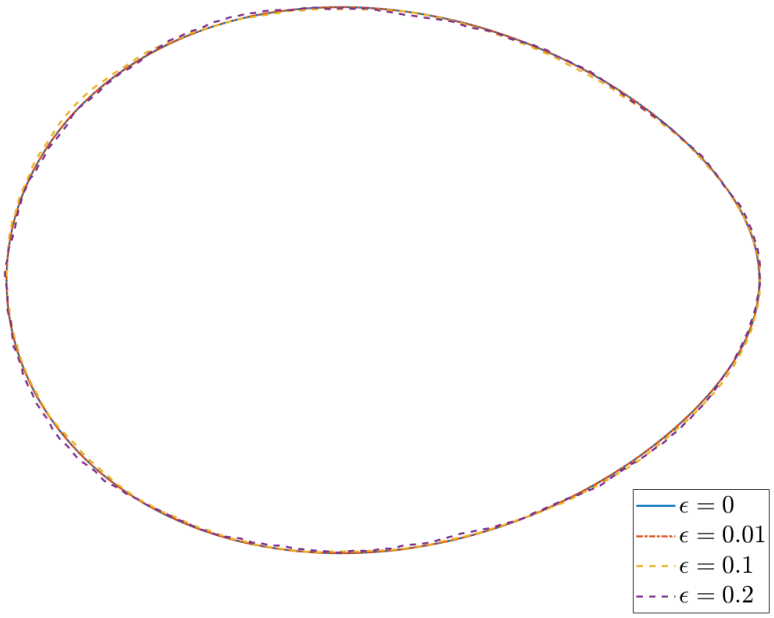

Figure 4.8: Comparison of the steady shapes of the propagation of a circular penguin huddle with Pe = 10, $\beta = 0.1$, $t_{max} = 20$ and different amplitudes ϵ of the random function $\mu(\theta)$: $\epsilon = 0$ (no randomness), $\epsilon = 0.01$, $\epsilon = 0.1$ and $\epsilon = 0.2$.

heat flux on the windward side of the huddle than on the leeward side.

While dimensionless quantities have been used throughout the chapter, it is useful to estimate the dimensional time scale associated with the huddle evolution. As noted in Sect.4.1.1, the appropriate dimensional time scale is $t_r = \lambda \text{Pe}(L/U)t^*$ where t^* is dimensionless time, and the choice $\lambda = 1$ has been made. A large huddle of, for example, 6000 penguins (Le Maho, 1977), is assumed and taking the radius of each penguin to be $r \approx 0.1$m (Williams et al., 2015) gives $L \approx 10$m. Now assume a sufficiently strong wind of $U \approx 20\text{m}s^{-1}$ for Pe = 100. Considering figure 4.3c where $t^* = t_{max} = 50$, the total real time for this experiment is $t_r = 2500$ seconds or ≈ 42 minutes. Thus it is concluded that the penguin huddle motion described in this work occurs over roughly a one hour period, in agreement with previous modelling and field observations (Kirkwood and Robertson, 1999; Gilbert et al., 2006; Waters et al., 2012), and justifying the choice $\lambda = 1$.

Following the theme of this thesis, a continuum model has here been used to evaluate the evolution of the huddle boundary at the expense of tracking individual penguin movements. While there are pre-existing discrete models for penguin huddling (and other animal grouping dynamics) (Waters et al., 2012; Gerum et al., 2013, 2018; Bernardi and Scianna, 2020), treating a penguin huddle as a continuum appears to be new. One of the advantages of the continuum model developed here is its computational efficiency, with a typical runtime of around 5-10 minutes on a standard laptop for a huddle to reach a steady shape. This can be sped up further (to the order of seconds) by reducing the Laurent series truncation N.

Care should be taken to ensure that the accuracy of the results is not compromised, yet based on the analysis performed in Sect.3.3.3, a suitable level of accuracy can still be achieved when reducing the series truncation from $N = 128$ to $N = 32$.

When considering the 'exterior only' ($\beta = 0$) penguin problem, the results from this chapter matched well with those from Waters et al. (2012), who did not include the interior effect of penguin reorganisation in their model. As discussed in Sect.4.1.1, fully turbulent wind flows have $\beta \approx 0$ and hence are well modelled by considering exterior effects alone. The representative value $\beta = 0.1$, which is likely to be an overestimate, chosen in this chapter demonstrates that the interior heating of the colony only provides a weak effect in determining the steady shape of the huddle, see figure 4.4f. Larger values of β resulting in more circular huddle shapes have been included for completeness. Furthermore, the model results match well with real world observations: penguin huddles are seen to march downwind over time and observed huddle shapes resemble the egg-like steady shapes found here - see Le Maho (1977); Gerum et al. (2013); Ancel et al. (2015); Richter et al. (2018); Mina and Min (2018).

The remainder of the thesis explores extensions to the wildfire model developed in Ch.3 and develops models for other interfacial problems in nature. Consequently, this is the sole chapter concerned with penguin huddle dynamics, though there are numerous extensions of interest to the penguin huddle model. A time-varying wind could be considered, where the variations in direction and magnitude are on the order of an hour. It is expected that, when the wind direction changes, the huddle will seek to propagate back to the optimal (egg) steady shape in the new windward direction. Time dependent stochastic terms could also be incorporated into the model, as done in Waters et al. (2012) and as an extension to the steady random perturbation introduced at the end of Sect.4.3. Such stochastic terms would include random variations in the direction and magnitude of the wind and in the interior and exterior heat fluxes. As noted in Sect.4.3, the numerical method would need to be adapted to handle these stochastic terms and use stochastic differential equation (SDE) solvers rather than deterministic ODE solvers. As in Ch.3, only Laurent shapes are considered in this chapter. Incorporating the extension to non-Laurent shapes into the numerical method as detailed in Ch.5 would allow for any arbitrary huddle shape to be analysed; this would allow for direct comparison between the model outputs and observational penguin huddle data.

Multiple and multiply-connected penguin huddles could also be considered, such as those with penguin-free holes or the interaction, and possible merger, of initially disjoint huddles. This is a similar extension to that of Ch.7 where the interaction of multiple wildfires is explored, noting that the AAA-LS method introduced in this chapter is capable of handling such multiply-connected geometries (Costa, 2020; Trefethen, 2020;

Costa and Trefethen, 2023). A more complicated exterior environment could also be incorporated into the model setup, such as a surface with slopes, hills or holes in the ice. As noted in Sect.4.1, the wind is taken to be inviscid such that conformal mapping methods can be used in the numerical method. Instead, a full analysis of the viscous boundary layers around the huddle boundary could be undertaken. There may also be boundary layers over the top of the huddle, necessitating a 3D model to assess vertical heat flux and wind flow. Furthermore, while the steady heat equation gives a good description of the interior heat transfer (given that the penguins seek to diffuse the heat in the huddle), alternative interior temperature distributions could be considered. Based on the description of penguin movements given in Le Maho (1977), it is speculated that some convective equation could accurately describe interior penguin motion.

Finally, consider the normal velocity of the penguin huddle boundary - equation (4.1.13a) - and its associated PG equation (4.2.10). The right-hand side is constructed by exterior ($\hat{\boldsymbol{n}} \cdot \boldsymbol{\nabla} T_\Omega$), interior ($\beta \hat{\boldsymbol{n}} \cdot \boldsymbol{\nabla} T_R$) and area conservation (C(t)) effects. By inclusion and exclusion of these three terms, equation (4.1.13a) encapsulates six possible free boundary problems:

1. The dissolution problem: exterior effect only. A permeable object is placed in a uniform stream of some dissolving agent - see for example Dutka et al. (2020); Ladd et al. (2020).

2. The Poisson growth problem: interior effect only. Applicable to squeeze flow and the evaporation of thin liquid films - see Crowdy and Kang (2001); Agam (2009); McDonald and Mineev-Weinstein (2014).

3. The two-phase melting/freezing problem: exterior and interior effects. Porous media flow about freeze pipes where interior and exterior temperature gradients are in effect - see Goldstein and Reid (1978); Rycroft and Bazant (2016).

4. The 'exterior only' penguin problem: exterior and area conservation effects. Huddle problems where interior reorganisation is not represented, such as if individuals in the centre are unable to move or there exists a 'pecking order' in the population - see Waters et al. (2012).

5. The 'bat huddle' problem: interior and area conservation effects. Huddle problems with no wind effect, for example bats huddling in caves sheltered from exterior winds. To the authors' knowledge, there is no mathematical work on this problem, but for biological context see e.g. Herreid (1963); Ryan et al. (2019).

6. The 'full' penguin problem: exterior, interior and area conservation effects. This is the full huddle

continuum problem covered in this chapter.

Therefore, the numerical method developed here can be used to model and simulate additional free boundary problems, such as those from the fields of fluid mechanics and mathematical biology.

Part II

WILDFIRE SPREAD AND WIND EFFECTS

Chapter 5

Deterministic rate of spread

So far in this thesis, the wildfire models of Ch.2 and Ch.3 have included, without derivation, a basic rate of spread (ROS) term. This is an assumed constant normal velocity representing the combined effects of convection and radiation and the physical, chemical and thermodynamic properties of the fuel being burnt in the absence of all other external factors. Typically, the basic ROS is calculated by some proposed formula - the most renowned of these was in Rothermel (1972) which has predicted wildfire spread to good agreement with observational data and thus laid the basis for the majority of wildfire modelling to this day. However, it is speculated whether this basic ROS effect could be obtained deterministically. For example in Dipierro et al. (2024), the normal velocity of the fire line follows from their constitutive equation (1.1).

A similar idea is proposed in this chapter which results from the study of a certain type of free boundary problem. In the classical Hele-Shaw (or Laplacian growth) free boundary problem (e.g. Gustafsson and Vasil'ev, 2006), the normal velocity of the free boundary depends on the gradient of a harmonic function. This function typically has logarithmic singularities, which can be thought of as sources and sinks that drive the free boundary evolution. The free boundary problem considered in this chapter is similar, except that the normal velocity is inversely related to the gradient of the harmonic field. Lundberg and Totik (2013) considered the same reciprocal growth law in their work and used arguments based on potential theory and Green's functions to show that polynomial lemniscates are exact solutions. This led them to use the description *'lemniscate growth'* for this type of free boundary problem which showed markedly different properties to classical Laplacian growth. Generalized growth laws for other types of Laplacian growth problems have also been studied, see e.g. Niemeyer et al. (1984) and Gubiec and Szymczak (2008). This chapter further develops lemniscate growth by formulating analytical and numerical approaches. The

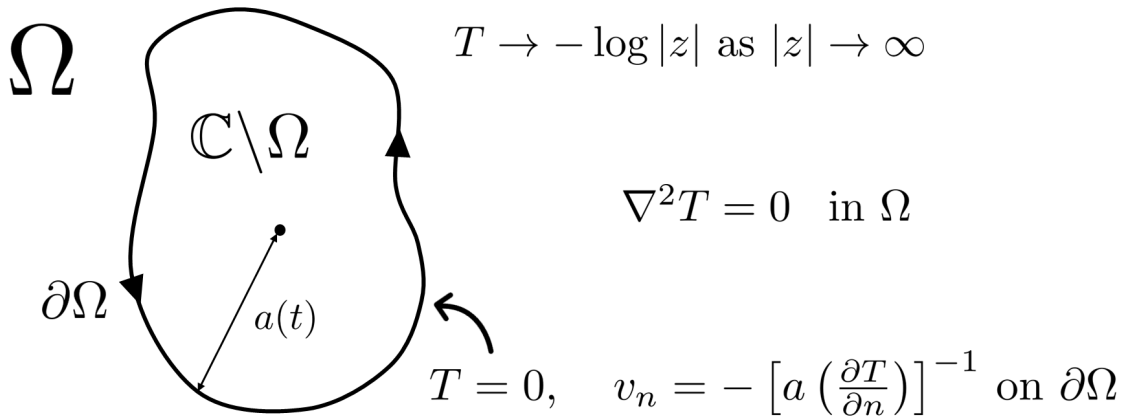

Figure 5.1: Schematic diagram of the free boundary problem where T is a harmonic function in the exterior (infinite) domain Ω and a is the conformal radius of the finite domain $\mathbb{C}\backslash\Omega$. The arrows on the boundary $\partial\Omega$ give the sense in which the arc length parameter s increases.

work in this chapter was published in McDonald and Harris (2024).

5.1 Free boundary problem with reciprocal growth law

As shown in figure 5.1, let Ω be the simply-connected, infinite domain exterior to a smooth, non-intersecting, time-dependent closed curve $\partial\Omega(t)$ in the complex $z-$plane, where $z = x + iy$. Suppose $T(x, y)$ is a harmonic function in Ω such that $T \to -\log|z|$ as $|z| \to \infty$ and $T = 0$ on $\partial\Omega$. The free boundary $\partial\Omega(t)$ evolves according to

$$v_n = -\left[a\left(\frac{\partial T}{\partial n}\right)\right]^{-1}, \tag{5.1.1}$$

where v_n is the normal velocity of the curve directed from the interior to the exterior domain. The conformal radius $a(t) > 0$ of the finite interior domain $R = \mathbb{C}\backslash\Omega$ is related to the logarithmic capacity of the exterior domain Ω (e.g. Baddoo and Trefethen, 2021). Note that the conformal radius was denoted by '$a_{-1}(t)$' in previous chapters yet here is denoted simply by '$a(t)$' to match with the notation used in McDonald and Harris (2024).

Unusually, the normal velocity equation (5.1.1) of the free boundary is here posed as the inverse of the normal gradient of T. In classical Hele-Shaw free boundary problems, the free boundary velocity would instead be for example $v_n = \partial_n T$ with T identified as the real velocity potential. The boundary conditions on T used in this chapter imply that the gradient of T in the normal direction is negative and so equation (5.1.1) leads to growth: the finite interior domain R increases in area over time. As will be shown in Sect.5.2, such growth is stable. The dependency of equation (5.1.1) on the time-varying conformal radius $a(t)$ slows the rate of growth of the free boundary as $a(t)$ increases. Its presence effectively

amounts to a rescaling of time and prevents exponential growth in time of the radius of the free boundary; this makes for a more realistic growth law when applied to the wildfire problem - see Sect.5.5. Thus, this rescaling in $a(t)$ is included here, yet is not necessary in deriving exact and numerical solutions of the problem.

The problem can also be formulated as a PG type equation, see e.g. Ch.3, in terms of the conformal map $z = f(\zeta, t)$ from the exterior of the unit disk in the $\zeta-$plane to Ω. This will be used in the upcoming numerical method, see Sect.5.4. Recalling from Sect.2.4 that the unit normal velocity can be written as $n = \zeta f_\zeta/|f_\zeta|$ and the normal velocity on $\partial\Omega$ as

$$v_n = \mathrm{Re}\left[\frac{f_t\overline{\zeta f_\zeta}}{|f_\zeta|}\right], \tag{5.1.2}$$

then evaluating equation (5.1.1) gives

$$v_n = -\left[\frac{a}{2}\left(\frac{\partial(W+\overline{W})}{\partial n}\right)\right]^{-1} = -\left[\frac{a}{2}\mathrm{Re}\left(n\overline{\nabla}(W+\overline{W})\right]^{-1} = -\left[a\,\mathrm{Re}\left(n\frac{\partial}{\partial z}(W+\overline{W})\right)\right]^{-1}$$
$$= -\left[a\,\mathrm{Re}\left(n\frac{\partial W}{\partial z}\right)\right]^{-1}, \tag{5.1.3}$$

where the equivalence $\overline{\nabla} \equiv \partial_x - i\partial_y = 2\partial_z$ has been used. In the $\zeta-$plane, the function $W = -\log\zeta$ is analytic and hence $W_z = -(\zeta f_\zeta)^{-1}$ thus equating equations (5.1.2) and (5.1.3) gives on $|\zeta| = 1$

$$a\,\mathrm{Re}\Big[f_t\overline{\zeta f_\zeta}\Big] = |f_\zeta|^2. \tag{5.1.4}$$

For comparison, in the Hele-Shaw case with a source of strength Q at the origin within a finite blob of fluid, the PG equation is $\mathrm{Re}\Big[f_t\overline{\zeta f_\zeta}\Big] = Q$ with the sign of Q determining whether the free boundary of the fluid blob expands or contracts.

Finally, the free boundary problem can also be formulated in terms of the Schwarz function $S(z)$ of the curve $\partial\Omega$ in the $z-$plane. This is the unique function analytic in the neighbourhood of $\partial\Omega$ and such that $S(z) = \bar{z}$ on $\partial\Omega$ (Davis, 1974). Representing curves in the $z-$plane using $S(z)$ has proved successful in obtaining exact solutions for a range of free boundary problems including those of the Hele-Shaw class (Howison, 1992; Mineev-Weinstein et al., 2000; Gustafsson and Vasil'ev, 2006), 2D vortex dynamics, (Saffman, 1995; Crowdy, 1999; Riccardi, 2020) and industrial coating flows (Johnson and McDonald, 2009; Marshall, 2011). The Schwarz function formulation is given in detail in McDonald and Harris (2024) and yields equivalent results to the PG formulation.

5.2 Stability

A linear stability analysis similar to those in Ch.2 and Ch.3 is performed here. Consider the base state of a circle with radius $a(t)$ which has the conformal map $z = f(\zeta, t) = a(t)\zeta$. Substituting this into equation (5.1.4) and using the fact that $\overline{\zeta} = \zeta^{-1}$ on $|\zeta| = 1$ gives $\dot{a} = 1$. Hence $a(t) = a_0 + t$ where a_0 is the initial radius of $\partial\Omega$. This relation can also be obtained using the Schwarz function, see McDonald and Harris (2024).

Now consider the perturbed circular interface and harmonic field T of the form

$$R = a + \delta_n \cos n\theta, \quad T = -\log\left(\frac{R}{a}\right) + \beta_n \left(\frac{a}{R}\right)^n \cos n\theta, \quad n = 1, 2, \cdots, \tag{5.2.1}$$

where $\delta_n(t) \ll a$ and $\beta_n(t) \ll 1$ are small time-varying amplitudes of the perturbation and the summation sign has been dropped for brevity as in e.g. Ch.2. Since $T = 0$ on the boundary $R = a + \delta_n \cos n\theta$, it follows to leading order from equation (5.2.1) that $\delta_n = a\beta_n$. Furthermore, evaluating equation (5.1.1) to leading order gives

$$\dot{a} + \dot{\delta}_n \cos n\theta = \left(\frac{a}{R} + n\beta_n \frac{a^{n+1}}{R^{n+1}} \cos n\theta\right)^{-1}. \tag{5.2.2}$$

The relation $R = a + \delta_n \cos n\theta$ is then substituted into equation (5.2.2) and the leading order term gives $\dot{a} = 1$, as expected. To assess the stability of perturbations, the relative growth rate $g(n)$ must be examined. As introduced in Ch.3, this is the growth of perturbations relative to the overall growth of the free boundary (Dallaston and Hewitt, 2014); stable behaviour is observed if perturbations grow slower than the conformal radius $a(t)$. Evaluating equation (5.2.2) gives

$$g(n) = \frac{\dot{\delta}_n}{\delta_n} - \frac{\dot{a}}{a} = \frac{1}{a}\big(1 - n - 1\big) = -\frac{n}{a}. \tag{5.2.3}$$

As equation (5.2.3) is negative for all n, all perturbations decay in time and thus the free boundary growth is stable. The above stability analysis of interface growth appears to be new, though the general stability of Laplacian growth problems where $v_n \sim |\nabla T|^\eta$ at the interface with $\eta < 0$ (note that here $\eta = -1$) is noted in Gubiec and Szymczak (2008). The problem is time reversible (as noted in Lundberg and Totik, 2013), but is unstable since the sign of the RHS of equation (5.2.3) changes.

5.3 Exact solutions for the growth problem

In addition to the trivial circular solution used in the stability analysis of Sect.5.2, there exist two other classes of exact solution: ellipses and polynomial lemniscates. Three examples of such solutions are given

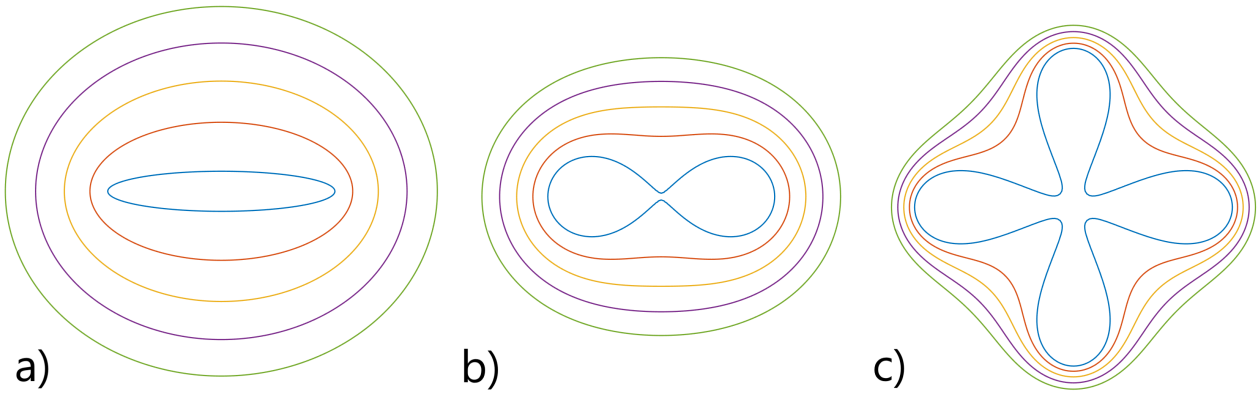

Figure 5.2: (a) Growth of an elliptical boundary according to equation (5.3.2) with $c_0 = 1$ and $d_0 = 0.7$, with plots of $\partial\Omega$ shown at equal time intervals between $t = 0$ and $t = 2$. (b) Growth of a Cassini oval $|z^2 - 1| = e^2$ with $e = t + 1.001$ between $t = 0$ and $t = 1$. (c) Growth of the lemniscate $|z^4 - 1| = e^4$ with $e(0) = 1.0001$ between $t = 0$ and $t = 0.25$.

in figure 5.2. Detailed derivations of both classes of exact solution are given in McDonald and Harris (2024) using both Schwarz function and PG formulations; the analysis involving the PG type equation (5.1.4) is restated in the upcoming subsections.

5.3.1 Ellipse

Let $z = f(\zeta, t) = c\zeta + d/\zeta$ (where $c(t)$ and $d(t)$ are real, time-varying parameters) be the conformal map from the exterior of the unit $\zeta-$disk to the exterior of an ellipse with axes of length $|c + d|$ and $|c - d|$. Substituting $f(\zeta, t)$ into equation (5.1.4) and letting $\zeta = \exp(i\theta)$ gives terms which are either $\theta-$independent or linear in $\cos 2\theta$. Equating like terms gives two ODEs for the unknown coefficients c and d

$$\begin{aligned} a\left(c\dot{c} - \dot{d}d\right) &= c^2 + d^2, \\ a\left(c\dot{d} - d\dot{c}\right) &= -2cd. \end{aligned} \tag{5.3.1}$$

As c is equivalent to the conformal radius a, equation (5.3.1) has solutions

$$c = t + c_0, \quad d = \frac{c_0 d_0}{t + c_0}, \tag{5.3.2}$$

where $c(0) = c_0$ and $d(0) = d_0$. Thus the ellipse grows, becoming more circular as the ratio $|d/c|$ decreases with increasing time t. An example with $c_0 = 1$ and $d_0 = 0.7$ is shown in figure 5.2a.

5.3.2 Cassini oval and polynomial lemniscates

Let $\partial\Omega$ be a Cassini oval, an example of a polynomial lemniscate, given by $|z^2-1|=e^2$, where $e>1$. From Symm (1967), the conformal map from the exterior of the unit $\zeta-$disk to the exterior of the Cassini oval is

$$z=\sqrt{e^2\zeta^2+1}. \tag{5.3.3}$$

The leading order term in the expansion of equation (5.3.3) as $\zeta\to\infty$ is $e\zeta$, which shows that the conformal radius $a\equiv e$. Direct substitution of equation (5.3.3) into equation (5.1.4) using $\zeta=\exp(i\theta)$ shows that it is an exact solution provided $\dot{e}=1$ and so $e(t)=t+e_0$ where $e_0=e(0)>1$. The above steps can be followed to show that any polynomial lemniscate of the form $|z^M-1|=e^M$, $M=2,3,\cdots$ is an exact solution given that $\dot{e}=e/a$, in agreement with the original work of Lundberg and Totik (2013) (who do not include the time scaling in a). With the realisation that the conformal map is now $z=\sqrt[M]{e^M\zeta^M+1}$, it follows that the conformal radius $a\equiv e$ and so $\dot{e}=1$ for $M=2,3,\cdots$. Figure 5.2b shows a growing Cassini oval and figure 5.2c the growth of the lemniscate $|z^4-1|=e^4$ with $e(0)=1.0001$.

5.4 Numerical procedure and examples

The evolution of more general free boundary shapes $\partial\Omega(t)$ is found by solving equation (5.1.4) numerically to find the conformal map from the exterior of the unit $\zeta-$disk to Ω. The numerical procedure follows the same approach as in e.g. Ch.4: it is assumed that the free boundary is a Laurent shape with a conformal map of the form of the truncated Laurent series

$$z=f(\zeta,t)=a(t)\zeta+\sum_{k=0}^{\infty}c_k(t)\zeta^{-k}, \tag{5.4.1}$$

where, with no loss of generality, the conformal radius $a(t)>0$ is real, and $c_k(t)=a_k(t)+ib_k(t)$ are complex functions in time (i.e. there are no imposed lines of symmetry as in e.g. Ch.3). The series is truncated at N terms and $n=2N+3$ equispaced points around the unit $\zeta-$disk are selected, thus equation (5.1.4) becomes a system of n coupled ODEs in time which can be solved using the MATLAB routine *ode15i* to find the coefficients $a(t), c_k(t)$.

The method is tested by comparing numerical results with exact solutions from Sect.5.3. The ellipse has a conformal map immediately in the form of equation (4.2.11): $z=a(t)\zeta+c_1(t)\zeta^{-1}$. The map of the

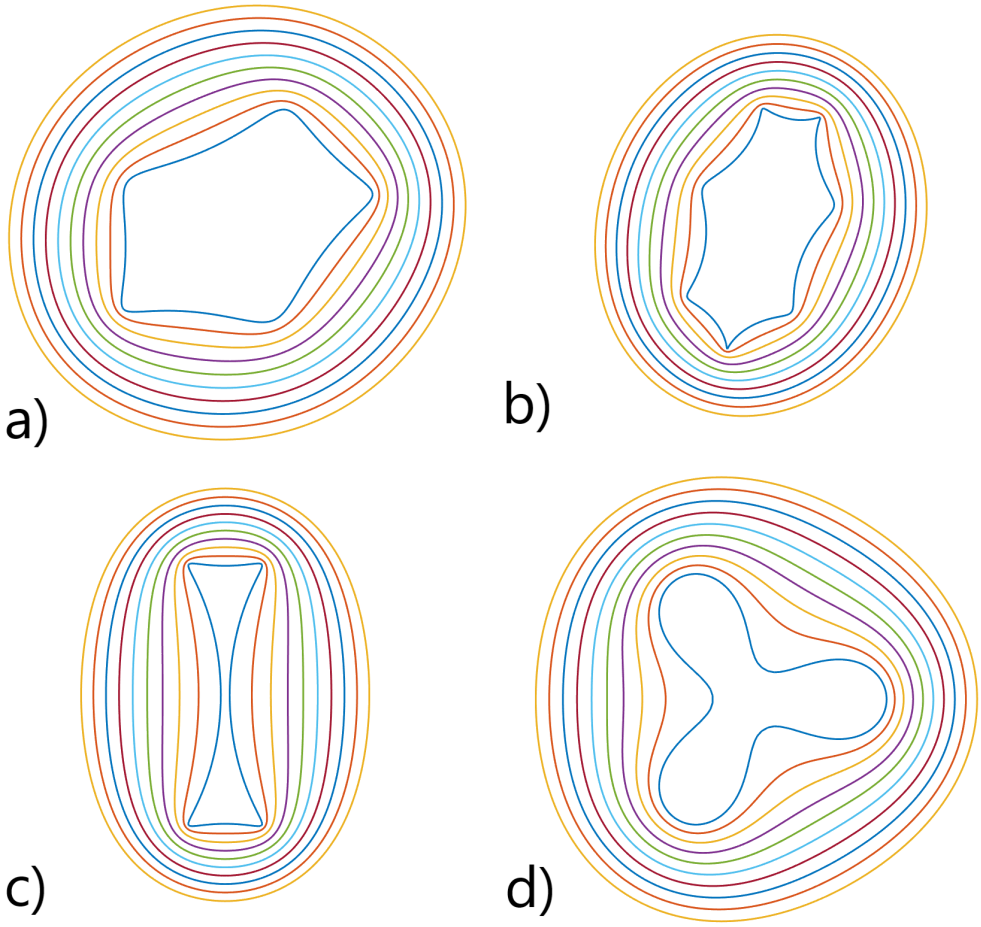

Figure 5.3: Growth of Laurent shapes from $t = 0$ to $t = 1$ with Laurent series truncation $N = 128$, (a) irregular pentagon, (b) irregular object, (c) hourglass. (d) A lemniscate with $e(0) = 1.01$, $M = 3$ and $N = 256$.

general polynomial lemniscate of degree M can also be written as a Laurent series

$$z = (e^M \zeta^M + 1)^{1/M} = e\zeta + \sum_{k=1}^{\infty} \binom{1/M}{k} (e\zeta)^{1-kM}, \tag{5.4.2}$$

where the identification $a(t) = e(t)$ is made. The same set of points around the $\zeta-$disk is mapped using both the numerical and exact solutions for z, allowing for direct comparison. It is found that the distance between corresponding exact and numerical points has a relative error of $\mathcal{O}(10^{-7})$ at all time.

Figure 5.3 gives examples of the free boundary evolution under equation (5.1.1) for a variety of Laurent shapes: an irregular pentagon, an irregular object, an hourglass - all with Laurent series truncation $N = 128$ - and the lemniscate $|z^3 - 1| = e^3$ with $e(0) = 1.01$, $M = 3$ and $N = 256$. The Laurent coefficients at $t = 0$ of these shapes (excluding the lemniscate) are taken from Rycroft and Bazant (2016) – see their figures 5a, 2f and 7a. In all plots, concave and convex regions are 'smoothed out' as each shape approaches a growing circle. The time scale to which it reaches a circular shape (within some level of

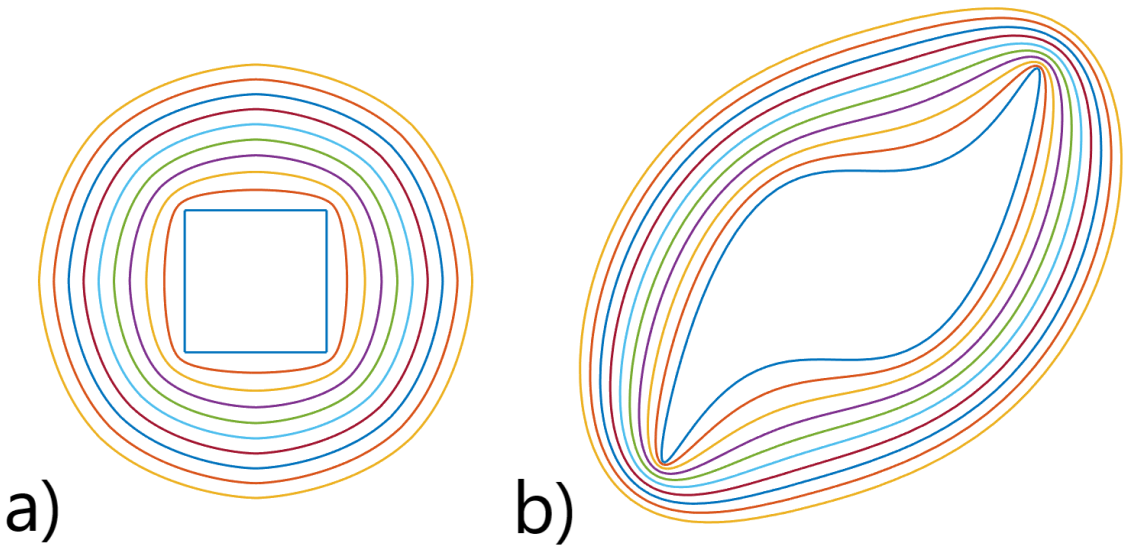

Figure 5.4: Growth of non-Laurent shapes from $t = 0$ to $t = 1$ with series truncation $N = 128$, (a) a square, (b) a blade.

approximation) depends on the initial shape; while the irregular pentagon has almost reached a circle in figure 5.3a, the hourglass remains notably non-circular at $t = 1$ in figure 5.3c.

As noted in Ch.2, many shapes (at least initially) are not well approximated by the truncated version of the Laurent series equation (4.2.11): these are called 'non-Laurent shapes'. In such cases, the numerical approach is modified as follows: the conformal map of the initial, arbitrary shape can be found numerically using the Schwarz-Christoffel (SC) Toolbox (Driscoll, 1996). The Toolbox function *extermap* is used, which finds the map $g(\zeta)$ from the *interior* of the unit $\zeta-$disk to the exterior Ω of the free boundary. Then, a power series in ζ is added to the initial map g as follows

$$z = f(\zeta, t) = a^*(t)g(\zeta) + \sum_{k=0}^{\infty} c_k(t)\zeta^k, \tag{5.4.3}$$

where $a^*(0) = 1$ and $c_k(0) = 0$, $\forall k$. This is a restatement of the conformal map equation (2.4.8) given in Ch.2. There are two points to note: (i) the series powers of ζ are opposite in sign from equation (4.2.11) as the map transforms the interior of the $\zeta-$disk to Ω; and (ii) the conformal radius is now $a(t) = a^*(t)A$, where A is the conformal radius of the map $g(\zeta)$. The series in equation (5.4.3) is then truncated at N terms and solved using *ode15i*. Note the SC Toolbox need only be used once at the start of the numerical simulation. Figure 5.4 shows the evolution of two non-Laurent shapes found using this method: a square and a blade (Gopal and Trefethen, 2019b), which both expand and smooth towards a circular shape, as expected.

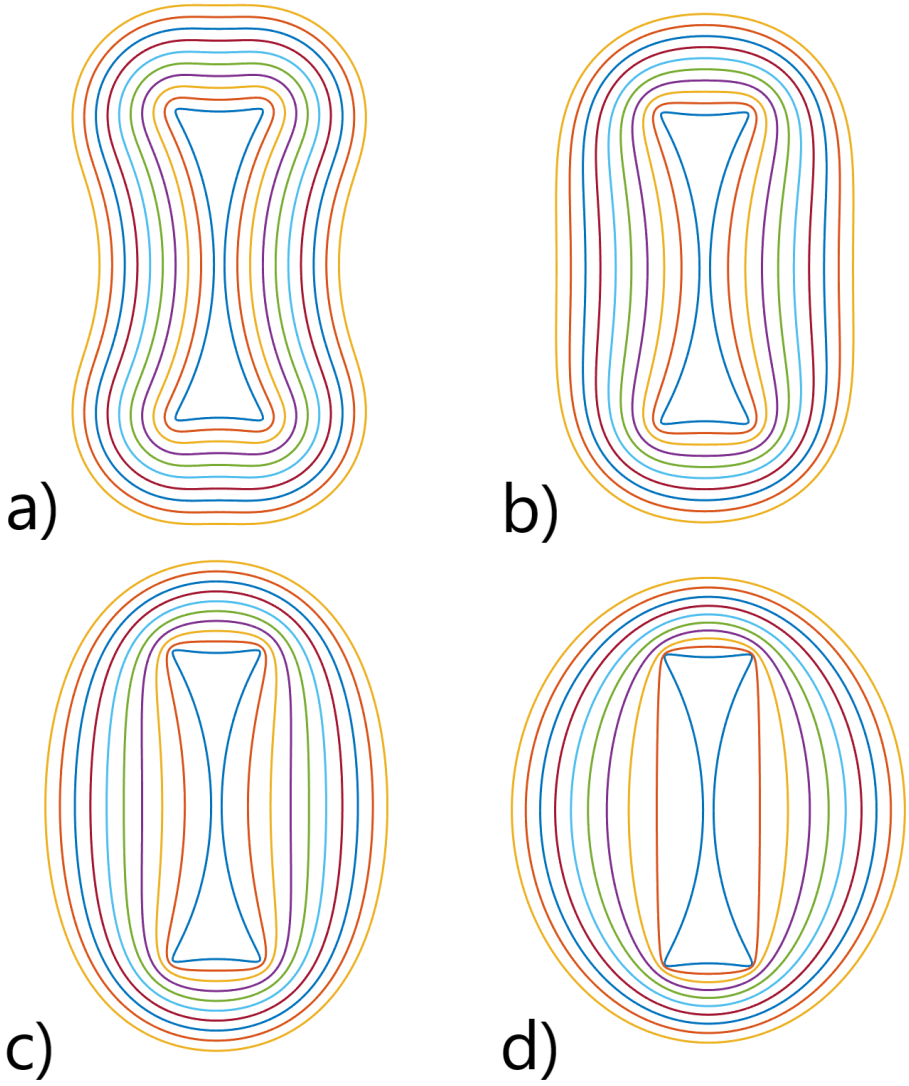

Figure 5.5: Growth of an hourglass from $t = 0$ to $t = 1$, series truncation $N = 128$, under the general growth law equation (5.4.5) where a) $\alpha = 0.1$, b) $\alpha = 0.5$, c) $\alpha = 1$, d) $\alpha = 2$.

The numerical method can also be used to find solutions to a more general growth law

$$v_n = -\left[a\left(\frac{\partial T}{\partial n}\right)\right]^{-\alpha}, \tag{5.4.4}$$

where the constant $\alpha > 0$ is chosen to be positive for stability. In this case, the PG equation becomes

$$a^{\alpha}\,\mathrm{Re}\left[f_t\overline{\zeta f_\zeta}\right] = |f_\zeta|^{1+\alpha}. \tag{5.4.5}$$

It is straightforward to show that a circle with $\dot{a} = 1$ is an exact solution of equation (5.4.5) for all α. However, additional exact solutions (e.g. ellipses, lemniscates) have not been found for $\alpha \neq 1$. Figure 5.5 shows the evolution of an hourglass with Laurent series truncation $N = 128$ from $t = 0$ to $t = 1$ under

different values of α: $0.1, 0.5, 1$ and 2. It is observed that, for larger values of α, the hourglass evolves into a circular shape more quickly than for smaller values. Comparing figures 5.5a and 5.5d shows this most clearly: the final free boundary shape in figure 5.5a still resembles the initial hourglass shape whereas the final shape of figure 5.5d is almost a circle.

5.5 Relation to the spread of wildfires

In the context of wildfire growth, the free boundary problem with reciprocal growth law has two appealing features. First, it does not impose an ad-hoc constant ROS; rather the ROS is deterministic, depending on the gradient of the harmonic function T in the unburnt region Ω via the growth law equation (5.1.1). The quantity T can be thought of as temperature which is hottest $T = 0$ (using dimensionless quantities) at the fire line $\partial\Omega$ where it can be considered as the combustion temperature of the surrounding fuel. Away from the fire line, the temperature decreases such that $T \to -\infty$ as $r \to \infty$. Although this unbounded limit in T is physically unrealistic, the slow logarithmic decay in T in the vicinity of the fire line is the important property in this model. Since T is harmonic, its behaviour can be interpreted physically as the diffusion of heat. While it should be cautioned that there is no observational evidence that wildfires are driven diffusively, some wildfire models do explicitly include diffusive terms for heat in the vicinity of the fire line, see e.g. Weber (1991).

Second, the model mimics the effect of curvature from Ch.2 - as will be seen in Ch.6, the pyrogenic wind also produces an analogous effect. In particular, the growth of the fire line is enhanced near concave regions in comparison to convex regions. This property is evident in figure 5.2c and figure 5.3 which show concave (indented) regions evolving more rapidly and the fire line becoming more circular as time increases. Physically, the fire grows by intense (diffusive) heating of surrounding unburnt fuel which warm until they reach the ignition temperature $T = 0$. Temperature contours in the unburnt region are closer in convex regions, resulting in a larger heat gradient there. Since the fire line progresses to the contour $T = 0$ at the same instant, it does so at a greater normal velocity in the regions where the temperature gradient is less, as modelled by the reciprocal growth law. Note that the inclusion of the conformal radius factor in equation (5.1.1) does not affect the geometric evolution of the free boundary, merely how quickly it evolves. This implies that the rate of change of the conformal radius with time is constant, analogous to the concept that, in the absence of other effects such as wind and curvature, the wildfire ROS is constant as supposed in, e.g. Anderson et al. (1982); Hilton et al. (2016, 2018).

To test whether the free boundary problem with reciprocal growth law is able to model aspects of wildfire spread, numerical results are compared against both experimental fire data and against the outputs

of an existing wildfire spread model, namely the pyrogenic potential model developed in Hilton et al. (2018). As suggested by its name, this model attributes the stabilising behaviour of wildfire spread to the convective effect of the self-induced pyrogenic wind. With good success, Hilton et al. (2018) compare their model outputs to a number of experiments performed in the CSIRO Pyrotron - the full details of these experiments are given in Sullivan et al. (2019). The results of figure 7 of Hilton et al. (2018) - the development of a V-shaped junction fire at angle $\theta = \pi/2$ - are considered and compared against in this chapter.

One numerical approach would be to find the conformal map $g(\zeta)$ of the initial junction fire using the SC Toolbox, then use the *ode*15*i* method for the resulting map in equation (5.4.3) as outlined in Sect.5.4. Alternatively, consider the work of Derrida and Hakim (1992) which presents the conformal map from the unit $\zeta-$disk to a general 'star shape' of n needles – see their equation (4). A junction fire is visually similar to the case of $n = 2$ competing needles with angle $\theta \leq \pi$ between them. However, in order to have a domain enclosed by a smooth free boundary with non-zero area for use in the numerical method, an inflated V-shape is desired instead of the two needle shape. This is achieved by taking the conformal map from a disk of radius $B = (1 + \epsilon)$, where $0 < \epsilon \ll 1$, as opposed to the unit disk. In other words, the unit $\zeta-$disk is mapped to the $B-$disk, which is then mapped to the inflated V-shape. This means that the conformal map from the exterior of the unit $\zeta-$disk to the exterior of the inflated V-shape is given by the first term on the RHS of the following

$$z = f(\zeta, t) = a(t)\zeta\left(1 - \frac{1}{B\zeta}\right)^{\beta}\left(1 - \frac{e^{i\pi}}{B\zeta}\right)^{2-\beta} + \sum_{k=0}^{\infty} c_k(t)\zeta^{-k}, \tag{5.5.1}$$

where $\beta = \theta/\pi$ (Derrida and Hakim, 1992) and the conformal radius of the map equation (5.5.1) is $a(t)$. The second term on the RHS involving the power series with coefficients $c_k(t)$, which vanish at $t = 0$, accounts for the deviation from the initial shape as time increases, similar to equation (5.4.3).

The experiments of Hilton et al. (2018) are performed in the presence of a unidirectional, constant strength ambient wind $\boldsymbol{u}_a$. Assuming the fire line responds purely in an advective manner to such winds, their effect is easily incorporated into the present model by writing

$$v_n = \max\left(0,\ -\left[a\left(\frac{\partial T}{\partial n}\right)\right]^{-1} + \lambda\hat{\boldsymbol{n}} \cdot \boldsymbol{u}_a\right), \tag{5.5.2}$$

with resulting PG equation

$$a\,\mathrm{Re}\left[f_t\overline{\zeta f_\zeta}\right] = \max\left(0,\ |f_\zeta|^2 - \lambda\,\mathrm{Re}\left[\zeta f_\zeta \overline{u_a}\right]\right), \tag{5.5.3}$$

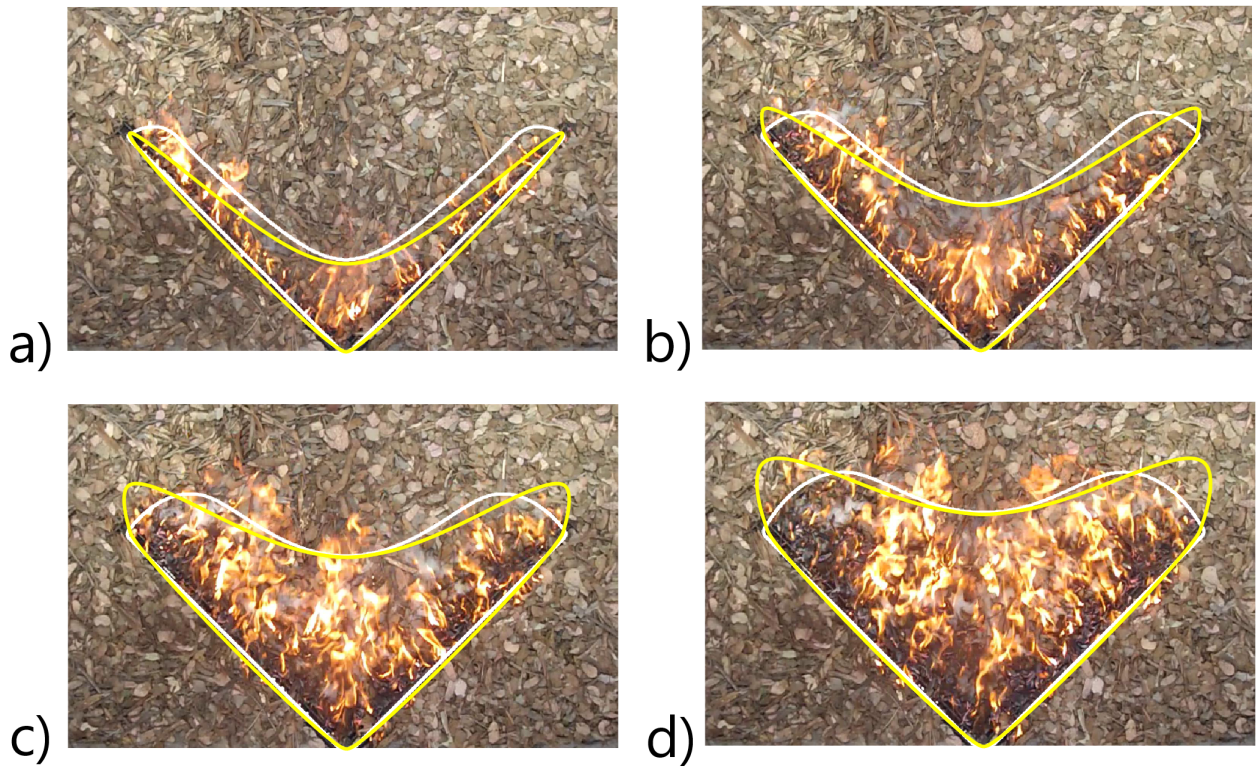

Figure 5.6: Comparison with a junction fire in the presence of an ambient wind flowing in the positive imaginary $z-$direction. In each figure, the background image is the experimental fire (Sullivan et al., 2019), the white curve is the output from the pyrogenic potential model (Hilton et al., 2018) and the yellow curve is the output from the model in this chapter (equation (5.5.3)). Each figure shows the fire at dimensional time t in seconds, where a) $t = 5$, b) $t = 10$, c) $t = 15$, d) $t = 20$.

where u_a is the complex representation of the ambient wind vector $\boldsymbol{u}_a$ and the constant $\lambda = 3$ is here chosen to match with experimental data from Hilton et al. (2018); Sullivan et al. (2019). The RHS of equation (5.5.3) has been modified such that the normal velocity v_n is non-negative. Physically, this enforces the entropy condition (Sethian, 1985) as explained in e.g. Ch.2.

Figure 5.6 shows the comparison between the experimental fire data in Sullivan et al. (2019) (background image), results from the pyrogenic potential model in Hilton et al. (2018) (white curve) and the results from the model of this chapter (yellow curve) at times $t = 5, 10, 15$ and 20 seconds. The constant ambient wind flows in the positive imaginary $z-$direction, with the section of the fire line facing the oncoming wind identified as the windward side and the opposing side as the leeward side. It is noted that the windward side propagates very little, if at all. In this chapter, it is simply assumed that the ambient wind is strong enough to halt the wildfire spread on the windward side. This assumption is explored further in Ch.6 where it is hypothesised that the ambient wind is strong enough to stop wildfire spread by convection but not by radiation.

The behaviour at the tips of the junction fire is quite different between the pyrogenic model and the model

of this work, particularly in figure 5.6d. This is likely due to the approximation of the initial junction fire as an inflated V-shape, resulting in the initial shapes differing in figure 5.6a. Additionally, there may be some discrepancies between how the curvature/pyrogenic wind effect and the diffusive heat effect act on the tips and the time scales over which they do so. In general, however, both models reproduce the experimental fire line well, especially in the trough region of the leeward side.

Finally, it is worth speculating on the relevance of the reciprocal growth law to wildfire spread. Adjacent to the fire line, intense heating causes surrounding unburnt fuel to warm until it reaches the ignition temperature T_i; this is the mechanism by which the wildfire grows. Given that the heating is diffusive, contours of temperature in the unburnt region are such that they are closer together in convex regions and further apart in concave regions. For example, the contour on which T_i is constant will be further from the fire line in the trough region than it is at the tips in figure 5.6. Hence, close to the fire line, the heat gradient is larger in the convex regions than in concave regions. Since the fire line progresses to the contour T_i at the same instant, it does so at a greater normal velocity in the regions where the temperature gradient is less. Indeed, the reciprocal law models this behaviour.

5.6 Discussion

In this chapter, the idea of finding a deterministic rate of spread law, rather than imposing the basic ROS, is explored. It is speculated that wildfire growth bears some resemblance to the free boundary growth problem in which the normal velocity of the boundary is the reciprocal of the gradient of the harmonic function with a logarithmic singularity at infinity. This reciprocal growth free boundary problem is studied in detail with elliptical and lemniscatic boundaries found to be exact solutions. These are found by formulating the problem as a PG type equation in terms of the conformal map from the exterior of the unit disk to the exterior of the growing free boundary. This method additionally provides the basis for the numerical approach, enabling the evolution of more general initial shapes, and more general growth laws, to be computed.

To conclude, let us speculate whether this reciprocal growth law is indeed a good model for wildfire spread. On the one hand, it provides a dynamical model for the rate of spread of the fire line based on the solid physical foundations of diffusive heat transfer when realising the harmonic function T to be the temperature. The model also reproduces the stabilising behaviour of convex and concave portions of the fire line as in the model of Ch.2 and the upcoming model of Ch.6. There is also reasonable agreement of the model outputs to experimental data as shown in figure 5.6. On the other hand, there is no empirical evidence that (to leading order) wildfires are driven diffusively. The diffusive smoothing that occurs may

be subtly different to, for example, the advective stabilising effect of the pyrogenic wind. Additionally, there is currently no coupling in the model of the temperature field to an ambient wind, which would add significant complexity to the model and perhaps affect the results. Therefore, further research is required in these areas to fully assess the relevance of the reciprocal growth law in modelling wildfire spread. Furthermore, consider the generalised growth law in equation (5.4.5): other choices of $\alpha > 0$ also qualitatively reproduce the stabilising fire line behaviour seen in figure 5.6. Thus further investigation is also required to determine which choice of α would best model the wildfire spread.

Chapter 6

Single wildfire model

In this chapter, the wildfire model of Ch.3 is extended to incorporate the effect of wind. There are two components to this: a constant, unidirectional ambient wind and the pyrogenic (or fire) wind which is induced by the wildfire itself. Note that the pyrogenic wind was present in Ch.3: it was responsible for the advection of oxygen to the fire line. However, the direct effect of the pyrogenic wind on the wildfire propagation was not considered - it is in this chapter. The work in this chapter was completed in Harris and McDonald (2024a).

6.1 Model setup

Consider a single wildfire spreading under the conditions and assumptions stated in Sect.2.1: this is illustrated in figure 6.1. The normal velocity v_n of the fire line curve γ separating the burnt R and unburnt Ω regions is sought. While various factors can affect the wildfire spread, as noted in Ch.1 and as showcased in the wildfire model of Ch.3, only the three effects of highest order are considered in this chapter: the basic ROS, the ambient wind and the pyrogenic wind.

The basic ROS term v_0 was introduced in Ch.2 and represents the physical, chemical and thermodynamic processes involved in fuel ignition and heat transfer. While it was speculated in Ch.5 that the value of v_0 could be found deterministically, further research beyond the scope of this PhD thesis is required before being able to confidently include such a mechanism into the wildfire model. Therefore, it is taken in this chapter that the basic ROS is some given constant, the exact value of which shall not be investigated in this thesis and remains an open question (see the review articles by e.g. Sullivan (2009a) and Morvan et al. (2022)). As convective wind effects are also considered in this chapter, the basic ROS shall here be split

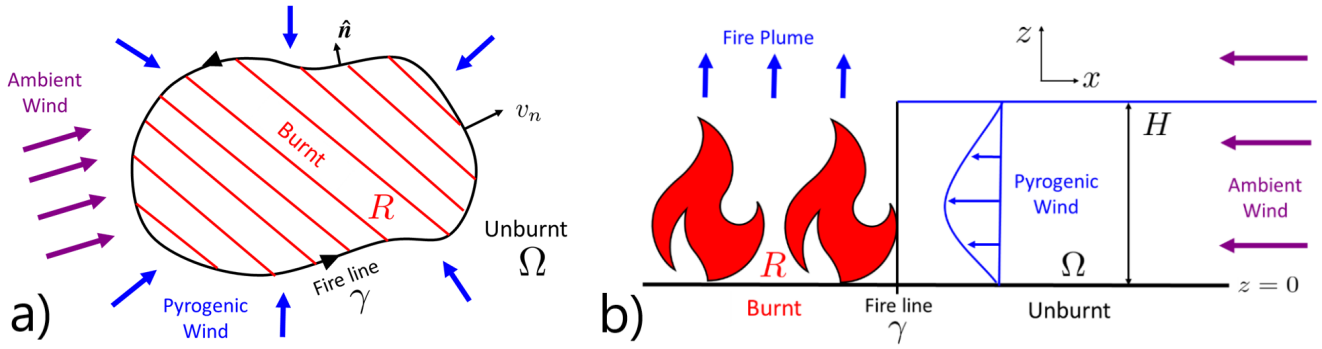

Figure 6.1: The single wildfire model (a) plan view, (b) side view. The blue arrows represent the direction of the pyrogenic (fire) wind and the purple arrows the direction of an ambient wind.

into its radiative and convective components[1] as $v_0 = \alpha v_0 + (1-\alpha)v_0$ where $\alpha \in [0,1]$ is a given constant representing the proportion of the basic ROS relating to radiative effects (similarly $(1-\alpha)$ represents the convective effect). This explicit distinction between radiative and convective terms has been similarly proposed in previous literature. For example, the work of Beer (1991) evaluates the energetics of each distinct heat transfer mechanism in fire spread and a similar dimensionless parameter P representing the ratio of radiative heating by the flame and convective cooling of the fuel bed was introduced in Baines (1990). A thorough analysis into the value of α is also not performed in this thesis.

There is a unidirectional, constant strength ambient wind $\boldsymbol{u}_a = U_a \hat{\boldsymbol{u}}_a$ present, of magnitude $U_a \text{ms}^{-1}$ and dimensionless, unit direction $\hat{\boldsymbol{u}}_a$. It is assumed that the fire line γ is entirely permeable to this ambient wind, thus all sections of the fire line experience the same (constant) ambient wind effect. The side of the fire line facing the oncoming ambient wind is labelled as the windward side and the opposite side as the leeward side. Additionally, the wildfire itself generates a pyrogenic (or fire) wind $\boldsymbol{u}_p$ (Trelles and Pagni, 1997; Lareau and Clements, 2017; Thomas et al., 2017; Hilton et al., 2018; Sullivan et al., 2019) driven by the fire plume, the dynamics of which are detailed in Ch.3. The overall wind vector can then simply be written as the linear combination of the ambient and pyrogenic winds $\boldsymbol{u} = \boldsymbol{u}_p + \boldsymbol{u}_a$.

While the basic ROS and ambient wind $\boldsymbol{u}_a$ have purely kinematic effects on the fire line evolution, the pyrogenic wind is dynamical as it is determined by the shape of the fire line. Thus the co-evolution of $\boldsymbol{u}_p$ and the fire line represent a nonlinear, two-dimensional free boundary problem. With the introduction of an ambient wind, some further simplifying assumptions are made. First, the ambient wind is such that it is not deviated by the fire plume (the permeability assumption mentioned above). Second, any (vertical) deviations of the fire plume induced by the ambient wind do not affect the fire spread at the horizontal, surface plane. Third, the strength Q of the fire plume is assumed constant for all time in this chapter,

[1] It is assumed that conductive effects are sufficiently weak that they can be neglected.

yet such an extension to a time varying plume strength as detailed in Ch.3 is plausible.

While the basic ROS and ambient wind are given constants, the pyrogenic wind must be solved in the fire line exterior Ω for the evolving fire line γ. The same governing equation, boundary and far field conditions from Ch.3 are here used: the velocity potential ϕ, where $\boldsymbol{u}_p = \boldsymbol{\nabla}\phi$, satisfies the Laplace equation

$$\nabla^2\phi = 0 \quad \text{in } \Omega. \tag{6.1.1}$$

Recall the Reynolds number $\mathrm{Re} = UH/D$, where H is the shallow flame height, U is the representative pyrogenic wind speed and D is its horizontal (momentum) diffusivity. From figure 6 of Bebieva et al. (2020) and table III of Beer (1991) using a representative ambient wind speed of $U_a = 1\mathrm{ms}^{-1}$, it follows that $U = 0.5\mathrm{ms}^{-1}$, $H = 0.5\mathrm{m}$ and $D = 1\mathrm{m}^2\mathrm{s}^{-1}$ and so $\mathrm{Re} \approx 0.25$. Thus the shallow pyrogenic wind flow is of sufficiently low Reynolds number here such that the Navier-Stokes equations reduce to Stokes flow. Following the reasoning in Ch.3, the velocity potential ϕ is thus proportional to the negative pressure $-p$ and the boundary condition $p = \phi = 0$ holds on γ without loss of generality. In the far field, the fire plume is observed as an effective sink of strength Q and thus $\phi \to -(Q/2\pi)\log r$ as $r \to \infty$. Note that Hilton et al. (2018) treat the fire plume differently, instead solving an additional Poisson equation in the burnt region R dependent on the upwards air flow $\nu = -w_z$. As shown in Ch.7, the formulation of the pyrogenic wind used here gives similar quantitative results and matching with experimental data as in Hilton et al. (2018).

Following the wildfire model of Hilton et al. (2018), the equation for v_n is now formulated as

$$Av_n = v_0 + \tilde{\beta}\hat{\boldsymbol{n}} \cdot \boldsymbol{\nabla}\phi + \tilde{\lambda}\hat{\boldsymbol{n}} \cdot \boldsymbol{u}_a, \tag{6.1.2}$$

where $\tilde{\beta}$, $\tilde{\lambda}$ are dimensional constants and A is a non-dimensional constant found *a posteriori* when comparing the wildfire propagation with experimental data - see Sect.7.5. When comparing equation (6.1.2) with the previous wildfire model equation (3.1.1) from Ch.3, there are two important omissions to note. First, the oxygen effect is here neglected as it is assumed to be of sufficiently lower order than the wind effects, which are the focus of this chapter. Considering the transport of oxygen through the combined wind vector rather than simply the pyrogenic wind is also non-trivial and beyond the scope of this thesis.

Second is the curvature effect. It was postulated in Ch.2, Ch.3 and the works of e.g. Sharples et al. (2013); Sharples and Hilton (2017) that curvature was responsible for the stabilisation of the fire line, with such curvature-based models having successfully reproduced stabilising fire behaviour, for example that of junction fires. However, it was introduced in e.g. Hilton et al. (2018) that the pyrogenic wind produced an

analogous stabilising effect. Moreover, the pyrogenic wind could recreate the interaction between disjoint wildfires whereas the curvature effect could not. Thomas et al. (2017) and Thomas (2019) performed a thorough investigation into the relative importance of the curvature effect in governing the rate of spread of a wildfire and found that, on both large and small scales, there was a negligible relation. Therefore, it was concluded that the curvature effect was simply a 'proxy' for pyrogenic wind (Speer and Goodrick, 2022; Sharples et al., 2022) and so curvature was dropped from the model of Hilton et al. (2018). It is noted that the curvature effect is still physically meaningful: it is analogous to the intensified radiative heat transfer ahead of concave fire line regions. This process is not captured by the pyrogenic wind effect, which is purely convective. Moreover, the analysis performed in Thomas (2019) uses the wildfire simulator WRF-Fire which, as the authors acknowledge, includes only convective and not radiative effects. Nevertheless, it is still concluded that the curvature effect is of lower magnitude than that of pyrogenic wind and hence the curvature is largely omitted from the wildfire model of this chapter. However, a low order ($\mathcal{O}(10^{-1})$) curvature effect is still included in some 'extreme' wildfire geometries to provide added numerical stability - see Sect.6.3.

One final modification must be made to equation (6.1.2) to ensure the fire line satisfies the entropy condition (Sethian, 1985) that $v_n \geq 0$, as introduced in Ch.2. The radiative proportion of the basic ROS αv_0 satisfies this automatically. However, the convective effects of the basic ROS $(1-\alpha)v_0$, the pyrogenic wind $\boldsymbol{u}_p$ and the ambient wind $\boldsymbol{u}_a$ may be large and negative, especially on the windward side of the fire. This wind may be sufficiently strong to stop wildfire spread by convection (not radiation) but not so strong as to push the fire line backwards, which is nonphysical. Therefore, equation (6.1.2) is modified as

$$Av_n = \alpha v_0 + \max[0, (1-\alpha)v_0 + \tilde{\beta}\hat{\boldsymbol{n}} \cdot \boldsymbol{\nabla}\phi + \tilde{\lambda}\hat{\boldsymbol{n}} \cdot \boldsymbol{u}_a], \tag{6.1.3}$$

ensuring that convective (wind) terms have a non-negative effect on the fire line velocity.

6.1.1 Non-dimensionalisation

Non-dimensional quantities are introduced by scaling with respect to a characteristic velocity and length: the basic ROS velocity v_0 and the initial wildfire radius $R_0 = R(0)$. In particular, R_0 is the conformal radius (Bazant and Crowdy, 2005) as used in Ch.3 and in conjunction with the conformal mapping method in Sect.6.2. The pyrogenic potential is also scaled by Q, the (constant) strength of the fire plume. The resulting (starred) dimensionless variables are

$$\boldsymbol{x} = R_0\boldsymbol{x}^*, \quad t = \frac{AR_0}{v_0}t^*, \quad \boldsymbol{\nabla} = \frac{1}{R_0}\boldsymbol{\nabla}^*, \quad \phi = \frac{Q}{2\pi}\phi^*. \tag{6.1.4}$$

Dropping stars immediately, the normal velocity equation (6.1.3) becomes

$$v_n = \alpha + \max[0,\ (1-\alpha) + \beta \hat{\boldsymbol{n}} \cdot \boldsymbol{\nabla}\phi + \lambda \hat{\boldsymbol{n}} \cdot \boldsymbol{u}_a]. \tag{6.1.5}$$

where the new dimensionless parameters are

$$\beta = \frac{\tilde{\beta}\left(\frac{Q}{2\pi R_0}\right)}{v_0} = \frac{\tilde{\beta} U_p}{v_0}, \quad \lambda = \frac{\tilde{\lambda} U_a}{v_0}. \tag{6.1.6}$$

Note the labelling $U_p = Q/2\pi R_0$: this is the dimensional magnitude of the pyrogenic wind. The full non-dimensional system governing the motion of the fire line γ is thus given by

$$v_n = \alpha + \max[0,\ (1-\alpha) + \beta \hat{\boldsymbol{n}} \cdot \boldsymbol{\nabla}\phi + \lambda \hat{\boldsymbol{n}} \cdot \hat{\boldsymbol{u}}_a] \quad \text{on } \gamma, \tag{6.1.7}$$

$$\nabla^2 \phi = 0 \quad \text{in } \Omega, \tag{6.1.8}$$

$$\phi = 0 \quad \text{on } \gamma, \tag{6.1.9}$$

$$\phi \to -\log r \quad \text{as } r \to \infty. \tag{6.1.10}$$

Finally, consider the relative magnitudes of the parameters in equation (6.1.7) by comparing with the values used in Hilton et al. (2018) and observations made in Beer (1991). Wind is the dominant effect and so $\beta, \lambda = \mathcal{O}(10)$, though some $\mathcal{O}(1)$ values may be used in this work for illustrative purposes. By comparing the values of fire and ambient ('mid-flame') winds from Table III of Beer (1991), it is assumed that $\lambda \approx 2\beta$. Similarly from their Table II, comparing convective and non-convective (radiative) heat fluxes in the absence of an ambient wind gives an approximate value of $\alpha \approx 0.5$. Unless stated otherwise, these parameter values will be used throughout this chapter.

6.2 Conformal mapping numerical method

The two-dimensional wildfire problem can once again be formulated in the complex $z = x + iy$ plane and a conformal mapping method such as the one used in e.g. Ch.3 can be applied. The conformal map $z = f(\zeta, t)$ from the interior/exterior of the unit $\zeta-$disk to the exterior of the fire line γ in the $z-$plane is then to be found. As in Ch.2 and Ch.5, the conformal map for Laurent shapes is the truncated Laurent series

$$z = f(\zeta, t) = a_{-1}(t)\zeta + \sum_{k=0}^{N} c_k(t)\zeta^{-k}, \tag{6.2.1}$$

where $a_{-1}(0)$ is the initial conformal radius R_0 of the wildfire as defined in Sect.6.1.1 and $c_k(t) = a_k(t) + ib_k(t)$ are some complex functions in time. For general non-Laurent shapes, equation (6.2.1) is a poor approximation of the fire line and so the conformal map is instead

$$z = f(\zeta, t) = a_{-1}(t)g(\zeta) + \sum_{k=0}^{N} c_k(t)\zeta^k, \tag{6.2.2}$$

where $g(\zeta)$ is the initial conformal map of the fire line computed with the SC Toolbox (Driscoll, 2005) with $a_{-1}(0) = 1$ and $c_k(0) = 0$, $\forall k$. The initial conformal radius R_0 is now $a_{-1}(0)A$ where A is the conformal radius of the map g. Note that the Laurent map equation (6.2.1) transforms the exterior of the unit $\zeta-$disk to the exterior of the fire line γ, whereas equation (6.2.2) maps the interior to the exterior. In both cases, the power series is truncated at N terms to give $n = 2N + 3$ unknown real functions in time to be found: $a_{-1}(t)$, $a_k(t)$ and $b_k(t)$.

The system of equations (6.1.7) to (6.1.10) is converted to a PG type equation, then n points selected around the unit $\zeta-$disk to give a system of n ODEs in time to be solved using the MATLAB routine *ode15i*. The Laplace equation (6.1.8) and the Dirichlet boundary condition equation (6.1.9) are conformally invariant and thus the pyrogenic potential ϕ can be solved exactly in the $\zeta-$plane as

$$\phi(\zeta) = -\log|\zeta|. \tag{6.2.3}$$

Recall also the following relations from Dallaston and McCue (2013) used in Ch.3

$$v_n = \frac{\mathrm{Re}\Big(f_t\overline{\zeta f_\zeta}\Big)}{|f_\zeta|}, \qquad n = \frac{\zeta f_\zeta}{|f_\zeta|}, \tag{6.2.4}$$

where $n = n_x + in_y$ is the complex representation of the outward unit normal vector in the $z-$plane. The pyrogenic wind contribution in equation (6.1.7) can be written as

$$\hat{\boldsymbol{n}} \cdot \boldsymbol{\nabla}\phi = \frac{\partial\phi}{\partial n} = \mathrm{Re}[n\overline{\nabla}\phi] = 2\mathrm{Re}\left[n\frac{\partial\phi}{\partial z}\right] = -\frac{1}{|f_\zeta|} \quad \text{on } |\zeta| = 1, \tag{6.2.5}$$

where $\overline{\nabla} = \partial_x - i\partial_y$. This uses the exact solution equation (6.2.3) and the equivalence $|\zeta| = (\zeta\overline{\zeta})^{1/2}$ such that $\partial\phi/\partial\zeta = -1/(2\zeta)$ on the unit $\zeta-$disk: $|\zeta| = 1$. Similarly, the ambient wind contribution is

$$\hat{\boldsymbol{n}} \cdot \hat{\boldsymbol{u}}_a = \mathrm{Re}[n\ \overline{u_a}] = \frac{1}{|f_\zeta|}\mathrm{Re}\Big[\zeta f_\zeta\overline{u_a}\Big] \quad \text{on } |\zeta| = 1, \tag{6.2.6}$$

where u_a is the unit ambient wind vector written in complex notation. Thus the PG type equation

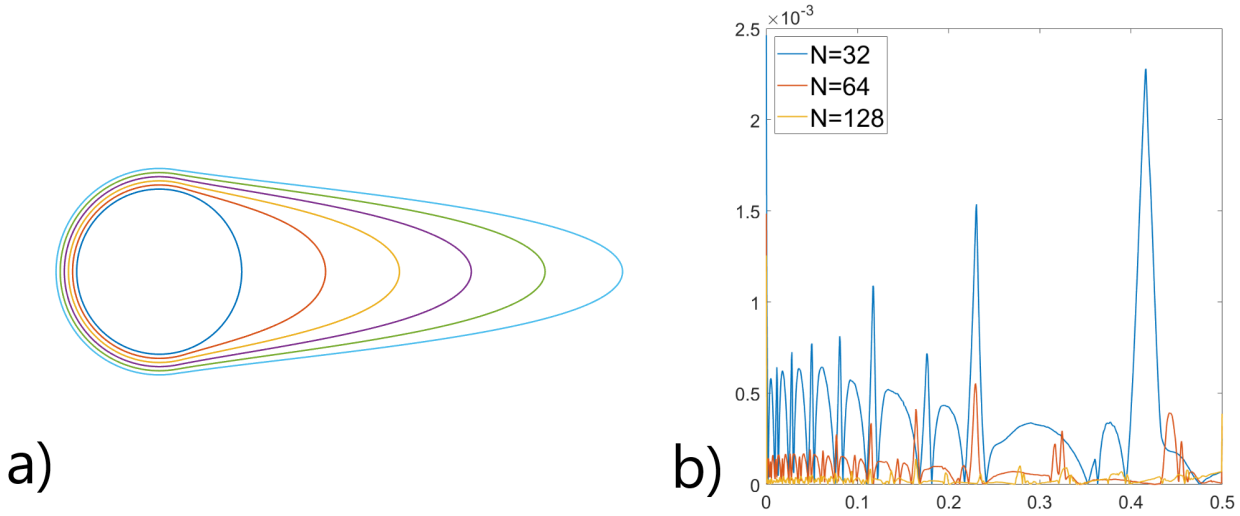

Figure 6.2: (a) Evolution of an initially circular wildfire between $t = [0, 0.5]$ in a uniform ambient wind of unit strength in the positive real z direction. The pyrogenic and ambient wind parameters are $\beta = 10$ and $\lambda = 20$ and the Laurent series truncation is $N = 128$. Six isochrones at equal time increments are plotted. (b) Relative error of the RCA law of the wildfire in (a) with Laurent series truncations $N = 32, 64$ and 128.

is

$$\mathrm{Re}\Big(f_t\overline{\zeta f_\zeta}\Big) = \alpha|f_\zeta| + \max\Big[0,\ (1-\alpha)|f_\zeta| - \beta + \lambda\mathrm{Re}\big(\zeta f_\zeta\overline{u_a}\big)\Big]. \tag{6.2.7}$$

6.2.1 Rate of change of area law

Following the approach to derive similar laws in Ch.2 and Ch.3, an expression for the rate of change of the area $A(t)$ enclosed by the fire line $\gamma(t)$ can be derived, referred to as the rate of change of area (RCA) law. The RCA law can then be used to check the upcoming numerical results. By integrating the velocity v_n over the curve γ and substituting equation (6.1.7), the RCA is given by

$$\frac{\mathrm{d}A}{\mathrm{d}t} = \int_\gamma v_n \mathrm{d}s = \alpha\int_\gamma \mathrm{d}s + \int_\gamma \max[0,\ (1-\alpha) + \beta\hat{\boldsymbol{n}}\cdot\boldsymbol{\nabla}\phi + \lambda\hat{\boldsymbol{n}}\cdot\hat{\boldsymbol{u}}_a]\mathrm{d}s. \tag{6.2.8}$$

By definition, the first term on the RHS is the length $L(t)$ of the fire line curve γ. The second term is converted to the $\zeta-$plane by integrating along the unit disk $\zeta = e^{i\theta}$ for $\theta \in [0, 2\pi)$, thus $\mathrm{d}s = |f_\zeta|\mathrm{d}\theta$ where f is the conformal map. Using equations (6.2.5) and (6.2.6) gives the RCA law

$$\frac{\mathrm{d}A}{\mathrm{d}t} = \alpha L(t) + \int_0^{2\pi} \max\Big[0,\ (1-\alpha)|f_\zeta| - \beta + \lambda\mathrm{Re}\big[\zeta f_\zeta\overline{u_a}\big]\Big]\mathrm{d}\theta. \tag{6.2.9}$$

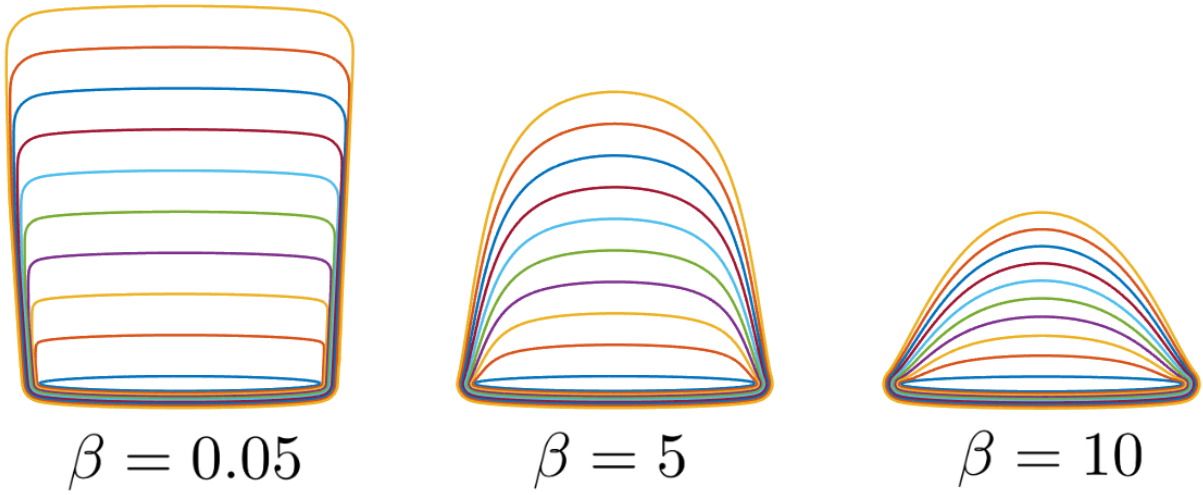

Figure 6.3: Evaluating the effect of pyrogenic wind. Three line fires (approximated by thin ellipses) spread in the presence of a uniform, unit strength ambient wind flowing in the positive imaginary z direction. The ambient and pyrogenic wind parameters are $\lambda = 10$ and (a) $\beta = 0.05$, (b) $\beta = 5$ and (c) $\beta = 10$. In each figure, ten isochrones at equal time increments are plotted.

6.3 Results

Consider the simplest case of an initially circular wildfire with unit radius in a uniform ambient wind of strength $U_a = 1$ in the real z direction. The pyrogenic and ambient wind parameters are $\beta = 10$ and $\lambda = 20$, respectively, and the wildfire evolves for $t = [0, 0.5]$. The circle is a Laurent shape and thus equation (6.2.1) is a good approximation for the conformal map $z = f(\zeta, t)$, with a series truncation $N = 128$ chosen. Figure 6.2a shows the wildfire evolution where six isochrones (the initial fire line and five time steps at equal time intervals) have been plotted. The evolution of the fire line is as expected: the windward side grows solely due to the (radiative) basic ROS whereas growth on the leeward side is amplified in the direction of the ambient wind and rounded into the signature parabolic shape by the pyrogenic wind (Sharples et al., 2022). The relative error (RE) of the RCA law equation (6.2.9) - see Sect.6.2.1 - is computed over time and presented in figure 6.2b for the wildfire problem in figure 6.2a with Laurent series truncations of $N = 32$, 64 and 128. As expected, this error decreases as the series truncation is increased: the average RE is of $\mathcal{O}(10^{-3})$ for $N = 32$ and of $\mathcal{O}(10^{-5})$ for $N = 128$. The truncation $N = 128$ is thus used for all future results unless stated otherwise.

Following Hilton et al. (2018) - see their figure 3 - the effect of the pyrogenic wind on the fire line propagation is investigated. Consider a straight line fire perpendicular to an ambient wind flowing in the imaginary z direction. The initial line fire is approximated by a thin ellipse with Laurent conformal map equation (6.2.1) where $a_{-1}(0) = 1$, $c_1(0) = 0.9$ and $c_k(0) = 0$ for all remaining $k \in [0, 128]$. The fire line evolves for $t = [0, 0.5]$ for a constant ambient wind parameter $\lambda = 10$ and varying pyrogenic wind

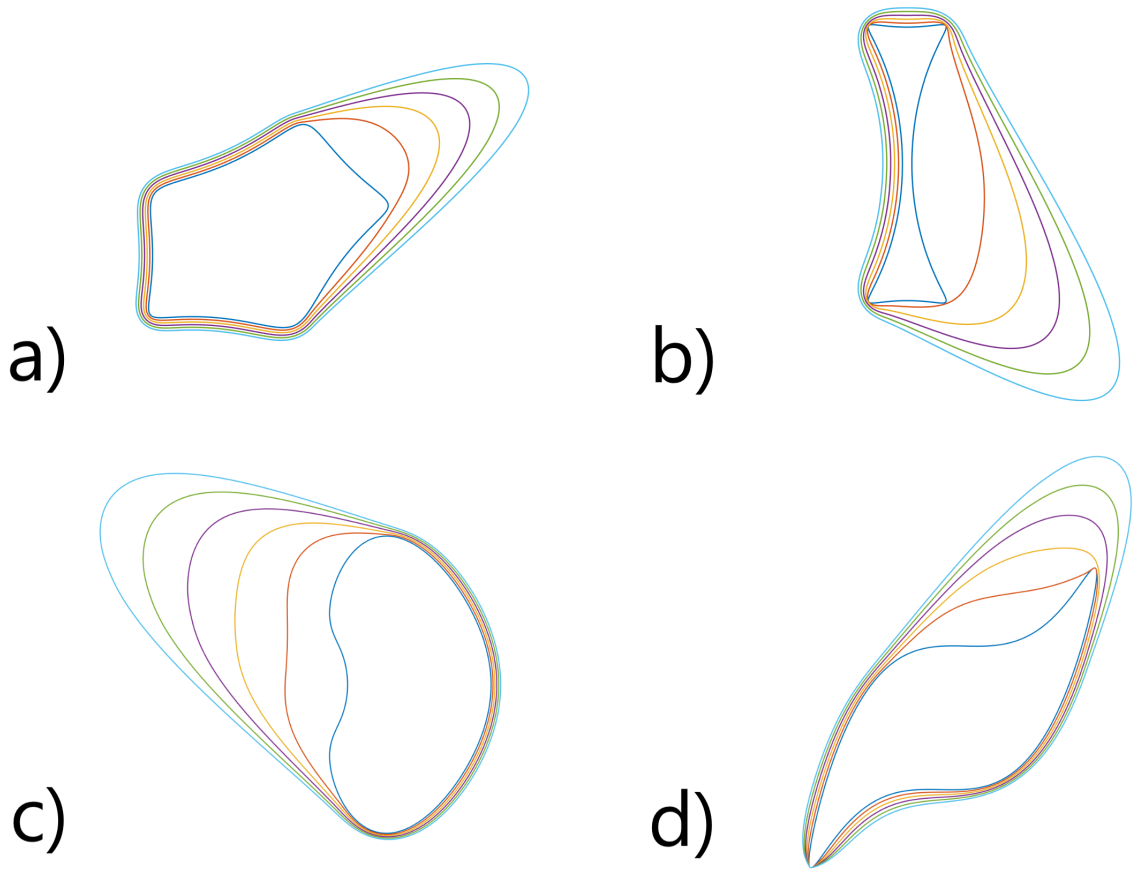

Figure 6.4: Fire line evolution of Laurent (a,b) and non-Laurent (c,d) shapes under a constant ambient wind of strength $U = 1$ at angle θ to the horizontal (real axis). (a) Irregular pentagonal fire, $\beta = 10$, $\lambda = 20$, $\theta = \pi/6$, $t = [0, 0.25]$. (b) Hourglass fire, $\beta = 18$, $\lambda = 25$, $\theta = -\pi/4$, $t = [0, 0.4]$. (c) Bean fire, $\beta = 10$, $\lambda = 20$, $\theta = 5\pi/6$, $t = [0, 0.2]$. (d) Blade fire, $\beta = 6$, $\lambda = 15$, $\theta = \pi/3$, $t = [0, 0.2]$.

effects $\beta = 0.05, 5$ and 10. The isochrones of these three experiments are given in figures 6.3a, b and c, respectively. In agreement with the results of Hilton et al. (2018), it is found that a stronger pyrogenic wind effect causes an increased rounding of the leeward fire line edge into a more pronounced parabolic shape. Additionally, the fire line head does not propagate as far under stronger pyrogenic winds.

Figure 6.4 shows the evolution of a variety of initial Laurent and non-Laurent fire line shapes under the influence of different ambient wind directions and wildfire parameter values - these are given in the figure caption. Figures 6.4a,b are Laurent shapes: an irregular pentagon and an hourglass, respectively. These shapes and their initial Laurent coefficients come from Rycroft and Bazant (2016), see their figures 5a and 7a, respectively. The remaining figures 6.4c,d show the evolution of initial non-Laurent fire line shapes: a bean and a blade, respectively. These come from the work Gopal and Trefethen (2019b), see their figure 10. Each experiment uses a series truncation $N = 128$ with runtimes in the range of 90 seconds (pentagon) to 25 minutes (blade) on the standard laptop used throughout this thesis. If the user desires, a smaller series truncation $N = 32$ can alternatively be used to obtain quicker runtimes (on the order of

seconds) while still providing a solution of good accuracy - as demonstrated in figure 6.2b.

In producing the results of figure 6.4, a small curvature effect was imposed for added numerical stability. Its magnitude was of $\mathcal{O}(10^{-2})$ for Laurent shapes and $\mathcal{O}(10^{-1})$ for non-Laurent shapes; these were of sufficiently lower order compared to the basic ROS ($\mathcal{O}(1)$) and wind effects ($\mathcal{O}(10)$) such that the main features of the wildfire evolution were unchanged. The curvature effect is especially important on the windward side of the fire line where there is (generally) no pyrogenic wind contribution which also has a stabilising effect. There may be some numerical instabilities due to the crowding phenomenon which is a known challenge in numerical conformal mapping procedures, see e.g. Driscoll (2005). While the n points selected in the $\zeta-$plane are spaced equally around the unit disk, they may not be equally spaced in the physical plane when transformed onto the fire line. This can result in a lack of resolution at some points of the fire line, such as in deep 'troughs'. The curvature effect helps to smooth out any of these instabilities in the numerical method.

6.4 Discussion

In this chapter, the wildfire model of Ch.3 was modified and extended to incorporate ambient and pyrogenic wind effects. As the previously considered effects of curvature and oxygen are of sufficiently lower order than the wind contributions, these effects have been neglected from the model except for a small magnitude curvature effect imposed for numerical stability. The resulting numerical evolution of the fire line computed using a conformal mapping method is produced quickly and appears to be qualitatively accurate. That is, the fire line is elongated in the windward direction and smoothed into a parabolic shape due to the pyrogenic wind, in agreement with the conclusions of Hilton et al. (2018). A more conclusive validation of the model would be to compare its outputs to experimental data - this is done in the next chapter and further discussion of this model, as well as its extension to multiple wildfire scenarios, is continued there.

Chapter 7

Multiple spotfires model

This chapter is a continuation of Ch.6 and has also been completed in Harris and McDonald (2024a). Consider now the case of multiple wildfires spreading, interacting and perhaps merging with each other. These fires may have started independently or be a system of spotfires attributed to one or more main wildfires. While the stochastic generation of spotfires is a topic of interest - see for example Boychuk et al. (2009); Kaur et al. (2016) and Martin and Hillen (2016) - the production of spotfires is not considered in this thesis. The added complexity is that the exterior domain Ω is multiply connected, punctured by the multiple wildfires/spotfires present. As a result, the conformal mapping method used so far throughout this thesis is no longer applicable to such a geometry and so an extension to the AAA-LS algorithm introduced in Ch.4 is instead used. A procedure to detect overlapping fire lines and merge them together is also developed in this chapter.

7.1 Model setup

The multiple spotfires problem is illustrated in figure 7.1. The assumptions of Sect.2.1 hold once more and the wildfires spread in the presence of some uniform, unidirectional constant ambient wind. It is assumed that there are $J \geq 1$ wildfires present initially and that J will not increase over time; it may only decrease if two or more wildfires merge. The total burnt region is defined as $R = R_1 \cup R_2 \cup \cdots \cup R_J$, where R_j is the burnt region of wildfire j with fire line $\partial R_j = \gamma_j$, and $\Omega = \mathbb{C} \setminus R$ is the unburnt region. The velocity $[v_n]_j$ of fire line γ_j in the direction of its outward unit normal vector $\hat{\boldsymbol{n}}_j$ is of the same form as equation (6.1.7) of the previous chapter

$$[v_n]_j = \alpha + \max[0,\ (1-\alpha) + \beta \hat{\boldsymbol{n}}_j \cdot \boldsymbol{\nabla}\phi + \lambda \hat{\boldsymbol{n}}_j \cdot \hat{\boldsymbol{u}}_a] \quad \text{on } \gamma_j. \tag{7.1.1}$$

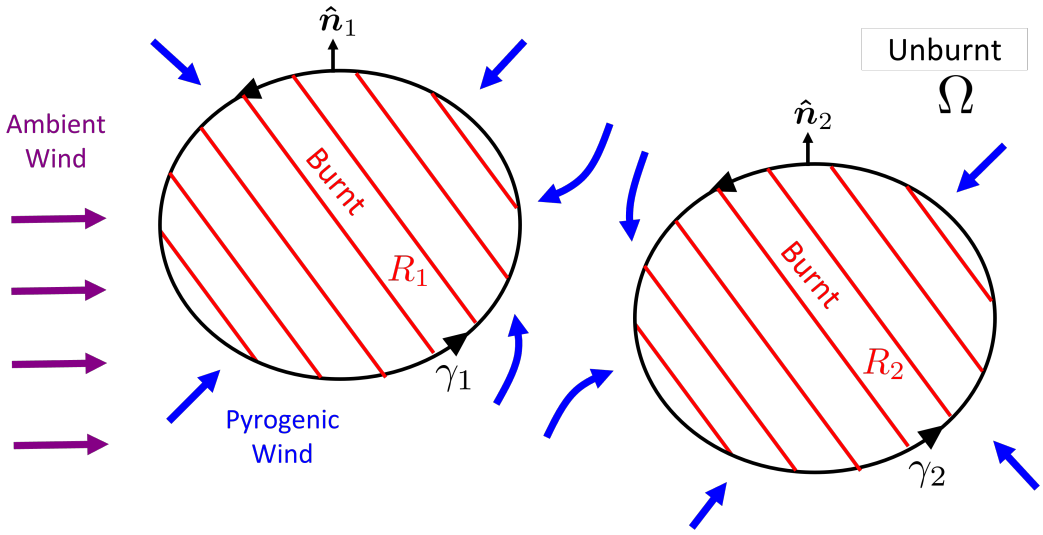

Figure 7.1: The multiple spotfires model. The figure shows two wildfires from a plan view. The blue arrows represent the direction of the pyrogenic (fire) wind and the purple arrows the direction of the ambient wind.

The pyrogenic potential ϕ must be solved in the exterior region Ω. The wind is once more assumed to be the irrotational flow of an incompressible fluid, and the gradient of the dynamic pressure as in Sect.6.1, satisfying Laplace's equation (6.1.8) with Dirichlet boundary condition equation (6.1.9) at all γ_j. Each wildfire j has a fire plume above its burnt region D_j and it is assumed that these plumes do not interact with each other (nor with the ambient wind as assumed in Sect.6.1). Therefore, each wildfire is observed in the far field as a point sink at $z = z_j$, where z_j is the conformal centre of wildfire j. Therefore, the dimensionless system of equations governing the pyrogenic potential ϕ is

$$\nabla^2\phi = 0 \ \text{ in } \Omega, \tag{7.1.2}$$

$$\phi = 0 \ \text{ on } \gamma_j, \tag{7.1.3}$$

$$\phi \to -\log|\Pi_{j=1}^{J}(z - z_j)| = -\log|h(z)| \ \text{ as } r \to \infty. \tag{7.1.4}$$

The system of equations (7.1.1) to (7.1.4) has been non-dimensionalised using the same scalings as in Sect.6.1 - see equation (6.1.4). The characteristic length scale R_0 is now the conformal radius of the largest initial wildfire and the velocity scale is still v_0: the basic ROS of the fuel. Furthermore, it is assumed that each wildfire generates a fire plume of constant strength Q which is used in scaling the potential ϕ. This is a simplification, and an alternative scenario not explored here is that smaller fires may have weaker plumes and thus a smaller effective Q. The starting wildfires in this chapter are all of comparable size.

7.2 AAA-least squares numerical method

The conformal mapping numerical method used for computing the evolution of a single wildfire in Sect.6.2 cannot be used in the multiple spotfires scenario. The issue is that the conformal map from the multiply connected domain to some canonical domain (which is no longer the simple unit disk) cannot be written as a simple, truncated Laurent series for all time. Therefore, an alternative method is needed. This would involve explicit time stepping which adds to the computation cost, thus quick methods are sought at each time step to make this procedure more appealing for operational use. There are three processes to consider in constructing this numerical method: how the pyrogenic potential ϕ in the exterior region Ω is calculated at each time step; how each fire line γ_j is updated between time steps and; how two or more overlapping wildfires are detected and merged into one new wildfire.

7.2.1 Calculating the pyrogenic potential

For over five years, the AAA-LS algorithm has been created and developed for solving two-dimensional Laplace problems, see the recent review article by Nakatsukasa et al. (2023). The algorithm is based on the method of fundamental solutions (or the 'charge simulation' method, see e.g. Amano (1994)) and combines the AAA algorithm for finding a rational approximation to some boundary data (Costa, 2020) with an LS fitting procedure, such as in the Lightning Laplace solver (Gopal and Trefethen, 2019c). The algorithm is fast, running in seconds on a standard laptop, and boasts root-exponential convergence with respect to the number of simple poles used (Gopal and Trefethen, 2019c). This method is also designed to handle non-smooth domain boundaries with corner and cusp singularities and can be extended to the domain exterior as well as to multiply connected domains (Trefethen, 2020); all of these extensions are of interest in this chapter.

The original interior, singly-connected, one-domain algorithm from Costa and Trefethen (2023) was introduced in this thesis in Ch.4 and is restated here. This algorithm solves the one-domain Dirichlet problem

$$\nabla^2\phi = 0 \ \text{ in } D, \qquad \phi = h(z) \ \text{ on } \gamma, \tag{7.2.1}$$

where D is either the interior or exterior domain to a Jordan curve γ and h is a given function. The algorithm can also be used for problems with Neumann boundary condition $\phi_n = 0$ on γ. The potential ϕ can be expressed as the real part of an analytic function $F(z)$ in D which, in turn, is approximated by

$$\phi = \mathrm{Re}[F(z)] = \mathrm{Re}\left(\sum_{k=1}^{N} a_k (z - z_c)^k + \sum_{k=1}^{M} \frac{b_k}{z - p_k} \right), \tag{7.2.2}$$

where N is the series truncation (for numerical purposes) and z_c is a point located in the interior domain. The first sum is known as the smooth (Runge) part and the second as the singular (Newman) part. It is assumed that D is the interior domain in equation (7.2.2); the powers of $(z - z_c)$ are negative in the Runge part when considering the exterior domain.

The AAA algorithm uses the boundary condition for ϕ to find suitable poles p_k which lie in the region $\Omega = \mathbb{C}\backslash D$. Some of the poles generated may be spurious poles or so-called numerical Froissart doublets, see e.g. Nakatsukasa et al. (2018). These are either poles with very small residue or pole-zero pairs that are so close together they effectively cancel. While activating the *cleanup* routine of the AAA algorithm can remove many of these spurious poles (Nakatsukasa et al., 2018), a manual routine referred to in this thesis as 'pole control' is also implemented. This removes any poles of tiny residue $< \mathcal{O}(10^{-8})$ or sufficiently close (at distances less than $\mathcal{O}(10^{-2})$) to the boundary: this is particularly important for the upcoming spotfires scenario where $\phi = 0$ on each fire line.

The convergence of the approximation given by equation (7.2.2) depends upon the number of simple poles produced. In particular, the AAA-LS method offers root-exponential convergence with errors $\mathcal{O}(\exp(-C\sqrt{n}))$, where $C > 0$ is some constant and n are the number of simple poles generated (Gopal and Trefethen, 2019c). Typically in this chapter, $M = \mathcal{O}(100)$ (non-spurious) poles are produced on each run of the AAA algorithm, and thus it is deemed that the solutions of this chapter are of suitable accuracy. Therefore, a small value of the power series truncation N can be chosen that still produces convergent results (Trefethen, 2018, 2020). In this chapter, and in general throughout this thesis, the value $N = 20$ is chosen, following the representative value used in Costa and Trefethen (2023).

The complex coefficients a_k and b_k are then found using an LS algorithm applied to a set of points on the boundary γ. Constructing a matrix of basis vectors A and the vector $H = h(z_b)$, the unknown vector of coefficients $c = [a_k; b_k]$ can then be found by the backslash operation $c = H\backslash A$. An Arnoldi orthogonalisation can also be coupled to the construction of the Vandermonde matrix A for added numerical stability, see Brubeck et al. (2021). The one-domain, singly-connected AAA-LS algorithm is summarised in algorithm 1.

Now, the AAA-LS algorithm is extended as in e.g. figure 4 of Costa and Trefethen (2023) to consider the exterior region punctured by multiple holes i.e. the multiple spotfires problem of this chapter. This will be referred to as the one-domain, multiply connected problem. Note that the harmonic, pyrogenic potential ϕ is zero on each fire line and the far field condition equation (7.1.4) must also be imposed. Therefore, the potential ϕ in the unburnt region Ω can be approximated by $\phi = -\log|h(z)| + g(z)$ where g decays

Algorithm 1 One-domain, singly-connected AAA-LS algorithm

1: Input boundary data $\gamma : z = z_b$, interior point z_c, series truncation N and boundary condition $\phi = H = h(z_b)$ on γ.
2: Run AAA algorithm to find suitable exterior poles p_k for given H. Use the routines *cleanup* and *pole control* to eliminate Froissart doublets.
3: Create matrix A of basis vectors $(z_b - z_c)^k$ and $1/(z_b - p_k)$. Use Arnoldi orthogonalisation if desired.
4: Run LS algorithm to find vector of coefficients $c = [a_k; b_k] = H \backslash A$.
5: Form ϕ from equation (7.2.2).

in the far field and $g(z) = \log|h(z)|$ on each γ_j such that the boundary condition equation (7.1.3) holds. Then g can be written as $g(z) = \mathrm{Re}[F(z)]$, where F is some complex, analytic function in Ω (Trefethen, 2020) approximated as

$$F(z) \approx \sum_{j=1}^{J} \left[D_j \log\left(\frac{z - z_j}{z - z_{j'}}\right) + \sum_{n=1}^{N} A_{jn}(z - z_j)^{-n} + \sum_{p_{jk} \in D} \frac{B_{jk}}{z - p_{jk}} \right], \tag{7.2.3}$$

where $j' = j \pmod J + 1$, z_j is the conformal centre of wildfire j and A_{jn}, B_{jk} are unknown complex coefficients. This approximation consists of three terms. First, a sum of logarithmic terms with unknown real coefficients D_j, where $\sum_{j=1}^{J} D_j = 0$ is implicitly imposed such that there is non-singular behaviour as $z \to \infty$ (Trefethen, 2018; Costa and Trefethen, 2023). Second, a smooth Runge polynomial term truncated at N; the value $N = 20$ is used in this chapter. Third, a singular Newman part consisting of simple poles p_{jk} clustered exponentially near corner and cusp singularities in the burnt region i.e. the unphysical region of the problem. The AAA algorithm is used once more with the function $\log|h(z)|$ to find suitable poles and the *cleanup* and *pole control* routines employed to eliminate Froissart doublets. The vector of unknown coefficients $c = [A_{jn}; B_{jk}; D_j]$ is found using an LS algorithm applied to the boundary data z_{jb} of each fire line γ_j, utilising the boundary condition $\mathrm{Re}[F(z_{jb})] = \log|h(z_{jb})| = H(z_{jb})$ on γ_j. Constructing the Vandermonde matrix A of basis vectors (with Arnoldi orthogonalisation included for improved stability) gives the expression $Ac = H$ and thus c can be found using the backslash operator $c = H \backslash A$. The one-domain, multiply-connected AAA-LS algorithm is summarised in algorithm 2.

Algorithm 2 One-domain, multiply-connected AAA-LS algorithm

1: Input number of boundaries J, boundary data $\gamma_j : z_j = z_{jb}$, interior points z_j, series truncation N and boundary condition $g(z) = H = \log|h(z_{jb})|$ on γ_j.
2: Run AAA algorithm to find suitable interior poles p_{jk} for given H. Use the routines *cleanup* and *pole control* to eliminate Froissart doublets.
3: Create matrix A of basis vectors $(z_{jb} - z_j)^{-n}$, $1/(z_{jb} - p_{jk})$ and $\log\left((z_{jb} - z_j)/(z_{jb} - z_{j'})\right)$. Use Arnoldi orthogonalisation if desired.
4: Run LS algorithm to find vector of coefficients $c = [A_{jn}; B_{jk}; D_j] = H \backslash A$.
5: Form $F(z)$ from equation (7.2.3) then $\phi = -\log|h(z)| + \mathrm{Re}[F(z)]$.

Finally, using the relation $\nabla\phi = \overline{F'(z)}$ from Trefethen (2018), where ∇ is the complex representation of the corresponding vector, it follows that

$$\hat{\boldsymbol{n}}_j \cdot \boldsymbol{\nabla}\phi = \mathrm{Re}[\hat{n}_j \overline{\nabla}\phi] = \mathrm{Re}[\hat{n}_j(-h'(z)/h(z) + F'(z))], \tag{7.2.4}$$

which is the pyrogenic wind effect given in equation (7.1.1). Thus the normal velocity $[v_n]_j$ can be computed for each fire line at a given time step t: the values α, β, λ and $\hat{\boldsymbol{u}}_a$ are known constants and the normal vector $\hat{\boldsymbol{n}}_j$ of each fire line can be computed from the boundary data z_{jb}.

7.2.2 Explicit time-stepping using Runge-Kutta methods

The AAA-LS algorithm runs at each time step, with the fire line then propagated through time from t to $t+\Delta t$ using standard Runge-Kutta (RK) methods, see e.g. Butcher (1996). Consider the normal velocity equation (7.1.1) of the fire line and rewrite as follows

$$\frac{\mathrm{d}\boldsymbol{x}_j}{\mathrm{d}t} \approx \frac{\boldsymbol{x}_j(t+\Delta t) - \boldsymbol{x}_j(t)}{\Delta t} = f(t, \boldsymbol{x}_j(t)) = (\alpha + \max[0,\ (1-\alpha) + \beta\hat{\boldsymbol{n}}_j \cdot \boldsymbol{\nabla}\phi + \lambda\hat{\boldsymbol{n}}_j \cdot \hat{\boldsymbol{u}}_a])\hat{\boldsymbol{n}}_j \quad \text{on } \gamma_j, \tag{7.2.5}$$

where $\boldsymbol{x}_j(t)$ represents the position vector of a point $z = x + iy$ on fire line j at time t. The position of each point on the fire line at the next time step can be written as

$$\boldsymbol{x}_j(t+\Delta t) = \boldsymbol{x}_j(t) + \Delta t \Delta\boldsymbol{x}. \tag{7.2.6}$$

The simplest expression for equation (7.2.6) is when $\Delta\boldsymbol{x} = f(t, \boldsymbol{x}_j(t))$; this is known as Euler's method or first order Runge-Kutta (RK1). More accurate methods include second (RK2) and fourth order Runge-Kutta (RK4) which use $\Delta\boldsymbol{x} = k_2$ and $\Delta\boldsymbol{x} = \frac{1}{6}(k_1 + 2k_2 + 2k_3 + k_4)$, respectively, where

$$\begin{aligned} k_1 = f(t, \boldsymbol{x}_j), \quad k_2 = f\Big(t + \frac{\Delta t}{2}, \boldsymbol{x}_j + \frac{\Delta t}{2}k_1\Big), \\ k_3 = f\Big(t + \frac{\Delta t}{2}, \boldsymbol{x}_j + \frac{\Delta t}{2}k_2\Big), \quad k_4 = f(t + \Delta t, \boldsymbol{x}_j + (\Delta t)k_3). \end{aligned} \tag{7.2.7}$$

Each method has an accuracy of $\mathcal{O}(\Delta t^n)$ where n is the order of the RK algorithm used, with the AAA-LS method used n times at each time step. Both decreasing the size of the time step and increasing the order of the RK method improves the accuracy of the solution but adds to the runtime of the code. For a given time step Δt, RK1 is the quickest method but RK4 is much more accurate, with RK2 sitting somewhere between the two. However, a larger time step can often be used in higher order RK methods to produce a solution of equivalent accuracy, allowing RK2 and RK4 methods to thus run quicker than RK1 in some

cases. All three RK algorithms are incorporated into the numerical method, with the user able to pick the algorithm and time step that provides the best balance of speed and accuracy for their needs.

In this thesis, RK4 is generally used with an $\mathcal{O}(10^{-2})$ time step. However, RK1 may be used for simple scenarios (eg circular wildfires) where a similar level of accuracy can be achieved using the same order of time step. The AAA-LS algorithm with RK time stepping offers the speed desired, with an RK1 time step running in around two seconds and RK4 in 8 seconds on a standard laptop; this is comparable with previous runtimes of the AAA-LS algorithm stated in e.g. Trefethen (2020); Costa and Trefethen (2023).

7.2.3 Detecting and merging two overlapping fire lines

The merging (and splitting) of two free boundaries is a common problem in vortex dynamics (see e.g. Xue et al. (2017)) where the boundaries represent the interface between rotational and irrotational flow. The numerical method of contour surgery pioneered by Dritschel (1988) has been successful in enabling complex vortex interaction to be studied. Typically, the numerical problem involves calculating the minimum distance between the two free boundaries and, when this distance falls below some tolerance level, drawing two additional segments to connect the two contours into a single, new closed curve. The MATLAB function *union* used here offers a simple approach, with the function correctly ordering and orienting the boundary points of the new merged fire line in the anticlockwise direction. However, the *union* function will only merge the two fire lines if the curves are overlapping and are not just sufficiently close to each other. This is of no consequence to the AAA-LS algorithm which can easily calculate the pyrogenic potential ϕ, even when the fire lines are close together - the potential is very small in the gap region and hence is effectively zero there.

As soon as the fire lines overlap, they are then merged into a single contour. However, the RK4 method will only merge the fire lines (if applicable) at the end of the time stepping procedure. Thus this method will fail if the fire lines overlap during the time step as the AAA-LS algorithm is not designed to handle overlapping contours. Therefore, if a merge occurs during a RK4 step, the code will reset to the beginning of the time step and perform a simple RK1 time step instead. To allow the solution to achieve the same level of accuracy throughout, the RK1 time step will be sufficiently smaller than the one used for the higher order RK method; in this chapter, an 'emergency' RK1 step size of $\mathcal{O}(10^{-4})$ is typically used. This is another reason why RK1 time stepping may be used instead of RK4: the isochrones of RK4 may not be at equal time intervals between each other if any emergency RK1 steps were used. Therefore RK1 is useful for ensuring that all isochrones are plotted at equal time intervals and thus for comparing

isochrones at specific times - this is particularly important in Sect.7.5 when comparing the model outputs with experimental data.

Some additional procedures are imposed at each time step over the entire numerical process for added numerical stability. The function *self-intersect* created by Canós (2024) identifies any segments of the fire line which have self-intersected between time steps and removes them from the list of boundary points such that the fire line remains a simple, singly connected curve. Self-intersection is common in the case of extreme junction fires ie V-shaped fires (see e.g. Viegas et al. (2012); Ribeiro et al. (2023)) for example those resulting from a fire merger. If the *self-intersect* procedure occurs during an RK4 time step, the time step is aborted and a smaller, emergency RK1 time step is instead performed, similar to how it is employed in the merging procedure. The MATLAB function *smoothdata* smooths any noise in the fire line data without affecting the overall shape of the fire line. Such provisions are necessary for two reasons. First, to allow the user to use a larger time step and still obtain a numerically stable solution; this means the code is computationally quicker and cheaper which is vital for operational use. Second, while the pyrogenic wind is a stabilising effect, the entropy condition in equation (7.1.1) means that there is no stabilising behaviour on the leeward side of the fire or (often) in the valley between fires. In the single wildfire case, the small magnitude stabilising curvature effect was used when necessary to impose the stability in these regions. In the multiply connected case, where the explicit computation of curvature could also create numerical errors, the *self-intersect* and *smoothdata* functions are used instead. Finally, the function *interparc* created by D'Errico (2024) interpolates the polygon at each time step to maintain the same resolution of points on the fire line as the wildfire grows.

7.3 Results

Figure 7.2 gives the simplest multiple spotfires example of two growing circular wildfires interacting with each other before merging occurs. Six independent scenarios are presented. The bottom and top rows of figure 7.2 show the growth of the wildfires with and without a unit strength vertical ambient wind present, respectively. The three columns from left to right show the effect of increasing the value of α - the ratio of radiative to convective basic ROS - from 0 (fully convective) to 0.5 (the representative value taken throughout this chapter and Ch.6) to 1 (fully radiative). In each figure, the values $\beta = 1.5$ and $\lambda = 3$ are selected for illustrative purposes. Furthermore, the wildfires evolve in the time $[0, 0.25]$ with isochrones plotted at intervals $t = 0.05$, with RK1 timestepping used to allow for more direct comparison between the wildfire scenarios at specific time increments. Each result was created in under four minutes of runtime.

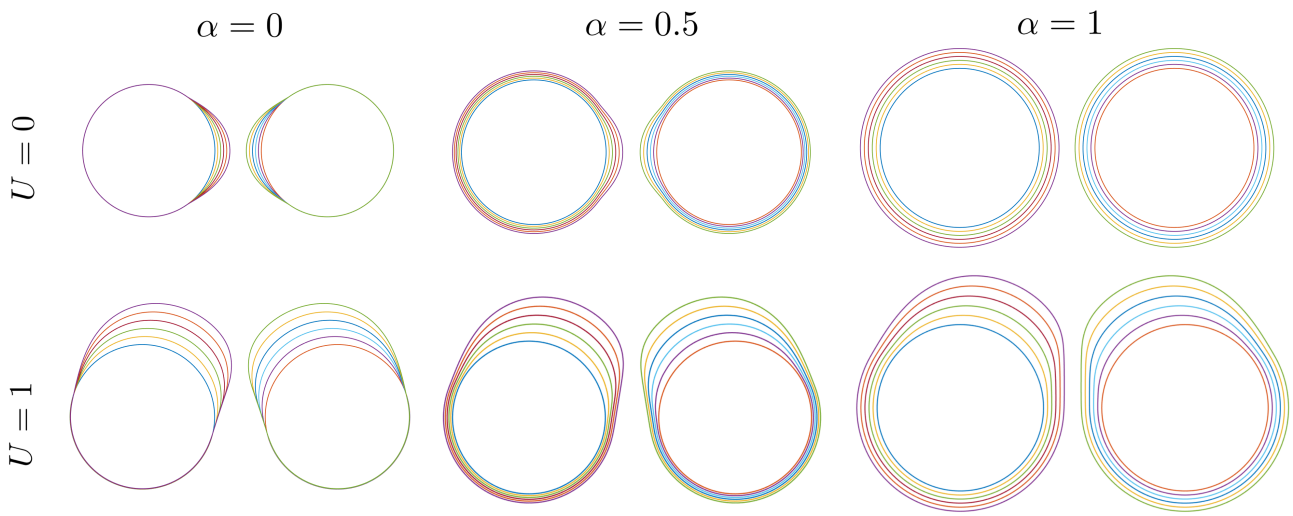

Figure 7.2: Six independent subfigures showing the growth of two circular wildfires with (bottom row) and without (top row) a unit strength ambient wind in the positive imaginary z direction for the values $\alpha = 0$ (left), $\alpha = 0.5$ (centre) and $\alpha = 1$ (right). Each wildfire grows with $\beta = 1.5$ and $\lambda = 3$ for $t = [0, 0.25]$, with isochrones plotted at $t = 0.05$ increments.

The subfigures of figure 7.2 show distinctive behaviour. Considering $U = 0$, the example $\alpha = 0$ shows wildfire growth only in the region between the two wildfires - the incoming pyrogenic wind is sufficiently strong enough on the remaining sections of each fire line to stop fire spread entirely, so that the most pronounced effect is the wildfires growing towards each other. The other extreme case where $\alpha = 1$ shows the two wildfires growing entirely independently of each other, with the pyrogenic wind effect completely ignored at all points of the fire line due to the entropy condition. However, this is inconsistent with the observations and conclusions drawn in e.g. Hilton et al. (2018) which state that two wildfires will interact and grow towards each other (even in the absence of ambient wind). While treating the basic ROS as fully radiative or convective had little to no consequence in the single wildfire models of Ch.2, Ch.3 and Ch.6, neglecting either radiative or convective basic ROS in the multiple wildfires problem results in two (unphysical) extreme cases. Careful consideration has consequently been taken in this chapter (and in the setup of Ch.6) to separate radiative and convective basic ROS effects. The example where $\alpha = 0.5$ gives a good balance between these two extremes: the wildfires grow towards each other but convective effects are not strong enough to entirely stop wildfire spread on non-facing segments of the fire line. The examples with ambient wind $U = 1$ in the imaginary z direction show much the same effects, now with the added rounding of the fire head on the leeward side. Additionally, there is evidence even in the $\alpha = 1$ case that the wildfires grow towards each other. However, this is only seen at the fire head; there is no apparent interaction (as mathematically expected) in the region between the wildfires. Once more, this is inconsistent with theoretical work and experimental observations - see Sect.7.5.

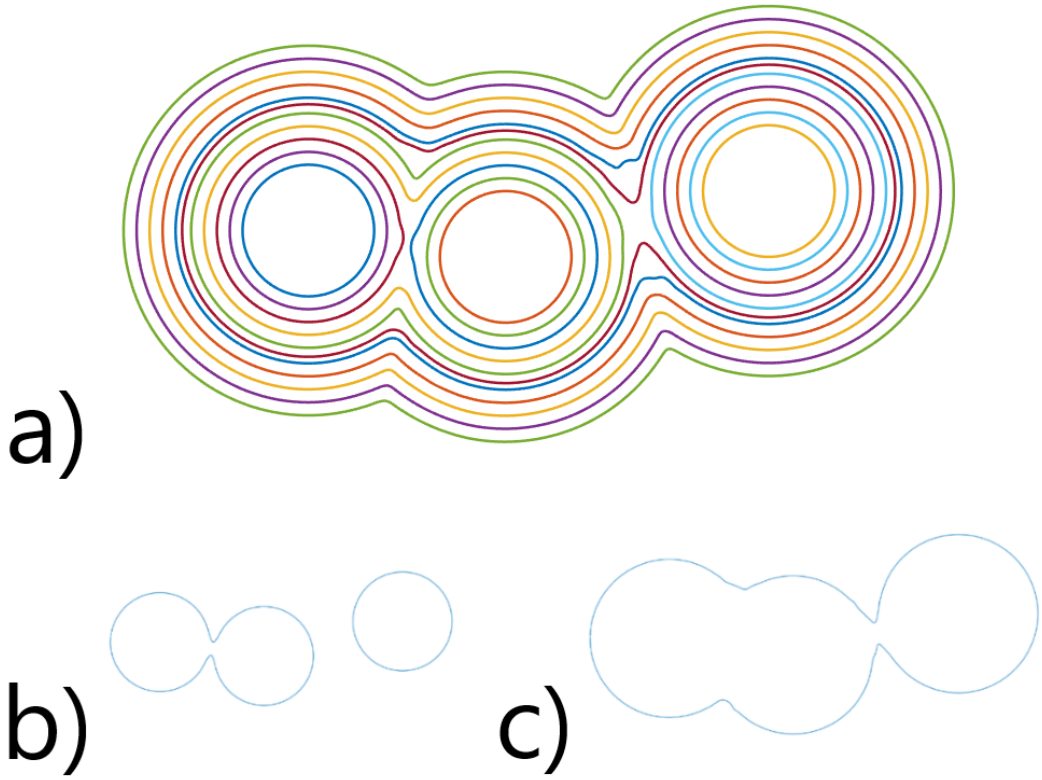

Figure 7.3: The spread and merger of three circular wildfires in the absence of ambient wind with pyrogenic wind effect $\beta = 20$ and RK4 timestepping with time steps $t = 0.02$. Of the 100 isochrones calculated, 11 are plotted in (a), with the contours of the first (b) and second (c) mergers identified.

Figure 7.3 shows the growth and eventual merger of three circular wildfires in the absence of ambient wind. The parameter $\beta = 20$ is used and RK4 timestepping is employed, with time steps $t = 0.02$ for each RK4 step and $t = 5 \times 10^{-4}$ for any emergency RK1 time steps. A total of 100 steps are performed with 11 of these steps plotted in figure 7.3a; note that these isochrones are now not necessarily at equal time intervals due to the use of RK1 at times of merger and numerical instability - as detailed in Sect.7.2.3. The first and second merger steps are displayed in figures 7.3b and 7.3c, respectively, and all results were produced in 28 minutes of runtime. The resulting wildfire growth is as expected: the fires grow more strongly towards each other as they approach and the concave regions of the fire line following a merger are quickly smoothed out, with both of these effects attributed to the pyrogenic wind. Furthermore, the overall fire line evolution looks smooth, with any numerical instabilities successfully smoothed out while not changing the main features of the wildfire spread. This is observed between the second and third isochrones after the second merger: the temporary instabilities in the fire junction are smoothed away.

7.4 Firebreaks

A brief investigation is made in this section into the effect of firebreaks on wildfire spread. A firebreak is here defined as a segment of the fuel bed which is unable to burn, for example a road, river, lake or an area of previous controlled burning. Firebreaks can be incorporated simply into the wildfire model developed in this chapter, such an extension was hinted at at the end of Ch.3. It is assumed that the firebreaks are sufficiently flat so that both ambient and pyrogenic winds are unaffected by their presence. The positioning of such firebreaks may result in the evolution of fire lines with sharp corners, see for example the upcoming figure 7.5 (left) where the fire line develops corners at it spreads through a rectangular gap. As the AAA-LS method is well equipped to handle such corner and cusp singularities (Costa and Trefethen, 2023) and can compute the evolution of a single or multiple wildfires, the AAA-LS method is used exclusively in this section.

Consider the generalised multiple spotfires scenario of J wildfires with burnt regions R_j and fire lines γ_j, respectively, with the unburnt region defined as $\Omega = \mathbb{C} \setminus [R_1 \cup R_2 \cup \cdots \cup R_J]$. Initially and therefore for all time, there is a (perhaps disconnected) region I consisting of incombustible fuel which is a subset of the unburnt region Ω. A very simple addition is made to the normal velocity equation (7.1.1) on each fire line γ_j as follows

$$[v_n]_j = \tau(z)\Big[\alpha + \max[0,\ (1-\alpha) + \beta\hat{\boldsymbol{n}}_j \cdot \boldsymbol{\nabla}\phi + \lambda\hat{\boldsymbol{n}}_j \cdot \hat{\boldsymbol{u}}_a]\Big], \qquad \tau(z) = \begin{cases} 0, & z \in I \\ 1, & z \notin I. \end{cases} \tag{7.4.1}$$

Although not considered here, inhomogeneous fuel beds could also be described using a similar equation, where sections of the fuel bed speed up or slow down wildfire spread rather than stop it altogether. In such a scenario, consideration must be made whether this would affect the entire normal velocity or simply the basic ROS contributions. The modified normal velocity equation (7.4.1) is implemented into the multiple wildfires model and various scenarios considered - there is zero ambient wind in each scenario but pyrogenic wind is still present.

Figure 7.4 shows an example involving three initially circular fires on either side of a straight road which is modelled by an infinite strip parallel to the imaginary direction. The initial radii and centres of these wildfires are given in the figure caption. The motivation for this example is that the two fires on the right of the road are smaller spotfires produced from the main wildfire on the left. As stated in section 7.3, the generation of these spotfires is not discussed in this work. Seven of the 73 isochrones calculated are plotted, where RK1 with a time step of $t = 0.05$ is used. The three initial wildfires are plotted in

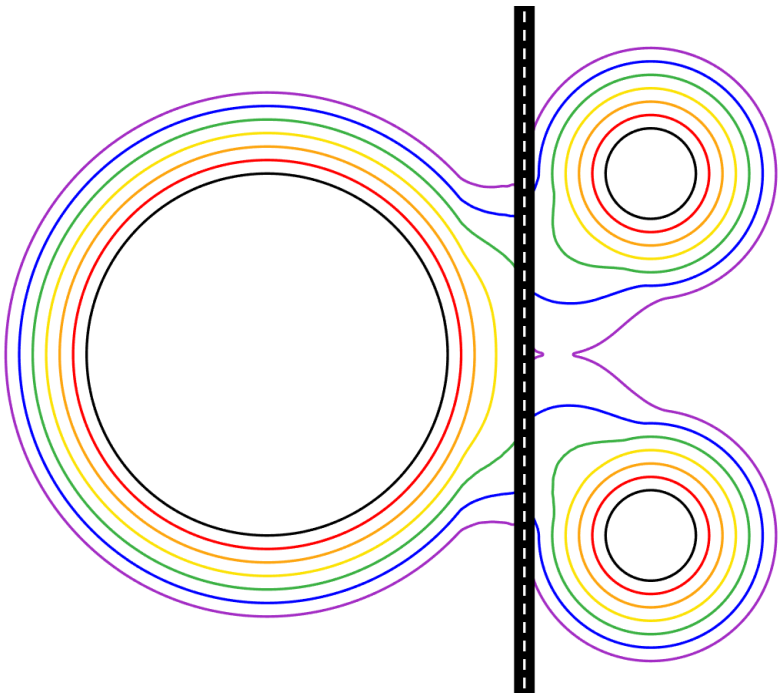

Figure 7.4: Three fires spreading in the absence of an ambient wind on either side of a straight road - the infinite strip. The initial wildfire on the left is of radius $r_1 = 2$, centre $c_1 = -1.25$, the two spotfires on the right have initial radii $r_2 = r_3 = 0.5$ and centres $c_2 = 3 + 2i$ and $c_3 = 3 - 2i$. The parameters used are $\beta = 10$, $\alpha = 0.25$ and RK1 timestepping with 73 steps of $t = 0.05$: seven of these are plotted showing the wildfire spread at equal time increments. The three initial fire lines are plotted in black, then each fire line is plotted in the same colour at a specific time interval.

black, then the isochrones of each fire line are plotted in the same colour for a specific time instance. The parameters $\beta = 10$ and $\alpha = 0.25$ are used for illustrative purposes and the code runs in 770 seconds. None of the three fires penetrate into the road and thus the numerical method successfully accounts for the firebreak. Furthermore, the three fires continue to grow towards each other due to the pyrogenic wind - note the lower value of $\alpha = 0.25$ is taken here to emphasise this effect. The two spotfires grow towards the main fire and each other and eventually merge, as visible at the final (purple) isochrone.

Two further firebreak examples involving only a single, initially circular wildfire are given in figure 7.5. The first in figure 7.5a shows the previous infinite strip scenario with an opening in the middle; this could represent a gap between two purpose-built firebreaks designed to slow the wildfire spread rather than stop it altogether. The parameter $\beta = 20$ is taken and RK1 is used with time step $t = 0.1$ for 30 steps, running in a time of 122 seconds. The wildfire successfully penetrates through the gap in the firebreak, yet the radius of the wildfire spread on the right side is largely reduced from that on the left, as expected. Figure 7.5b shows the spread of the wildfire with $\beta = 10$ around a circular lake - the filled, blue circle of radius 0.5. Here, RK4 is used with time step $t = 0.1$ for 40 steps, running in a time of 570 seconds. The wildfire splits into two arms which grow around the lake and towards the other arm, with the simulation stopped

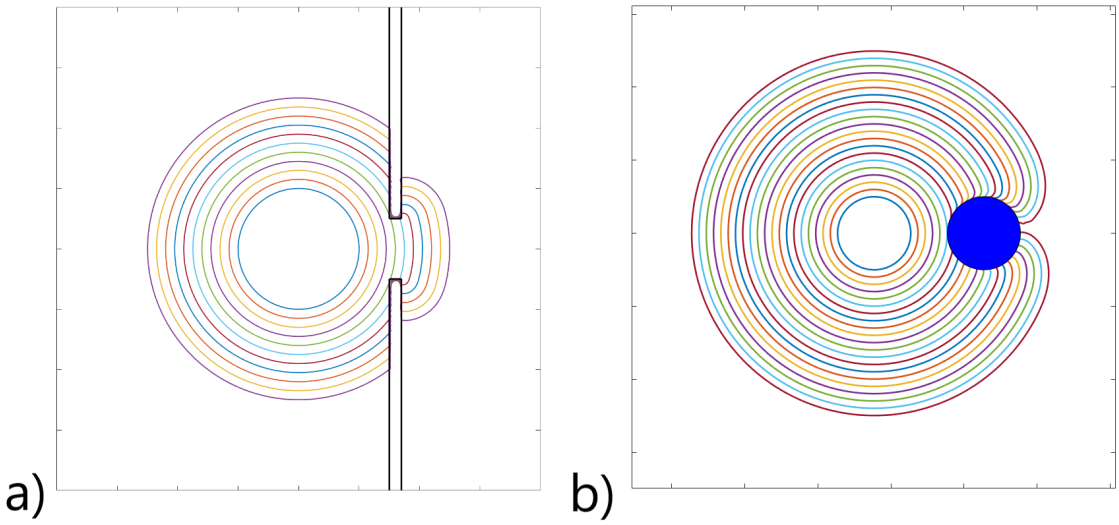

Figure 7.5: Evolution of an initially circular wildfire in the presence of various fire breaks and in the absence of an ambient wind. Isochrones of the wildfire evolution (coloured lines) are plotted in each figure. (a) A gap in the firebreak - the infinite strip between the black lines. Initial wildfire has radius 1 and is centred at the origin. Parameters used are $\beta = 20$ and RK1 timestepping with 30 steps of $t = 0.1$: 11 isochrones are plotted. (b) A circular lake - the filled, blue circle with radius 0.5 and centred at the origin. Initial wildfire also has radius 0.5 and centre -1.5. Parameters used are $\beta = 10$ and RK4 timestepping with 40 steps of $t = 0.1$: 21 isochrones are plotted.

before the two arms merge. The multiple wildfire model of this chapter cannot account for this type of merger as it would result in two disconnected 'exterior' domains, yet such an extension to the AAA-LS algorithm is possible; this is discussed in Ch.10.

7.5 Comparison with results from Hilton et al. (2018)

The wildfire models that have been developed over the course of this thesis have been inspired by the continuous works of Hilton, Sharples and colleagues over the past decade. In particular, the single wildfire and multiple spotfires models of this chapter and Ch.6 are motivated by the pyrogenic potential model of Hilton et al. (2018). Both the present numerical model and the pyrogenic potential model treat the surface fire as a two-dimensional free boundary problem and model the exterior, pyrogenic wind flow by a Laplace equation of the pyrogenic potential. Furthermore, both consider a basic ROS, pyrogenic and ambient wind effects, with equation (6.1.7) an exact analogy of equation (12) from Hilton et al. (2018). There are, however, three notable differences between the present numerical model and the pyrogenic potential model. First, while this thesis uses the conformal mapping and AAA-LS methods, Hilton et al. (2018) use the SPARK framework (Miller et al., 2015) to compute the evolution of the fire line, which is based on the level set method (Osher and Sethian, 1988; Mallet et al., 2009). All methods produce

comparable results and have comparable runtimes, with the SPARK framework running on the order of seconds (Sharples and Hilton, 2020) and the numerical methods of this thesis on the order of seconds to minutes. It is not determined which numerical method is superior, nor is that the aim of this thesis, which is to present alternative, accurate approaches based on the conformal mapping and AAA-LS numerical methods.

Second, Hilton et al. (2018) model the fire plume above the wildfires' burnt regions by an additional interior Poisson equation with forcing term ν which must be solved for. In this thesis, the fire plume is simply modelled as an effective sink of strength Q, reducing the problem to the exterior region of the wildfire only to allow the use of the conformal mapping and AAA-LS methods. Third, the basic ROS term in this chapter and in Ch.6 is explicitly split into its radiative and convective components. This is a substantial and non-trivial distinction to make: the convective basic ROS term will interact directly with the wind field while the radiative part will not. As has been seen in Sect.7.3, the exclusion of either term results in two extreme, unphysical scenarios. It should be noted that neither of these scenarios appear in the work of Hilton et al. (2018), suggesting that this distinction is implicitly included in their model as their basic ROS is taken to be a single joint constant u_0.

It is thus natural to test the accuracy and robustness of the models of this thesis by reproducing some of the results from Hilton et al. (2018). In particular, their figures 5, 7 and 8 are considered which show the evolution of a line fire and a connected and unconnected junction fire[1], respectively, all in the presence of an ambient wind flowing in the positive imaginary z direction. The results of the pyrogenic potential model of Hilton et al. (2018) are then compared with experimental fire data performed in the CSIRO Pyrotron - see Sullivan et al. (2019) for the full details of each experiment. The figures and additional data from these experiments, in particular further time steps of figure 8, were kindly provided by the authors of Hilton et al. (2018) and Sullivan et al. (2019) for use in this thesis.

All three experiments use the same parameters and so the same (equivalent) parameters are to be found and used here. As in Hilton et al. (2018), the basic ROS is $v_0 = 5 \times 10^{-4}\text{ms}^{-1}$ and the ambient wind is of strength $U_a = 1\text{ms}^{-1}$ flowing in the positive imaginary z direction. As in Sect.6.1, it is taken that $\alpha = 0.5$ and $\lambda = 2\beta = \mathcal{O}(10)$, with the value $\lambda = 20$ found to best match the results. The experiments in figures 5 and 7 of Hilton et al. (2018) run for $t = 15$ seconds whereas figure 8 runs for $t = 40$ seconds. It was found that the value $A = 0.24$ gives the best fit to all results, recalling the dimensionless number A from Sect.6.1 which scales the time, see equation (6.1.4). Each line fire has initial length 0.8m, yet recall from Sect.4.1.1 that the R_0 scaling used here is the conformal radius (of the largest initial fire).

[1]This is a V-shaped fire composed of two line fires at an angle θ to each other; the wildfires considered here have $\theta = \pi/2$.

The SC Toolbox was used to calculate the initial conformal radii for each experiment, noting that the fire line at dimensional time $t = 5$ seconds is taken to be the initial fire line here. The scales of the figures are also taken into account when calculating R_0 - figure 5 is displayed on a 1m×1m grid and figures 7 and 8 on a 1.4m×1m grid. The initial conformal radii for figures 5, 7 and 8 of Hilton et al. (2018) are $R_0 = 0.25\text{m}, 0.38\text{m}$ and 0.24m, respectively.

The dimensionless final time t_{max} for each experiment can then be calculated using the scaling in equation (6.1.4): for figures 5, 7 and 8 these are $t_{max} = 1.25, 0.8125$ and 3.52, respectively. Note that the dimensionless scaling in time in equation (6.1.4) depends upon the conformal radius R_0 and so while figures 5 and 7 run for the same dimensional time of 15 seconds, their dimensionless times are different. For the single wildfire scenarios of figure 5 and 7, the conformal mapping method from section 6.2 is used. A Laurent series truncation of $N = 128$ is chosen and an $\mathcal{O}(10^{-2})$ curvature effect is included for added stability. For the two wildfire scenario of figure 8, the AAA-LS method is used; RK1 is used with a time step of $t = 4.4 \times 10^{-3}$ for 800 steps such that isochrones at specific times can be compared with the figures of Hilton et al. (2018) (see Sect.7.2.3). As these results are produced for comparative purposes, a longer overall runtime (which is a consequence of using RK1 with a smaller time step) is acceptable. Finally, all relevant parameters are scaled by a factor 10^{-1}, e.g. $\lambda = 2$ rather than 20, to allow for greater numerical stability. It should again be noted that the same parameters are used for all three experiments here and care has been taken to ensure they match as well as possible with the parameters used in Hilton et al. (2018).

Figures 7.6, 7.7 and 7.8 are analogues of figures 5, 7 and 8 from Hilton et al. (2018), respectively, and superimpose the results from the code of this thesis (yellow isochrones), the results from the pyrogenic potential model of Hilton et al. (2018) (white isochrones) and the experimental data from Sullivan et al. (2019) (background image) all onto the same plot. Figures 7.6 and 7.7 show the development of a single line fire and a single connected junction fire, respectively, both of which are perpendicular to the ambient wind. Each scenario had a runtime of around 27 minutes when using the conformal mapping method, though there was little difference in the results compared to those using $N = 32$, which ran in 15 seconds. The single wildfire model of Ch.6 successfully captures the main features of the wildfire development in both experiments: the development of the fire line head into a parabolic shape in the windward direction in figure 7.6 and the closing of the junction fire in figure 7.7. Furthermore, the fire line shapes qualitatively agree with those from the model of Hilton et al. (2018), though quantitatively the fire lines differ more noticeable at larger times. However, there is still good agreement between the model of Ch.6 and the experiment; the model still appears to enclose the burnt region of the fire at all times.

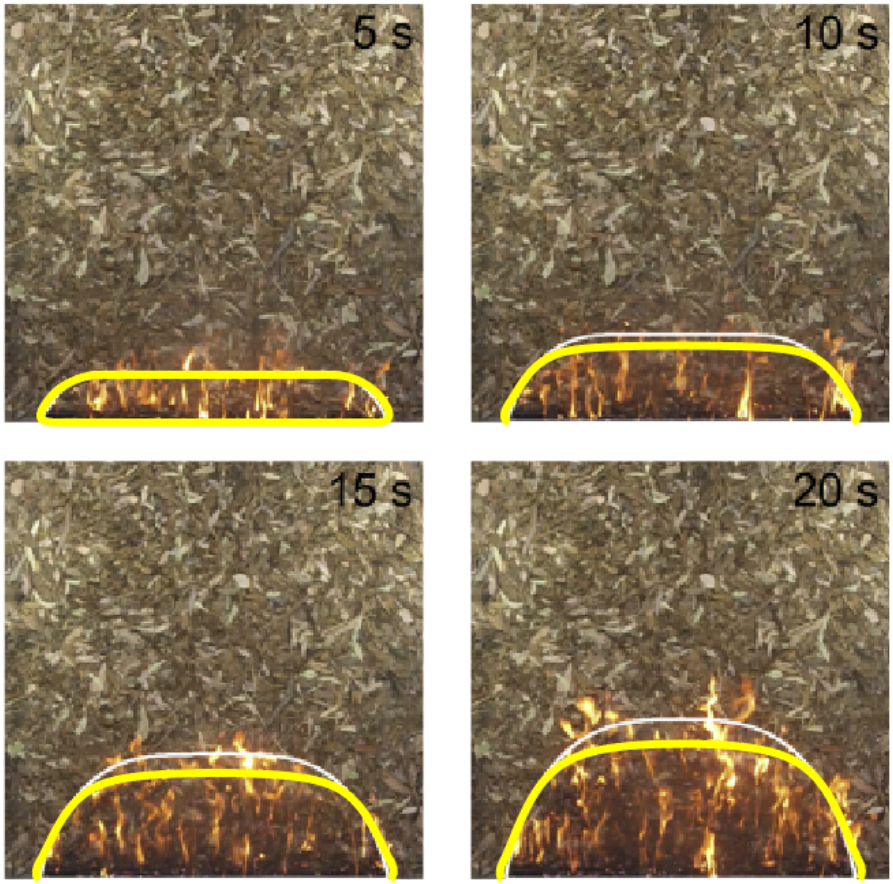

Figure 7.6: Propagation of a line fire in an ambient wind: comparison of the single wildfire model with figure 5 of Hilton et al. (2018). Each subfigure shows a snapshot of the experimental wildfire performed in Sullivan et al. (2019) and the predicted wildfire spread from both the present numerical model (yellow line) and the pyrogenic potential model of Hilton et al. (2018) (white line). The experiment is performed on a 1m $\times$ 1m grid and the wildfire spread is displayed at times 5s, 10s, 15s and 20s from ignition (from left to right, top to bottom). The conformal mapping numerical method from Ch.6 is used with Laurent series truncation $N = 128$ and runs in 27 minutes.

Figure 7.8 shows the development of an initially disconnected junction fire - two line fires angled towards each other - which had a runtime of around 50 minutes using the AAA-LS method. There is once again good agreement between the model of this chapter, the experimental fire and the model of Hilton et al. (2018) over all time. There is some evidence of 'over-rounding' of the fire line: the eastern and western flanks are more curved than in Hilton et al. (2018) and the southern-most points of the wildfire round out also. This is a consequence of the smoothing processes, namely the function *smoothdata* as detailed in Sect.7.2, applied during the multiple spotfires code to help eliminate numerical instabilities. These small errors are acceptable given that the aim of this thesis is to produce an operational model capable of capturing the main features of the wildfire spread. Furthermore, the final fire line at time $t = 45$ seconds reproduces the burnt region well, noting that the two line fires have successfully merged by this time. Unfortunately, the image is cut off such that the head of the fire is not visible in the photo, nor is there a

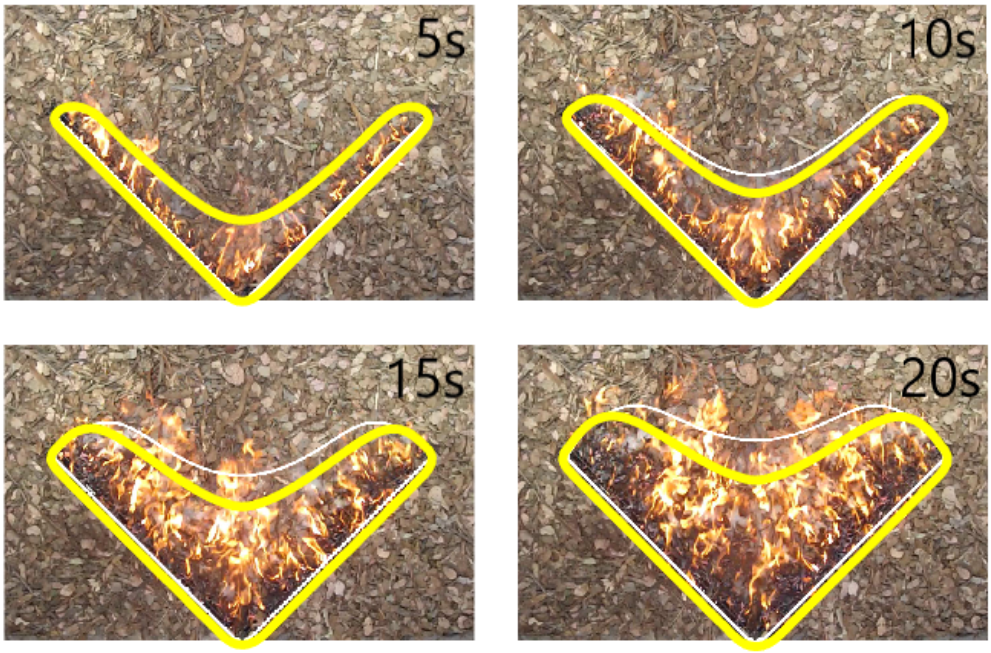

Figure 7.7: Evolution of a connected junction fire: comparison of the single wildfire model with figure 7 of Hilton et al. (2018). Each subfigure shows a snapshot of the experimental wildfire performed in Sullivan et al. (2019) and the predicted wildfire spread from both the present numerical model (yellow line) and the pyrogenic potential model of Hilton et al. (2018) (white line). The experiment is performed on a 1.4m $\times$ 0.9m grid and the wildfire spread is displayed at times 5s, 10s, 15s and 20s from ignition (from left to right, top to bottom). The conformal mapping numerical method from Ch.6 is used with Laurent series truncation $N = 128$ and runs in 27 minutes.

comparison with the work of Hilton et al. (2018) at this final time step. Nonetheless, it is seen that the model of this work reproduces the burnt region well at this final time step, noting that the two line fires have successfully merged by this time.

To conclude, the present numerical model captures well the main features of the experimental wildfire spread performed in Sullivan et al. (2019) which was also modelled in Hilton et al. (2018). Both the present numerical model and the pyrogenic potential model give qualitatively the same fire behaviour: the development of the leading edge of the line fire into a parabolic head; the closing of the V-shape in the junction fire; and the growth of the two separate line fires towards each other. There are slight differences in the results of each model owing to a number of reasons. While care was made to ensure that the parameters used here match those used in Hilton et al. (2018), the exact parameter values may differ between the models due to the subtle difference in the present model setup, in particular the treatment of the fire plume and the basic ROS. The disparity in outputs may also be due to the difference in numerical methods used and their associated numerical errors. Note also that neither the present numerical model nor the pyrogenic potential model can account for the 3D projection of flames forward of the wildfire and so, even though the fire line successfully encloses the burnt region, there is still evidence

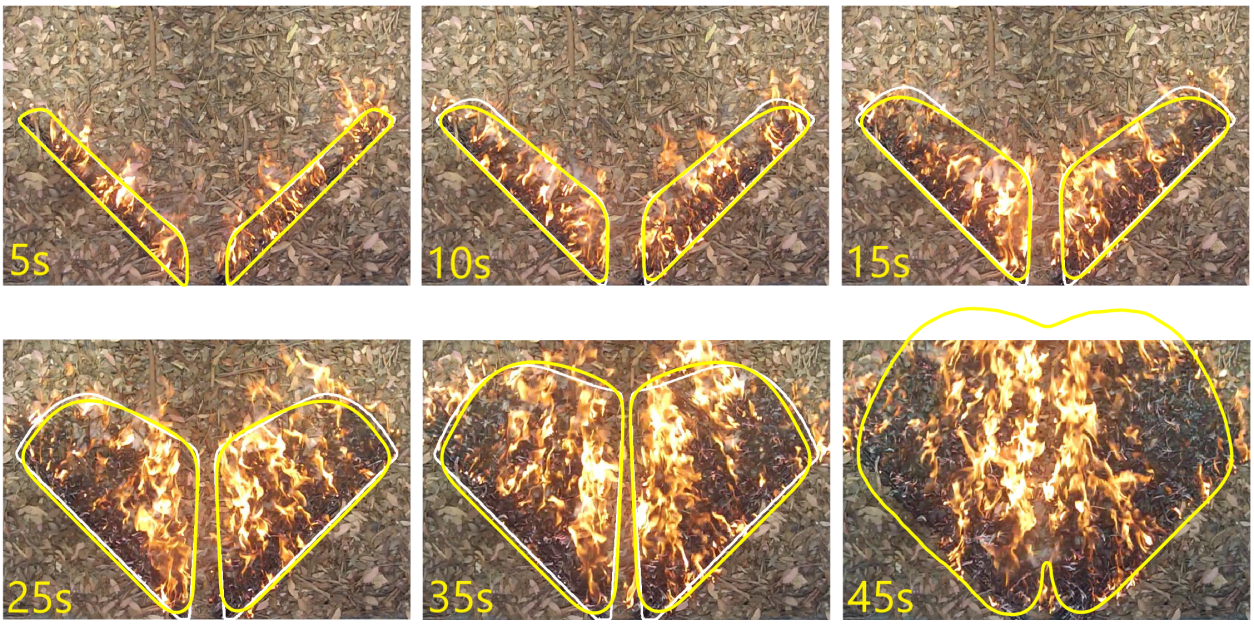

Figure 7.8: Evolution of an unconnected junction fire: comparison of the multiple spotfires model with figure 8 of Hilton et al. (2018). Each subfigure shows a snapshot of the experimental wildfire performed in Sullivan et al. (2019) and the predicted wildfire spread from both the present numerical model (yellow line) and the pyrogenic potential model of Hilton et al. (2018) (white line). The experiment is performed on a 1.4m $\times$ 0.9m grid and the wildfire spread is displayed at times 5s, 10s, 15s, 25s, 35s and 45s from ignition (from left to right, top to bottom). The AAA-LS numerical method of this chapter is used and runs in 50 minutes.

of flames extending beyond the fire line. A thorough quantitative comparison between both models and the experimental fires is beyond the scope of this thesis. Instead, it is concluded, in line with the purpose of this chapter and Ch.6, that both the present numerical model and the pyrogenic potential model of Hilton et al. (2018) capture well the main features of the wildfire spread and the progression of the fire line.

7.6 Discussion

Over the previous two chapters, wind effects have been successfully incorporated into the wildfire model developed in Ch.3. In the single wildfire case of Ch.6, the conformal mapping method formulated so far in this thesis was once again employed to quickly compute the fire line evolution. Yet this conformal mapping method was not applicable to the multiple spotfires scenario considered in this chapter and so the multiply-connected AAA-LS algorithm was instead employed explicitly at each time step, with an RK time stepping routine used to compute the evolution of the wildfires. A procedure to detect and merge overlapping fire lines was also implemented. Compared to the dominant wind effects, the low order effects of curvature and oxygen included in the model of Ch.3 were here neglected, except for a small magnitude curvature effect employed in the single wildfire model for numerical stability. Thus the wildfire spread

was dependent on three main effects: the basic rate of spread divided explicitly into its radiative and convective components; the ambient wind and; the pyrogenic wind.

To demonstrate the efficacy of these new numerical models, their outputs are compared against those from the pyrogenic potential model of Hilton et al. (2018) and the experimental results of Sullivan et al. (2019). It is found that both models perform well in representing the main features of wildfire spread: the parabolic rounding of the fire line head; the closing of the V-gap in junction fires; and the growth of multiple wildfires towards each other. Furthermore, both models have comparable computational speed on a standard laptop, with the pyrogenic potential model running in the order of seconds (Hilton et al., 2018; Sharples and Hilton, 2020) and the present numerical models on the order of seconds to minutes, depending on the desired accuracy of the output. There are subtle differences in the exact fire line evolution outputted by each model; this is likely due to a disparity in actual parameter values resulting from the differences in each model setup and due to a difference in numerical errors offered by the level set and conformal mapping/AAA-LS methods. It is difficult to identify the burnt region from the experimental images due to the inclined flames (a similar conclusion was reached in Hilton et al. (2018)) and thus it cannot be determined which model most accurately computes the wildfire evolution. Instead, it is concluded that both models are of comparable accuracy and thus the models of Ch.6 and Ch.7 successfully reproduce the results from Hilton et al. (2018).

The effects of the two parameters, the ratio α of the radiative to convective basic ROS effects and the strength β of the pyrogenic wind effect, have also been studied in the previous two chapters. In agreement with the conclusions of Hilton et al. (2018), a higher β value causes a stronger rounding of the fire line head that progresses at a slower rate. Increasing α decreases the ability of two wildfires to grow towards each other which, in the case of zero ambient wind, resulted in the two extreme limits: $\alpha = 0$ where wildfire growth was completely halted on the non-facing portions of the fire line and $\alpha = 1$ where there was no interaction between the two wildfires at all. Interestingly, the pyrogenic potential model of Hilton et al. (2018) does not produce either of these extreme limits, despite making no explicit distinction between radiative and convective basic ROS - their equation (12) implies they consider only radiative basic ROS. It is assumed that the additional differences in their modelling assumptions, for example their treatment of the fire plume, implicitly prevents the two unphysical extreme cases. Firebreaks - regions of the fuelbed where wildfire spread is entirely stopped - were also incorporated into the model to study how wildfires interact with features such as roads, lakes and disconnected man-made fire barriers.

The model (e.g. equations (6.1.7) to (6.1.10)) is closely related to the pyrogenic potential model of Hilton et al. (2018). Both treat the surface fire as a two-dimensional free boundary problem and model the

exterior, pyrogenic wind flow by a Laplace equation of the velocity potential. Furthermore, both consider basic ROS, pyrogenic and ambient wind effects, with equation (6.1.7) being an exact analogy with eq. (12) from Hilton et al. (2018). However, there are some noteworthy differences. First is the explicit distinction between radiative and convective rate of spread which in Hilton et al. (2018) was taken to be a single joint constant u_0. Second, the dynamics of the fire plume are treated differently. In the work of Hilton et al. (2018), the authors solve an additional Poisson equation in the wildfire interior involving a forcing term ν representing the upward air flow, whereas the fire plume is observed as a point sink of strength Q in the far field in this thesis. Third, Hilton et al. (2018) use a level set method to obtain numerical results rather than a conformal mapping or AAA-LS method. As shown in Sect.7.5, both models produce equivalent results that compare well with experimental data, displaying that the modelling and numerical methods developed in this thesis are practical alternatives in solving the wildfire problem.

Note that the results produced throughout Ch.6 and Ch.7 (excluding those in section 7.5) are entirely non-dimensional. Thus the features of the coupled wildfire-atmosphere model developed here, in particular the effect of the pyrogenic wind, can be modelled across length scales. The work of Hilton et al. (2018) conclude this also: not only do they validate their model against the metre-scale laboratory experiments of Sullivan et al. (2019), they also show good accuracy when compared to field experiments with initial fire lines on the order of tens of metres - see their figures 10 and 11. It is thus concluded that the present numerical model of this thesis is also applicable to wildfires on the metre to tens of metres scale.

It is speculated whether the present numerical model is also applicable in the case of kilometre scale wildfires. While no such analysis is performed in Hilton et al. (2018) and is beyond the scope of this thesis, other wildfire-atmosphere models such as WRF-Fire (Mandel et al., 2011) and ForeFire/Meso-NH (Filippi et al., 2011) can scale from the tens of metres to kilometre scales - see table 1 of Bakhshaii and Johnson (2019). It must be cautioned that wildfires of such large scales may introduce more complex atmospheric coupling not currently considered in the present numerical model. One such example is the dynamics of the fire plume - it is expected that a kilometre scale wildfire would have a substantial fire plume which would significantly interact with the background ambient wind field. For example, the presence of the fire plume may divert the background flow, this interaction is neglected in this thesis.

Finally, it is concluded that the present numerical model can perform on the order of seconds to minutes. When comparing between the experimental results of Sullivan et al. (2019) in Sect.7.5, some amount of computational speed was sacrificed to obtain results of improved accuracy. Various procedures, such as decreasing the Laurent series truncation in the conformal mapping method or using higher order RK timestepping with larger timesteps in the AAA-LS method, can be used to reduce the runtime further.

All other results here are non-dimensional, thus comparing the runtime of the code with the physical time of the wildfire spread is not possible until suitable dimensions are added. Some representative dimensions are considered for the example of two circular wildfires growing towards each other in figure 7.2. The final dimensionless time is $t^* = 0.25$ and it is assumed that the values $A = 0.24$ and $v_0 = 5 \times 10^{-4}$ as used in section 7.5 are also applicable in this wildfire problem. Thus the final dimensional time in minutes of the wildfire spread is $t = 20R_0$, where R_0 is the initial dimensional radius of the wildfire. On the metre scale, assuming $R_0 = 1$m gives that $t = 20$ minutes and on the tens of metres scale with $R_0 = 10$m gives that $t = 200$ minutes $= 3$ hours and 20 minutes. The runtime of the numerical method is under four minutes which is substantially faster than real time and it is observed that the larger the scale of the wildfire, the quicker the numerical model in comparison to the associated real time scale. Should the present numerical model be applicable to wildfires on the kilometre scale, the numerical method would still run in under four minutes to compute the associated wildfire evolution on the order of days.

This is the final chapter of this thesis for which wildfire modelling is investigated. Final thoughts on the wildfire models developed throughout this thesis, and further scopes for extension, are discussed in Ch.10.

Part III

TWO-DOMAIN LAPLACE PROBLEMS

Chapter 8

Electrostatic interaction between flowers and arthropods

While the conformal mapping approach introduced in Ch.2 and used throughout this thesis is a powerful numerical tool, its scope is nevertheless limited. This was evident in Ch.4 where an additional interior Poisson equation had to be solved and in Ch.7 where the harmonic potential in the multiply-connected domain was to be found. In both cases, the AAA-LS method alternatively provided a numerical method that ran at a speed comparable to that of the original conformal mapping approach. These final two chapters explore the extension of the AAA-LS algorithm to a new scenario: two-domain problems. While this was in fact done in Ch.4 where the interior and exterior of the penguin huddle were both considered, it was imposed that the temperature T was constant on the boundary, thus the interior and exterior could be solved separately. The problems in the upcoming chapters involve mixed value boundary problems of the continuity (or 'jump') type, which subsequently couple the interior and exterior problems. Conformal mapping cannot be used in these cases as a single map $z = f(\zeta, t)$ will only transform one domain, interior or exterior, from the canonical to the physical plane. However, the AAA-LS method can be extended to this new scenario, with the extension introduced in this thesis being new to the field.

The first two-domain scenario is in the field of biological electrostatics. It was recently discovered that terrestrial arthropods such as bees, spiders and hoverflies can detect and locate disturbances in electrical fields, a process known as electroreception (Clarke et al., 2013; Greggers et al., 2013; Clarke et al., 2017; Morley and Robert, 2018). The coevolution of plants and arthropods motivates an investigation into floral electrostatics - how a flower presents itself electrically. Along with features such as shape, scent and colour, the disturbance of the flower in the electric field may be another cue used to attract potential pollinators.

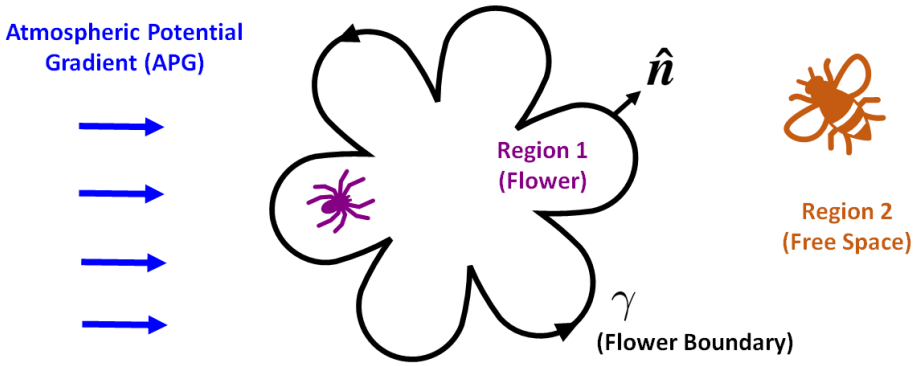

Figure 8.1: Diagram of the arthropod and uniform field problem. Three types of electrical source/sink are shown: (i) an external planar field (e.g. the Earth's atmospheric potential gradient), (ii) a point charge outside of the flower boundary (a bee), (iii) a point charge inside the flower boundary (a spider).

In this chapter, the two-domain AAA-LS algorithm is introduced and some results on the floral-arthropod electrostatic interaction presented. This work was completed in Harris et al. (2024).

8.1 Model setup

Consider a flower which is treated as a 2D dielectric – see figure 8.1. The shape of the flower is traced out by some Jordan curve γ orientated such that the unit normal vector $\hat{\boldsymbol{n}}$ is outward pointing. Let the interior of the flower be labelled region 1 and the exterior as region 2.

An electric field $\boldsymbol{E}$ is present in both regions 1 and 2 due to the dielectric nature of the flower. This field can be written as the gradient of some scalar potential $\boldsymbol{E} = -\boldsymbol{\nabla} V$ which satisfies the Poisson equation $\nabla^2 V = -\rho/\epsilon$ by Gauss' law, where ρ is the charge density and $\epsilon = \epsilon_0(1 + \chi_e) = \epsilon_0 \epsilon_r$ is the absolute permittivity. Here, $\epsilon_0 \approx 8.85 \times 10^{-12}$ Fm^{-1} is the permittivity of free space, χ_e the electric susceptibility and $\epsilon_r = 1 + \chi_e$ the relative permittivity. In the exterior (free space) region, it holds that $\epsilon_r = 1$ and so $\epsilon_2 = \epsilon_0$, whereas in the interior flower region $\epsilon_r = 10$ to 100 and so $\epsilon_1 = 10\epsilon_0$ to $100\epsilon_0$.

Dimensionless quantities are introduced via the following scalings, where henceforth starred variables are dimensional. Lengths are scaled as $\boldsymbol{x}^* = L\boldsymbol{x}$, where L is the length scale of the flower; it follows that $\nabla^* = (1/L)\nabla$. There are three possible generators of the electric field $\boldsymbol{E}$, which will determine the scaling of the potential V:

(a) A uniform electric field such as the atmospheric potential gradient.

(b) Arthropods exterior (e.g. bees) and interior (e.g. spiders) to the flower.

(c) A combination of (a) and (b). This is illustrated in figure 8.1.

The governing equations and boundary conditions are identical in all three problems and independent of the scaling of V. The system of dimensionless equations is thus

$$\nabla^2 V_1 = -\rho L^2/\epsilon \quad \text{in } 1, \tag{8.1.1}$$

$$\nabla^2 V_2 = -\rho L^2/\epsilon \quad \text{in } 2, \tag{8.1.2}$$

$$V_1 = V_2 \quad \text{on } \gamma, \tag{8.1.3}$$

$$\frac{\partial V_1}{\partial n} = \tilde{\epsilon}\frac{\partial V_2}{\partial n} \quad \text{on } \gamma, \tag{8.1.4}$$

where $\tilde{\epsilon} = \epsilon_2/\epsilon_1$ is the ratio of the absolute permittivities. In all three problems, the charge density ρ is zero everywhere except at point charges (arthropods), thus equations (8.1.1) and (8.1.2) become Laplace equations everywhere excluding the singularities. Boundary condition equations (8.1.3) and (8.1.4) are a consequence of the continuity of the electrical potential across the boundary and of Gauss' Law, respectively (Griffiths, 2023). The far field condition on the potential V_2 and the charge density ρ depend upon the generator of $\boldsymbol{E}$.

8.1.1 Uniform electric field

Let a uniform background electric field be present with strength E_∞ far from the flower. There are no arthropods present in this problem, hence the charge density ρ is zero. The interior and exterior potentials V_1 and V_2, respectively, are scaled by LE_∞ as $V^* = LE_\infty V$. The far field condition is thus

$$V_2 \to -x \quad \text{as } r \to \infty. \tag{8.1.5}$$

where x is the horizontal direction and r is the radial direction. In general, the uniform electrical field may possess an 'out of plane' component, relative to the flower. In this instance, only the component that lies in-plane with the flower is considered. Additionally, since the orientation of the flower within the model is arbitrary, the $x-$axis can be chosen to align with the uniform field. When the flower boundary γ is a circle or an ellipse, an exact solution to equations (8.1.1) to (8.1.5) can be found; these solutions are given in Appendix A.1 of Harris et al. (2024).

8.1.2 Bees and spiders

Consider an arthropod with associated electric charge λ. The creature is centered at the point z_1^* which is typically of $\mathcal{O}(L)$ and can be either inside (spider) or outside (bee) the flower. It is assumed the arthropod is not on the flower boundary and is sufficiently small to be considered as a point charge. In a 2D system,

the electric potential of a point charge in free space is known

$$V^* = -\frac{\lambda}{2\pi\epsilon}\log|z^* - z_1^*| = -Q\log|z^* - z_1^*|, \tag{8.1.6}$$

where the absolute permittivity is $\epsilon = \epsilon_1|\epsilon_2$ for $z_1 \in 1|2$. The potential V is scaled by Q as $V^* = QV$ and so the far field condition is

$$V_2 \to -\log|z| - \log|L| \quad \text{as } r \to \infty. \tag{8.1.7}$$

The charge density ρ is given by

$$\rho = (\lambda/Q)\delta(z - z_1), \tag{8.1.8}$$

where δ is the Dirac delta function. Exact solutions to the system of equations (8.1.1) to (8.1.4) and equation (8.1.7) can be found for a circular flower boundary; these are given in Appendix A.2 of Harris et al. (2024).

8.1.3 Swarming arthropods in the electric field

The problems of Sect.8.1.1 and Sect.8.1.2 can be combined to model how an arthropod of electric charge λ_1 interacts with a uniform electric field of far field strength E_∞. The potential V is again scaled as $V^* = LE_\infty V$, giving the far field condition

$$V_2 \to -x - A_1\log|z| - B_1 \quad \text{as } r \to \infty, \tag{8.1.9}$$

where the dimensionless parameter $A_1 = Q_1/(LE_\infty)$ and the constant $B_1 = A_1\log|L|$ have been introduced. The charge density ρ is then given by

$$\rho = (\lambda_1/(LE_\infty))\delta(z - z_1), \tag{8.1.10}$$

where δ is once more the Dirac delta function. Including multiple arthropods (a swarm) can be achieved by including additional $A_j\log|z| + B_j$ terms to the RHS of equation (8.1.9) and additional $(\lambda_j/(LE_\infty))\delta(z - z_j)$ terms to the RHS of equation (8.1.10), where arthropod j centered at the point $z_j^* = Lz_j$ has charge λ_j. If there is no background electric field, the $-x$ term in equation (8.1.9) is excluded and the new dimensionless parameters $A_j = Q_j/Q_1$ are instead used. The exact solution of equations (8.1.1) to (8.1.4) and equation (8.1.9) for a circular flower is just a linear combination of the solutions in Appendices A.1 and A.2 of Harris et al. (2024).

8.2 Two-domain AAA-LS numerical method

All three variants of the flower problem in Sect.8.1 can be solved numerically using an extension of the AAA-LS method as introduced in Ch.4 and Ch.7. Recall that the original one-domain, singly-connected AAA-LS algorithm was summarised in algorithm 1 in Sect.7.2 and the method was also extended to the one-domain, multiply-connected scenario of multiple spotfire spread, see algorithm 2. One of the key ideas is that the 'given' function h in the boundary condition $\phi = h(z)$ is used in the AAA algorithm to generate suitable simple poles p_k and in the LS fitting to find the unknown coefficients a_k, b_k. The difficulty in adapting the AAA-LS method to a two-domain scenario is that there is now no given function h: there is instead a pair of boundary conditions imposing either continuity or jumps in the unknowns V_1 and V_2 and their normal derivatives. The proposed remedy is to consider the combined quantity $V_1 - V_2$ with known functions to be used in the AAA and LS algorithms arising from the far field conditions.

Since both the interior and exterior potentials V_1 and V_2 are harmonic by equations (8.1.1) and (8.1.2), each can be written as the real part of some analytic function plus some correction term to account for the far field condition. Consider the general case of a system of J arthropods in a uniform electric field, where arthropod j is located at $z = z_j$. The potentials V_1 and V_2 are expressed as

$$\begin{aligned} V_1 &= -\mathrm{Re}[G_1(z)] + \mathrm{Re}[F_1(z)] \\ &= -\mathrm{Re}\bigg(\sum_{j=1}^{J} \Gamma\tilde{\epsilon} A_j \log(z - z_j)\bigg) + \mathrm{Re}\bigg(\sum_{k=1}^{N_1} a_k (z - z_c)^k + \sum_{k=1}^{M_1} \frac{b_k}{z - p_k}\bigg), \end{aligned} \tag{8.2.1}$$

$$\begin{aligned} V_2 &= -\mathrm{Re}[G_2(z)] + \mathrm{Re}[F_2(z)] \\ &= -\mathrm{Re}\bigg(z + \sum_{j=1}^{J} A_j \log(z - z_j)\bigg) + \mathrm{Re}\bigg(\sum_{k=1}^{N_2} c_k (z - z_c)^{-k} + \sum_{k=1}^{M_2} \frac{d_k}{z - q_k}\bigg), \end{aligned} \tag{8.2.2}$$

where $\Gamma = 1|0$ for $z_j \in 1|2$, $z_c = 0$ is the centre of the flower and N_1 and N_2 are series truncations; the values $N_1 = N_2 = 20$ are used in this chapter. The dimensionless parameters A_j are given in Sect.8.1.3 and if there is no uniform electric field, the z term in equation (8.2.2) can be excluded.

Now, consider the Dirichlet boundary condition equation (8.1.3) expressed as $V_1 - V_2 = 0$ on γ. Substituting equations (8.2.1) and (8.2.2) into equation (8.1.3) and rearranging gives

$$\mathrm{Re}[F_1(z)] - \mathrm{Re}[F_2(z)] = -\mathrm{Re}[H_1(z)], \tag{8.2.3}$$

labelling

$$H_1(z) = z + A_j(1 - \Gamma\tilde{\epsilon}) \log(z - z_j), \tag{8.2.4}$$

where the summation sign has been dropped for brevity. The Neumann boundary condition equation (8.1.4) can be expressed similarly. Note that $\partial V/\partial n = \hat{\boldsymbol{n}} \cdot \boldsymbol{\nabla} V = \mathrm{Re}[n\overline{\nabla}V]$, where $n = n_x + in_y$ and ∇ are complex representations of the normal vector to γ and the gradient operator, respectively. Furthermore, equation (5) from Trefethen (2018) gives that $\overline{\nabla}[\mathrm{Re}[F(z)]] = F'(z)$. Therefore, the Neumann boundary condition becomes

$$\mathrm{Re}[nF_1'(z)] - \tilde{\epsilon}\mathrm{Re}[nF_2'(z)] = -\mathrm{Re}[H_2(z)], \tag{8.2.5}$$

where

$$H_2(z) = \tilde{\epsilon}n + A_j\tilde{\epsilon}(1-\Gamma)n/(z-z_j). \tag{8.2.6}$$

The functions H_1 and H_2 are known and can be evaluated for some given boundary data z_b, therefore it is these functions that are to be used in the AAA and LS algorithms.

First, the collection of M_1 poles p_k in region 1 for V_1 and M_2 poles q_k in region 2 for V_2 are found using the AAA algorithm. This is achieved by finding interior and exterior poles relevant to the function $-\mathrm{Re}[H_1(z)]$ and labelling these as p_{dk} and q_{dk}, respectively, to signify these are the poles relating to the Dirichlet boundary condition. Similarly, the AAA algorithm is used again to find the poles relevant to the function $-\mathrm{Re}[H_2(z)]$ with these labelled as p_{nk} and q_{nk}. Combining the two sets then gives all the required poles $p_k = [p_{dk} \quad p_{nk}]$ and $q_k = [q_{dk} \quad q_{nk}]$. There may be the occurrence of 'over-counting': singularities resulting from V_1 also appear (unnecessarily) in the equation for V_2 and vice versa. Similarly, 'under-counting' may occur if a pole relevant to only one potential is not relevant to the combined quantity $V_1 - V_2$. These occurrences are inconsequential here as any exponential clustering of poles near corner singularities (Gopal and Trefethen, 2019c) is suitable for use in equations (8.2.1) and (8.2.2). As detailed in Sect.7.2, the routines *cleanup* and *pole control* are implemented to remove Froissart doublets.

Finally, an LS method similar to the one-domain problem is used to evaluate equations (8.2.3) and (8.2.5). However, the matrices and vectors are now 'twice as large' to account for the two potentials that are to be found. By creating a matrix of basis vectors A and the vector $H = -\mathrm{Re}[H_1(z); H_2(z)]$, the vector of unknown coefficients $c = [a_k; b_k; -c_k; -d_k]$ can be found once more with the backslash operation $c = H\backslash A$. As in Sect.7.2, construction of the matrix A can be coupled with an Arnoldi orthogonalisation (Brubeck et al., 2021) for added numerical stability. However, this additional step was not performed in this chapter as no such numerical instabilities were evident. Thus, the potentials V_1 (equation (8.2.1)) and V_2 (equation (8.2.2)) are found numerically. Using $\nabla[\mathrm{Re}[F(z)]] = \overline{F'(z)}$, the electric field vector expressed

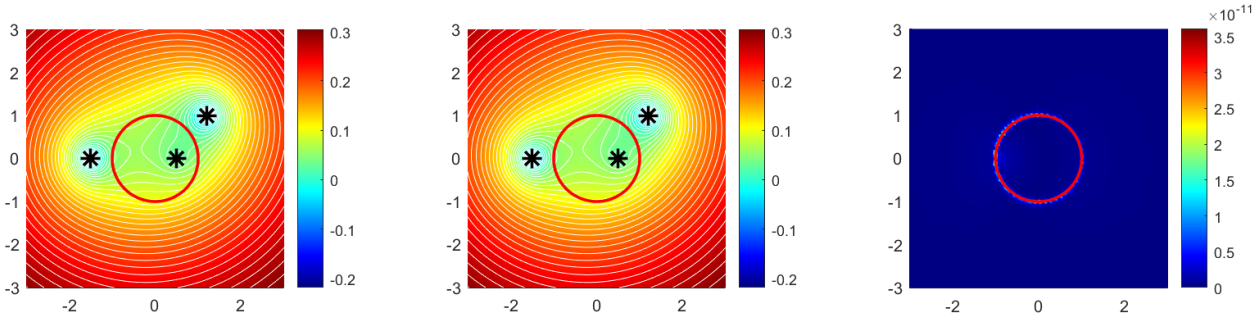

Figure 8.2: Comparison between the AAA-LS and exact solutions of the magnitude of the electric potential of a swarming arthropods scenario. The relative error (right) between the exact (left) and AAA-LS (centre) solutions is found to be of $\mathcal{O}(10^{-11})$.

in complex notation as $E = -\nabla V$ are obtained by

$$E_i = \overline{G_i'(z)} - \overline{F_i'(z)}, \tag{8.2.7}$$

where $i = 1, 2$ corresponds to regions 1 and 2 with G_i, F_i given in equations (8.2.1) and (8.2.2). As the interior and exterior of only a single flower is considered, this extension is known as the two-domain, singly-connected AAA-LS algorithm and is summarised in algorithm 3.

Algorithm 3 Two-domain, singly-connected AAA-LS algorithm

1: Input boundary data $\gamma : z = z_b$, interior point z_c, series truncations N_1, N_2 and boundary condition functions H_1, H_2 from equations (8.2.3) and (8.2.5).
2: Run AAA algorithm to find suitable interior and exterior poles p_{dk}, q_{dk} for the function $-\mathrm{Re}[H_1(z)]$. Use the routines *cleanup* and *pole control* to eliminate Froissart doublets.
3: Run AAA algorithm to find suitable interior and exterior poles p_{nk}, q_{nk} for the function $-\mathrm{Re}[H_2(z)]$. Use the routines *cleanup* and *pole control* to eliminate Froissart doublets.
4: Combine interior and exterior poles as $p_k = [p_{dk}, p_{nk}]$ and $q_k = [q_{dk}, q_{nk}]$.
5: Create matrix A of basis vectors. Use Arnoldi orthogonalisation if desired.
6: Run LS algorithm to find vector of coefficients $c = [a_k; b_k] = H \backslash A$.
7: Form V_1, V_2 from equations (8.2.1) and (8.2.2) and E_1, E_2 from equation (8.2.7).

To test the accuracy of this method, the numerical results from the two-domain, singly-connected AAA-LS algorithm were compared against the exact solutions given in Appendices A.1 and A.2 of Harris et al. (2024). For each of the three flower problems, a circular flower of unit radius was considered; for the uniform electric field only problem, ellipses with major and minor axes lengths a and b, respectively, were also considered. The interior and exterior potentials were computed on a 100×100 grid in the range $x, y \in [-3, 3]$ and the relative error between AAA-LS and exact solutions calculated at gridpoints. One such comparison of the swarming arthropods problem of Sect.8.1.3 is displayed in figure 8.2. Filled contour plots of the magnitude of the interior and exterior electric potentials V_1 and V_2 for the exact (left) and AAA-LS (centre) solutions are shown, as well as a plot of the relative error (right).

In the problem with no arthropods, the relative error was of $\mathcal{O}(10^{-16})$ for a circular flower, demonstrating excellent agreement between the AAA-LS method and the exact solution. This error was persistently small for near-circular ellipses, for example an ellipse of axes $a = 1.3$ and $b = 0.7$ gave an error of $\mathcal{O}(10^{-14})$. For more elongated ellipses, the error gradually increased yet remained comparatively small, with an ellipse of axes $a = 1.7$ and $b = 0.3$ giving an error of $\mathcal{O}(10^{-6})$. Furthermore, results from a finite element method (FEM) model produced in COMSOL 6.1 were also compared against the exact solution and found to have a consistent relative error of $\mathcal{O}(10^{-2})$ for all circle and ellipse examples performed. In problems involving arthropod(s) interior/exterior to a circular flower, the relative errors between AAA-LS and exact solutions were of $\mathcal{O}(10^{-11})$, for example the scenario in figure 8.2.

Two key results can be drawn from these tests. First, the two-domain, singly-connected AAA-LS method gives highly accurate solutions at the order of magnitude expected from the one-domain algorithm (Costa and Trefethen, 2023). This helps affirm that the method is performing correctly and gives us the confidence to continue using the algorithm for more complicated geometries. Second, the AAA-LS method consistently outperforms the more standard FEM solver in accuracy by several orders of magnitude. Combined with the algorithm's speed and simplicity, this makes the AAA-LS method a competitive tool to use, as has been noted since its development five years ago (Nakatsukasa et al., 2023).

8.3 Biologically motivated application: floral electrical fields

The two-domain, singly-connected AAA-LS method is now used to investigate several scenarios that illustrate possible pollinator-plant interactions. Note that a thorough analysis into the electrostatic interactions between plants and pollinators is not the focus of this thesis - the aim of this chapter is instead the introduction of the two-domain AAA-LS method in an applicable, biological context. Therefore, only some key results are here presented to give a glimpse of the outputs possible from the two-domain AAA-LS method. For a substantial investigation of the biological context, please see Harris et al. (2024) where the results of this section are also taken from.

In the upcoming results, the topic of interest is how a polarised dielectric flower alters the existing electrical field. Therefore, the following 'perturbation field' is defined to measure how the flower perturbs the source field

$$V_P = V - V_B, \tag{8.3.1}$$

$$\|\mathbf{E}_P\| = \|\mathbf{E} - \mathbf{E}_B\|, \tag{8.3.2}$$

where the subscript P indicates a perturbation value, B relates to a background electrical field (defined case-by-case), and the terms without subscripts are those of the full modelled scenario. The perturbation field is thus studied in the upcoming results since the external field is often stronger than the flower's polarised field and dominates results. From a sensory perspective, it is assumed that the source (e.g. bee) does not detect itself, and thus the perturbation field may be interpreted as the 'floral electrical information' from an arthropod's perspective.

Finally, it is worth reiterating that the results are non-dimensionalised and hold across varying source field strengths, flower sizes and scales, i.e. field strengths are proportional of the source field magnitude. For all upcoming contour plots of the perturbed electrical field magnitude (see for example figure 8.3), the flower is centred at the origin and has unit petal length. Therefore, the coordinates used in these plots ($x = [-4, 4], y = [-4, 4]$) can be thought of in terms of petal lengths: the perturbed electrical field at up to four petal lengths away from the flower centre is displayed. The dimensional implications of these results are discussed in section 8.4.

8.3.1 A pollinator's presence

The example of a flower polarising in the presence of a uniform electrical field is not presented in this section, see instead Sect.4.1 in Harris et al. (2024) and the associated figures 2,3 and 4. Instead, consider the case of a charged pollinator (a bee) in the presence of an uncharged flower. The perturbation field is then given by the bee's electrical field in the presence of a flower minus its field without a flower. The flower's relative permittivity is taken as $\epsilon_R = 20$, a representative value used throughout this section, and the point source (the bee) is located at $x = -5$, $y = 0$. The perturbation electrical field (colourmap) and potential (contours) are shown in figure 8.3 both internally and externally for flower shapes of two to five petals. The perturbation electrical potentials show horizontal symmetry for odd and even numbered petals, reflecting their alignment to the source field. Since the electrical field is the gradient of the potential, larger perturbation field magnitudes are seen for an increasing number of petals due to the stronger variation and therefore gradients in the flower geometries. Furthermore, the strongest regions of the perturbed electrical field are found internally in the flower, aligning with the background field.

Figure 8.4 then presents the values of the perturbation potentials (top row) and electrical field magnitudes (bottom row) along circles, centred on the flower, with different radii, $r = 2, 3, 4$, e.g. $1, 2$ and 3 petal lengths from the flower boundary. This is to investigate how a flower's polarisation could communicate information through the perturbed field. The perturbation potential is reasonably similar for all flower shapes, thus it simply indicates the presence of a flower. However, the perturbation field shows clear

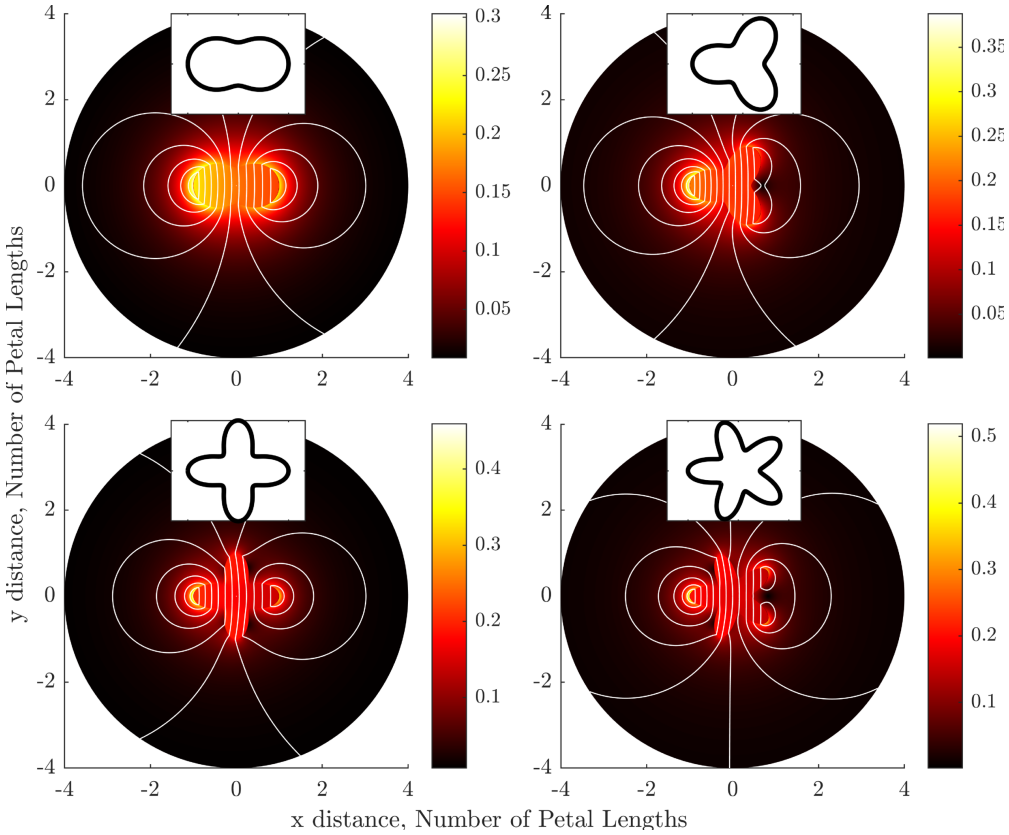

Figure 8.3: Perturbation electrical field magnitude $\|\mathbf{E}_P\|$ (colourmap) and potential V_P (contours) for an uncharged flower polarising in the presence of a charged pollinator (external point charge).

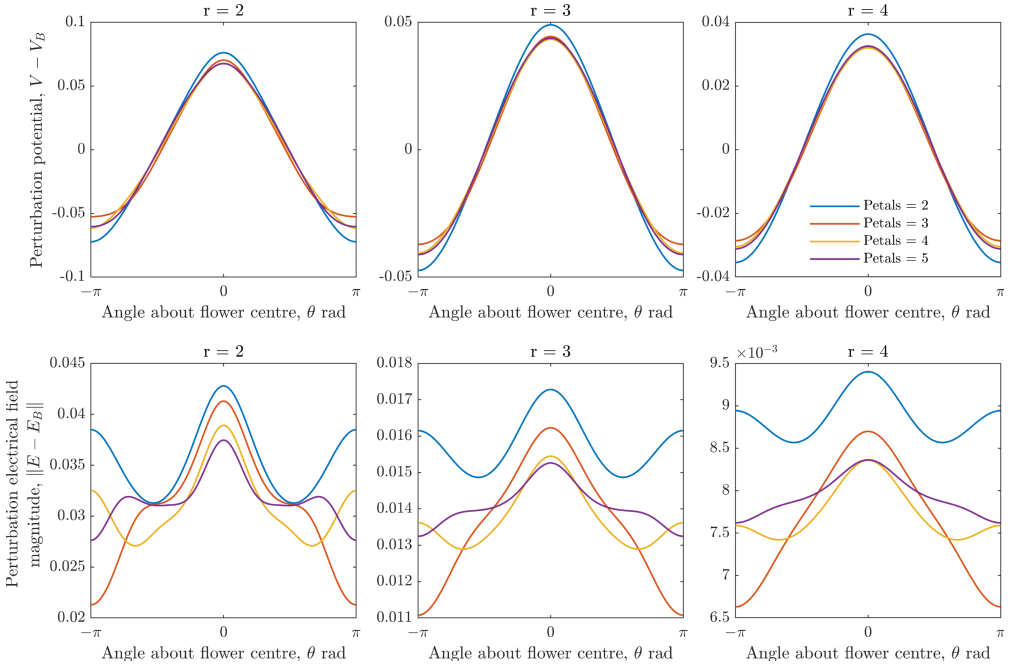

Figure 8.4: Perturbation electrical potential and field magnitude of flower polarisation in the presence of a pollinator (external point charge) at increasing radii from the flower centre, $r = 2, 3, 4$.

distinctions between the different flower shapes, and thus also conveys information about the flower morphology. Both signals decay with distance but still persist up to three petal lengths away. By $r = 4$, the electrical field variation is $\mathcal{O}(10^{-3})$, yet considering the acute sensitivity of arthropod mechanosensors and the non-dimensionalised results, it is not unreasonable to conclude that these variations will still be detectable and determinable by an arthropod. In Harris et al. (2024), it is also found that the perturbation (potential) signal decreases the further the arthropod is from the flower (see their figure 7) and that the signal is strongest if the arthropod is aligned with a flower petal (see their figure 8).

8.3.2 Two bees or not two bees?

Consider the scenario where two equally charged pollinators approach the same (five-petalled) flower from different directions. To see whether the flower communicates the presence of each pollinator to the other, the perturbation field here is that of the flower and pollinators compared to the scenario without the flower. The first arthropod is located at $(-5, 0)$ and the second at $(-5\cos(\theta_B),\ 5\sin(\theta_B))$, for $\theta_B = \pi/4,\ \pi/2,\ 3\pi/4$, and π. Figure 8.5 (top four plots) once again shows the perturbation electrical field (colourmap) and potential (contours) for each scenario, and the radial measures of the perturbation potential (bottom left) and field magnitude (bottom right) at distance $r = 2$. In comparison to figure 8.3, the additional arthropod seeks to reorientate the local perturbation field, in general causing the horizontal symmetry to be lost. The presence of the flower thus strongly influences the interaction of multiple pollinators and the flower can electrically communicate the presence of several pollinators through the change in local field geometry and strength.

Consider now the varying location of the second arthropod. When located on the same side of the flower, the two arthropods serve to increase the flower's polarisation, enhancing its electrical field contribution and thus its perturbation field. However, as the second arthropod moves around the flower, each pollinator's polarisation effect begins to cancel out, greatly reducing the floral signal here. Thus, at each location around the flower, the perturbation field takes a distinct form; the arthropods not only know of each other's presence but also the location of the other arthropod. Most interestingly, when the pollinators are on opposite sides, the diminishing of the perturbation field and potential to zero is a clear indicator of the other's presence.

8.3.3 Electrical subterfuge

Finally, consider a predator-prey interaction. This may be interpreted as either, 1) a predator (such as a crab spider) hiding within the flower's petals, awaiting the arrival of a charged pollinator (see e.g. Huey and Nieh (2017)); or, 2) a charged predator (such as a wasp) approaching a flower upon which potential

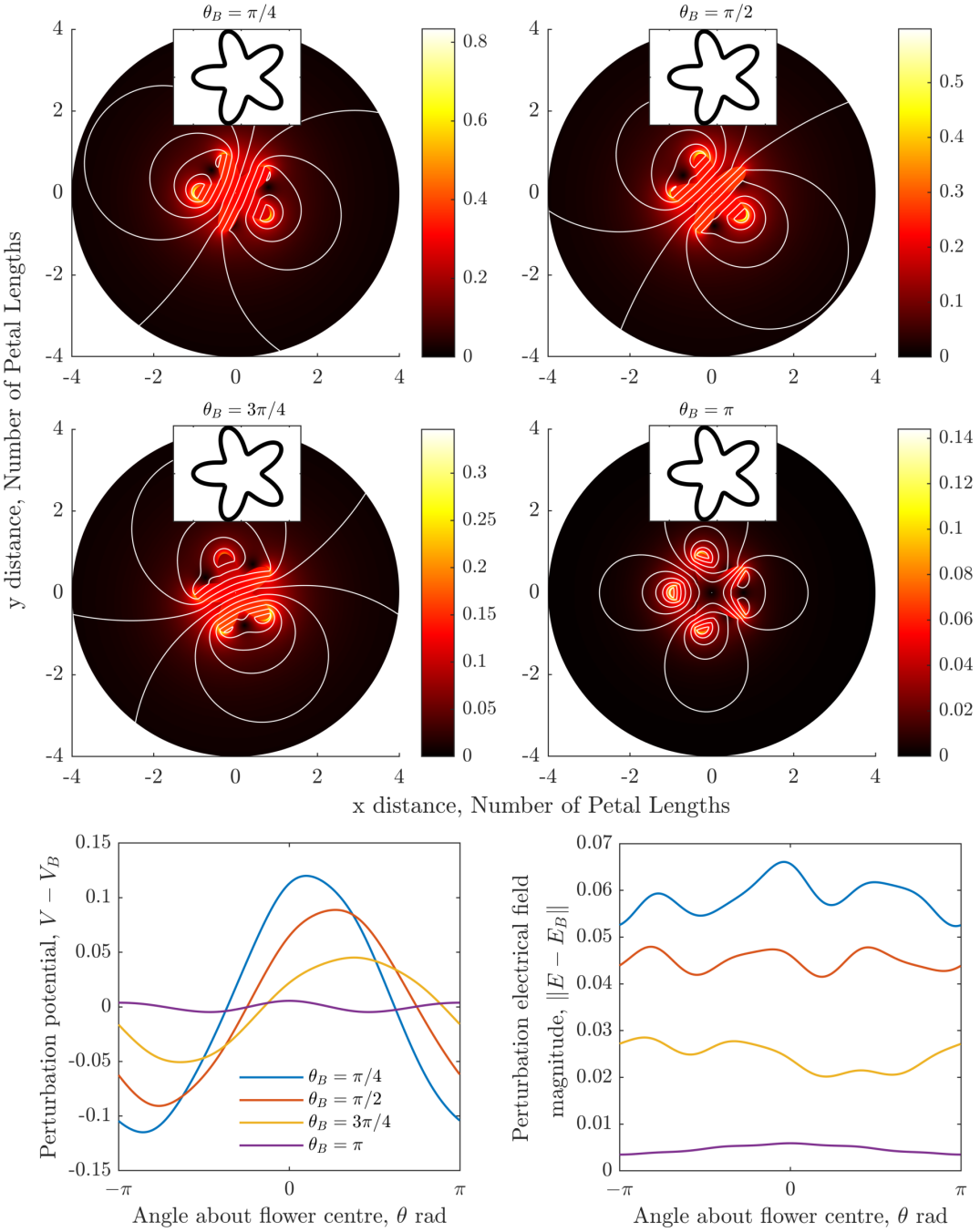

Figure 8.5: Top four plots: Perturbation electrical field magnitude $\|\mathbf{E}_P\|$ (colourmap) and potential V_P (contours) for an uncharged five-petal flower polarising in the presence of two charged pollinators (external point charges at $(-5, 0)$ and $(-5\cos(\theta_B),\ 5\sin(\theta_B))$, for $\theta_B = \pi/4,\ \pi/2,\ 3\pi/4$, and π). Bottom row: Perturbation electrical potential and field magnitude, each at $r = 2$.

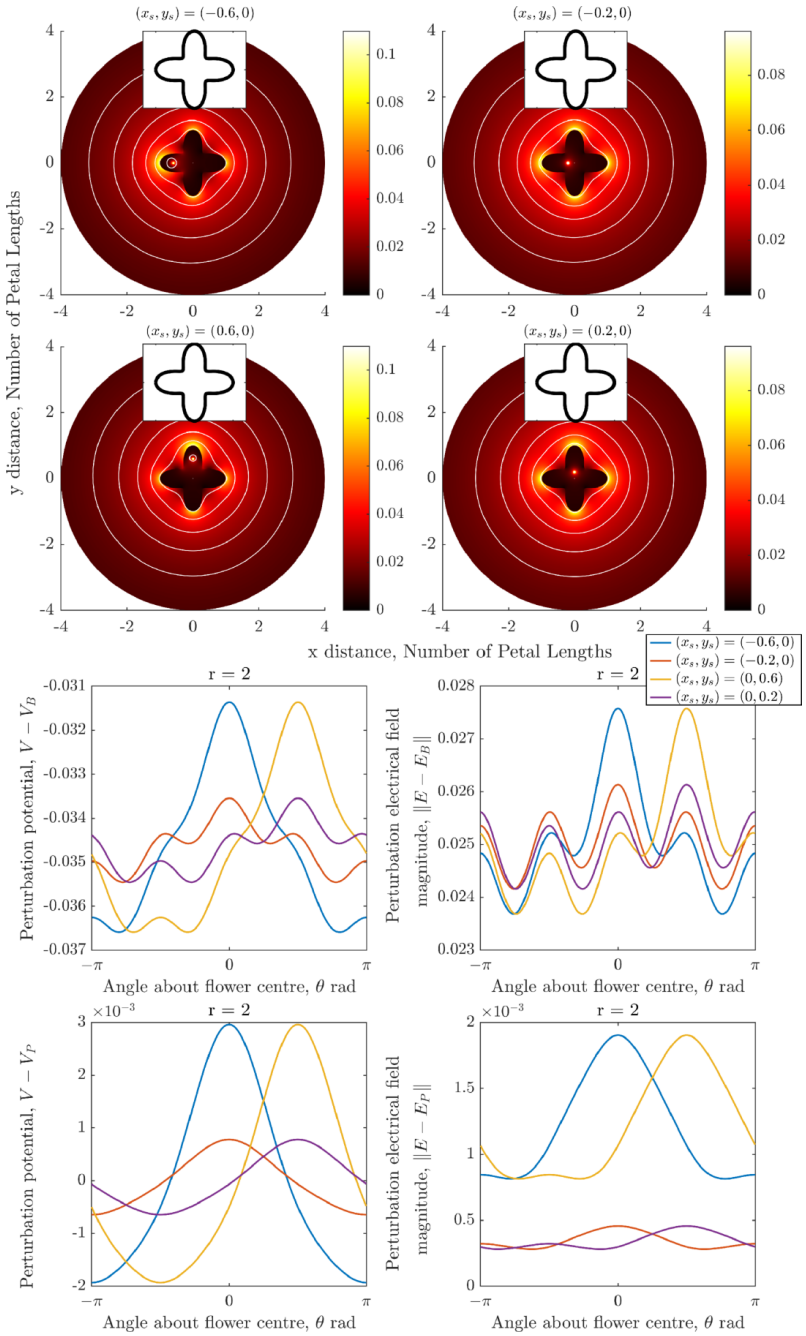

Figure 8.6: Perturbation electrical field magnitude (colourmap) and potential (contours) for flower polarisation in the presence of a charged pollinator (external charge, $x = -5, y = 0$) and a spider (internal charge, $(x_i, y_i) = (-0.6, 0),\ (-0.2, 0),\ (0, 0.2),\ (0, 0.6)$). The colourmap/contour plots and third row compare the pollinator-spider scenario to that without a spider. The bottom row compares the pollinator-spider scenario to the pollinator pollen scenario, e.g. a point charge at $(0, 0)$.

prey is located. This scenario is similar to the pollen problem investigated in Sect.4.2.2. in Harris et al. (2024), see their figure 10, where a pollen-rich flower is modelled with a point charge (the pollen) in its centre of equal and opposite charge to the exterior arthropod. Here, the flower-dwelling arthropod is also treated as an equal and opposite point charge on the flower.

Examining a four-petal flower, the perturbation field is given by comparing the electrical field with and without the flower-dweller present. This is to assess how 'far' the electrical presence of the dweller may be detected and whether it can successfully 'hide' itself within the flower. The exterior point charge is located at $(x_e, y_e) = (-5, 0)$ and four internal positions of the internal charge are considered: $(x_i, y_i) = (-0.6, 0),\ (-0.2, 0),\ (0, 0.2),\ (0, 0.6)$. Figure 8.6 shows the colourmaps and contour plots (top two rows) of these four scenarios, and the radial measures of the perturbation potential and field magnitude compared to the scenario without the flower-dweller present (third row) and to the pollen scenario of Sect.4.2.2. in Harris et al. (2024).

When the flower-dweller is closer to the petal boundary, $(-0.6, 0)$ and $(0, 0.6)$, the surface and contour plots show stronger perturbation electrical field magnitudes and greater deformation in the potential contours near the flower. The radial metrics displayed in the third row (the comparison with and without internal charge) show this effect at two petal lengths from the flower centre. However, away from the peak, all other perturbation field values are of a similar order. Thus, overall, when a charge is closer to the flower centre it leads to a less distinct electrical field perturbation. In comparison to the pollen scenario (bottom row), the difference between the two cases are very small for all cases. Thus, if a flower-dwelling arthropod seeks to cloak/hide itself on the flower, it is best to remain closer to the centre of a flower and hope its adversary mistakes it for pollen.

8.4 Discussion

In this chapter, the AAA-LS method of Trefethen (2020); Costa and Trefethen (2023) was extended to solve two-domain, singly-connected Laplace problems. This method was able to compute the electrostatic potential and resulting electrical field for problems with multiple point sources/sinks (internal or external to the polarisable material) and a uniform background field, both of which cause an object with a fixed boundary to polarise. The algorithm was then applied to a biological context: the electrostatic interaction between arthropods (generators of the electric field) and flowers (polarisable, dielectric objects within the field). As seen in Sect.8.3, flowers produce distinct electrical 'signatures' within the electrical field, revealing information about the flower's shape, the quantity of pollen available and the presence of nearby predators.

As noted previously, the two-domain extension of the AAA-LS method presented in this chapter is new. The added mathematical complexity lies in the boundary conditions: instead of a single boundary condition relating the harmonic function ϕ to a given function h, there now exists a coupled pair of boundary conditions involving the two unknowns V_1 and V_2. Handling this added complexity by considering the boundary conditions of the combined quantity $V_1 - V_2$ still uses the fundamentals of the original, one-domain AAA-LS method. However, quantities such as the list of poles and the basis vector matrix are now 'twice as large' to account for the finding of two harmonic functions V_1, V_2 across two domains.

While a thorough review of the floral-arthropod electrostatic interaction is presented in Harris et al. (2024), the key results are here stated. First, while the model of this chapter is dimensionless, adding in suitable dimensions finds that the electrical disturbances caused by flowers in an electrical field are strong enough to deflect arthropod mechanosensors (Palmer et al. (2021); Palmer et al. (2022)), meaning that arthropods would be able to detect these perturbations a number of petal lengths away from the flower. Second, different floral shapes displayed strong qualitative and quantitative changes in the electrical field, making different floral geometries electrically distinct. Third, additional information about the available pollen on, and the location of other arthropods around, the flower is also conveyed through the electrical field. It is in the best interest of a predator to minimise its disturbance of the electrical field in order to hide itself more absolutely from unsuspecting prey.

In the work of Harris et al. (2024), the results of the AAA-LS method are also compared against equivalent results produced in COMSOL 6.1 using a 3D FEM model - see their Sect.5 and associated figure 13. It is concluded that there is notable qualitative agreement between the AAA-LS and FEM results. While this agreement is stronger for the unphysical case of a thicker flower, even some of the salient 3D features of the thinner flower scenario are still well captured in the AAA-LS results, thus showing the power of the 2D analysis of this chapter for examining these biological cases broadly.

There are several areas of work that would benefit from further theoretical and empirical research. First, the two-domain, singly-connected AAA-LS method can be readily adapted to a variety of additional problems, including fluid flow scenarios (e.g. potential flows) or magnetic fields. Another such two-domain problem is explored in Ch.9. Second, while only a single flower was considered in this chapter, multiple flowers (perhaps of heterogeneous materials) could be incorporated into the system to consider the electrostatic interaction between arthropods and an entire meadow of flowers. A further extension of the AAA-LS algorithm to a so-called 'two-domain, multiply-connected' scenario would need to be developed: this is plausible but beyond the scope of this thesis.

Third, more physically relevant descriptions of flowers and arthropods could be incorporated. In this chapter, the flowers have been treated as dielectrics and the arthropods as point charges. Whilst petals and leaves generally present dielectric properties on their surface, conductivity can play a significant role in floral electrostatics. For example, rainfall will increase surface conductivity and change their electrical properties. To model the flower as a conductive medium, the interior Laplace equation would become a Poisson equation with non-constant RHS, unlike the Poisson equations with constant RHS considered in Ch.4 and Ch.9. In addition, the point charge approximation is most appropriate when the petal length is much greater than the arthropod/pollen size. Modelling the arthropods as rods or ellipses may be more appropriate when considering smaller floral scales.

Fourth, the system can be readily adapted and used to investigate time-dependent predator-prey and pollinator-flower dynamics. Under the assumption that the electrical fields vary quasi-statically compared to the timescale of insect movement and sensation (Palmer et al., 2023b), moving arthropods and dynamic floral responses can be readily incorporated. This is a potentially fruitful avenue of future work, with recent results highlighting the role of time-varying electrostatics for predators and prey (England and Robert, 2024; O'Reilly et al., 2024).

Finally, systematic, empirical 3D modelling would further reveal the ecological relevance of floral signals. While the 2D results match well for thick flower petals, considering 3D effects are important in the true, biological setting. In general, the 2D results provide a qualitative intuition and understanding of the 3D scenario: the speed and adaptability of the AAA-LS method allows for a number of biological scenarios to be analysed and biologically relevant conclusions to be drawn which warrant further empirical investigation. Gaining a deeper understanding of environmental and ecological electrical interactions will add to our knowledge of plant-pollinator co-evolution and enhance our understanding of the sensory electroreceptive mechanism.

Chapter 9

Vortex patch equilibria

Previously in Ch.8, an extension of the AAA-LS method to solve two-domain Laplace problems was introduced and applied to a problem in biological electrostatics: the polarisation of a flower when exposed to the electrical charge produced by a background field and/or nearby, positively charged arthropods. In this chapter, the two-domain AAA-LS algorithm is applied to a second problem, this time in the field of vortex dynamics. A singly connected vortex patch - a finite region of fluid flowing with constant, non-zero vorticity - surrounded by irrotational flow is considered and equilibrium solutions are sought - solutions where the shape of the patch is unchanging over time in some rotating frame. Exact and numerical solutions to this problem have been found previously, for example in the works of Saffman (1995), Wu et al. (1984) and Xue et al. (2017). No new solutions are given in this chapter, instead the aim is to demonstrate that the two-domain AAA-LS method can reproduce these known solutions to a degree of accuracy comparable with the original one-domain AAA-LS method. The two-domain AAA-LS algorithm is thus presented here as an alternative to contour dynamics methods which have been used previously in the literature to solve such problems in vortex dynamics, see e.g. Wu et al. (1984); Dritschel (1985); Xue et al. (2017). The work in this chapter was completed in Harris and McDonald (2024b).

9.1 Vortex patch model

Consider the singly connected vortex patch problem shown diagrammatically in figure 9.1. The vortex patch has (conformal) radius L and positive (without loss of generality) constant vorticity ω. Define the Jordan curve γ as the boundary separating the interior vortex patch (region 1) and the exterior fluid (region 2). Both interior and exterior fluids are incompressible and inviscid, and the exterior flow is irrotational. The stream function ψ and the velocity $\boldsymbol{u}$ are continuous across the boundary γ; the vorticity

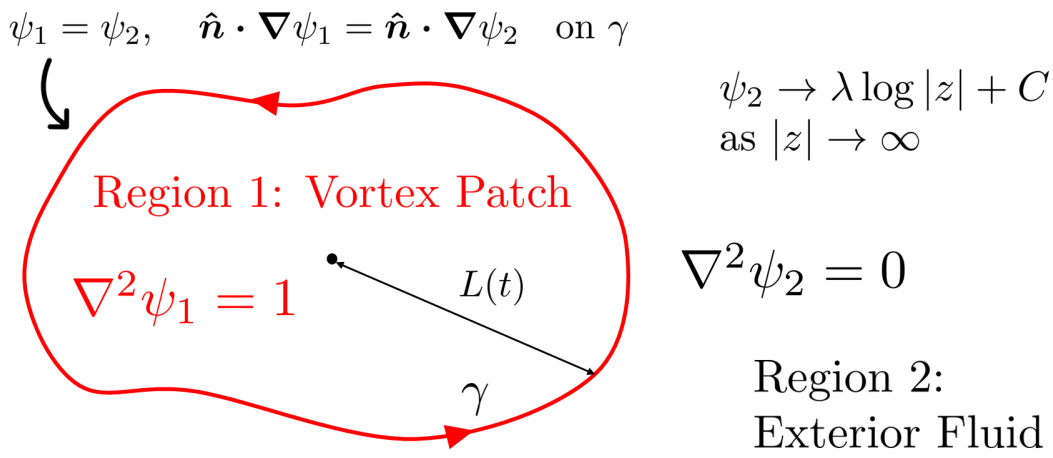

Figure 9.1: The singly connected vortex patch problem showing the non-dimensional governing equations for the stream function, boundary conditions on the interface γ of the two domains (regions 1 and 2) and the far field condition at infinity.

jumps from zero to ω. In the far field, the vortex patch appears as a line vortex with circulation $\Gamma = \omega A$, where A is the area enclosed by γ. The scalings $\boldsymbol{x} = L\boldsymbol{x}^*$ and $\psi = (\omega L^2)\psi^*$ are introduced, where starred variables are dimensionless. Dropping stars immediately, the non-dimensional system is thus

$$\nabla^2\psi_1 = 1 \quad \text{in } 1, \tag{9.1.1}$$

$$\nabla^2\psi_2 = 0 \quad \text{in } 2, \tag{9.1.2}$$

$$\psi_1 = \psi_2 \quad \text{on } \gamma, \tag{9.1.3}$$

$$\hat{\boldsymbol{n}} \cdot \boldsymbol{\nabla}\psi_1 = \hat{\boldsymbol{n}} \cdot \boldsymbol{\nabla}\psi_2 \quad \text{on } \gamma, \tag{9.1.4}$$

$$\psi_2 \to \lambda \log|z| + C \quad \text{as } r \to \infty, \tag{9.1.5}$$

where $\lambda = A/(2\pi L^2)$ and the constant $C = A\log|L|/(2\pi L^2)$; the value $L = 1$ is taken throughout this chapter unless stated otherwise and thus the constant C can be ignored. To find the velocity vector, note that $\boldsymbol{u} = \hat{\boldsymbol{z}} \times \boldsymbol{\nabla}\psi = -\psi_y\hat{\boldsymbol{x}} + \psi_x\hat{\boldsymbol{y}}$. Using complex notation where $\nabla = \partial_x + i\partial_y$, the velocity is $u + iv = i\nabla\psi = i(\psi_x + i\psi_y) = -\psi_y + i\psi_x$.

In this chapter, vortex patch equilibria are sought - solutions where the vortex patch is either stationary or steadily translating/rotating. The shape of the vortex patch is thus invariant up to this steady translation or rotation. This implies that the vortex patch boundary is a stream line; the normal velocity v_n of fluid at the vortex patch boundary is zero with tangential velocity matching at the boundary between the interior and exterior fluid. These conditions are encapsulated in the boundary condition equations (9.1.3) and (9.1.4).

9.2 Numerical method

Numerical solutions for the stream function ψ, which satisfies equations (9.1.1) to (9.1.5), are found using the two-domain AAA-LS algorithm, summarised in algorithm 3 in Sect.8.2. In this chapter, an additional step is needed: the substitution $\psi_1 = \widetilde{\psi_1} + |z - z_c|^2/4$ transforms the interior Poisson equation (9.1.1) into Laplace's equation for $\widetilde{\psi_1}$. Note that z_c is the centre of the vortex patch, though it is assumed that $z_c = 0$ throughout this chapter. The exterior stream function ψ_2 is also modified as $\psi_2 = \widetilde{\psi_2} + \lambda \log|z - z_c|$ so that $\widetilde{\psi_2}$ decays in the far field. The variables $\widetilde{\psi_1}, \widetilde{\psi_2}$ can be written as $\widetilde{\psi_i} = \mathrm{Re}[F_i(z)]$ where $F_i(z)$ is analytic in the respective domain of $\widetilde{\psi_i}$ (Trefethen, 2020; Costa and Trefethen, 2023). A rational approximation for each F can then be written as

$$\psi_1 = \frac{|z|^2}{4} + \mathrm{Re}[F_1(z)] = \frac{|z|^2}{4} + \mathrm{Re}\bigg(\sum_{k=0}^{N_1} a_k (z - z_c)^k + \sum_{k=1}^{M_1} \frac{b_k}{z - p_k} \bigg), \tag{9.2.1}$$

$$\psi_2 = \lambda \log|z| + \mathrm{Re}[F_2(z)] = \lambda \log|z| + \mathrm{Re}\bigg(\sum_{k=1}^{N_2} c_k (z - z_c)^{-k} + \sum_{k=1}^{M_2} \frac{d_k}{z - q_k} \bigg), \tag{9.2.2}$$

where N_1 and N_2 are series truncations; the values $N_1 = N_2 = 20$ are used in this chapter.

Following the procedure in Sect.8.2, the Dirichlet and Neumann boundary conditions are rewritten in terms of the combined quantity $\psi_1 - \psi_2$. Substituting equations (9.2.1) and (9.2.2) into the Dirichlet boundary condition equation (9.1.3) and rearranging gives

$$\mathrm{Re}[F_1(z)] - \mathrm{Re}[F_2(z)] = \lambda \log|z| - \frac{|z|^2}{4} = H_1(z). \tag{9.2.3}$$

For the Neumann boundary condition equation (9.1.4), note that $\hat{\boldsymbol{n}} \cdot \boldsymbol{\nabla} \psi = \mathrm{Re}[n \overline{\nabla} \psi]$, where $n = n_x + i n_y$ and ∇ are complex representations of the corresponding vectors. Note also that $\overline{\nabla} = 2\partial_z$ and that $|z|^2 = z\overline{z}$. Furthermore, equation (5) from Trefethen (2018) gives that $\overline{\nabla}[\mathrm{Re}[F(z)]] = F'(z)$. Therefore, equation (9.1.4) becomes

$$\mathrm{Re}[nF_1'(z)] - \mathrm{Re}[nF_2'(z)] = \lambda \mathrm{Re}[nz^{-1}] - \frac{1}{2}\mathrm{Re}[n\overline{z}] = H_2(z). \tag{9.2.4}$$

These conditions can now be written as the product $Ac = H$ where A is a matrix of suitable basis vectors, $c = [a_k; b_k; -c_k; -d_k]$ is the vector of unknown coefficients and $H = [H_1(z); H_2(z)]$ is a vector of given functions. The unknown c can then be found with a standard LS fitting procedure using the backslash operator $c = H \backslash A$.

Suitable simple poles are found with the AAA algorithm using both the functions $\mathrm{Re}[H_1]$ and $\mathrm{Re}[H_2]$.

The union of these poles are then taken and separated into the exterior p_k and interior q_k poles as used in equations (9.2.1) and (9.2.2). As in Sect.8.2, the routines *cleanup* and *pole control* are implemented to remove Froissart doublets. An Arnoldi orthogonalisation could also be implemented in the construction of the Vandermonde matrix A (see e.g. Brubeck et al. (2021)), though this was not performed in this chapter as solutions were sufficiently stable.

To find the velocity vector in each region, recall that $u + iv = i\nabla\psi$ and that $\nabla[\mathrm{Re}[F(z)]] = \overline{F'(z)}$. Therefore

$$u_1 + iv_1 = i\left(\frac{z}{2} + \overline{\sum_{k=0}^{N_1} k a_k (z - z_c)^{k-1} - \sum_{k=1}^{M_1} \frac{b_k}{(z - p_k)^2}}\right), \tag{9.2.5}$$

$$u_2 + iv_2 = i\left(\frac{\lambda}{\overline{z}} - \overline{\sum_{k=1}^{N_2} k c_k (z - z_c)^{-(k+1)} - \sum_{k=1}^{M_2} \frac{d_k}{(z - q_k)^2}}\right). \tag{9.2.6}$$

The accuracy and robustness of the AAA-LS algorithm is then be tested by comparing its outputs with known solutions.

9.3 Rankine and Kirchhoff vortices

Two exact equilibrium solutions of equations (9.1.1) to (9.1.5) are known - see chapter 9 of Saffman (1995) and the references therein. The simplest solution is the Rankine vortex: a circular vortex patch of radius L and vorticity ω. Setting $\psi_1 = \psi_2 = 0$ on γ, the dimensionless solution for the stream function is

$$\psi = \begin{cases} \frac{1}{4}(|z|^2 - 1), & z \in 1, \\ \frac{1}{2}\log|z|, & z \in 2, \end{cases} \tag{9.3.1}$$

with velocity

$$u + iv = \begin{cases} \frac{iz}{2}, & z \in 1, \\ \frac{iz}{2|z|^2}, & z \in 2. \end{cases} \tag{9.3.2}$$

The Kirchhoff vortex is then a generalisation of equation (9.3.2) to an elliptical vortex patch of constant vorticity ω with semi axes of lengths a and b and, in a rotating frame, a fixed angle φ between its major axis and the real z axis. Note, without loss of generality, the choice $\varphi = 0$ can be made but a non-zero choice is made here in order to provide a more stringent test of the AAA-LS method. The conformal map

from the exterior of the unit disk to the exterior of this ellipse is

$$z = e^{i\varphi}\Big(\alpha\zeta + \frac{\beta}{\zeta}\Big), \quad \alpha = \frac{a+b}{2}, \;\; \beta = \frac{a-b}{2}. \tag{9.3.3}$$

By definition, the conformal radius is $\alpha = L$ and so define the new dimensionless quantity $B = \beta/L$, and use ω^{-1} as the timescale. On the boundary of the ellipse, the Schwarz function $\overline{z} = \Phi(z)$ can be written as

$$\overline{z} = \left(Be^{-2i\varphi}z\right) + \left(\frac{2(1-B^2)}{z + \sqrt{z^2 - 4Be^{2i\varphi}}}\right) = F(z) + G(z). \tag{9.3.4}$$

By equation (9.2.11) from Saffman (1995), the velocity field is defined by

$$u - iv = \begin{cases} -\frac{i}{2}(\overline{z} - F(z)), & z \in 1, \\ -\frac{i}{2}G(z), & z \in 2, \end{cases} \tag{9.3.5}$$

and therefore

$$u - iv = \begin{cases} -\frac{i}{2}(\overline{z} - Be^{-2i\varphi}z), & z \in 1, \\ -i(1-B^2)/(z + \sqrt{z^2 - 4Be^{2i\varphi}}), & z \in 2. \end{cases} \tag{9.3.6}$$

The AAA-LS method is used to compute the Rankine vortex and an example Kirchhoff vortex with $\varphi = \pi/6$ and semi axes $a = 1.5$ and $b = 0.5$. The AAA-LS solutions are shown in the left column of figure 9.2 for the Rankine (top row) and Kirchhoff (bottom row) vortices, with the exact solutions given in the centre column. To test the accuracy of the AAA-LS method in comparison to the exact solutions, the following relative error (RE) of known quantities is found

$$RE = \left|\frac{\Phi_A - \Phi_E}{\Phi_E}\right| \tag{9.3.7}$$

where Φ_A is the quantity calculated by the AAA-LS method and Φ_E the exact solution. For cases where $\Phi_E \approx 0$ (in particular the criteria $\Phi_E = \mathcal{O}(10^{-4})$ is used in this chapter), the absolute error (AE) is instead used

$$AE = \big|\Phi_A - \Phi_E\big|. \tag{9.3.8}$$

For the Rankine vortex, the stream function is the compared quantity, hence $\Phi = \psi$ where $\Phi_E = \psi_E$ is given by equation (9.3.1). For the Kirchhoff vortex, the magnitude of the velocity is the compared quantity, thus $\Phi = |u + iv|$ where Φ_E is found by taking the magnitude of the exact velocity $u - iv$ in equation (9.3.6). For each point in the 500×500 grid of each subplot of figure 9.2, the relative error of the compared quantity is calculated and plotted in the right column. For the stream function of the Rankine

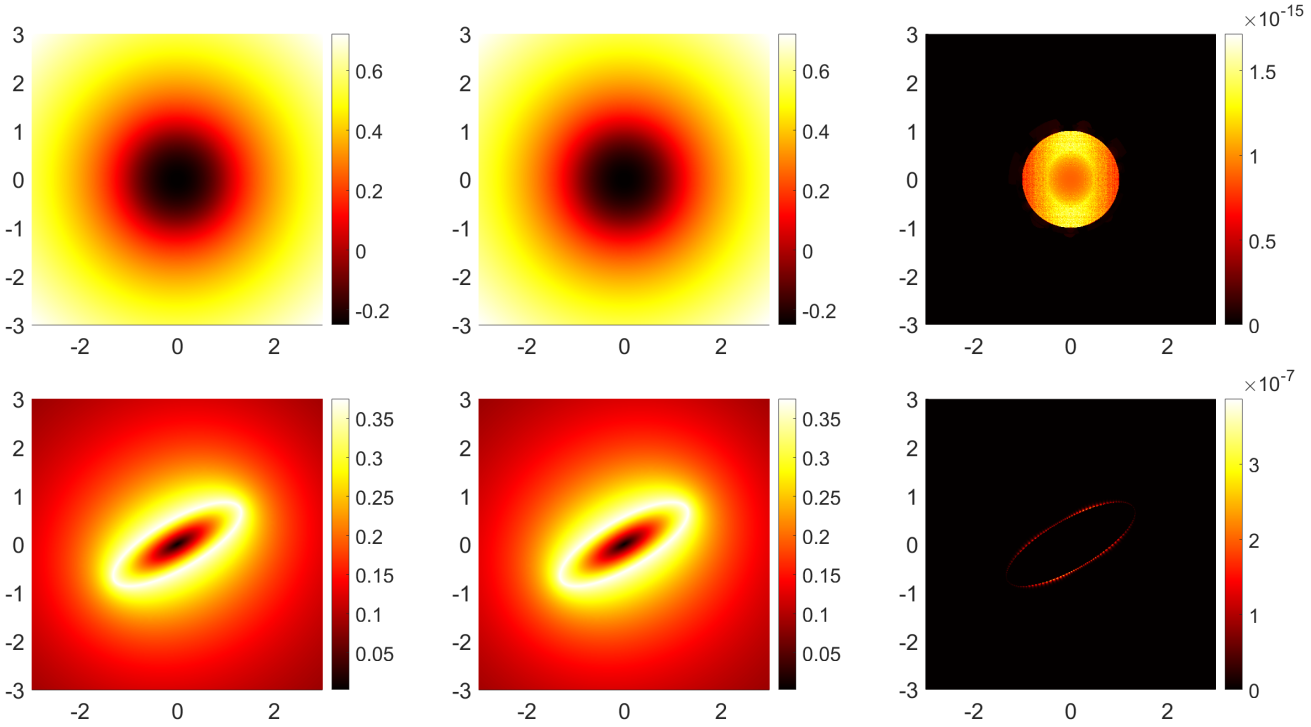

Figure 9.2: Comparison of the AAA-LS and exact solutions of the Rankine vortex and a Kirchhoff vortex with semi axes $a = 1.5$ and $b = 0.5$ and at an angle $\varphi = \pi/6$ to the real axis. The relative error (right column) between the AAA-LS (left column) and exact (centre column) solutions are found for the stream function of the Rankine vortex (top row) and the velocity magnitude of the Kirchhoff vortex (bottom row).

vortex, there is an $\mathcal{O}(10^{-15})$ error while for the magnitude of the fluid velocity of the Kirchhoff vortex, there is an $\mathcal{O}(10^{-7})$ error. This is comparable to the error for solving Laplace's equation with Dirchlet boundary conditions in one domain (Trefethen, 2020; Costa and Trefethen, 2023).

The Kirchhoff ellipse rotates steadily with angular velocity Ω given by Saffman (1995)

$$\Omega = \frac{1 - B^2}{4}, \tag{9.3.9}$$

which has been non-dimensionalised as in Sect.9.1. Subtracting the associated stream function $\psi = \Omega r^2/2$ and velocity $u + iv = i\Omega z$ from the corresponding global quantities then gives a vortex patch with zero normal velocity on its boundary i.e. $\hat{\boldsymbol{n}} \cdot \boldsymbol{v} = v_n = 0$. That is, its boundary is a streamline as required for equilibrium. The error in this normal velocity is obtained using $\Phi = v_n$ in equation (9.3.8); note that the absolute error is used here since $\Phi_E = 0$. Figure 9.3 shows this absolute error at boundary points with $\arg(z) = \theta$ of the ellipse in figure 9.2; the AAA-LS solution is accurate to $\mathcal{O}(10^{-9})$.

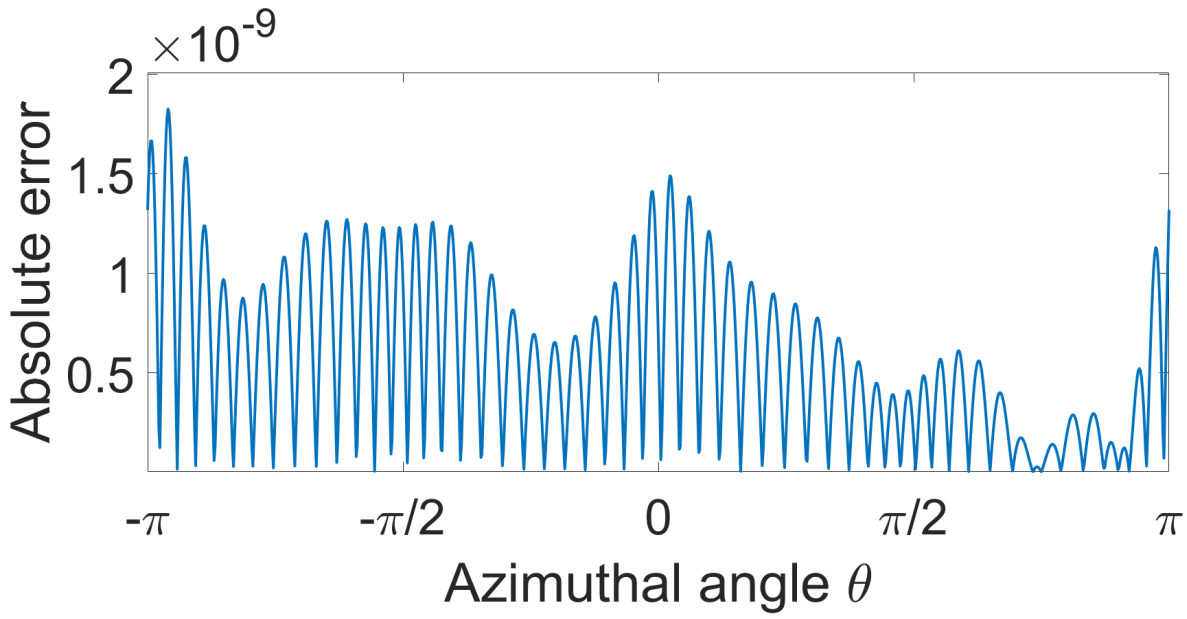

Figure 9.3: Absolute error of the normal velocity on the vortex patch boundary of the AAA-LS solution in the equilibrium frame.

9.4 Wu, Overman and Zabusky equilibria

Wu, Overman and Zabusky numerically compute $m-$fold symmetric equilibrium solutions ('V-states') to the vortex patch system of equations (9.1.1) to (9.1.5) (Wu et al., 1984). The aim of this section is to combine their iteration algorithm (referred to as 'WOZ' hereafter) with the AAA-LS method developed in section 9.2, and reproduce results from Wu et al. (1984). In essence, the WOZ algorithm (which is summarised in appendix B) takes some initial vortex patch and iterates the boundary towards a shape where the normal velocity v_n of fluid on the boundary approaches zero, to within some tolerance level.

Since an $m-$fold symmetric equilibrium necessarily retains its symmetry throughout the iterative process, only a $1/2m$ segment of the boundary need be considered. The vortex patch boundary γ consists of N equispaced boundary points, where Z is the list of these points $z = x + iy$. Then Z_s is the list of the $M+1 < N$ points which make up the desired $1/2m$ segment of the boundary. At each iteration n, the new radial distance $R(\theta)^{(n+1)}$ is found for each boundary point with $\arg(z) = \theta$ and the boundary updated accordingly. The end points z_1 and z_{M+1} are held fixed with $R_1^{(n)} = R_1^{(1)} = R_a$ and $R_{M+1}^{(n)} = R_b$ for all iterations n where R_a and R_b are some constants.

Consider the $m-$fold symmetric rotating V-states investigated in Sect.6.1 of Wu et al. (1984). For a given

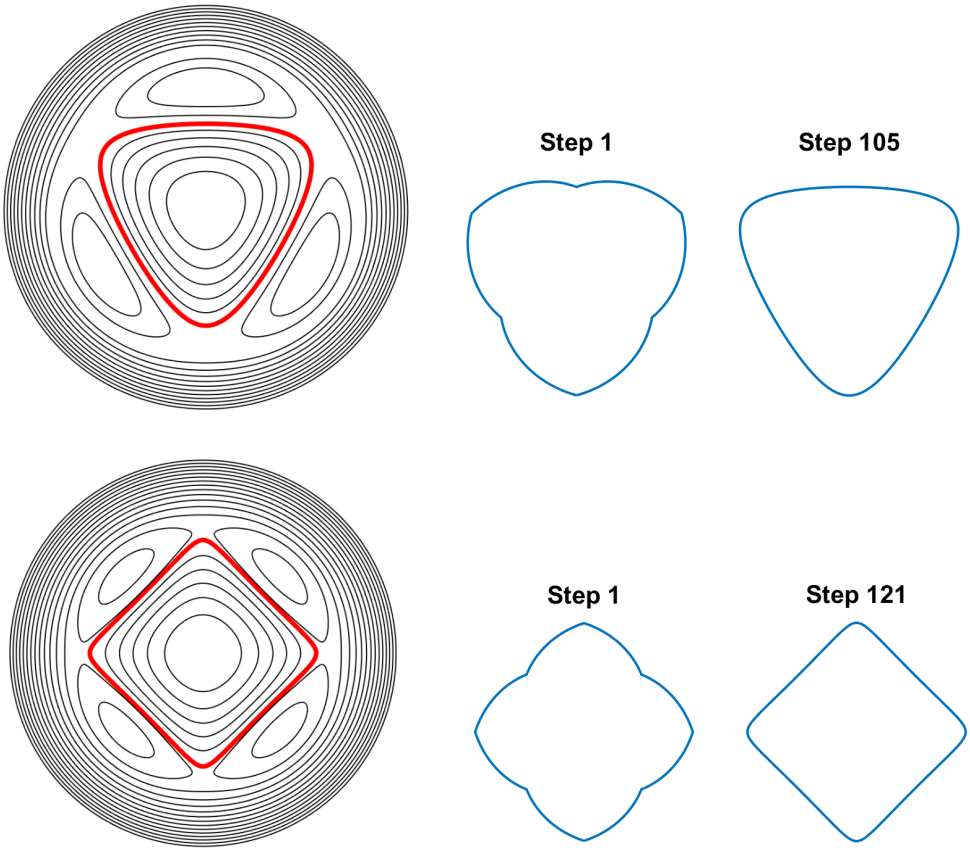

Figure 9.4: Streamline plots of the equilibrium solutions of the AAA-LS + WOZ algorithm on $m-$fold rotating V-states (left, the boundary of the patch is shown in red), with separate plots of the initial (centre) and final (right) shapes of the vortex patch. Top: three-fold shape, $R_a = 1.39256$, 105 iterations. Bottom: four-fold shape, $R_a = 1.34127$, 121 iterations.

starting value of R_a, the initial state of the vortex patch is defined by

$$R(\theta) = R_a + \frac{m^2}{\pi^2}(1 - R_a)\left(\theta + \frac{\pi}{2}\right)\left(\frac{2\pi}{m} - \theta - \frac{\pi}{2}\right), \tag{9.4.1}$$

for the $1/2m$ segment of the vortex patch boundary $-\pi/2 \leq \theta \leq \pi/m - \pi/2$; note that this fixes $R_b = 1$. The results from the AAA-LS + WOZ algorithm are compared with the results in Wu et al. (1984) for the symmetries $3 \leq m \leq 6$ with a selection of $M = 120$ points taken on each $1/2m$ segment, following the choice in Wu et al. (1984). The iteration process in each case continues until the tolerance $\epsilon = \mathcal{O}(10^{-6})$ (see equation (B.0.5)) is reached or until $n_{max} = 500$ iterations are computed. All results presented in this chapter converge to an equilibrium in under n_{max} iterations. Note that the AAA-LS solutions are not scaled with respect to R_a to allow for easier direct comparison with the WOZ solutions.

Figure 9.4 displays streamline plots of the equilibrium solutions for the three- (top) and four-fold (bottom) rotating V-shapes (left, with the boundary of the vortex patch highlighted in red), where the initial (centre) and final steady state (right) shapes are also plotted separately. The choice of R_a for each shape is given in

the figure caption as is the number of iterations computed. There is a qualitative agreement between the results in figure 9.4 and those displayed in e.g. figure 7 of Wu et al. (1984). For a quantitative comparison, the values of the angular velocity, area and perimeter of the final equilibria are compared with the associated values listed in table III of Wu et al. (1984). The relative error (equation (9.3.7)) is calculated for each quantity and the results are as follows: the angular velocity agrees to $\mathcal{O}(10^{-4})$; the area agrees to $\mathcal{O}(10^{-5})$ and; the perimeter agrees to $\mathcal{O}(10^{-6})$. There is thus convincing qualitative and quantitative agreement between the solutions of Wu et al. (1984) and the AAA-LS + WOZ algorithm.

Furthermore, the typical runtime of one iterative step of the AAA-LS + WOZ algorithm on the standard laptop used throughout this thesis is around 0.65 seconds. This value is closer to a step per second for higher fold symmetries, which is expected as these contain more boundary points for the same value $M = 120$.

9.5 Point vortex - vortex patch equilibria

A natural extension to the problem set up in Sect.9.1 is to consider an $m-$fold symmetric vortex patch surrounded by m symmetrically positioned point vortices outside of the patch. This problem was studied in Xue et al. (2017); Xue (2017) and labelled as the '$m+1$ point vortex $-$ vortex patch equilibrium'. The system of governing equations and boundary conditions (equations (9.1.1) to (9.1.4)) are unchanged, however the far field condition equation (9.1.5) is now

$$\psi_2 \to \lambda \log|z| + \sum_{j=1}^{m} \lambda_s \log|z - z_j| + D \quad \text{as } r \to \infty, \tag{9.5.1}$$

where $z_j = (b/L)\exp(2\pi i j/m)$ is the (dimensionless) position of the j^{th} point vortex and b is the radial distance of the point vortices from the origin. Each point vortex has the same circulation Γ_s therefore $\lambda_s = \Gamma_s/2\pi\omega L^2$ and $D = (A + m\Gamma_s/\omega)\log|L|/(2\pi L^2)$ following the non-dimensionalisation in Sect.9.1. The characteristic length L is now chosen to be the radial distance b and so $b = 1$ is normalised throughout this work, once again giving $D = 0$.

By linearity, the point vortices contribution can simply be added to both interior (equation (9.2.1)) and

exterior (equation (9.2.2)) stream functions. Therefore, the stream function is given by

$$\psi = \begin{cases} \psi_1 = \frac{|z|^2}{4} + \sum_{j=1}^{m} \lambda_s \log|z - z_j| \\ \quad + \mathrm{Re}\left(\sum_{k=0}^{N_1} a_k (z - z_c)^k + \sum_{k=1}^{M_1} \frac{b_k}{z - p_k} \right), \quad z \in 1, \\ \psi_2 = \lambda \log|z| + \sum_{j=1}^{m} \lambda_s \log|z - z_j| \\ \quad + \mathrm{Re}\left(\sum_{k=1}^{N_2} c_k (z - z_c)^{-k} + \sum_{k=1}^{M_2} \frac{d_k}{z - q_k} \right), \quad z \in 2, \end{cases} \tag{9.5.2}$$

and using that $u + iv = i\nabla\psi$, the velocity vector (in complex notation) is

$$u + iv = \begin{cases} u_1 + iv_1 = i\left(\frac{z}{2} + \sum_{j=1}^{m} \lambda_s / (\overline{z - z_j}) \right. \\ \quad \left. + \overline{\sum_{k=0}^{N_1} k a_k (z - z_c)^{k-1} - \sum_{k=1}^{M_1} \frac{b_k}{(z - p_k)^2}} \right), \quad z \in 1, \\ u_2 + iv_2 = i\left(\frac{\lambda}{\bar{z}} + \sum_{j=1}^{m} \lambda_s / (\overline{z - z_j}) \right. \\ \quad \left. - \overline{\sum_{k=1}^{N_2} k c_k (z - z_c)^{-(k+1)} - \sum_{k=1}^{M_2} \frac{d_k}{(z - q_k)^2}} \right), \quad z \in 2. \end{cases} \tag{9.5.3}$$

Three of the four parameters $[R_a, R_b, b \text{ and } \gamma_s]$ must be prescribed to uniquely determine the solution. By freeing the parameter R_b, the WOZ algorithm detailed in appendix B can once again be used to numerically iterate towards equilibrium solutions. To do this, the algorithm is now implemented on a $1/m$ segment of the vortex patch (rather than a $1/2m$ segment as before) made up of $2M + 1$ points such that $R_b = R_{2M+1} = R_1 = R_a$. Note that equation (B.0.1) for velocity $\Omega^{(n)}$ at step 2 of the WOZ algorithm can no longer be used since $R_b = R_a$. Instead, the condition that the point vortex is fixed in the rotating frame is used, giving the alternative expression for the angular velocity

$$\Omega^{(n)} = |u(\Gamma_s, b, z_k^{(n)})|/b, \tag{9.5.4}$$

where $z_k^{(n)} = x_k^{(n)} + iy_k^{(n)}$ is the k^{th} boundary point at the n^{th} iteration and $|u|$ is the speed at a point vortex; by symmetry, each point vortex experiences the same speed. A given point vortex does not interact with itself, thus the corresponding singular term at $z = z_j$ is omitted in the velocity equation (9.5.3) at that point vortex.

Figure 9.5 shows streamline plots of two equilibrium solutions having three and four-fold symmetries, where the initial vortex patch shape is a circle of radius R_a in each case. In the three-fold example (left), the point vortices have the same signed circulation as the vortex patch, with $|\Gamma_s| = \pi/2$, $R_a = 0.25$ and the equilibrium is reached after 55 iterations. In the four-fold example (right), the point vortices have

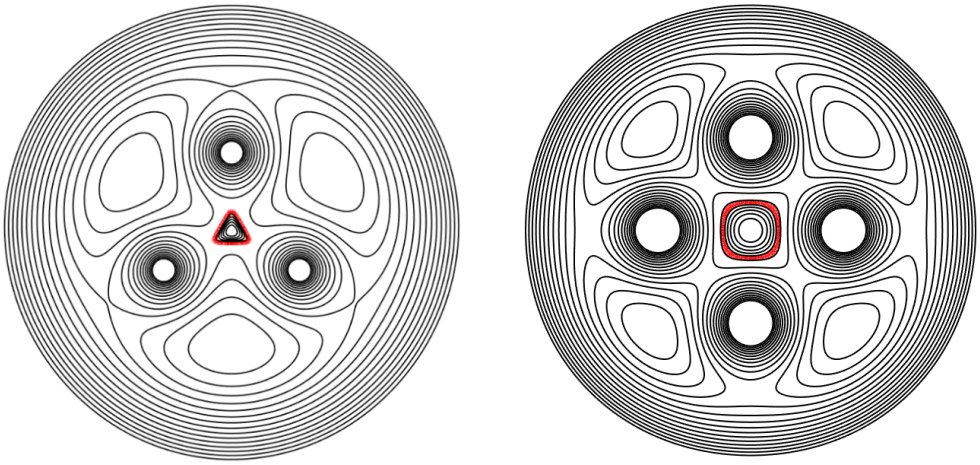

Figure 9.5: Streamline plots of the equilibrium solutions of the AAA-LS + modified WOZ algorithm for the point vortex − vortex patch problem, where the boundary of the vortex patch is shown in red in each figure. Left: three-fold problem with same signed circulation of the patch and point vortices, where $|\Gamma_s| = \pi/2$ and $R_a = 0.25$. Equilibrium computed in 55 iterations. Right: four-fold problem with opposite signed circulation of the patch and point vortices, where $|\Gamma_s| = 2\pi$ and $R_a = 0.3$. Equilibrium computed in 9 iterations.

oppositely signed circulation to the vortex patch; the equilibrium is reached in 9 iterations, with $|\Gamma_s| = 2\pi$ and $R_a = 0.3$.

9.6 Discussion

In this chapter, a second application of the two-domain AAA-LS algorithm was explored. The flow in and around a vortex patch was calculated, including scenarios with satellite point vortices placed symmetrically around the vortex patch. Previous analytical and numerical equilibrium solutions of such vortex patch configurations were then reproduced with good agreement using the two-domain AAA-LS method. It is also noted in Harris and McDonald (2024b) that the AAA-LS and associated least-squares methods can be efficiently employed to numerically solve further vortex dynamics problems, including vortex sheet equilibria and those having doubly-connected geometries.

The success of the two-domain AAA-LS method developed here, and the related least-squares methods explored in Harris and McDonald (2024b), provides a new numerical approach for finding new families of vortex equilibria. Of course, there still exists the standard approach to computing vortex patch equilibria using contour dynamics (see e.g. Dritschel (1985)) in which the dynamics is reduced to a line integral around the patch boundary; such a method is also efficient and accurate. The two-domain AAA-LS algorithm and related least-squares methods usefully add to the numerical approaches available to computing vortex equilibria. A combination of these methods could be used to numerically compute further

equilibria solutions, for example those involving a mix of vortex patches, sheets, points and solid objects - there are currently no known examples of equilibria involving both patches and sheets together.

The two-domain AAA-LS algorithm developed in the previous two chapters has been utilisied to simply and efficiently solve two problems: the electrostatic interaction between a flower and its pollinators; and the flow in and around a vortex patch in equilibrium. It is envisioned that the two-domain AAA-LS method developed in this thesis is applicable to a range of other problems. In addition to further problems in vortex dynamics and in electro- and magnetostatics as noted above and in the previous chapter, other problems include flow through a two-phase Hele-Shaw cell (Muskat, 1934; Howison, 2000; Żukowski et al., 2024) and more advanced phase-change problems (Goldstein and Reid, 1978; Ladd et al., 2020), where the melting/freezing interface is not just a fixed temperature but involves some mixed value boundary conditions. The penguin huddle problem of Ch.4 could be extended in a similar way, using a more complicated boundary condition coupling the interior and exterior temperatures.

Chapter 10

Conclusion

The aim of this thesis was to develop simple, computationally efficient mathematical modelling tools to solve the evolution of various two-dimensional interfacial problems in nature. Wildfire spread was primarily studied, where a reduced-order wildfire-atmosphere model was developed to incorporate effects such as the curvature of the fire line, oxygen transport, a deterministic rate of spread and the pyrogenic and ambient winds. This wildfire model successfully reproduced a variety of the main features observed in wildfire spread, such as fire fingering and the attraction of two wildfires towards each other, while running on the order of seconds to minutes on a standard laptop. The modelling tools used for the wildfire problem were then applied to further interfacial problems in nature, including in penguin huddling, biological electrostatics and vortex dynamics. New extensions to these methods were developed to solve singly- and multiply-connected, one-domain problems, and coupled and un-coupled two-domain problems.

The two numerical methods developed throughout this thesis - the conformal mapping and AAA-LS methods - both offer different benefits. While the conformal mapping method is restricted to one-domain, singly-connected problems, it is simple and fast, even for a large number of time steps, and fundamentally consists only of a basic, implicit ODE solver. The AAA-LS method is more sophisticated yet still conceptually simple and fast, requiring the *chebfun* package (see e.g. Costa and Trefethen (2023)) to couple the AAA algorithm to a standard LS fitting procedure. To compute the evolution of a free boundary, this method also requires an explicit RK timestepping routine, which adds to the computation speed and introduces associated numerical errors. However, the AAA-LS method can be employed in one- and two-domain and singly- and multiply-connected problems. Furthermore, the algorithm can handle non-smooth interfaces containing corners and cusps; the conformal mapping method is less equipped to handle such geometries due to the crowding phenomenon, see e.g. Driscoll (2005). As both methods offer different

advantages and disadvantages, both have been developed and explored throughout this thesis.

Extensions to the wildfire model developed in this thesis are possible and of interest for future research. Topography has not been considered throughout this thesis, yet plays as crucial a role as wind in affecting wildfire spread. How terrain features such as slopes and valleys affect the surrounding wind field is also an important consideration. As suggested in Sharples and Hilton (2020), strategically placed vortices could act as an analogue to terrain effects, for example in reproducing the effect of vorticity-driven lateral spread. Point sources, sinks and vortices could additionally be used to model other wildfire features such as fire whirls and tornadoes (Soma and Saito, 1991; Forthofer and Goodrick, 2011; Tohidi et al., 2018; Lareau et al., 2022). Inhomogeneous fuel beds could also be incorporated, similar to the inclusion of firebreaks in Ch.7, and the model coupled with some existing fuelbed database.

Furthermore, the wildfire merging algorithm of Ch.7 could be adapted to compute more complicated scenarios. For example, multiple wildfires may merge in such a way that produces a ring fire - see figure 4.6 in Sharples et al. (2022) - which results in two disconnected 'inner and outer' unburnt domains. Locally, the opposite scenario may also appear where a 'doughnut' of unburnt fuel with a small fire at its centre is surrounded by a large outer fire on all sides. The AAA-LS algorithm can be extended to account for these types of domains (Trefethen, 2020; Costa and Trefethen, 2023). Spotfire production and generation was not also considered in this thesis. The present wildfire model could thus also be coupled to some spotfire generation model, similar to that of e.g. Boychuk et al. (2009), with spotfires appearing midway through a scenario and affecting the wildfire spread thereafter.

Finally, all of the interface problems considered in this thesis are entirely deterministic. In reality, physical systems are often stochastic, whether it be variations in ambient wind speeds and directions or changes in heat fluxes and electric permeability. Stochastic variables could thus be incorporated into the models developed in this thesis. In the wildfire problem, this could include an ambient wind with time-varying direction and magnitude, or some variability on the basic ROS terms corresponding to stochastic heat fluxes. However, this would require a significant overhaul of some of the numerical methods used, with SDE (rather than ODE) solvers required.

In conclusion, this thesis shows how simple, two-dimensional models can be used to reproduce the behaviours of various natural phenomena, from the hot and electrifying to the cold and cute. It is hoped that the simple yet elegant mathematical methods considered in this thesis undergo continued development in the future, to expand the range of possible problems these techniques can tackle. Additionally, it is hoped that there is continued study into environmental problems to better understand the beautiful

processes that make up our world. Mother nature remains largely unsolved, it is up to humanity to huddle together, ignite the flames of curiosity and spark inspiration to solve this whirlpool of environmental problems.

Appendix A

Derivation of the Markstein model

Despite the Markstein model (equation (2.2.1)) being over 70 years old, there is little work involving its derivation from physical principles (Markstein, 1951). In this appendix, such a derivation is provided, following an approach similar to appendix A of Nakayama et al. (1994).

Throughout this thesis, it is assumed that the wildfire spreads through some homogeneously distributed, bone-dry fuel source. When the fuel catches alight, some fraction of fuel is burnt up while heating surrounding fuel elements, yet it is assumed that there is always sufficient fuel available to propagate the wildfire, i.e. the scenario of all fuel being burnt up before the surrounding fuel ignites is impossible. Therefore, the concentration of fuel is not of interest, but rather the temperature profile T. The combustion process is well described by the Arrhenius law; combining this with the heat equation gives equation (2.1a) of Weber et al. (1997)

$$\frac{\partial T}{\partial t} = \delta \nabla^2 T + f(T), \tag{A.0.1}$$

with

$$f(T) = A_0 Y e^{-\lambda/T} + B_0(T - T_a), \tag{A.0.2}$$

where t is time, ∇^2 is the Laplace operator, (A_0, B_0, λ) are constants from Weber et al. (1997), Y is the concentration of fuel and T_a is the ambient air temperature. The constant δ, the same constant as in equation (2.2.1), is the thermal diffusivity, defined as

$$\delta = \frac{k}{\rho c_p}, \tag{A.0.3}$$

where k, ρ and c_p are the thermal conductivity, density and specific heat capacity of the fuel, respectively

(Jayalakshmy and Philip, 2010; Weber et al., 1997). The units of the thermal diffusivity δ is $\mathrm{m^2 s^{-1}}$, and hence the quantity $\delta\kappa$ is a velocity with units $\mathrm{ms^{-1}}$, as required. Reaction-diffusion equations are often used in flame propagation models (Sullivan, 2009a) and the following derivation can be applied to any such equation of the form of equation (A.0.1) (Nakayama et al., 1994).

Let the fire line be a simple, progressive wave, propagating at some velocity c, the rate of spread of the fire in the $x-$direction. Hence T can be written as $T = T(x - ct) = T(\xi)$ and by the chain rule

$$\frac{\partial T}{\partial t} = \frac{\mathrm{d}\xi}{\mathrm{d}t}\frac{\partial T}{\partial \xi} = -c\frac{\partial T}{\partial \xi}; \qquad \nabla^2 T = \frac{\partial^2 T}{\partial x^2} = \frac{\partial^2 T}{\partial \xi^2}. \tag{A.0.4}$$

Thus equation (A.0.1) can now be written as

$$\delta\frac{\partial^2 T}{\partial \xi^2} + c\frac{\partial T}{\partial \xi} + f(T) = 0. \tag{A.0.5}$$

The fire line can be expressed in a different way. By definition, the fire line γ is the line $T = T_i$, where T_i is the ignition temperature of the fuel source - the minimum temperature at which the fuel ignites and begins burning. Indeed, the fire line is the boundary separating burnt ($T > T_i$) and unburnt ($T < T_i$) regions of fuel, which by continuity is the line $T = T_i$. Define the position vector $\boldsymbol{x}$ of a point on curve γ intrinsically, in terms of the arclength s and time t. Using the standard Serret-Frenet formulae (Adams, 1975), the unit tangent and normal vectors, $\hat{\boldsymbol{t}} = \partial\boldsymbol{x}/\partial s$ and $\hat{\boldsymbol{n}}$, respectively, at a point $\boldsymbol{x}$ on γ are

$$\frac{\partial \hat{\boldsymbol{t}}}{\partial s} = \bar{\kappa}\hat{\boldsymbol{n}}, \qquad \frac{\partial \hat{\boldsymbol{n}}}{\partial s} = -\bar{\kappa}\hat{\boldsymbol{t}}. \tag{A.0.6}$$

The curve γ is traced out such that the normal vector $\hat{\boldsymbol{n}}$ points from the unburnt region 'inside' the fire line to the burnt region 'outside'. Thus the orientation of the curvature $\bar{\kappa}$ is such that sections of the fire line curved towards the unburnt region have negative curvature. It follows that $\bar{\kappa} = -\kappa$, where κ is the definition of the curvature used in equation (2.2.1).

In the neighbourhood N of γ, let ξ be a small, spatial displacement. A point $\boldsymbol{x}$ in N has the following Taylor series in ξ

$$\boldsymbol{x}(s, t, \xi) = \boldsymbol{x}(s, t) + \xi\hat{\boldsymbol{n}}(s, t) + O(\xi^2). \tag{A.0.7}$$

The metric g_{ij} in N is defined as follows

$$[g]_{i,j} = g_{ij} = \frac{\partial \boldsymbol{x}}{\partial X^i} \cdot \frac{\partial \boldsymbol{x}}{\partial X^j}; \qquad X^i = \{s, \xi\}. \tag{A.0.8}$$

Each element of the metric is found using equations (A.0.6) and (A.0.7)

$$\begin{aligned} g_{11} &= \frac{\partial}{\partial s}\big[\boldsymbol{x}+\xi\hat{\boldsymbol{n}}\big]\cdot\frac{\partial}{\partial s}\big[\boldsymbol{x}+\xi\hat{\boldsymbol{n}}\big]+O(\xi^2)=1-2\xi\bar{\kappa}+O(\xi^2),\\ g_{12}=g_{21} &= \frac{\partial}{\partial s}\big[\boldsymbol{x}+\xi\hat{\boldsymbol{n}}\big]\cdot\frac{\partial}{\partial \xi}\big[\boldsymbol{x}+\xi\hat{\boldsymbol{n}}\big]+O(\xi)=\hat{\boldsymbol{t}}(1-\xi\bar{\kappa})\cdot\hat{\boldsymbol{n}}+O(\xi)=O(\xi),\\ g_{22} &= \frac{\partial}{\partial \xi}\big[\boldsymbol{x}+\xi\hat{\boldsymbol{n}}\big]\cdot\frac{\partial}{\partial \xi}\big[\boldsymbol{x}+\xi\hat{\boldsymbol{n}}\big]+O(\xi^2)=\hat{\boldsymbol{n}}\cdot\hat{\boldsymbol{n}}+O(\xi^2)=1+O(\xi^2). \end{aligned} \tag{A.0.9}$$

The quantity g^{ij}, where $g_{ij}g^{ij}=I$ (I is the identity matrix), can also be constructed using the Taylor series for $(1+\epsilon)^{-1}$ where ϵ is some small quantity. This gives

$$g_{ij}=\begin{pmatrix}1-2\xi\bar{\kappa}+O(\xi^2) & O(\xi)\\ O(\xi) & 1+O(\xi^2)\end{pmatrix}, \tag{A.0.10}$$

$$g^{ij}=\begin{pmatrix}1+2\xi\bar{\kappa}+O(\xi^2) & O(\xi)\\ O(\xi) & 1+O(\xi^2)\end{pmatrix}. \tag{A.0.11}$$

The Laplacian ∇^2 is defined as

$$\nabla^2 T=|g|^{-1/2}\partial_i(|g|^{1/2}g^{ij}\partial_j T)=g^{ij}\partial_{ij}T+\left(\frac{1}{2}|g|^{-1}g^{ij}\partial_i|g|+\partial_i g^{ij}\right)\partial_j T, \tag{A.0.12}$$

where $|g|$ is the absolute value of the determinant of g_{ij}, and $\partial_i=\partial/\partial X^i$. Using $\partial T/\partial s\equiv 0$, as $T=T(\xi)$, the Laplacian can be simplified to

$$\begin{aligned} \nabla^2 T &= g^{22}\frac{\partial^2 T}{\partial\xi^2}+\left[\frac{1}{2}(1-2\xi\bar{\kappa})g^{22}\frac{\partial}{\partial\xi}(1-2\xi\bar{\kappa})+\frac{\partial}{\partial\xi}g^{22}\right]\frac{\partial T}{\partial\xi}+O(\xi^2)\\ &= \frac{\partial^2 T}{\partial\xi^2}+\left[\frac{1}{2}(1+2\xi\bar{\kappa}+...)(-2\bar{\kappa})\right]\frac{\partial T}{\partial\xi}+O(\xi^2). \end{aligned} \tag{A.0.13}$$

Therefore, $\nabla^2 T$ can be written as

$$\nabla^2 T=\frac{\partial^2 T}{\partial\xi^2}-\bar{\kappa}\frac{\partial T}{\partial\xi}+O(\xi^2). \tag{A.0.14}$$

The time derivative of T can also be expressed in terms of ξ as

$$\frac{\partial T}{\partial t}=-v_t\frac{\partial T}{\partial s}-v_n\frac{\partial T}{\partial\xi}=-v_n\frac{\partial T}{\partial\xi}, \tag{A.0.15}$$

where v_t and v_n are the tangential and normal velocities to the fire line γ, respectively.

Substituting equations (A.0.14) and (A.0.15) into equation (A.0.1) (the reaction-diffusion equation) gives

$$\delta \frac{\partial^2 T}{\partial \xi^2} + (v_n - \delta\bar{\kappa}) \frac{\partial T}{\partial \xi} + f(T) = 0. \tag{A.0.16}$$

Comparing equations (A.0.5) and (A.0.16) gives $v_n = c + \delta\bar{\kappa}$. Clearly $c = v_0$, and recalling that $\bar{\kappa} = -\kappa$ gives equation (2.2.1), as required.

Appendix B

WOZ numerical algorithm

This appendix summarises the numerical procedure developed and used by Wu, Overman and Zabusky (WOZ) in Wu et al. (1984) to compute $m-$fold symmetric V-states of the vortex patch system of equations (9.1.1) to (9.1.5). This algorithm iterates the inputted boundary shape to a state in which the kinematic boundary condition is satisfied to within some tolerance level, namely that the normal velocity of fluid on the boundary approaches zero. Recall that, by symmetry, only a $1/2m$ segment of the vortex patch boundary is considered which is made up of $M+1$ boundary points. The WOZ numerical routine is split into five steps at each iteration.

First, the velocity on each boundary point must be found, which Wu et al. (1984) calculate using contour dynamics techniques, see their equation (4.1). The AAA-LS algorithm is instead used in this work to find the velocity equation (9.2.5) (or equation (9.2.6) as the velocity is continuous across the boundary). Note that the AAA-LS algorithm requires the entire boundary data Z rather than just the segment Z_s. Furthermore, if the vortex patch has changed shape following a previous iterative step, the new shape must again be non-dimensionalised; it will have a new radius L and a new area A and thus the non-dimensional constant λ must be updated.

Second, the angular velocity is calculated:

$$\Omega^{(n)} = \frac{2}{R_a^2 - R_b^2} \sum_{k=1}^{M} u_{k+1/2}^{(n)} \Delta y_k^{(n)} - v_{k+1/2}^{(n)} \Delta x_k^{(n)}, \tag{B.0.1}$$

where $f_{k+1/2} = \frac{1}{2}[f_{k+1} + f_k]$ and $\Delta f_k = f_{k+1} - f_k$. Third, the following function is calculated using

Ω

$$F_{k+1/2} \equiv \frac{u_{k+1/2}\sin\theta_{k+1} - v_{k+1/2}\cos\theta_{k+1} + (\Omega/2)R_{k+1}}{u_{k+1/2}\sin\theta_k - v_{k+1/2}\cos\theta_k + (\Omega/2)R_k}. \tag{B.0.2}$$

Fourth, the velocity (u, v) and angular velocity Ω are used to evaluate the kinematic boundary condition - the condition that particles on the vortex patch boundary remain on the boundary. The second order discretisation of this condition (Wu et al., 1984) can be averaged and written as

$$-\frac{1}{2}F_{k-1/2}^{-1}\overline{R_{k-1}} + \overline{R_k} - \frac{1}{2}F_{k+1/2}\overline{R_{k+1}} = 0, \quad 2 \leq k \leq M, \tag{B.0.3}$$

where $\overline{R_1} = R_a$, $\overline{R}_{M+1} = R_b$ and F is the function given in equation (B.0.2). The system given in equation (B.0.3) can be written as the product $AX = Y$, where A is a tridiagonal matrix of coefficients and Y is the vector $(\frac{1}{2}F_{3/2}^{-1}R_a, 0, 0, ...0, \frac{1}{2}F_{M+1/2}R_b)$. The vector of unknowns $X = (\overline{R_2}, ..., \overline{R_M})$ can then be found using the MATLAB backslash operator $X = A\backslash Y$ and it follows that $\overline{R_k} \to \overline{R_k}^{(n+1)}$. The following relaxation procedure is then used

$$R_k^{(n+1)} = \mu\overline{R_k}^{(n+1)} + (1-\mu)R_k^{(n)}, \tag{B.0.4}$$

where $\mu = 0.6$ as in Wu et al. (1984).

Fifth, the boundary data Z and segment data Z_s are updated accordingly. Then, the iteration continues until the following error criterion is satisfied

$$\sum_{k=1}^{M+1} |R_k^{(n+1)} - R_k^{(n)}| < \epsilon, \tag{B.0.5}$$

for some tolerance $\epsilon = \mathcal{O}(10^{-6})$ or until some maximum number of iterations n_{max} is achieved; such an n_{max} is implemented to avoid exceptionally long runtimes. In this thesis, the value $n_{max} = 500$ is used, yet all results presented converge to an equilibrium in under n_{max} iterations.

Bibliography

Achtemeier, G. L. (2012). Field validation of a free-agent cellular automata model of fire spread with fire–atmosphere coupling. *Int. J. Wildland Fire*, 22(2):148–156.

Adams, J. A. (1975). The intrinsic method for curve definition. *Comput. Aided Des.*, 7(4):243–249.

Agam, O. (2009). Viscous fingering in volatile thin films. *Phys. Rev. E*, 79(2):021603.

Amano, K. (1994). A charge simulation method for the numerical conformal mapping of interior, exterior and doubly-connected domains. *J. Comput. Appl. Math.*, 53(3):353–370.

Ambroz, M., Balažovjech, M., Medl'a, M., and Mikula, K. (2019). Numerical modeling of wildland surface fire propagation by evolving surface curves. *Adv. Comput. Math.*, 45:1067–1103.

Ancel, A., Gilbert, C., Poulin, N., Beaulieu, M., and Thierry, B. (2015). New insights into the huddling dynamics of emperor penguins. *Anim. Behav.*, 110:91–98.

Anderson, D. H., Catchpole, E. A., De Mestre, N. J., and Parkes, T. (1982). Modelling the spread of grass fires. *ANZIAM J.*, 23(4):451–466.

Andrews, P. (2018). The Rothermel surface fire spread model and associated developments: A comprehensive explanation. *Gen. Tech. Rep. RMRS-GTR-371. Fort Collins, CO: US Department of Agriculture, Forest Service, Rocky Mountain Research Station. 121 p.*, 371.

Arnell, N., Freeman, A., and Gazzard, R. (2021). The effect of climate change on indicators of fire danger in the UK. *Environ. Res. Lett.*, 16(4):044027.

Attiwill, P. and Binkley, D. (2013). Exploring the mega-fire reality: A 'forest ecology and management' conference. *For. Ecol. Manag.*, 294:1–3.

Ausonio, E., Bagnerini, P., and Ghio, M. (2021). Drone swarms in fire suppression activities: A conceptual framework. *Drones*, 5(1):17.

Baddoo, P. J. (2020). Lightning solvers for potential flows. *Fluids*, 5(4):227.

Baddoo, P. J. and Trefethen, L. N. (2021). Log-lightning computation of capacity and Green's function. *Maple Trans.*, 1(1).

Baines, P. (1990). Physical mechanisms for the propagation of surface fires. *Math. Comp. Model.*, 13(12):83–94.

Bakhshaii, A. and Johnson, E. A. (2019). A review of a new generation of wildfire–atmosphere modeling. *Can. J. For. Res.*, 49(6):565–574.

Basu, P. (2018). *Biomass gasification, pyrolysis and torrefaction: Practical Design and Theory*. Academic Press, Boston.

Bazant, M. Z. (2004). Conformal mapping of some non-harmonic functions in transport theory. *Proc. R. Soc. A*, 460(2045):1433–1452.

Bazant, M. Z. and Crowdy, D. (2005). Conformal mapping methods for interfacial dynamics. In *Handbook of materials modeling*, pages 1417–1451. Springer.

Bebieva, Y., Oliveto, J., Quaife, B., Skowronski, N. S., Heilman, W. E., and Speer, K. (2020). Role of horizontal eddy diffusivity within the canopy on fire spread. *Atmosphere*, 11:672.

Beer, T. (1991). The interaction of wind and fire. *Bound.-Layer Meteorol.*, 54:287–308.

Bernardi, S. and Scianna, M. (2020). An agent-based approach for modelling collective dynamics in animal groups distinguishing individual speed and orientation. *Philos. Trans. R. Soc. B*, 375(1807):20190383.

Bhattacharya, K. and Vicsek, T. (2010). Collective decision making in cohesive flocks. *New J. Phys.*, 12(9):093019.

Bonta, M., Gosford, R., Eussen, D., Ferguson, N., Loveless, E., and Witwer, M. (2017). Intentional fire-spreading by "firehawk" raptors in northern Australia. *J. Ethnobiol.*, 37(4):700–718.

Boychuk, D., Braun, W., Kulperger, R., Krougly, Z., and Stanford, D. (2009). A stochastic forest fire growth model. *Environ. Ecol. Stat.*, 16:133–151.

Brakke, K. A. (2015). *The motion of a surface by its mean curvature.*, volume 20. Princeton University Press.

Brower, R. C., Kessler, D. A., Koplik, J., and Levine, H. (1984). Geometrical models of interface evolution. *Phys. Rev. A*, 29(3):1335.

Brown, J. W. and Churchill, R. V. (2009). *Complex variables and applications*. McGraw-Hill, 8 edition.

Brubeck, P. D., Nakatsukasa, Y., and Trefethen, L. N. (2021). Vandermonde with Arnoldi. *SIAM Rev.*, 63(2):405–415.

Brubeck, P. D. and Trefethen, L. N. (2022). Lightning Stokes solver. *SIAM J. Sci. Comput.*, 44(3):A1205–A1226.

Brueshaber, S. R., Sayanagi, K. M., and Dowling, T. E. (2019). Dynamical regimes of giant planet polar vortices. *Icarus*, 323:46–61.

Burger, M., Haškovec, J., and Wolfram, M.-T. (2013). Individual based and mean-field modeling of direct aggregation. *Physica D*, 260:145–158.

Butcher, J. C. (1996). A history of Runge-Kutta methods. *Appl. Numer. Math.*, 20(3):247–260.

Canós, A. J. (2024). Fast and robust self-intersections. MATLAB Central File Exchange. Retrieved August 1, 2024.

Catchpole, E. A., Hatton, T. J., and Catchpole, W. R. (1989). Fire spread through nonhomogeneous fuel modelled as a Markov process. *Ecol. Model.*, 48(1-2):101–112.

Choi, J., Margetis, D., Squires, T. M., and Bazant, M. Z. (2005). Steady advection–diffusion around finite absorbers in two-dimensional potential flows. *J. Fluid Mech.*, 536:155–184.

Clark, T. L., Jenkins, M. A., Coen, J., and Packham, D. R. (1996a). A coupled atmosphere-fire model: Role of the convective Froude number and dynamic fingering at the fireline. *Int. J. Wildland Fire*, 6(4):177–190.

Clark, T. L., Jenkins, M. A., Coen, J. L., and Packham, D. R. (1996b). A coupled atmosphere-fire model: Convective feedback on fire-line dynamics. *J. Appl. Meteorol. Climatol.*, 35(6):875–901.

Clarke, D., Morley, E., and Robert, D. (2017). The bee, the flower, and the electric field: electric ecology and aerial electroreception. *J. Comp. Physiol. A*, 203(9):737–748.

Clarke, D., Whitney, H., Sutton, G., and Robert, D. (2013). Detection and learning of floral electric fields by bumblebees. *Science*, 340(6128):66–69.

Conti, M. and Marconi, U. M. B. (2002). Fingering in slow combustion. *Physica A*, 312(3):381–391.

Conti, M. and Marconi, U. M. B. (2010). Diffusion limited propagation of burning fronts. In Perona, G. and Brebbia, C., editors, *Modelling, Monitoring and Management of Forest Fires II*, pages 37–45. WIT Press.

Costa, S. (2020). Solving Laplace problems with the AAA algorithm. *arXiv preprint arXiv:2001.09439*.

Costa, S., Costamagna, E., and Di Barba, P. (2024). Modelling permanent magnet excited uniform fields with rational approximations. *COMPEL*.

Costa, S. and Trefethen, L. N. (2023). AAA-least squares rational approximation and solution of Laplace problems. In *Euro. Congress Math.*, pages 511–534.

Crowdy, D. (1999). A class of exact multipolar vortices. *Phys. Fluids*, 11:2556.

Crowdy, D. and Kang, H. (2001). Squeeze flow of multiply-connected fluid domains in a Hele-Shaw cell. *J. Nonlinear Sci.*, 11(4):279–304.

Crowdy, D. and Marshall, J. (2004). Growing vortex patches. *Phys. Fluids*, 16(8):3122–3130.

Cummings, L. M., Hohlov, Y. E., Howison, S. D., and Kornev, K. (1999). Two-dimensional solidification and melting in potential flows. *J. Fluid Mech.*, 378:1–18.

Dallaston, M. C. and Hewitt, I. J. (2014). Free-boundary models of a meltwater conduit. *Phys. Fluids*, 26(8):083101.

Dallaston, M. C. and McCue, S. W. (2013). An accurate numerical scheme for the contraction of a bubble in a Hele–Shaw cell. *ANZIAM J.*, 54:C309–C326.

Dallaston, M. C. and McCue, S. W. (2016). A curve shortening flow rule for closed embedded plane curves with a prescribed rate of change in enclosed area. *Proc. R. Soc. A*, 472(2185):20150629.

Davis, P. J. (1974). *The Schwarz function and its applications*, volume 17. American Mathematical Soc.

Dawson, C., Vincent, J. F. V., Jeronimidis, G., Rice, G., and Forshaw, P. (1999). Heat transfer through penguin feathers. *J. Theor. Biol.*, 199(3):291–295.

D'Errico, J. (2024). interparc. MATLAB Central File Exchange. Retrieved August 1, 2024.

Derrida, B. and Hakim, V. (1992). Needle models of Laplacian growth. *Phys. Rev. A*, 45(12):8759.

Dipierro, S., Valdinoci, E., Wheeler, G., and Wheeler, V.-M. (2024). A simple but effective bushfire model: analysis and real-time simulations. *SIAM J. Appl. Math.*, 84(4):1504–1514.

Dold, J. W., Sivashinsky, G., and Weber, R. O. (2005). Onset of flow-induced fingering in bushfires. In *5th Asia-Pacific Conference on Combustion*, pages 177–180, The University of Adelaide, Adelaide, Australia.

Driscoll, T. A. (1996). Algorithm 756: A MATLAB toolbox for Schwarz-Christoffel mapping. *ACM Trans. Math. Softw.*, 22(2):168–186.

Driscoll, T. A. (2005). Algorithm 843: Improvements to the Schwarz-Christoffel toolbox for MATLAB. *ACM Trans. Math. Softw.*, 31(2):239–251.

Driscoll, T. A. and Trefethen, L. N. (2002). *Schwarz-Christoffel mapping*, volume 8. Cambridge University Press.

Dritschel, D. G. (1985). The stability and energetics of corotating uniform vortices. *J. Fluid Mech.*, 157:95–134.

Dritschel, D. G. (1988). Contour surgery: a topological reconnection scheme for extended integrations using contour dynamics. *J. Comp. Phys.*, 77(1):240–266.

Dutka, F., Starchenko, V., Osselin, F., Magni, S., Szymczak, P., and Ladd, A. J. C. (2020). Time-dependent shapes of a dissolving mineral grain: Comparisons of simulations with microfluidic experiments. *Chem. Geol.*, 540:119459.

England, S. J. and Robert, D. (2024). Prey can detect predators via electroreception in air. *Proc. Natl. Acad. Sci. U.S.A.*, 121(23):e2322674121.

Entov, V. M. and Etingof, P. I. (1991). Bubble contraction in Hele-Shaw cells. *Q. J. Mech. Appl. Math.*, 44(4):507–535.

Filippi, J.-B., Bosseur, F., Pialat, X., Santoni, P.-A., Strada, S., and Mari, C. (2011). Simulation of coupled fire/atmosphere interaction with the MesoNH-ForeFire models. *J. Combust.*, 2011(1):540390.

Finney, M. A. (1998). *FARSITE, Fire Area Simulator–model development and evaluation*. Number 4. US Department of Agriculture, Forest Service, Rocky Mountain Research Station.

Fons, W. L. (1946). Analysis of fire spread in light forest fuels. *J. Agric. Res.*, 72(3):92–121.

Forthofer, J. M. and Goodrick, S. L. (2011). Review of vortices in wildland fire. *J. Combust.*, 2011(1):984363.

Frankman, D., Webb, B. W., Butler, B. W., Jimenez, D., Forthofer, J. M., Sopko, P., Shannon, K. S., Hiers, J. K., and Ottmar, R. D. (2012). Measurements of convective and radiative heating in wildland fires. *Int. J. Wildland Fire*, 22(2):157–167.

Freire, J. G. and DaCamara, C. C. (2019). Using cellular automata to simulate wildfire propagation and to assist in fire management. *Nat. Hazard Earth Sys.*, 19(1):169–179.

Gage, M. and Hamilton, R. S. (1986). The heat equation shrinking convex plane curves. *J. Differ. Geom.*, 23:69–96.

Gerum, R., Richter, S., Fabry, B., Le Bohec, C., Bonadonna, F., Nesterova, A., and Zitterbart, D. P. (2018). Structural organisation and dynamics in king penguin colonies. *J. Phys. D: Appl. Phys.*, 51(16):164004.

Gerum, R. C., Fabry, B., Metzner, C., Beaulieu, M., Ancel, A., and Zitterbart, D. P. (2013). The origin of traveling waves in an emperor penguin huddle. *New J. Phys.*, 15(12):125022.

Gilbert, C., Robertson, G., Le Maho, Y., Naito, Y., and Ancel, A. (2006). Huddling behavior in emperor penguins: dynamics of huddling. *Physiol. Behav.*, 88(4-5):479–488.

Goldstein, M. E. and Reid, R. L. (1978). Effect of fluid flow on freezing and thawing of saturated porous media. *Proc. Roy. Soc. A.*, 364(1716):45–73.

Gopal, A. and Trefethen, L. N. (2019a). New Laplace and Helmholtz solvers. *Proc. Natl. Acad. Sci.*, 116(21):10223–10225.

Gopal, A. and Trefethen, L. N. (2019b). Representation of conformal maps by rational functions. *Numer. Math.*, 142(2):359–382.

Gopal, A. and Trefethen, L. N. (2019c). Solving Laplace problems with corner singularities via rational functions. *SIAM J. Numer. Anal.*, 57(5):2074–2094.

Grayson, M. A. (1987). The heat equation shrinks embedded plane curves to round points. *J. Differ. Geom.*, 26:285–314.

Greggers, U., Koch, G., Schmidt, V., Dürr, A., Floriou-Servou, A., Piepenbrock, D., Göpfert, M. C., and Menzel, R. (2013). Reception and learning of electric fields in bees. *Proc. Roy. Soc. B*, 280(1759):20130528.

Griffiths, D. J. (2023). *Introduction to electrodynamics*. Cambridge University Press.

Grodzki, P. and Szymczak, P. (2019). Reactive-infiltration instability in radial geometry: From dissolution fingers to star patterns. *Phys. Rev. E*, 100(3):033108.

Gu, W., Christian, J. K., and Woodson, C. B. (2018). A novel coupled fluid-behavior model for simulating dynamic huddle formation. *PLoS ONE*, 13(8):e0203231.

Gubiec, T. and Szymczak, P. (2008). Fingered growth in channel geometry: A Loewner-equation approach. *Phys. Rev. E*, 77:041602.

Gupta, S. C. (2017). *The classical Stefan problem: basic concepts, modelling and analysis with quasi-analytical solutions and methods*, volume 45. Elsevier, Amsterdam.

Gustafsson, B. and Vasil'ev, A. (2006). *Conformal and potential analysis in Hele-Shaw cells*. Springer Science & Business Media.

Harris, S. J. and McDonald, N. R. (2022). Fingering instability in wildfire fronts. *J. Fluid Mech.*, 943:A34.

Harris, S. J. and McDonald, N. R. (2023). Penguin huddling: a continuum model. *Acta Appl. Math.*, 185:7.

Harris, S. J. and McDonald, N. R. (2024a). Modelling wildfire spread and spotfire merger using conformal mapping and AAA-least squares methods. *Environ. Model. Softw.*, (Under Review).

Harris, S. J. and McDonald, N. R. (2024b). Vortex equilibria using least-squares methods. *Theor. Comput. Fluid Dyn.*, (Under Review).

Harris, S. J., Palmer, R. A., and McDonald, N. R. (2024). Modelling floral and arthropod electrostatics using a two-domain AAA-least squares algorithm. *SIAM J. Appl. Math.*, (Under Review).

Herreid, C. F. (1963). Temperature regulation of Mexican free-tailed bats in cave habitats. *J. Mammal.*, 44(4):560–573.

Hetzer, J., Forrest, M., Ribalaygua, J., Prado-López, C., and Hickler, T. (2024). The fire weather in Europe: large-scale trends towards higher danger. *Environ. Res. Lett.*, 19(8):084017.

Hilton, J. and Garg, N. (2021). Rapid wind–terrain correction for wildfire simulations. *Int. J. Wildland Fire*, 30(6):410–427.

Hilton, J. E., Miller, C., Sharples, J. J., and Sullivan, A. L. (2016). Curvature effects in the dynamic propagation of wildfires. *Int. J. Wildland Fire*, 25(12):1238–1251.

Hilton, J. E., Sullivan, A. L., Swedosh, W., Sharples, J., and Thomas, C. (2018). Incorporating convective feedback in wildfire simulations using pyrogenic potential. *Environ. Model. Softw.*, 107:12–24.

Howison, S. D. (1986). Fingering in Hele-Shaw cells. *J. Fluid Mech.*, 167:439–453.

Howison, S. D. (1992). Complex variable methods in Hele-Shaw moving boundary problems. *Eur. J. Appl. Math.*, 3:209–224.

Howison, S. D. (2000). A note on the two-phase Hele-Shaw problem. *J. Fluid Mech.*, 409:243–249.

Hu, X. and Sun, Y. (2007). Agent-based modeling and simulation of wildland fire suppression. In *2007 Winter Simulation Conference*, pages 1275–1283. IEEE.

Huey, S. and Nieh, J. C. (2017). Foraging at a safe distance: crab spider effects on pollinators. *Ecol. Entomol.*, 42(4):469–476.

Hunting, E. R., England, S. J., Koh, K., Lawson, D. A., Brun, N. R., and Robert, D. (2022). Synthetic fertilizers alter floral biophysical cues and bumblebee foraging behavior. *PNAS Nexus*, 1(5):1–6.

Izhaki, I. and Adar, M. (1997). The effects of post-fire management on bird community succession. *Int. J. Wildland Fire*, 7(4):335–342.

Jayalakshmy, M. S. and Philip, J. (2010). Thermophysical properties of plant leaves and their influence on the environment temperature. *Int. J. Thermophys.*, 31(11):2295–2304.

Johnson, E. R. and McDonald, N. R. (2009). Necking in coating flow over periodic substrates. *J. Eng. Math.*, 65(2):171–178.

Jolly, W. M., Cochrane, M. A., Freeborn, P. H., Holden, Z. A., Brown, T. J., Williamson, G. J., and Bowman, D. M. (2015). Climate-induced variations in global wildfire danger from 1979 to 2013. *Nat. Commun.*, 6(1):7537.

Kagan, L. and Sivashinsky, G. (2008). Pattern formation in flame spread over thin solid fuels. *Combust. Theory Model.*, 12(2):269–281.

Katz, Y., Tunstrøm, K., Ioannou, C. C., Huepe, C., and Couzin, I. D. (2011). Inferring the structure and dynamics of interactions in schooling fish. *Proc. Natl. Acad. Sci.*, 108(46):18720–18725.

Kaur, I., Mentrelli, A., Bosseur, F., Filippi, J.-B., and Pagnini, G. (2016). Turbulence and fire-spotting effects into wild-land fire simulators. *Commun. Nonlinear. Sci. Numer. Simul.*, 39:300–320.

Kaye, N. B. and Linden, P. F. (2004). Coalescing axisymmetric turbulent plumes. *J. Fluid Mech.*, 502:41–63.

Kehry, M., Klopper, W., and Holzer, C. (2023). Robust relativistic many-body Green's function based approaches for assessing core ionized and excited states. *J. Chem. Phys.*, 159(4).

Khan, N., Sutherland, D., and Moinuddin, K. (2023). Simulated behaviour of wildland fire spreading through idealised heterogeneous fuels. *Int. J. Wildland Fire*, 32(5):738–748.

Khan, S. A., Khan, K. A., Kubik, S., Ahmad, S., Ghramh, H. A., Ahmad, A., Skalicky, M., Naveed, Z., Malik, S., Khalofah, A., et al. (2021). Electric field detection as floral cue in hoverfly pollination. *Sci. Rep.*, 11(1):1–9.

Kirkwood, R. and Robertson, G. (1999). The occurrence and purpose of huddling by emperor penguins during foraging trips. *Emu*, 99(1):40–45.

Kittel, C., McEuen, P., and McEuen, P. (1996). *Introduction to solid state physics*, volume 8. Wiley New York, New York.

Ko, H., Yu, T.-Y., and Hu, D. L. (2022). Fire ant rafts elongate under fluid flows. *Bioinspir. Biomim.*, 17(4):045007.

Kooyman, G. L., Gentry, R. L., Bergman, W. P., and Hammel, H. T. (1976). Heat loss in penguins during immersion and compression. *Comp. Biochem. Physiol.*, 54(1):75–80.

Krishnamurthy, V. S., Wheeler, M. H., Crowdy, D. G., and Constantin, A. (2020). A transformation between stationary point vortex equilibria. *Proc. R. Soc. A.*, 476:20200310.

Ladd, A. J. C., Yu, L., and Szymczak, P. (2020). Dissolution of a cylindrical disk in Hele-Shaw flow: a conformal-mapping approach. *J. Fluid Mech.*, 903:A46.

Langer, J. S. (1980). Instabilities and pattern formation in crystal growth. *Rev. Mod. Phys.*, 52(1):1.

Lareau, N. P. and Clements, C. B. (2017). The mean and turbulent properties of a wildfire convective plume. *J. Appl. Meteorol. Climatol.*, 56(8):2289 – 2299.

Lareau, N. P., Nauslar, N. J., Bentley, E., Roberts, M., Emmerson, S., Brong, B., Mehle, M., and Wallman, J. (2022). Fire-generated tornadic vortices. *Bull. Am. Meteorol. Soc.*, 103(5):E1296–E1320.

Le Maho, Y. (1977). The emperor penguin: a strategy to live and breed in the cold: morphology, physiology, ecology, and behavior distinguish the polar emperor penguin from other penguin species, particularly from its close relative, the king penguin. *Am. Sci.*, 65(6):680–693.

Léger, J.-C. (1999). Menger curvature and rectifiability. *Ann. Math.*, 149(3):831–869.

Linn, R., Reisner, J., Colman, J. J., and Winterkamp, J. (2002). Studying wildfire behavior using FIRETEC. *Int. J. Wildland fire*, 11(4):233–246.

Liu, N., Lei, J., Gao, W., Chen, H., and Xie, X. (2021). Combustion dynamics of large-scale wildfires. *Proc. Combust. Inst.*, 38(1):157–198.

Lundberg, E. and Totik, V. (2013). Lemniscate growth. *Anal. Math. Phys.*, 3(1):45–62.

Malangone, L., Russo, P., and Vaccaro, S. (2011). Effects of wind and terrain slope on flames propagation in a vegetative fuel bed. *Submitted to the XXXIV Event of the Italian Section of the Combustion Institute*.

Mallet, V., Keyes, D., and Fendell, F. (2009). Modeling wildland fire propagation with level set methods. *Comput. Math. Appl.*, 57(7):1089–1101.

Mandel, J., Beezley, J., and Kochanski, A. (2011). Coupled atmosphere-wildland fire modeling with WRF 3.3 and SFIRE 2011. *Geosci. Model Dev.*, 4(3):591–610.

Markstein, G. (1964). Nonsteady Flame Propagation. *J. R. Aeronaut. Soc.*, 68(647):782–782.

Markstein, G. H. (1951). Experimental and theoretical studies of flame-front stability. *J. Aeronaut. Sci.*, 18(3):199–209.

Marshall, J. S. (2011). Steady uniform vortex patches around an assembly of walls or flat plates. *Q. J. Mech. Appl. Math.*, 65(1):27–60.

Martin, J. and Hillen, T. (2016). The spotting distribution of wildfires. *Appl. Sci.*, 6(6):177.

Masson-Delmotte, V., Zhai, P., Pirani, A., Connors, S. L., Péan, C., Berger, S., Caud, N., Chen, Y., Goldfarb, L., Gomis, M. I., Huang, M., Leitzell, K., Lonnoy, E., Matthews, J. B. R., Maycock, T. K., Waterfield, T., Yelekçi, O., Yu, R., and Zhou, B., editors (2021). *IPCC, 2021: Climate Change 2021: The Physical Science Basis. Contribution of Working Group I to the Sixth Assessment Report of the Intergovernmental Panel on Climate Change*. Cambridge University Press.

Maynard, T., Princevac, M., and Weise, D. R. (2016). A study of the flow field surrounding interacting line fires. *J. Combust.*, 2016.

McArthur, A. G. (1966). Weather and grassland fire behaviour. Forest Research Institute, Forest and Timber Bureau of Australia; 1966. Leaflet No. 100.

McCafferty, D., Gilbert, C., Thierry, A.-M., Currie, J., Le Maho, Y., and Ancel, A. (2013). Emperor penguin body surfaces cool below air temperature. *Biol. Lett.*, 9(3):20121192.

McDonald, N. R. and Harris, S. J. (2024). Exact and numerical solutions of a free boundary problem with a reciprocal growth law. *IMA J. Appl. Math.*, 89(2):374–386.

McDonald, N. R. and Mineev-Weinstein, M. (2014). Poisson growth. *Anal. Math. Phys.*, 5(2):193–205.

McWilliams, J. C. (1985). Submesoscale, coherent vortices in the ocean. *Rev. Geophys.*, 23(2):165–182.

Mell, W., Jenkins, M. A., Gould, J., and Cheney, P. (2007). A physics-based approach to modelling grassland fires. *Int. J. Wildland Fire*, 16(1):1–22.

Miller, C., Hilton, J., Sullivan, A., and Prakash, M. (2015). Spark–a bushfire spread prediction tool. In *International Symposium on Environmental Software Systems*, pages 262–271. Springer.

Mina, T. and Min, B.-C. (2018). Penguin huddling inspired distributed boundary movement for group survival in multi-robot systems using Gaussian processes. In *2018 IEEE International Conference on Robotics and Biomimetics*, pages 2177–2183. IEEE.

Mineev-Weinstein, M. (1998). Selection of the Saffman-Taylor finger width in the absence of surface tension: an exact result. *Phys. Rev. Lett.*, 80(10).

Mineev-Weinstein, M., Wiegmann, P. B., and Zabrodin, A. (2000). Integrable structure of interface dynamics. *Phys. Rev. Lett.*, 84:5106.

Miranda, J. and Widom, M. (1998). Radial fingering in a Hele-Shaw cell: a weakly nonlinear analysis. *Physica D*, 120(3-4):315–328.

Molina-Montenegro, M. A., Acuña-Rodríguez, I. S., Ballesteros, G. I., Baldelomar, M., Torres-Díaz, C., Broitman, B. R., and Vázquez, D. P. (2023). Electromagnetic fields disrupt the pollination service by honeybees. *Sci. Adv.*, 9(19):eadh1455.

Montgomery, C., Vuts, J., Woodcock, C. M., Withall, D. M., Birkett, M. A., Pickett, J. A., and Robert, D. (2021). Bumblebee electric charge stimulates floral volatile emissions in petunia integrifolia but not in antirrhinum majus. *Sci. Nat.*, 108:1–12.

Morley, E. L. and Robert, D. (2018). Electric fields elicit ballooning in spiders. *Curr. Bio.*, 28(14):2324–2330.

Morvan, D., Accary, G., Meradji, S., and Frangieh, N. (2022). Fifty years of progress in wildland fire modelling: from empirical to fully physical CFD models. *C.R. Mécanique*, 350(S1):1–9.

Mullins, W. W. and Sekerka, R. F. (1964). Stability of a planar interface during solidification of a dilute binary alloy. *J. Appl. Phys.*, 35(2):444–451.

Muskat, M. (1934). Two fluid systems in porous media. The encroachment of water into an oil sand. *Physics*, 5(9):250–264.

Nakatsukasa, Y., Sète, O., and Trefethen, L. N. (2018). The AAA algorithm for rational approximation. *SIAM J. Sci. Comp.*, 40(3):A1494–A1522.

Nakatsukasa, Y., Sete, O., and Trefethen, L. N. (2023). The first five years of the AAA algorithm. *arXiv preprint arXiv:231203565*.

Nakayama, K., Iizuka, T., and Wadati, M. (1994). Curve lengthening equation and its solutions. *J. Phys. Soc. Japan*, 63(4):1311–1321.

Nanda, I., De, R., et al. (2022). Study of electromagnetic radiation on flower. *Matrix Sci. Math.*, 6(2):58–63.

Nave Jr, G. K., Mitchell, N. T., Chan Dick, J. A., Schuessler, T., Lagarrigue, J. A., and Peleg, O. (2020). Attraction, dynamics, and phase transitions in fire ant tower-building. *Front. Robot. AI*, 7:25.

Newton, P. K. (2001). *The N-Vortex Problem*. Springer, Berlin.

Niemeyer, L., Pietronero, L., and Wiesmann, H. J. (1984). Fractal dimension of dielectric breakdown. *Phys. Rev. Lett.*, 52:1033–1036.

Osher, S. and Sethian, J. A. (1988). Fronts propagating with curvature-dependent speed: Algorithms based on Hamilton-Jacobi formulations. *J. Comput. Phys.*, 79(1):12–49.

O'Reilly, L. J., Palmer, R. A., Gaffney, J., Harris, B. H., Chenchiah, I. V., and Robert, D. (2024). Electromechanical sensitivity of spider hairs to prey-like electric fields. *J. Exp. Biol.*, (Under Review).

Palmer, R. A., Chenchiah, I. V., and Robert, D. (2021). Analysis of aerodynamic and electrostatic sensing in mechanoreceptor arthropod hairs. *J. Theor. Biol.*, 530:110871.

Palmer, R. A., Chenchiah, I. V., and Robert, D. (2022). The mechanics and interactions of electrically sensitive mechanoreceptive hair arrays of arthropods. *J. R. Soc. Interface*, 19(188):20220053.

Palmer, R. A., Chenchiah, I. V., and Robert, D. (2023a). Passive electrolocation in terrestrial arthropods: theoretical modelling of location detection. *J. Theor. Biol.*, 558:111357.

Palmer, R. A., O'Reilly, L. J., Carpenter, J., Chenchiah, I. V., and Robert, D. (2023b). An analysis of time-varying dynamics in electrically sensitive arthropod hairs to understand real-world electrical sensing. *J. R. Soc. Interface*, 20(205):20230177.

Papadopoulos, G. and Pavlidou, F.-N. (2011). A comparative review on wildfire simulators. *IEEE Syst. J.*, 5(2):233–243.

Pastor, E., Zárate, L., Planas, E., and Arnaldos, J. (2003). Mathematical models and calculation systems for the study of wildland fire behaviour. *Prog. Energy Combust. Sci.*, 29(2):139–153.

Paterson, L. (1981). Radial fingering in a Hele Shaw cell. *J. Fluid Mech.*, 113:513–529.

Pausas, J. G. and Keeley, J. E. (2019). Wildfires as an ecosystem service. *Front. Ecol. Environ.*, 17(5):289–295.

Perry, G. L. W. (1998). Current approaches to modelling the spread of wildland fire: a review. *Prog. Phys. Geogr.*, 22(2):222–245.

Pierrehumbert, R. T. (1980). A family of steady, translating vortex pairs with distributed vorticity. *J. Fluid Mech.*, 99(1):129–144.

Quaife, B. and Speer, K. (2021). A simple model for wildland fire vortex–sink interactions. *Atmosphere*, 12(8):1014.

Ribeiro, C., Viegas, D. X., Raposo, J., Reis, L., and Sharples, J. (2023). Slope effect on junction fire with two non-symmetric fire fronts. *Int. J. Wildland Fire*, 32(3):328–335.

Riccardi, G. (2020). Remarks on equilibria of two-dimensional uniform vortices with polygonal symmetry. *Eur. J. Mech. B/Fluids*, 83:1–14.

Richter, S., Gerum, R., Winterl, A., Houstin, A., Seifert, M., Peschel, J., Fabry, B., Le Bohec, C., and Zitterbart, D. P. (2018). Phase transitions in huddling emperor penguins. *J. Phys. D Appl. Phys.*, 51(21):214002.

Roberts, S. (1993). A line element algorithm for curve flow problems in the plane. *ANZIAM J.*, 35(2):244–261.

Rothermel, R. (1972). *A mathematical model for predicting fire spread in wildland fuels*, volume 115. Intermountain Forest & Range Experiment Station, Forest Service, US Department of Agriculture.

Ryan, C., Burns, L., and Broders, H. (2019). Changes in underground roosting patterns to optimize energy conservation in hibernating bats. *Can. J. Zool.*, 97(11):1064–1070.

Rycroft, C. and Bazant, M. (2016). Asymmetric collapse by dissolution or melting in a uniform flow. *Proc. Roy. Soc. A*, 472(2185):20150531.

Saffman, P. G. (1995). *Vortex dynamics*. Cambridge University Press.

Saffman, P. G. and Taylor, G. I. (1958). The penetration of a fluid into a porous medium or Hele-Shaw cell containing a more viscous liquid. *Proc. R. Soc. Lond. A.*, 245(1242):312–329.

Santoni, P. A., Bartoli, P., Simeoni, A., and Torero, J. L. (2014). Bulk and particle properties of pine needle fuel beds–influence on combustion. *Int. J. Wildland Fire*, 23(8):1076–1086.

Sethian, J. A. (1985). Curvature and the evolution of fronts. *Commun. Math. Phys.*, 101(4):487–499.

Sethian, J. A. (2001). Evolution, implementation, and application of level set and fast marching methods for advancing fronts. *J. Comp. Phys.*, 169(2):503–555.

Sharples, J. J. and Hilton, J. (2017). Modelling the dynamic behaviour of small scale junction fires using curvature flows. In *22nd International Congress on Modelling and Simulation.*, pages 1166–1172.

Sharples, J. J. and Hilton, J. E. (2020). Modeling vorticity-driven wildfire behavior using near-field techniques. *Front. Mech. Eng.*, page 69.

Sharples, J. J., Hilton, J. E., Badlan, R. L., Thomas, C. M., McRae, R. H. D., Speer, K., and Goodrick, S. (2022). Fire line geometry and pyroconvective dynamics. In *Wildland Fire Dynamics: Fire Effects and Behavior from a Fluid Dynamics Perspective*, pages 77–128. Cambridge University Press.

Sharples, J. J., Towers, I. N., Wheeler, G., Wheeler, V.-M., and McCoy, J. A. (2013). Modelling fire line merging using plane curvature flow. In *20th International Congress on Modelling and Simulation*, pages 256–262, Adelaide, Australia.

Smith, R. K., Morton, B. R., and Leslie, L. M. (1975). The role of dynamic pressure in generating fire wind. *J. Fluid Mech.*, 68(1):1–19.

Soma, S. and Saito, K. (1991). Reconstruction of fire whirls using scale models. *Combust. Flame*, 86(3):269–284.

Speer, K. and Goodrick, S. (2022). *Wildland Fire Dynamics: Fire Effects and Behavior from a Fluid Dynamics Perspective*. Cambridge University Press.

Sullivan, A. L. (2009a). Wildland surface fire spread modelling, 1990–2007. 1: Physical and quasi-physical models. *Int. J. Wildland Fire*, 18:349–368.

Sullivan, A. L. (2009b). Wildland surface fire spread modelling, 1990–2007. 2: Empirical and quasi-empirical models. *Int. J. Wildland Fire*, 18:369–386.

Sullivan, A. L. (2009c). Wildland surface fire spread modelling, 1990–2007. 3: Simulation and mathematical analogue models. *Int. J. Wildland Fire*, 18:387–403.

Sullivan, A. L., Speer, K., and Goodrick, S. (2022). Wildland fire combustion dynamics: The intersection of combustion chemistry and fluid dynamics. In *Wildland Fire Dynamics: Fire Effects and Behavior from a Fluid Dynamics Perspective*, pages 1–34. Cambridge University Press.

Sullivan, A. L., Swedosh, W., Hurley, R. J., Sharples, J. J., and Hilton, J. E. (2019). Investigation of the effects of interactions of intersecting oblique fire lines with and without wind in a combustion wind tunnel. *Int. J. Wildland Fire*, 28(9):704–719.

Sun, R., Krueger, S. K., Jenkins, M. A., Zulauf, M. A., and Charney, J. J. (2009). The importance

of fire–atmosphere coupling and boundary-layer turbulence to wildfire spread. *Int. J. Wildland Fire*, 18(1):50–60.

Symm, G. T. (1967). Numerical mapping of exterior domains. *Numer. Math.*, 10(5):437–445.

Taylor, G. and Saffman, P. (1959). A note on the motion of bubbles in a Hele-Shaw cell and porous medium. *Q. J. Mech. Appl. Math.*, 12(3):265–279.

Thomas, C. M. (2019). *Investigation of spotting and intrinsic fire dynamics using a coupled atmosphere-fire modelling framework*. PhD thesis, University of New South Wales.

Thomas, C. M., Sharples, J. J., and Evans, J. P. (2017). Modelling the dynamic behaviour of junction fires with a coupled atmosphere–fire model. *Int. J. Wildland Fire*, 26(4):331–344.

Tohidi, A., Gollner, M., and Xiao, H. (2018). Fire whirls. *Annu. Rev. Fluid Mech.*, 50(1):187–213.

Trefethen, L. (2020). Numerical conformal mapping with rational functions. *Comput. Methods Funct. Theory*, 20(3):369–387.

Trefethen, L. N. (2018). Series solution of Laplace problems. *ANZIAM J.*, 60(1):1–26.

Trelles, J. and Pagni, P. (1997). Fire-induced winds in the 20 October 1991 Oakland Hills fire. *Fire Saf. Sci.*, 5:911–922.

Tsai, V. and Wettlaufer, J. (2007). Star patterns on lake ice. *Phys. Rev. E*, 75(6):066105.

Urban, J. L., Song, J., Santamaria, S., and Fernandez-Pello, C. (2019). Ignition of a spot smolder in a moist fuel bed by a firebrand. *Fire Saf. J.*, 108:102833.

Viegas, D. X., Raposo, J. R., Davim, D. A., and Rossa, C. G. (2012). Study of the jump fire produced by the interaction of two oblique fire fronts. Part 1. Analytical model and validation with no-slope laboratory experiments. *Int. J. Wildland Fire*, 21(7):843–856.

Waters, A., Blanchette, F., and Kim, A. D. (2012). Modeling huddling penguins. *PLoS ONE*, 7(11):e50277.

Weber, R., Mercer, G., Sidhu, H., and Gray, B. (1997). Combustion waves for gases (L$e = 1$) and solids (L$e \to \infty$). *Proc. R. Soc. Lond. A*, 453(1960):1105–1118.

Weber, R. O. (1991). Modelling fire spread through fuel beds. *Prog. Energy Combust. Sci.*, 17(1):67–82.

Weihs, D. and Small, R. D. (1986). Interactions and spreading of adjacent large area fires. Technical report, Pacific-Sierra Research Corp., Los Angeles, CA (USA).

Wheeler, V.-M., Wheeler, G. E., McCoy, J. A., and Sharples, J. J. (2015). Modelling dynamic bushfire spread: perspectives from the theory of curvature flow. In *21st International Congress on Modelling and Simulation*, pages 319–325, Gold Coast, Australia.

Williams, C. L., Hagelin, J. C., and Kooyman, G. L. (2015). Hidden keys to survival: the type, density, pattern and functional role of emperor penguin body feathers. *Proc. R. Soc. B.*, 282(1817):20152033.

Wu, H. M., Overman II, E. A., and Zabusky, N. J. (1984). Steady-state solutions of the Euler equations in two dimensions: rotating and translating V-states with limiting cases. I. Numerical algorithms and results. *J. Comp. Phys.*, 53(1):42–71.

Xue, B. B. (2017). *Dynamics of beach vortices and multipolar vortex patches.* PhD thesis, University College London.

Xue, B. B., Johnson, E. R., and McDonald, N. R. (2017). New families of vortex patch equilibria for the two-dimensional Euler equations. *Phys. Fluids*, 29(12).

Xue, C., Xu, L., Wang, H., Liu, H., Yin, J., Li, X., and Li, B. (2023). A rational function approximation algorithm for the frequency sweep of microwave tube. In *2023 24th Int. Vacuum Electronics Conf. (IVEC)*, pages 1–2. IEEE.

Yfantidou, A., Zoka, M., Stathopoulos, N., Kokkalidou, M., Girtsou, S., Tsoutsos, M.-C., Hadjimitsis, D., and Kontoes, C. (2023). Geoinformatics and machine learning for comprehensive fire risk assessment and management in peri-urban environments: A building-block-level approach. *Appl. Sci.*, 13(18):10261.

Zik, O., Olami, Z., and Moses, E. (1998). Fingering instability in combustion. *Phys. Rev. Lett.*, 81:3868–3871.

Zitterbart, D., Wienecke, B., Butler, J., and Fabry, B. (2011). Coordinated movements prevent jamming in an emperor penguin huddle. *PLoS ONE*, 6(6):e20260.

Żukowski, S., Cornelissen, A. J. M., Osselin, F., Douady, S., and Szymczak, P. (2024). Breakthrough-induced loop formation in evolving transport networks. *Proc. Natl. Acad. Sci. U.S.A.*, 121(29):e2401200121.